

Forschungsbericht 2016-23

Experimental Investigation of Rarefaction Effects on Aerodynamic Coefficients of Slender and Blunt Re-entry Vehicles

Thomas Schlegat

Deutsches Zentrum für Luft- und Raumfahrt
Institut für Aerodynamik und
Strömungstechnik
Göttingen

134 Seiten

124 Bilder

7 Tabellen

97 Literaturstellen



DLR

Deutsches Zentrum
für Luft- und Raumfahrt

Experimental Investigation of Rarefaction Effects
on Aerodynamic Coefficients of
Slender and Blunt Re-entry Vehicles

*(Experimentelle Untersuchung der Verdünnungseffekte
auf die aerodynamischen Beiwerte von
schlanken und stumpfen Wiedereintrittskonfigurationen)*

Dissertation zur Erlangung des Doktorgrades der
Naturwissenschaftlichen Fakultät der Justus-Liebig-Universität
Gießen (Dr. rer. nat), I. Physikalische Institut

vorgelegt von

Thomas Schlegat

aus Ravensburg

Erstgutachter: Prof. Dr. Klaus Hannemann
Zweitgutachter: Prof. Dr. Markus Thoma

Tag der Disputation: 19. April 2018

Abstract

The prediction of the flight stability and of the aerodynamic coefficients in the transition region between the rarefied and the continuum flow regime is important for the design of hypersonic vehicles. The aim of this investigation is to analyse experimentally how aerodynamics – lift, drag and pitching moment – of re-entry and hypersonic transport vehicles is affected by rarefaction effects for classical “blunt bodies” and high lift / drag flight configurations. The analysis is conducted by experiments in the DLR Hypersonic Vacuum Wind Tunnel Göttingen (VxG), a continuously operating facility which can simulate hypersonic flows around vehicle configurations in this gas kinetic transition regime.

For the analysis of aerodynamic forces a measurement technique is established for the 2nd test section of the Hypersonic Vacuum Wind Tunnel Göttingen (V2G). The 3-component strain gauge force balance is based on the design of former V2G force balances, and is optimised to obtain a better resolution and improved zero-point stability which results in precision improvement of the output signal during the experiment.

Based on the relation of Knudsen number to Mach number and Reynolds number, the experimental test matrix is setup. For a non-ambiguous result it is important to vary only one parameter at a time. Applying the Mach number independence principle, it is straight forward to vary the Mach number since the resulting effect can be interpreted as a pure effect of rarefaction. Although the experimental setup allows a factor two of Mach number and, hence, an equal variation of Knudsen number, the variation is little considering the overall rarefaction regime covers about three magnitudes of Knudsen numbers. By performing several test series, each at a constant Reynolds number, it is possible to extend the Knudsen number variation to one order of magnitude. This assumption requires that the Reynolds number influence is of secondary importance. This and the applicability of the Mach number independence principle is addressed in the discussion of the results. Further the effect of the flow inhomogeneity is evaluated.

This analysis contains an investigation of one blunt test configuration (COLIBRI) and one slender test configuration (SHEFEX III) both investigated at angles of attack between 0° and 34° in 2° steps at 26 test conditions in the rarefied flow. The rarefaction effects are analysed and assessed individually for lift-, drag- and pitching moment coefficient and lift / drag ratio. Within the analysed Knudsen number range between $7 * 10^{-4}$ and $9 * 10^{-3}$, significant rarefaction effects could be observed in all considered aerodynamic coefficients. The effects are strong enough to cause a reduction in lift / drag ratio of up to more than 50%. In parallel to the evaluation of aerodynamic coefficients versus Knudsen number, the evaluation is conducted as well versus the rarefaction parameter. The rarefaction parameter is an appropriate parameter to distinguish flow regimes in the transition region between rarefied flow and continuum, where rarefaction effects start to arise but boundary layers are still defining the overall flow field.

Based on the obtained aerodynamic data, solvers for rarefied flow can be compared and simplified engineering methods, as e.g. bridging methods can be developed. These tools are especially important for the pre-design and optimisation phase where fast and simple tools are necessary.

Zusammenfassung

Die Vorhersage von Flugstabilität und aerodynamischen Beiwerten im Übergangsbereich zwischen verdünnter Strömung und Kontinuumsströmung sind von hoher Wichtigkeit für die Auslegung hypersonischer Flugobjekte. Ziel dieser Untersuchung ist eine experimentelle Analyse, wie Auftrieb, Widerstand und Nickmoment von Wiedereintrittsraumfahrzeugen und hypersonischen Transportflugzeugen durch Verdünnungseffekte beeinflusst werden. Verglichen wird dabei eine klassische stumpfe Flugkonfiguration mit einer fortschrittlichen Flugkonfiguration hoher Gleitzahl. Die Analyse wird basierend auf Experimenten im Hypersonischen Vakuumwindkanal Göttingen (VxG) durchgeführt, in welchem hypersonische Strömungen um Flugkonfigurationen im gaskinetischen Übergangsbereich bei kontinuierlichem Messbetrieb simuliert werden können.

Zur Analyse der aerodynamischen Kräfte wird an der zweiten Messtrecke des Hypersonischen Vakuumwindkanals Göttingen (V2G) eine Kraftmesstechnik etabliert. Angelehnt an die Bauweise früherer V2G Kraftwaagen wird eine 3-Komponenten-Dehnmessstreifenkraftwaage mit besserer Auflösung und verbesserter Nullpunktstabilität entwickelt.

Basierend auf der Beziehung zwischen Knudsen-, Mach- und Reynoldszahl wird die experimentelle Versuchsmatrix erstellt. Für eindeutige Ergebnisse ist dabei wichtig, dass in den Experimenten jeweils nur ein Parameter variiert wird. Unter Berücksichtigung des Machzahlunabhängigkeitsprinzips ist es für die Variation der Knudsenzahl naheliegend, bei konstanter Reynoldszahl die Machzahl zu variieren, da so die beobachteten Änderungen als reine Verdünnungseffekte interpretiert werden können. Um die Knudsenzahlvariation auf eine Größenordnung zu erweitern, werden weitere Testreihen bei jeweils konstant gehaltener Reynoldszahl durchgeführt. Dieses Vorgehen setzt voraus, dass der Reynoldszahleinfluss von untergeordneter Wichtigkeit ist, und wird bei der Ergebnisbewertung diskutiert. Dort wird auch der Effekt der Strömungsinhomogenität adressiert.

Für die Untersuchungen in dieser Arbeit werden eine stumpfe (COLIBRI) und eine schlanke Flugkonfiguration (SHEFEX III) gewählt. Analysiert werden die Konfigurationen im Anstellwinkelbereich zwischen 0° und 34° in 2° -Schritten an 26 Versuchsbedingungen im verdünnten Strömungsbereich. Die Verdünnungseffekte werden separat für Auftrieb-, Widerstand- und Nickmomentenbeiwert, sowie für die Gleitzahl analysiert und bewertet. Im analysierten Knudsenzahlbereich zwischen $7 \cdot 10^{-4}$ und $9 \cdot 10^{-3}$ können signifikante Verdünnungseinflüsse bei allen untersuchten aerodynamischen Beiwerten festgestellt werden, welche in Gleitzahleinbußen von bis zu über 50% resultieren. Parallel zur Untersuchung der aerodynamischen Beiwerte gegenüber der Knudsenzahl wird eine Betrachtung gegenüber dem Verdünnungsparameter durchgeführt. Dieser wird insbesondere für den Übergangsbereich zwischen dem verdünnten Strömungsbereich und der Kontinuumsströmung herangezogen, da trotz der beginnenden Verdünnungseffekte die Grenzschichten das Strömungsbild noch maßgeblich beeinflussen.

Die erhaltenen aerodynamischen Daten können als Vergleichsquelle für numerische Rechenverfahren im verdünnten Strömungsbereich, wie auch für die Erstellung vereinfachter Ingenieursmethoden zur Abschätzung der Aerodynamik, so genannter Bridging Methoden, genutzt werden. Diese Ingenieursmethoden sind von hoher Wichtigkeit für die Vorauslegung- und Optimierungsphase, welche schnelle und einfache Rechenverfahren erfordert.

Erklärung

Ich erkläre:

Ich habe die vorgelegte Dissertation selbstständig und ohne unerlaubte fremde Hilfe und nur mit den Hilfen angefertigt, die ich in der Dissertation angegeben habe.

Alle Textstellen, die wörtlich oder sinngemäß aus veröffentlichten Schriften entnommen sind, und alle Angaben, die auf mündlichen Auskünften beruhen, sind als solche kenntlich gemacht.

Ich stimme einer evtl. Überprüfung meiner Dissertation durch eine Antiplagiat-Software zu.

Bei den von mir durchgeführten und in der Dissertation erwähnten Untersuchungen habe ich die Grundsätze guter wissenschaftlicher Praxis, wie sie in der „Satzung der Justus-Liebig-Universität Gießen zur Sicherung guter wissenschaftlicher Praxis“ niedergelegt sind, eingehalten.

Table of Contents

Abstract.....	I
Zusammenfassung	II
Erklärung	III
Table of Contents	V
List of Figures.....	VII
List of Tables.....	XI
Abbreviations.....	XII
Nomenclature	XV
1 Introduction.....	1
1.1 Hypersonic High Altitude Flight	1
1.2 High Lift / Drag Design.....	4
1.3 Established Prediction Methods.....	6
1.4 Investigation of Rarefaction Effects – Present Status and Aim of Analysis	9
2 Characteristics of Rarefied Flow	11
2.1 Definition of Rarefied Flow.....	11
2.2 Molecule Surface Interaction.....	12
2.3 Similarity Parameters.....	13
2.4 Mach Number Independence Principle	17
3 Test Facility V2G	19
3.1 Operating Principle	19
3.2 Standard Measurement Technique.....	22
3.3 Supplemental Measurement Devices and Test Article Support	23
3.4 Force Balance	24
3.4.1 Requirements and Design Limitations	24
3.4.2 Load Determination	26
3.4.3 V2G Strain Gauge Balance Principle	27
3.4.4 Design & Concept.....	28
3.4.5 V2G Strain Gauge Circuitry	28
3.4.6 V2G Force Measurement Technique.....	30
3.4.7 Analytical Approach.....	32
3.5 Test Article Design	36
4 Preparation of Experiments	40
4.1 Facility Setup	40
4.2 Test Article Selection.....	40

4.3	Determination of Operating Conditions.....	43
4.4	Radial and Axial Pitot Pressure.....	46
4.5	Test Matrix Definition.....	50
4.6	Model Support	53
4.7	Balance Improvements	54
4.8	Balance Calibration	58
5	Performance of Force Measurements	61
5.1	Procedure	61
5.2	Measurements.....	64
5.3	Evaluation.....	65
6	Rarefaction Effects.....	72
6.1	Comparison at Constant Reynolds Number	72
6.1.1	Aerodynamic Coefficients versus Angle of Attack at Constant Reynolds Numbers.....	72
6.1.2	Aerodynamic Coefficients versus Knudsen Number at Constant Angles of Attack.....	79
6.1.3	Aerodynamic Coefficients versus Rarefaction Parameter at Constant Angles of Attack	87
6.1.4	Assessing Mach and Reynolds Number Effects.....	92
6.1.5	Comparing Effects of Rarefaction of Both Test Configurations.....	95
6.2	Comparison at Constant Knudsen Number	99
6.3	Comparison Flow Inhomogeneity at Constant Reynolds Number	103
7	Summary	108
8	Outlook and further Use for Numerical Comparisons.....	111
9	Acknowledgements	112
10	References	113
	Appendix A – General Facts, Specifications and Derivations	119
	Appendix B – Rarefaction Effects.....	123

List of Figures

Fig. 1: Layers of earth atmosphere based on data from various text books e.g. ^[57]	1
Fig. 2: Atmospheric entry flight paths on a velocity-altitude map modified from ^[4] and qualitatively sketched envelope of space tourism trajectories	2
Fig. 3: Trajectory of SpaceShipOne ^[71] (nm = nautical miles, ft = feet)	3
Fig. 4: Longitudinal and cross range depending on aerodynamic efficiency modified from ^[12]	4
Fig. 5: Aerodynamic efficiency of re-entry vehicles modified from ^[12]	5
Fig. 6: Rarefaction limits for numerical prediction methods modified from ^[6]	7
Fig. 7: Numerical and experimental methods	8
Fig. 8: Investigated blunt and slender configurations	10
Fig. 9: Constant Reynolds number analysis with V2G operating range	10
Fig. 10: Transition of flow regimes visualised by Legge ^[48]	11
Fig. 11: Gas body surface interaction, mirrored, diffuse and mixed reflection of molecules on the surface (top), detailed view of diffuse reflection on real surface (bottom) ^[45]	13
Fig. 12: Free path at ground level (top) and in space (bottom).....	14
Fig. 13: Constant Knudsen numbers in Mach number versus Reynolds number plot (based on ^[85])	15
Fig. 14: Drag coefficient for a sphere and cone cylinders gathered and compared by Anderson ^[4] from ^{[15], [27], [86]}	17
Fig. 15: V2G side view (top) and V2G sketch with roughly, in green sketched test rhombus (bottom).....	19
Fig. 16: Picture of vacuum pump facility in cellar with 21 pumps (left), picture of biggest vacuum pump in front compared to 2 m high door (right).....	20
Fig. 17: V2G force measurements (test article with the 3-component force balance located in water-cooled housing)	22
Fig. 18: Pitot tube test regime $0 \leq x \leq 449$ mm, $-187 \leq y \leq 187$ mm, $z = 0$ mm (left), Pitot tube coordinate system and CAD drawing (right)	22
Fig. 19: Standard surveillance measurement device positions and movable mechanics at V2G, tunnel coordinate system origin located at intersection between nozzle exit plane and tunnel axis	22
Fig. 20: Sphere for heat transfer measurements (located in V2G core flow).....	24
Fig. 21: Sketch of force measurement setup in V2G (top view), weight forces act normal to the drawing plane	25
Fig. 22: Sketch of V2G force balance.....	26
Fig. 23: Light weight COLIBRI test article, hull (left), inner structure (right)	26
Fig. 24: Strain gauge measurement principle (left), foil strain gauge (right).....	27
Fig. 25: Narrowing for strain gauge attachment	28
Fig. 26: 3-component balance (normal and tangential force transducer)	28
Fig. 27: Wheatstone bridge circuitry, half bridge (left), full bridge (right).....	29
Fig. 28: V2G force balance sketch (BM: bending moment signal, BYF, BYB: stain gauge positions, DX: axial drag signal, COG: centre of gravity).....	30
Fig. 29: Coordinate system transformation from balance to aerodynamic system	31
Fig. 30: Picture of V2G force balance	31
Fig. 31: Normal force transducer reference model with applied loads.....	32
Fig. 32: Reference model of tangential force transducer (left), simplified and subdivided (right)	33

Fig. 33: Statically determined tangential force transducer (left), together with local coordinate systems (right)	34
Fig. 34: Balance deformation caused by applied normal- and tangential loads and pitching moments.....	35
Fig. 35: Deformations shown on balance geometry	36
Fig. 36: Electrolytic metal separation on a positive core of SHEFEX III with adjustment planes for post-processing at the support structure in the background	37
Fig. 37: CAD drawing of V2G SHEFEX III test article	38
Fig. 38: CAD cut drawing of revised SHEFEX III test article.....	39
Fig. 39: CAD cut drawing of revised COLIBRI test article (heat shield not displayed).....	39
Fig. 40: Nozzle core parts with 2 mm and 10 mm throat diameter.....	40
Fig. 41: CAD drawing of SHEFEX III (left) and COLIBRI (right).....	41
Fig. 42: SHEFEX Development Strategy ^[17]	41
Fig. 43: Ratio of projected area / wetted area of test articles and reference configurations.....	42
Fig. 44: Sketch for the explanation of slenderness of flight configurations ^[4]	43
Fig. 45: Side view of CAD drawing of SHEFEX III (left) and COLIBRI (right)	43
Fig. 46: Qualitative V2G operating ranges	44
Fig. 47: Pitot pressure condensation measurements, $d^* = 2$ mm, Pitot tube at $x = 448$ mm, $y = 0$ mm	45
Fig. 48: Pitot pressure radial profile for cond. no. 3, see Table 3 or in detail ^[79] (M_1 , Re_1 , Kn_1 based on data at $x = 150$ mm, $y = 0$ mm, ref. length = 100 mm).....	47
Fig. 49: Sketch of V2G flow field and radial Pitot pressure profiles for both conical (top) and contoured nozzle (bottom).....	47
Fig. 50: Selected Pitot pressure radial profiles of Fig. 48 (contoured nozzle cond. no. 3, see Table 3 or in detail ^[79]).....	48
Fig. 51: Pitot pressure axial profile for cond. no. 3 with test article location (grey), see Table 3 or in detail ^[79]	49
Fig. 52: V2G operating conditions	50
Fig. 53: FAST20XX operating conditions vs. rarefaction parameters introduced by Schaaf & Chambré ^[73] shown with lifting body test article HERMES	51
Fig. 54: Test matrix of constant Reynolds number analysis with V2G operating range (shaded grey).....	52
Fig. 55: Model support (left), angle of attack adjustment (right).....	54
Fig. 56: Support frames allowing pre-setting of the angle of attack	54
Fig. 57: Improvement in reducing zero point drift for BYB, comparison of (») forward and («) backward sweep (FAST20XX cond. no. 5, $d^* = 2$ mm, $p_o = 10$ bar, $T_o = 778$ K, HERMES and present analysis cond. no. 4, $d^* = 2$ mm, $p_o = 40$ bar, $T_o = 1090$ K, SHEFEX III).....	56
Fig. 58: Pitching moment measurements at selected operating conditions: ¹ : FAST20XX results, ² : results of former test campaign in late 1980s	57
Fig. 59: Side (top) and top (bottom) view of balance calibration setup	58
Fig. 60: Balance response to a defined tangential load (y and σ in [V])	59
Fig. 61: Balance response to a defined normal load (y and σ in [V]).....	60
Fig. 62: Shielded test article during facility start-up and shut-down.....	61
Fig. 63: Test articles during experimental analysis: SHEFEX III (left), COLIBRI (right)	62
Fig. 64: Raw signal and averaged values (cond. 4)	63
Fig. 65: Frequency spectrum between 1 Hz and 160 Hz of raw signal (cond. 4, $\alpha = 0^\circ$).....	63

Fig. 66: Signal quick check for cond. no. 4, SHEFEX III, (») forward sweep («) backward sweep (see Table 3 or in detail ^[79])	64
Fig. 67: Compensated thermal zero point drift for cond. no. 4, SHEFEX III, (») forward sweep («) backward sweep (see Table 3 or in detail ^[79]).....	65
Fig. 68: Measurement plane (blue) and normal acting test article weight	65
Fig. 69: Forces and moments in aerodynamic coordinate system for cond. no. 4, SHEFEX III, (see Table 3 or in detail ^[79]).....	66
Fig. 70: Force and moment coefficients in aerodynamic coordinate system for cond. no. 4, SHEFEX III, (see Table 3 or in detail ^[79])	67
Fig. 71: Force and moment coefficients in aerodynamic coordinate system of cond. no. 4, COLIBRI, (see Table 3 or in detail ^[79]).....	67
Fig. 72: Detail of force and moment coefficients in aerodynamic coordinate system for cond. no. 4, SHEFEX III	69
Fig. 73: Pitching moment distortion due to inhomogeneous dynamic pressure.....	70
Fig. 74: Pitot pressure axial profile for cond. no. 3 with test article location (SHEFEX III) at different angles of attack (grey).....	70
Fig. 75: Rarefaction effects on aerodynamic coefficients ($Re_1 = 2.5e+4$, SHEFEX III).....	75
Fig. 76: Rarefaction effects on aerodynamic coefficients ($Re_1 = 4.6e+3$, SHEFEX III).....	76
Fig. 77: Rarefaction effects on aerodynamic coefficients ($Re_1 = 2.0e+4$, COLIBRI)	77
Fig. 78: Rarefaction effects on aerodynamic coefficients ($Re_1 = 3.8e+3$, COLIBRI)	78
Fig. 79: Rarefaction effects on aerodynamic coefficients shown vs. Knudsen number (SHEFEX III, $\alpha = 0^\circ$)	82
Fig. 80: Rarefaction effects on aerodynamic coefficients shown vs. Knudsen number (SHEFEX III, $\alpha = 10^\circ$)	82
Fig. 81: Rarefaction effects on aerodynamic coefficients shown vs. Knudsen number (SHEFEX III, $\alpha = 20^\circ$)	83
Fig. 82: Rarefaction effects on aerodynamic coefficients shown vs. Knudsen number (SHEFEX III, $\alpha = 30^\circ$)	83
Fig. 83: Rarefaction effects on aerodynamic coefficients shown vs. Knudsen number (COLIBRI, $\alpha = 0^\circ$)	84
Fig. 84: Rarefaction effects on aerodynamic coefficients shown vs. Knudsen number (COLIBRI, $\alpha = 10^\circ$)	84
Fig. 85: Rarefaction effects on aerodynamic coefficients shown vs. Knudsen number (COLIBRI, $\alpha = 20^\circ$)	85
Fig. 86: Rarefaction effects on aerodynamic coefficients shown vs. Knudsen number (COLIBRI, $\alpha = 30^\circ$).....	85
Fig. 87: Normal and tangential fractions of lift and drag (at the wall)	86
Fig. 88: Rarefaction effects on aerodynamic coefficients shown vs. rarefaction parameter (SHEFEX III, $\alpha = 0^\circ$)	88
Fig. 89: Rarefaction effects on aerodynamic coefficients shown vs. rarefaction parameter (SHEFEX III, $\alpha = 10^\circ$)	88
Fig. 90: Rarefaction effects on aerodynamic coefficients shown vs. rarefaction parameter (SHEFEX III, $\alpha = 20^\circ$)	89
Fig. 91: Rarefaction effects on aerodynamic coefficients shown vs. rarefaction parameter (SHEFEX III, $\alpha = 30^\circ$)	89
Fig. 92: Rarefaction effects on aerodynamic coefficients shown vs. rarefaction parameter (COLIBRI, $\alpha = 0^\circ$)	90

Fig. 93: Rarefaction effects on aerodynamic coefficients shown vs. rarefaction parameter (COLIBRI, $\alpha = 10^\circ$)	90
Fig. 94: Rarefaction effects on aerodynamic coefficients shown vs. rarefaction parameter (COLIBRI, $\alpha = 20^\circ$)	91
Fig. 95: Rarefaction effects on aerodynamic coefficients shown vs. rarefaction parameter (COLIBRI, $\alpha = 30^\circ$)	91
Fig. 96: Mach number effects on aerodynamic coefficients (SHEFEX III, $\alpha = 0^\circ$)	93
Fig. 97: Mach number effects on aerodynamic coefficients (SHEFEX III, $\alpha = 10^\circ$)	93
Fig. 98: Mach number effects on aerodynamic coefficients (COLIBRI, $\alpha = 0^\circ$)	94
Fig. 99: Mach number effects on aerodynamic coefficients (COLIBRI, $\alpha = 10^\circ$)	94
Fig. 100: Rarefaction effects on aerodynamic coefficients approximated with linear regression line for COLIBRI, $\alpha = 30^\circ$	95
Fig. 101: Ratio of lift coefficients of high to low Knudsen numbers (calculated with linear trend line at: $_1$: minimum Knudsen number, $_2$: maximum Knudsen number)	97
Fig. 102: Ratio of drag coefficients of high to low Knudsen numbers (calculated with linear trend line at: $_1$: minimum Knudsen number, $_2$: maximum Knudsen number)	98
Fig. 103: Ratio of lift / drag ratios of high to low Knudsen numbers (calculated with linear trend line at: $_1$: minimum Knudsen number, $_2$: maximum Knudsen number)	98
Fig. 104: Ratio of pitching moment coefficients of high to low Knudsen numbers (calculated with linear trend line at: $_1$: minimum Knudsen number, $_2$: maximum Knudsen number)	99
Fig. 105: Reynolds number effects on aerodynamic coefficients ($Kn_1 = 3.1e-3$, SHEFEX III)	101
Fig. 106: Reynolds number effects on aerodynamic coefficients ($Kn_1 = 3.8e-3$, COLIBRI)	102
Fig. 107: Mach number isolines : smooth nozzle contour (top), slight nozzle part misalignment and resulting time-independent spatial fluctuations (bottom) ^[80]	103
Fig. 108: Pitot pressure profiles with positive pressure peaks in core flow centre (cond. 10)	105
Fig. 109: Pitot pressure profiles with negative pressure peaks in core flow centre (cond. 15)	105
Fig. 110: Influence of flow inhomogeneity on aerodynamic coefficients ($Re_1 = 1.02e+4$, SHEFEX III)	106
Fig. 111: Influence of flow inhomogeneity on aerodynamic coefficients ($Re_1 = 8.33e+3$, COLIBRI)	107
Fig. 112: Sketch of VxG facility	120
Fig. 113: Sketch of VxG facility (reduced to V2G relevant infrastructure)	121
Fig. 114: Flow chart of data processing procedure ^[77]	122
Fig. 115: Rarefaction effects on aerodynamic coefficients ($Re_1 = 2.5e+4$, SHEFEX III)..	124
Fig. 116: Rarefaction effects on aerodynamic coefficients ($Re_1 = 1.5e+4$, SHEFEX III)..	125
Fig. 117: Rarefaction effects on aerodynamic coefficients ($Re_1 = 7.9e+3$, SHEFEX III)..	126
Fig. 118: Rarefaction effects on aerodynamic coefficients ($Re_1 = 4.6e+3$, SHEFEX III)..	127
Fig. 119: Rarefaction effects on aerodynamic coefficients ($Re_1 = 2.7e+3$, SHEFEX III)..	128
Fig. 120: Rarefaction effects on aerodynamic coefficients ($Re_1 = 2.0e+4$, COLIBRI)	129
Fig. 121: Rarefaction effects on aerodynamic coefficients ($Re_1 = 1.2e+4$, COLIBRI)	130
Fig. 122: Rarefaction effects on aerodynamic coefficients ($Re_1 = 6.4e+3$, COLIBRI)	131
Fig. 123: Rarefaction effects on aerodynamic coefficients ($Re_1 = 3.8e+3$, COLIBRI)	132
Fig. 124: Rarefaction effects on aerodynamic coefficients ($Re_1 = 2.2e+3$, COLIBRI)	133

List of Tables

- Table 1: Geometrical data of V2G force balance..... 31
- Table 2: FAST20XX test matrix with nominal V2G operating conditions (similarity parameters calculated by isentropic expansion for perfect gas^[18]) 51
- Table 3: Operating conditions used for constant Reynolds number analysis..... 53
- Table 4: Force and moment balance resolution..... 60
- Table 5: Changes of aerodynamic coefficients between maximum (2) and minimum (1) Knudsen number 81
- Table 6: Changes of aerodynamic coefficients between condition 15 (2) and condition 10 (1) exemplarily shown at $\alpha = 0^\circ$ and $\alpha = 10^\circ$ 104
- Table 7: V2G specifications 119

Abbreviations

AFE	Aeroassist Flight Experiment
Alt.	Altitude
AoA	Angle of attack
CAD	Computer-aided design
CCG	Contamination Chamber Göttingen (Kontaminationskammer Göttingen)
CFD	Computational fluid dynamics
CIRA	Centro Italiano Ricerche Aerospaziali
CNRS	Centre National de la Recherche Scientifique
cog	Centre of gravity
COLIBRI	Concept of a Lifting Body for Re-entry Investigations
Cond.	Operating condition
COS	Coordinate system
DLR	Deutsches Zentrum für Luft- und Raumfahrt e.V. (German Aerospace Center)
DSMC	Direct simulation Monte Carlo
e.g.	exempli gratia (for example)
EU	European Union
EXPRESS	Experiment Re-entry Space System
FAST20XX	Future High-Altitude High-Speed Transport 20XX
FB	Full Wheatstone bridge
FB#	Full Wheatstone bridge strain gauges (# = 1, 2, 3, 4)
ft	feet
HB	Half Wheatstone bridge
HB#	Half Wheatstone bridge strain gauges (# = 1, 2)
HOPE-X	H-2 Orbiting Plane, Experimental
HORUS	Hypersonic Orbital Upper Stage
HOTOL	Horizontal Take-off and Landing Satellite Launcher
i.e.	id est

ICBM	Intercontinental ballistic missile
IPA	Fraunhofer Institute for Manufacturing Engineering and Automation
ISS	International Space Station
ITAM	Institute of Theoretical and Applied Mechanics
KSC	Kennedy Space Center
MIRCA	Micro Reentry Capsule (in German referred to MIRKA (Mikro-Rückkehrkapsel))
N ₂	Nitrogen
nm	Nautical miles
no.	Number
nom.	Nominal data
ref.	Reference values
REX	Returnable Experiment
SCMV	STG-CCG data acquisition- and control software (STG-CCG-Messdatenerfassungs- und Verarbeitungssoftware)
SHEFEX I-III	Sharp-Edge-Flight-Experiment (Versions I, II, III)
SLS	Selective Laser Sintering
SSTO	Single stage to orbit
Std.Dev.	Standard deviation
STG	Chemical Space Propulsion Test Facility Göttingen (Simulationsanlage Treibstrahlen Göttingen)
STG-MT	Chemical Space Propulsion Test Facility Göttingen – Micro Thrusters (Simulationsanlage Treibstrahlen Göttingen – Mikro Triebwerke)
SR-71	Lockheed SR-71 “Blackbird” (Strategic Reconnaissance)
TV	Television
U2	Lockheed U-2 “Dragon Lady”
UK	United Kingdom
USA	United States of Amerika
V1G	1 st test section of the Hypersonic Vacuum Wind Tunnel Göttingen
V2G	2 nd test section of the Hypersonic Vacuum Wind Tunnel Göttingen
V3G	3 rd test section of the Hypersonic Vacuum Wind Tunnel Göttingen

VxG	Hypersonic Vacuum Wind Tunnel Göttingen
#NA	Not available

Nomenclature

Notation

BYB	Strain gauge position normal force transducer, back
BYF	Strain gauge position normal force transducer, front
DX	Strain gauge circuit of tangential force transducer
DXB	Strain gauge position tangential force transducer, back
DXF	Strain gauge position tangential force transducer, front
na, nb, nc, nd, ne, nf, ng, nh	Integration regimes normal force transducer
tA, tCDE, tEF, tFGL, tGH, tHI, tIJ, tJK, tLM, tM, tDN, tDN', tNO, tKOP, tPQ, tQ, tQ'	Nodes of tangential force transducer
ta, tb, tc, td, te, tf, tg, th, ti, tj, tk, tl, tm, tn, to, tp, tq	Integration regimes tangential force transducer

Latin letters

<i>A</i>	Area	[m ²]
<i>a</i>	Speed of sound	[m/s]
<i>BM</i>	Bending moment	[Nm]
<i>c</i>	Aerodynamic coefficient	[–]
\bar{c}	Average molecule speed	[m/s]
<i>c1</i>	Integration constant 1	[°]
<i>c2</i>	Integration constant 2	[m]
<i>cp</i>	Molar heat capacity at constant pressure	[J/(kg*K)]
<i>d</i>	Diameter	[m]
<i>Da</i>	Damköhler number	[–]
<i>E</i>	Young's modulus	[MPa]
<i>F</i>	Force	[N]
<i>Fn</i>	Normal force	[N]
<i>Ft</i>	Tangential force	[N]
<i>J</i>	Moment of area	[m ⁴]

k_B	Boltzmann constant	[J/K]
Kn	Knudsen number	[-]
L, l	Length	[m]
M	Mach number	[-]
m	Molecular mass	[kg]
\dot{m}	Mass flow	[kg/s]
N	Number of measured values	[-]
Nu	Nusselt number	[-]
p	Pressure	[Pa]
PM	Pitching moment	[Nm]
Pr	Prandtl number	[-]
p_s	Static pressure	[Pa]
p_t	Total pressure	[Pa]
Q	Integral heat transfer	[W/m ²]
q	Heat transfer	[W/m ²]
qp	Dynamic pressure	[Pa]
R	Specific gas constant	[J/(kg * K)]
r	Radius	[m]
R^2	Coefficient of determination	[-]
Re	Reynolds number	[-]
St	Stanton number	[-]
T	Temperature	[K]
T_s	Static temperature	[K]
U	Voltage	[V]
u	Velocity	[m/s]
R	Resistance	[Ω]
x	Coordinate axis, flow direction	[mm]
y	Coordinate axis, radial direction in horizontal plane	[mm]
z	Coordinate axis, radial direction in vertical plane	[mm]

Greek letters

α	Angle of attack	[°]
γ	Ratio of specific heats	[-]
δ	Laminar boundary layer thickness	[m]
η_n	Normal bending deformation	[m]
η_t	Tangential bending deformation	[m]
λ	Mean free path	[m]
μ	Viscosity	[kg/(m * s)]
π	Ratio of a circle's circumference to its diameter Ludolph's constant ≈ 3.14	[-]
ρ	Density	[kg/m ³]
σ	Particle hard shell diameter	[m]
σ	Standard deviation	[%]
ϕ	Bending angle	[°]

Subscripts

0	Reservoir conditions
1	Free stream conditions
2	Conditions behind normal compression shock
<i>aw</i>	Condition at adiabatic wall
<i>beam</i>	Bending beam properties
<i>bridge</i> (#)	Bridge voltage for (# = half bridge, full bridge)
<i>BYB</i>	BYB strain gauge position
<i>BYF</i>	BYF strain gauge position
<i>COG</i>	Centre of gravity position
<i>cooler</i>	Located just before the cooler
<i>D</i>	Drag
<i>L</i>	Lift
<i>M</i>	Pitching moment

<i>nom.</i>	Nominal data
<i>nozzle</i>	Located at the nozzle
<i>ref.</i>	Reference data
<i>s</i>	Static flow conditions
<i>supply</i>	Power supply
<i>total</i>	Total flow conditions, static and dynamic fraction
<i>tunnel(1)</i>	Located at the tunnel past the test section (left side)
<i>tunnel(2)</i>	Located at the tunnel past the test section (right side), connected to Pitot traverse mechanism
<i>w</i>	Condition at wall

1 Introduction

1.1 Hypersonic High Altitude Flight

The prediction of aerodynamic coefficients in the gas kinetic transition region between rarefied and continuum flow is important for the design of hypersonic vehicles which either cross this regime, i.e. re-entry vehicles, or which are designed to fly in this regime, i.e. hypersonic transport vehicles. High altitude flight is usually referring to a flight regime far above the commercial or military jet aircraft. The atmospheric layers are described by a non-linear change of density with altitude. The specific layers and representatively selected vehicles are visualized in Fig. 1 with their operational altitude. While commercial jet aircrafts are usually travelling at 10 to 12 km in the upper region of the Troposphere, military planes even operate at up to 25 km in the Stratosphere as the Lockheed SR-71 "Blackbird" demonstrated. Hypersonic speeds at higher altitudes are accessible for military rockets, like Intercontinental ballistic Missiles (ICBMs) which reach an apogee of about 1,300 km, and by re-entry vehicles, like e.g. Apollo, Sojus capsules, or the Space Shuttle orbiter, returning back from an earth orbit or from an interplanetary mission while passing through all atmospheric layers. Since re-entry vehicles are able to operate outside of the earth atmosphere, they are not shown in Fig. 1.

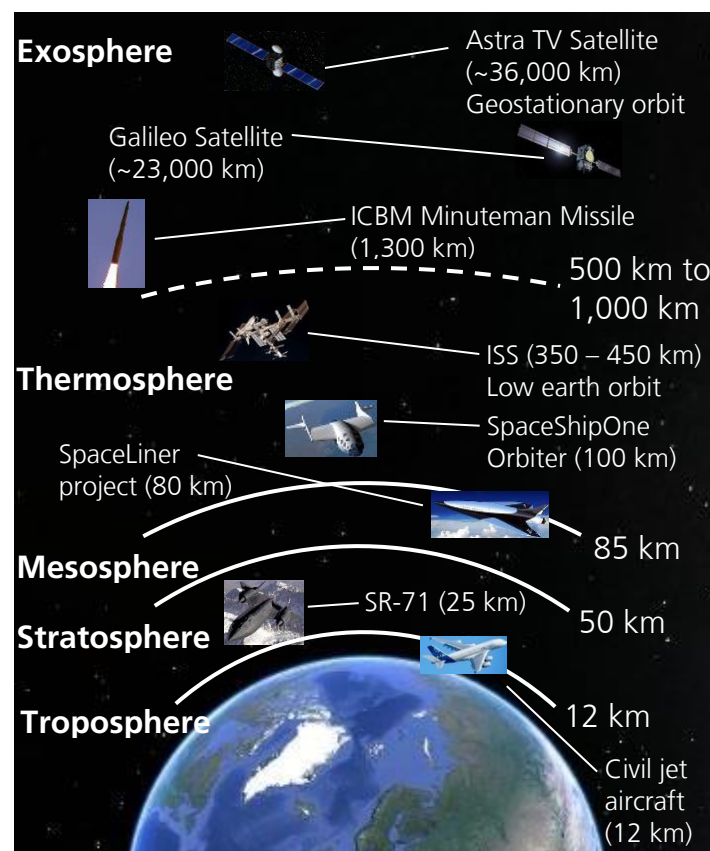


Fig. 1: Layers of earth atmosphere based on data from various text books e.g. ^[57]

In the early years of space flight, mainly capsule-shaped vehicles were used. Due to the low aerodynamic forces in the low-density regime, the re-entry vehicles dropped through the rarefied regime. These capsule-shaped configurations are decelerated at

lower altitudes where the atmosphere density significantly increases. During re-entry the density increases from about $5.6 \cdot 10^{-7} \text{ kg/m}^3$ at 100 km altitude, where typically the aerodynamic decelerating process starts, to 1.2 kg/m^3 at sea level. Newer concepts in turn aim more and more at lifting re-entry vehicles^[25] which decelerate already at higher altitudes by using high altitude aero-breaking. Therefore, detailed knowledge on rarefaction effects is essential for developing new vehicle configurations.^[43] An overview about typical re-entry trajectories is presented in a velocity-altitude diagram in Fig. 2.

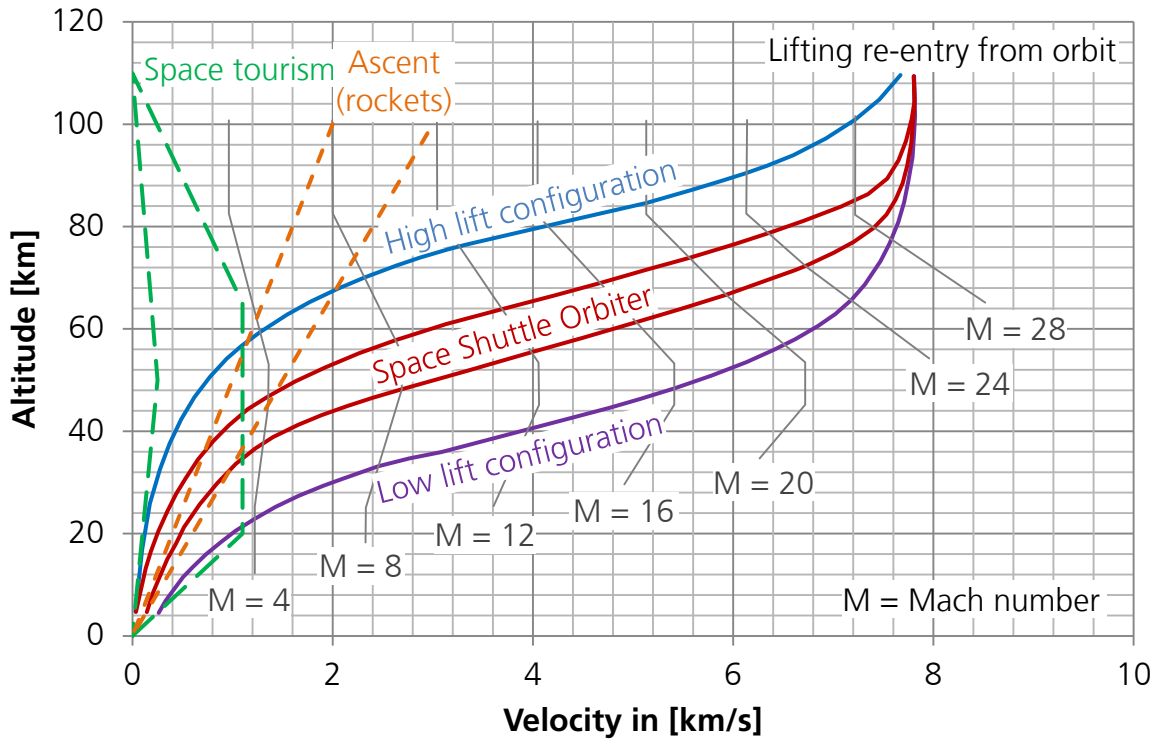


Fig. 2: Atmospheric entry flight paths on a velocity-altitude map modified from^[4] and qualitatively sketched envelope of space tourism trajectories

New hypersonic transport concepts, e.g. the DLR SpaceLiner^[82], are designed to extend the altitude range of transport vehicles to fly at altitudes of about 80 km. This altitude corresponds to the upper limit of the Mesosphere and is just below the Thermosphere. The aim is to reduce the atmospheric drag and simultaneously use the remaining atmosphere for an unpowered gliding flight phase.

In the last decades the research in the hypersonic rarefied flow regime was intensified^[61], and many numerical prediction methods were established^{[7], [67], [72]} since more and more applications require a more sophisticated knowledge about the flow behaviour and processes. Fuelled by increased computational capacities, more complex flow phenomena are analysed in detail in dilute gases using the direct simulation Monte Carlo (DSMC) method^[6]. These processes enable the design and evaluation of highly advanced flight configurations, with shapes more reminding of airplanes, which are able to fly with hypersonic speeds in the high atmospheric fringe layers.

The research related to the rarefied flow regime can be distinguished into two applications of hypersonic high altitude flight: re-entry of space vehicles into the earth-

atmosphere and hypersonic transport connecting two locations on the earth. Since both application branches are relevant for this work, they are briefly described in this chapter.

Both re-entry and hypersonic transport vehicles have in common that they are usually travelling with hypersonic speeds in high atmospheric layers by unpowered gliding. Apart from this, they are two totally different applications resulting in different vehicle geometries. Re-entry vehicles, like the Space Shuttle Orbiter, have usually a blunt geometric shape and fly at high angles of attack in order to maximize drag. By using the aerodynamic drag forces for deceleration, the use of reverse thrusters can be avoided and, due to less fuel carriage, the payload can be increased. For hypersonic transport applications in contrast, mostly slender vehicles are used at low angles of attack to minimize aerodynamic drag. This decides whether they are technically feasible at all.

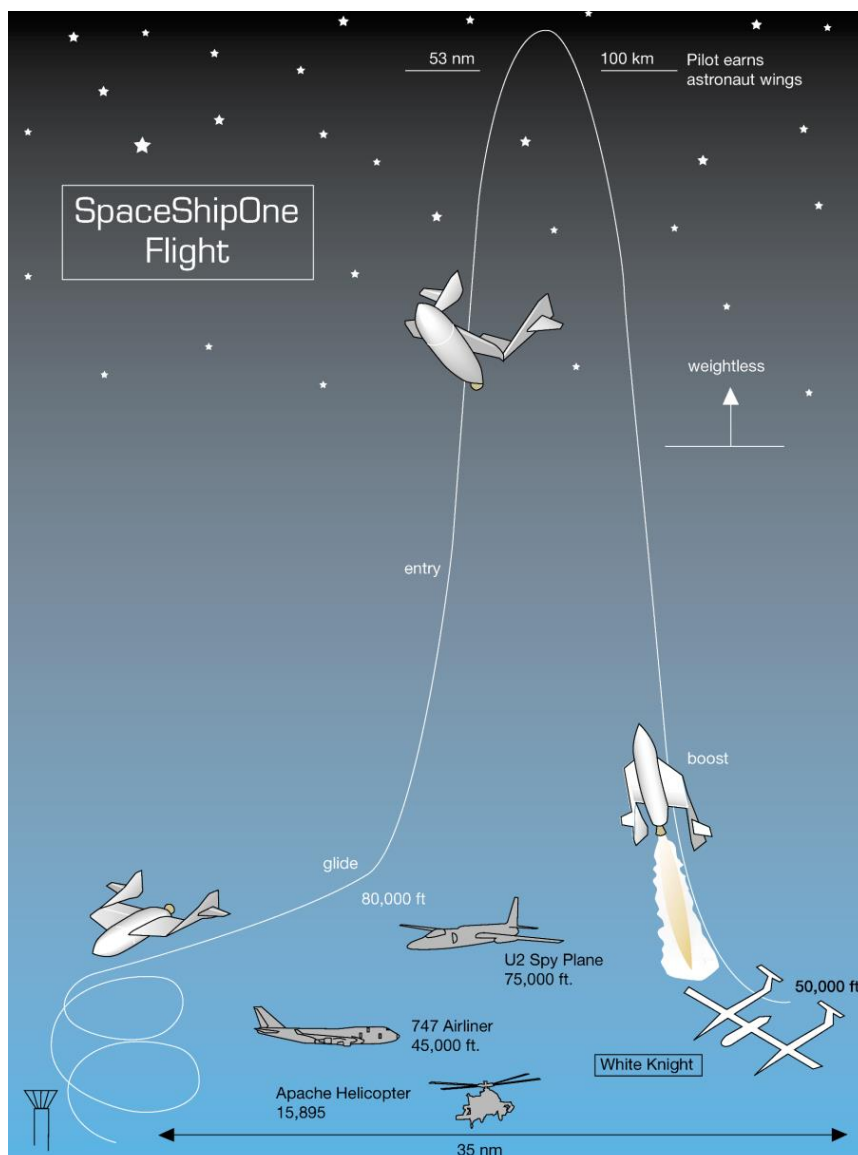


Fig. 3: Trajectory of SpaceShipOne^[71] (nm = nautical miles, ft = feet)

During ascent to space the rarefied flow regime is crossed as well but the velocities are not as high as during the re-entry phase, see Fig. 2. Possible rarefaction effects onto the aerodynamic coefficients in this flight phase are not as important because the aerodynamic forces are far smaller compared to those accelerating the vehicle.

Vehicles developed for space tourism are usually not concerned by hypersonic low-density flight. Although the space tourism vehicles can reach hypersonic Mach numbers in low atmospheric layers, they lose their velocity when they catapult themselves with a parabola flight trajectory out of the atmosphere. In the apogee they are decelerated to nearly zero velocity such that they do not require a very high developed aerodynamic in that high altitude regime. This is visualised in Fig. 2 at 0 and 110 km altitude. In between the vehicle reaches supersonic Mach numbers but remains at far lower speeds compared to a re-entry. As example the flight path from SpaceShipOne^[71], the first commercial space tourism spaceplane, is sketched in Fig. 3.

1.2 High Lift / Drag Design

Relating the lift of an aeroplane or spacecraft to its drag is an established method to assess the aerodynamic efficiency. From the reciprocal of the lift / drag ratio directly follows the possible flight distance to a given altitude decrease during unpowered gliding. Re-entry or hypersonic transport vehicles with slender, more plane-like shapes with a corresponding higher lift / drag ratio have many advantages, compared to blunt and capsule shaped vehicles with a low aerodynamic efficiency. The most important one is that the longitudinal range and cross range are strongly increasing, see Fig. 4 where both are presented with lift / drag ratio as parameter.

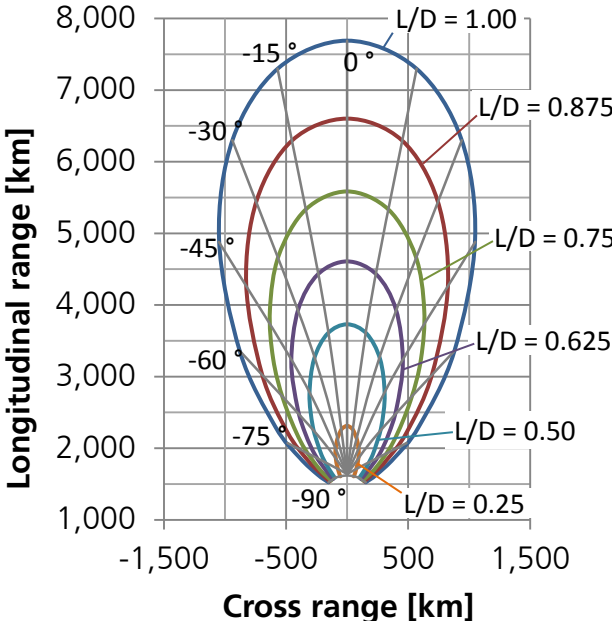


Fig. 4: Longitudinal and cross range depending on aerodynamic efficiency modified from ^[12]

The diagram shows the possible landing area on the earth, depending on the vehicles lift / drag ratio. It can be seen that it is possible to reach more and further distant landing sites which are not directly on the path of the re-entry trajectory of a specific inclined orbit. Simultaneously, the time slot for return scenarios is increased since the landing sites can be reached from more positions on the orbit. Usually a vehicle with a higher aerodynamic efficiency has also an improved aerodynamic steerability due to its large flaps and rudders, compared to a blunt vehicle. Typically blunt vehicles are equipped with one or two body flaps and use mainly thrusters for attitude control. This

aerodynamic steerability is also a basic requirement for the horizontal landing ability and the resulting shorter turn-around times. Due to these advantages hypersonic vehicle concepts are consistently aiming at a better aerodynamic efficiency, i.e. an increased lift / drag ratio, as e.g., Sänger, Space Shuttle Orbiter, Buran, HOPE-X, HOTOL, Sänger II / HORUS, HERMES, X-33, SHEFEX I-III / REX-Free Flyer and Skylon, see Fig. 5. Especially the increased longitudinal and cross range was a central reason for the development of the SHEFEX project.

As explained, there are many reasons suggesting a high lift / drag ratio design of re-entry vehicles which are though typically accompanied by higher heat loads. The reason is that re-entry vehicles with a higher aerodynamic efficiency have usually a smaller nose radius r , the stagnation point heat load q , however, increases inversely proportional to the square root of the nose radius, see (1-1). [19], [29], [47], [70], [87]

$$q \propto \frac{1}{\sqrt{r}} \tag{1-1}$$

Consequently, an advanced design is only possible if the excessive aerodynamic heating can be handled by new thermal protection systems which can withstand the increasing heat loads, or can be protected by active cooling or controlled ablation.

Currently Reaction Engines Limited is developing with the SKYLON project a highly aerodynamic efficient single stage to orbit (SSTO) concept. The concept aims at a challenging vehicle with a very high lift / drag ratio of above 4 which is not only able to land horizontally but also to take off from a commercial airport runway. [56]

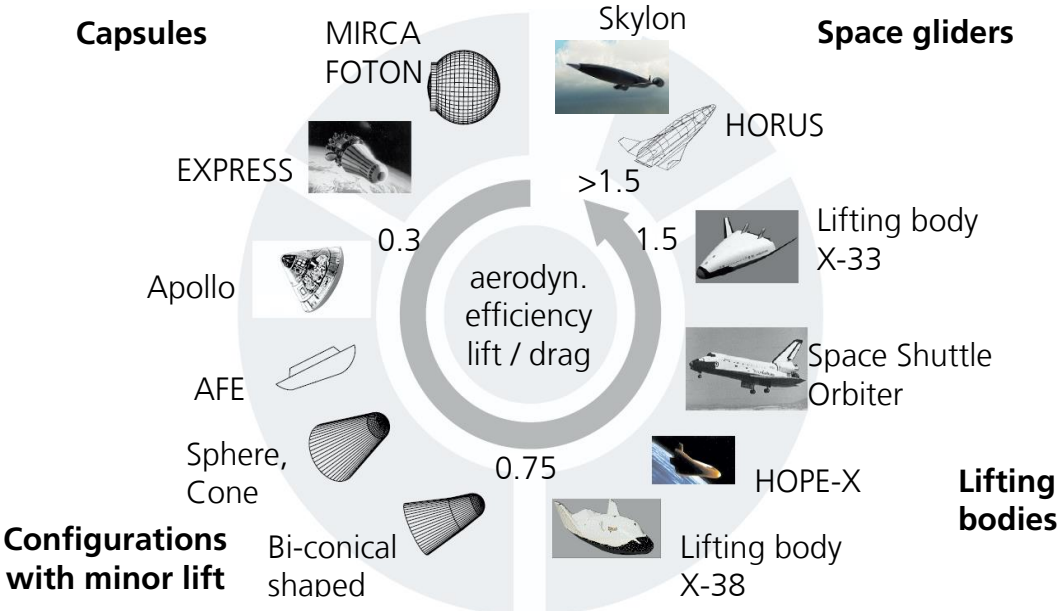


Fig. 5: Aerodynamic efficiency of re-entry vehicles modified from [12]

1.3 Established Prediction Methods

For re-entry and hypersonic transport applications, an aerodynamic configuration has to be chosen which allows a stable flight in all passing flow regimes. It is essential that the flight behaviour is predictable over the whole flight trajectory either with numerical or experimental approaches.

Due to the variety of appearing effects along a re-entry trajectory, it is not possible to use a single wind tunnel facility or a single numerical tool for predictions of aerodynamic effects at all parts along the total trajectory. Depending on the trajectory part, different physical effects govern the aerodynamic behaviour. For example, from outer space the re-entry vehicle passes through different regimes where the governing effects can be described as follows: First the flow can be regarded as free molecular flow where interactions between molecules are negligible. With increasing density the interaction between molecules increases which leads to the disturbed molecular flow. When the density is further increasing, the re-entry vehicle passes initially the laminar and later the turbulent phase of hypersonic flight. Subsequently the re-entry vehicle passes the supersonic, the transonic and finally the subsonic flow regime.

In this work the focus is on hypersonic rarefied flow. The governing aerodynamic effects are usually described by so called similarity parameters^[4]. For this work the relevant similarity parameters are especially the Knudsen number, Mach number and Reynolds number which can be related as follows, see (1-2):

$$Kn \propto \frac{M}{Re} \quad \mathbf{(1-2)}$$

Since the assumption that the fluid behaves like a continuum, which leads to the derivation of the Navier-Stokes equations, is not applicable to the rarefied flow regime, alternative computational fluid mechanics tools are required. A well-established numerical tool for the rarefied flow regime is the direct simulation Monte Carlo method, a numerical method for solving the Boltzmann equation. The applicability of numerical prediction methods in different rarefaction regimes is shown in Fig. 6.^[6] Even though computationally expensive, the current prediction methods allow an accurate determination of flight stability and steerability in the low-density regime when they are compared to experiments conducted at similar conditions. They can provide insights in flow properties which are hard to measure. Both approaches can be used for a mutual completion of the data set. But due to its computational costs, the numerical simulations are usual limited to a few selected positions along the flight path and selected flight attitudes. With increasing density in the transition to continuum, the DSMC method becomes very time consuming. DSMC, with its modelling of solely two-body collisions between particles, is valid as long as the gas can be treated as a perfect gas, i.e., as long as the attractive or repulsive forces between particles are negligibly small. An approach to make the predictions more efficient is to initially apply or modify computationally less expensive continuum solvers to predict the flight behaviour in the rarefied flow regime. To determine the error magnitude in this particular case the results are compared to the experimentally obtained data. A typical modification is, e.g., the introduction of a wall slip condition where temperature or even velocity discontinuities are allowed at the wall. When the resulting difference between both methods is

assessed to be acceptable, the numerical tool can be applied to similar predictions in a second step.^[89] The applicability is, however, limited to similar flow fields, i.e. flight configuration, flight attitude and degree of rarefaction.

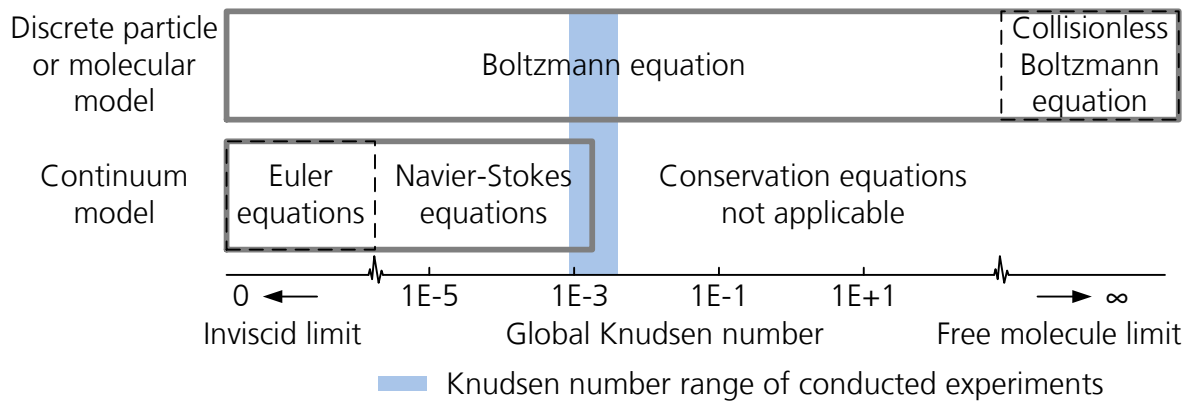


Fig. 6: Rarefaction limits for numerical prediction methods modified from^{[6] 1}

Experimental data is essential for comparison of available numerical data and the assumptions made within, as e.g., in case of the DSMC method the selection of the accommodation coefficients. While numerical simulations only contain physics explicitly modelled, experiments contain per definition all the physics although not necessarily all the physics of the real flight conditions. It is important to consider that the physics of the conducted experiment can differ from the physics of the actual research problem to be analysed, when simplified experiments are performed. An example is here the noise of wind tunnels which can influence the flow field by shifting the laminar turbulent transition upstream, while in a real flight without noise the transition is further downstream. Depending on the setup, experiments can further support the numerical prediction by identifying trends due to changing flight attitudes.

In the 1960s and 1970s many hypersonic ground test facilities have been put into operation around the world for basic research and for investigations of aerodynamic forces in the gas kinetic transition regime between continuum and rarefied flow. Well-known facilities are the N-3 at the Princeton University (New Jersey, USA)^[88], the VxG with its three test sections V1G, V2G and V3G at the German Aerospace Centre (DLR) in Göttingen (Germany)^{[24], [31], [32], [93], [94]}, the SR3 at the Centre national de la recherche scientifique (CNRS) in Meudon (France)^{[1], [2], [3]}, the Imperial College Graphite Heated Hypersonic Wind Tunnel at the Imperial College London (UK)^[22], the Low Density Wind Tunnel HS3 (LDWT) at the University of Oxford (UK)^[68], and the T-327 at the Institute of Theoretical and Applied Mechanics (ITAM) in Novosibirsk (Russia)^[53]. In the last two decades, however, hardly any publications describing experiments in the listed facilities appeared.

¹ Due to a lack of available data, the definition of a local Knudsen number proposed by Bird is not possible. Instead a global Knudsen number is used based on the continuum definition $M/\sqrt{Re} < 0.1$ by Koppenwallner^[45]. Inserting eq. (1-2) yields $Kn\sqrt{Re} < 0.1$. Since the Reynolds numbers of the conducted experiments are in the order of $\sim 10,000$, the axis description has to be scaled with a factor of 100, and the continuum limit can be determined to be about $Kn < 0.001$. The depicted Navier-Stokes equations regime can be extended by implementing wall slip conditions.

Another prediction method is the so called bridging. This is an engineering method which uses a suitable interpolation of locally predicted results in the range between continuum and free molecular flow. The bridging methods have a limited accuracy and are not uncontroversial due to their strong dependence on the flow field, flight configuration and attitude. ^{[11], [54], [66], [76], [90], [91]}

An overview about available numerical and experimental methods is presented in Fig. 7.

CFD	<ul style="list-style-type: none"> • Numerical tool for continuum flow • Limited extension potential into rarefied flow by "wall slip" conditions
DSMC	<ul style="list-style-type: none"> • Numerical tool for predictions in free molecular and rarefied flow • Time consuming for increasing density
Ground tests with, e.g. V2G	<ul style="list-style-type: none"> • Simulates selected similarity parameters, e.g., Kn, M, Re • V2G Operates in continuum near rarefied flow • Used for comparison purposes of numeric tools
Bridging	<ul style="list-style-type: none"> • 'Suitable' interpolation between continuum and free molecular flow • Based on locally predicted results • Lift and drag prediction possible with restrictions • Pitching moment prediction unreliable

Fig. 7: Numerical and experimental methods

Over the last years most of the research in the rarefied flow regime has been conducted numerically, possibly due to the increased numerical capabilities. This led to a lack of extent and diversity of available experimentally obtained data, required for the comparison of numerical codes. For the comparison of current numerical codes, over twenty year old experimental results are used. ^[69] However, a good agreement between numerical and experimental results of former, possibly simple shaped and purely convex, configurations does not necessarily imply a good agreement between results of todays more complex shaped, winged configurations with concave edges like Skylon. In 2006, Padilla et al. ^[65] strongly recommended to conduct more experimental studies to broaden the available data basis. Within this work such experiments are conducted by means of ground tests in the DLR Hypersonic Vacuum Wind Tunnel Göttingen (V2G) with the focus to directly compare rarefaction effects on aerodynamic coefficients between a blunt and a slender flight configuration in hypersonic rarefied flow.

1.4 Investigation of Rarefaction Effects – Present Status and Aim of Analysis

In the past many investigations have been conducted to predict the aerodynamic coefficients of lift, drag and pitching moment from blunt capsules^{[39], [58], [59]}, to lifting configurations as the Space Shuttle Orbiter^{[8], [9]}, up to slender wave riders^[67]. The focus of these studies was to determine the aerodynamic properties close to their respective trajectory. Many such studies were conducted in the DLR Hypersonic Vacuum Wind Tunnel Göttingen^{[13], [14], [36], [37], [38], [40], [41], [42], [60], [83], [84], [96]}. In opposite to those investigations, the main focus of this study is on a more fundamental research scope. In the present work the effect of rarefaction on the aerodynamic coefficients is regarded more systematically by directly comparing a blunt re-entry flight configuration with a low lift / drag ratio, to a slender re-entry flight configuration with a high lift / drag ratio, at different flight attitudes. This distinguishes this study from earlier conducted studies.

In a prior study, within the EU co-funded “Future High-Altitude High-Speed Transport 20XX” project (FAST20XX) between 2009 and 2012, the rarefaction effects were analysed on a lifting body configuration by means of force measurements in the DLR Hypersonic Vacuum Wind Tunnel Göttingen (V2G) by the author of this study. For that reason a 3-component strain gauge force balance, able to measure simultaneously lift, drag and pitching moment, has been designed and optimised based on former V2G balance designs^[77]. Although the precision of the force balance was improved, compared to former V2G measurements, a further development demand especially on the balance zero-point stability was identified.

The results of the low-density force measurements in FAST20XX qualitatively showed a distinct measurable effect between the different degrees of rarefaction in the analysed Knudsen number range. However, there is an ambiguity whether the observable effect is based on rarefaction effects or on the simultaneously changing Reynolds number. Due to the Mach number independence principle of Oswatitisch^[63], the Mach number effect plays a minor role, see chapter 2.4.

The motivation of the present work is to concentrate on the extraction of the rarefaction effects from the measured differences and to quantify the rarefaction effects. During the performance of the FAST20XX measurements, some room for improvements was identified concerning the measurement technique and the measurement procedure. For the present analysis both are optimised, in particular to increase the accuracy, precision and zero point stability. The focus on investigating the rarefaction effects along a trajectory is changed to a systematic analysis at constant Reynolds numbers. Assuming the applicability of the Mach number independence principle, the effects can be interpreted as a pure effect of rarefaction. To investigate whether the rarefaction effects depend on the bluntness of the configuration both a slender and a blunt flight configuration are selected (Fig. 8) to be analysed at different flight attitudes.

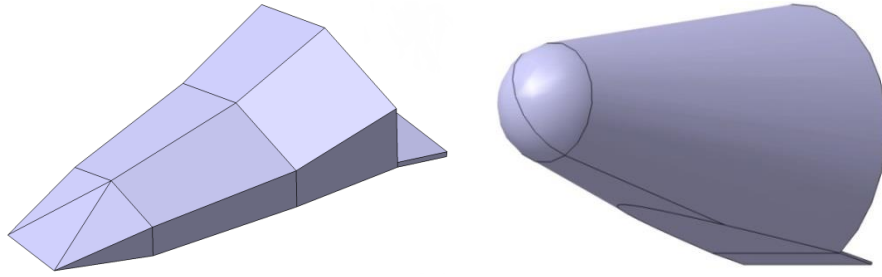


Fig. 8: Investigated blunt and slender configurations

Recalling (1-2) it can be seen that the Knudsen number is scaling linearly with changes in Mach number. Due to the V2G operating range, see Fig. 9, the experiments allow a Mach number variation between about 10 and 26 only, which is a factor of about 2.5. This is not very much when it is compared to the rarefied flow regime which covers at least three decades of Knudsen number variation. To extend the analysable regime and to utilize the whole V2G operating range, the constant Reynolds number analyses are conducted at five different Reynolds numbers sketched in Fig. 9. In the evaluation it is differentiated between results measured at one constant Reynolds number and between results where the Reynolds number is varied. Based on that procedure it is possible to evaluate and assess the Reynolds number effect onto the aerodynamic coefficients.

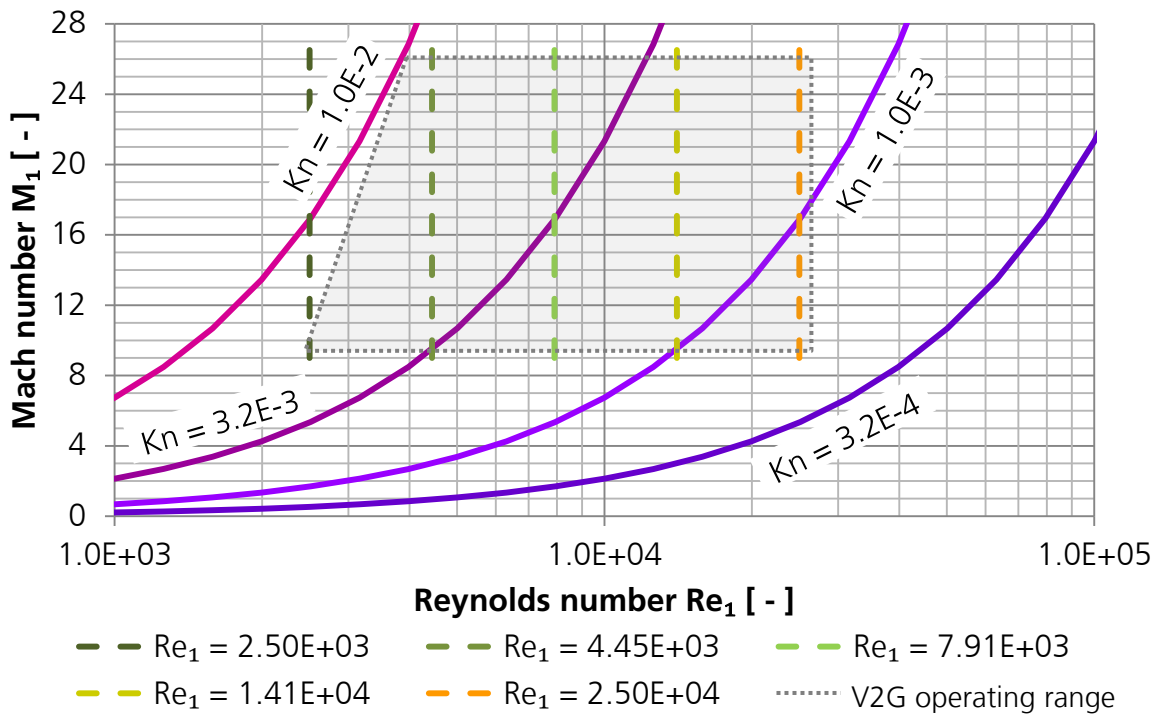


Fig. 9: Constant Reynolds number analysis with V2G operating range

Summarising, the aim of the present work is to analyse by means of experiments how the aerodynamic coefficients of lift, drag and pitching moment of a blunt lifting body, and a slender high lift configuration are affected by rarefaction effects at different flight attitudes from angles of attack between $0^\circ \leq \alpha \leq 34^\circ$. The experiments cover for each test article one order of magnitude in Knudsen number and are performed between $7 \cdot 10^{-4} < Kn < 9 \cdot 10^{-3}$. The corresponding Reynolds numbers and Mach numbers are $2.2 \cdot 10^3 < Re < 2.5 \cdot 10^4$ and $10 < M < 26$.

2 Characteristics of Rarefied Flow

2.1 Definition of Rarefied Flow

Due to the gradual change of the atmospheric properties from the ground level to space, there is not a single well defined characteristic flow behaviour for a vehicle crossing these regimes with hypersonic speeds. With decreasing density, there are rather different flow characteristics which dominate the flow field in a certain range. In the following the characteristic behaviour is briefly explained from continuum to free molecular flow in space. Legge^[48] distinguishes between four different flow phenomena in front of the vehicle, occurring in the transition regime between ground and space and illustrates the dominating phenomena as they appear with increasing altitude, see Fig. 10. Since the beginning and ending of the phases are strongly depending on further influences, as e.g. the body shape, the figure describes the phases only qualitatively and no quantities are given. For each phase the pressure and the velocity characteristic along the stagnation point stream line are depicted for a blunt body configuration. Additionally, the shape of the compression shock and boundary layer are sketched.

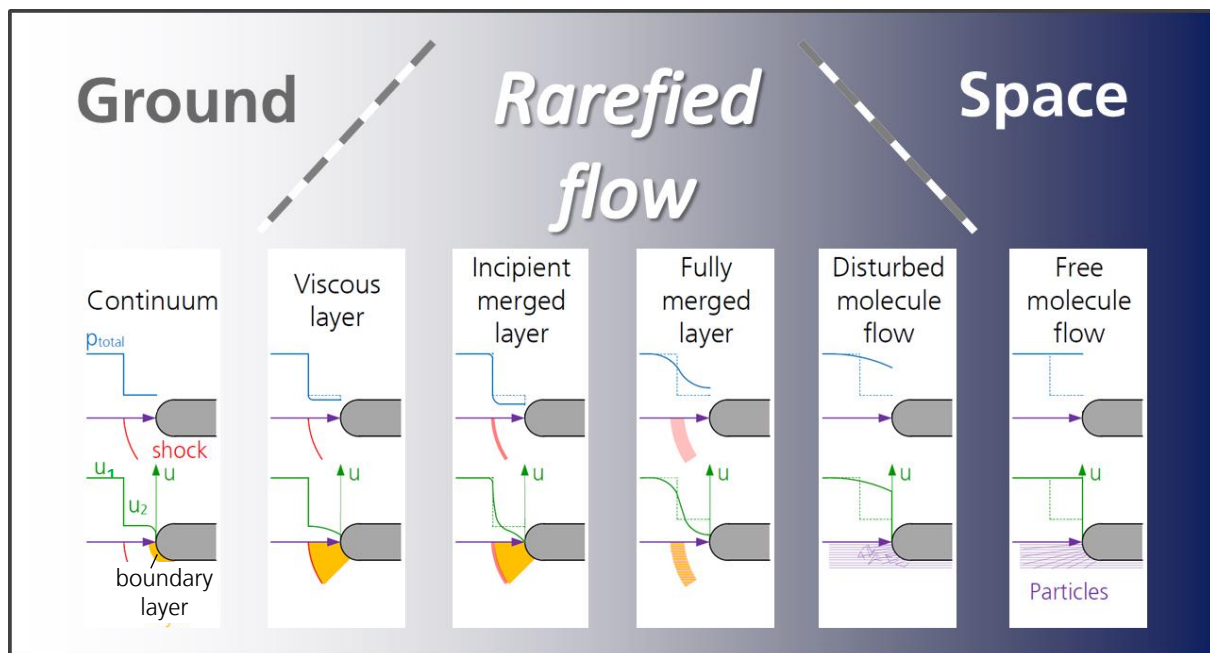


Fig. 10: Transition of flow regimes visualised by Legge^[48]

Continuum

The total pressure and velocity is undisturbed until the streamline reaches the detached normal bow shock, see Fig. 10. Along the stagnation point streamline, the total pressure drops across the shock abruptly down to the value which can be calculated from the Rankine-Hugoniot relations. During this irreversible process the entropy is rising. The compression shock is then followed by an inviscid isentropic compression before the flow reaches the viscous boundary layer where the entropy continues to increase. The velocity drops at the discontinuity down as well before it is finally decelerated at the stagnation point. Hypersonic continuum flow is characterised by small bow shock stand-off distances and sharp discontinuities. In case of a sufficiently large Reynolds number and a boundary layer thickness far smaller than the distance of the detached bow shock

to the vehicle's surface, significant viscous effects occur within the displacement thickness only. The displacement thickness is a definition of the classical boundary layer theory and describes a procedure to separate a flow field into an inviscid far field region and a viscous region around the vehicle.

Viscous Layer

With decreasing density the boundary layer becomes thicker until it fills the full regime between body surface and detached bow shock. The compression shock is still a sharp discontinuity but the total pressure decreases further than in the continuum case. Since the boundary layer is thicker, the particles on the stagnation point streamline start to decelerate earlier.

Incipient Merged Layer

In this phase the shock starts to blur and broadens. This layer can still be described as continuum but the classical Rankine-Hugoniot-relations lose their validity. Due to the shock blurring the velocity discontinuity changes into a steep slope. The regime between detached bow shock and body surface is completely filled with the boundary layer.

Fully Merged Layer

In the fully merged layer phase, there is no shock existent and the total pressure at the stagnation point rises. The velocity decreases down to a value greater than zero at the stagnation point, i.e., a velocity slip at the wall is present.

Disturbed Molecular Flow

Macroscopic parameters, like e.g. temperature, are irrelevant in this phase. The molecules reflect from the wall and collide with incoming molecules with a certain probability. The total pressure at the stagnation point and velocity right before the stagnation point increase further and approach the total values of the free stream with increasing rarefaction. Since the incoming flow is affected by the reflected molecules, the principle of free molecular flow is not valid yet but the numerical treatment can be simplified, for example, by limiting interactions between incoming and reflected molecules to one collision only.

Free Molecular Flow

In this phase the reflected molecules collide with the incoming at distances far away from the body surface so that the resulting effects can be neglected. The total pressure and velocity values on the stagnation point streamline remain practically unchanged until the molecules collide with the wall.

2.2 Molecule Surface Interaction

Molecules impinging on a surface are re-emitted into the flow mainly depending on the surface roughness. Three cases can be distinguished, see Fig. 11 (top)^[45]:

- Mirrored reflection (only very smooth and clean surface)
 - Reflection depends on incidence angle only
 - Normal momentum is transferred to the body surface
 - Tangential momentum remains unchanged

- Diffuse reflection (typical for rough surfaces)
 - Reflection depends on surface conditions only
 - Molecules are initially adsorbed and normal and tangential momentum is transferred to the body surface
 - Molecules adopt the surface temperature and leave by diffuse effusion with the thermal velocity
- Mixed reflection
 - Empirical description with accommodation parameters^[73]

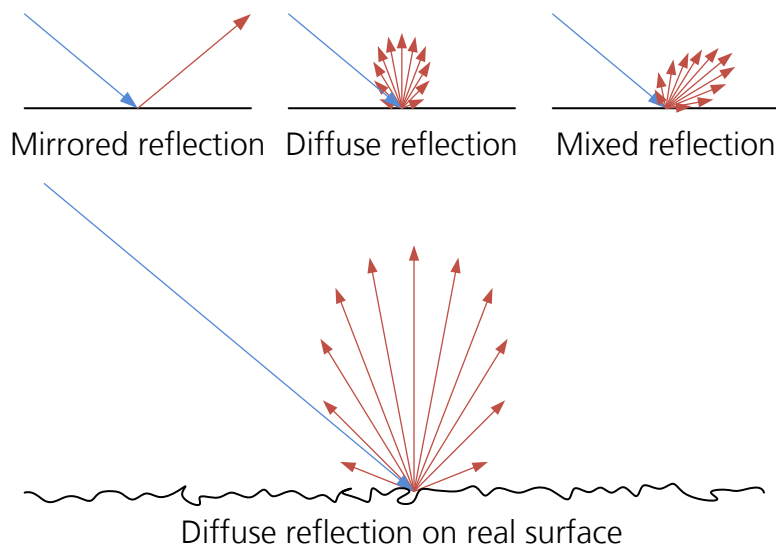


Fig. 11: Gas body surface interaction, mirrored, diffuse and mixed reflection of molecules on the surface (top), detailed view of diffuse reflection on real surface (bottom)^[45]

For a better imagination of the reason for the diffuse reflection, a real surface can be sketched, see Fig. 11 (bottom). An impinging molecule enters some kind of cavity where it impinges several times, loses all its momentum, before it randomly escapes with solely thermal velocity.

2.3 Similarity Parameters

In fluid mechanics many so called similarity parameters are introduced to allow a scaling and simplification in the treatment of similar fluid dynamic problems. Depending on the configuration and the details of the flow problem, some similarity parameters are more relevant than others. An important parameter for the analysis of rarefied flows is the Knudsen number Kn , the ratio of the mean free path to an appropriately chosen reference length L of the considered geometry (2-1). Depending on the considered flow problem, the reference length has to be varied, i.e., for example for investigations at the stagnation point the nose radius would be an appropriate reference length, while for investigations of overall aerodynamic coefficients the total body length would rather be suitable. In this work L is always the total vehicle length. The appearance of the previously explained rarefaction effects can be distinguished by this ratio. The mean free path λ is the average distance, travelled by a moving particle, e.g. a molecule or atom, between successive collisions.

$$Kn = \frac{\lambda}{L} = \left[\frac{\text{mean free path}}{\text{reference length}} \right] \quad (2-1)$$

Fig. 12 sketches a flow field at ground level (top) and in space (bottom). The molecules, sketched as blue dots, are always in motion, however, for clarity the red velocity vectors are displayed for few selected molecules only. The green velocity vector indicates the movement of the considered flight vehicle. The free path λ' denotes the travelled length of the chosen particle to its next collision. Considering the whole flow field, the free path of all molecules can be averaged to obtain the mean free path.

At ground level (see Fig. 12, top) the mean free path is far smaller than the reference length ($\lambda \ll L$), hence, the molecule-molecule interactions are dominant compared to the molecule-wall interactions. The gas dynamic problem can be treated as a continuum flow using the macroscopic approach with pressure p , temperature T and density ρ .

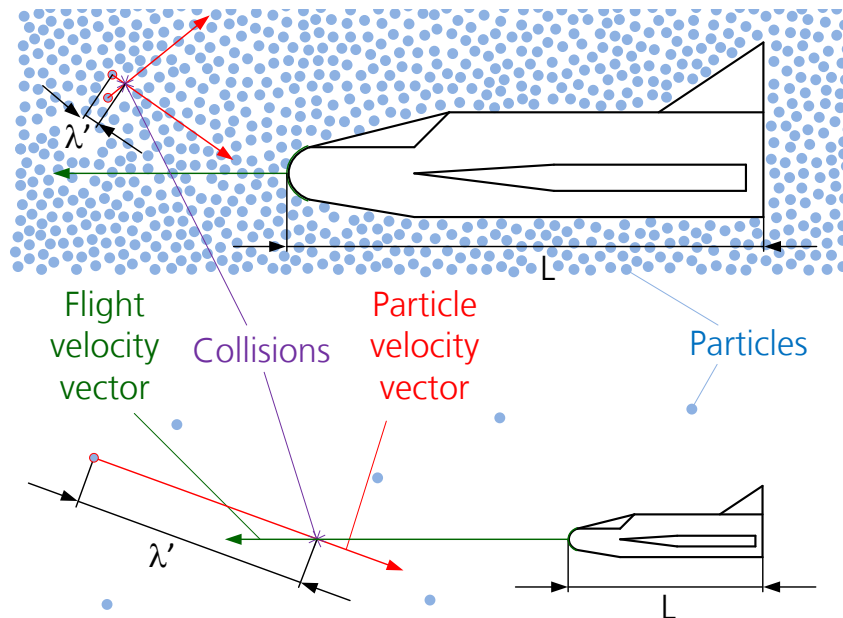


Fig. 12: Free path at ground level (top) and in space (bottom)

At the other extreme in space (see Fig. 12, bottom), the density is far less and the mean free path is greater than the reference length ($\lambda > L$). The molecule-wall interactions become dominant which characterises free molecular flow.

The similarity rules can be applied to geometric similar flight configurations. In case of the rarefaction, for instance, that means that for a test article length of 10 cm and a flight configuration length of 10 m, the rarefaction effects in both cases are equal if the mean free path is 100 times greater in case of the flight configuration, such that both Knudsen numbers are equal.

Apart from the Knudsen number, the Mach number and the Reynolds number are considered. The Mach number M describes the flight velocity u in relation to the local speed of sound a (2-2). The Reynolds number Re in turn relates the inertial forces to the viscous forces (2-3). ρ is the density, L an appropriately chosen reference length and μ the dynamic viscosity.

$$M = \frac{u}{a} = \left[\frac{\text{flight velocity}}{\text{speed of sound}} \right] \quad (2-2)$$

$$Re = \frac{\rho u L}{\mu} = \left[\frac{\text{inertial forces}}{\text{viscous forces}} \right] \quad (2-3)$$

The three introduced similarity parameters are not independent from each other but can be related, see (2-4).^[81]

$$Kn = \frac{M}{Re} \sqrt{\frac{\gamma \pi}{2}} \quad (2-4)$$

γ is there the ratio of specific heats and π the Ludolph's constant. This relation is of particular importance for this work since the similarity parameters Mach number and Reynolds number can be independently adjusted in the experimental test facility, utilised for this work. For the evaluation of rarefaction effects, the results are presented as a function of both the Knudsen number and the rarefaction parameter described on the next page.

In classical continuum fluid mechanics Mach number and Reynolds number can be selected individually to fit the research problem. Due to arising importance of the Knudsen number in the rarefied flow and its direct relation to Mach and Reynolds number, the mutual dependence has to be taken into account. Plotting relation (2-4) in a diagram with Mach number versus reciprocal Reynolds numbers shows that lines with constant Knudsen numbers describe a hyperbolic characteristic, see Fig. 13.

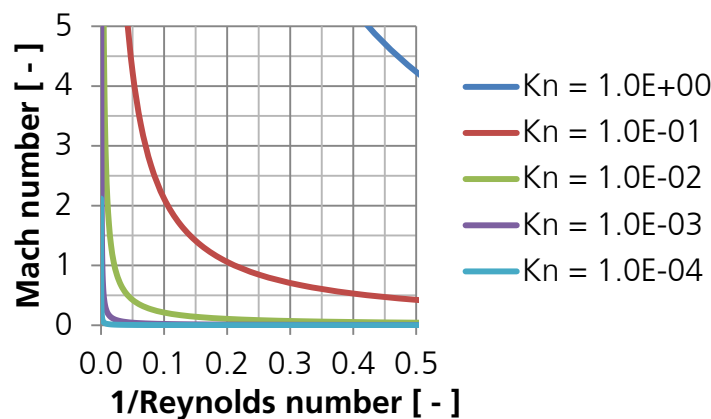


Fig. 13: Constant Knudsen numbers in Mach number versus Reynolds number plot (based on^[85])

In continuum where the Knudsen number approaches zero, the plot collapses to a quasi one-dimensional region which is either mainly defined by compressible or by viscous effects. Where the reciprocal Reynolds number approaches zero, i.e., the Reynolds number approaches infinity for a selected Mach number, the boundary layer thickness tends to zero and compressible effects dominate the flow field. On the other limiting case where the Reynolds number approaches an order of magnitude of one and the Mach number tends to zero, there is no boundary layer existent. Instead viscous effects range over the whole flow field. In case of rarefied or free molecular flow, both compressible and viscous effects can be simultaneously significant in the flow field.

Additionally to the Knudsen number, the rarefaction parameter M/\sqrt{Re} , introduced by Schaaf & Chambre^[73], serves to classify the transition regime between continuum and rarefied flow. Investigations of Koppenwallner^{[37], [38], [40], [41], [42]} showed, that in this transition regime it can be valuable to plot the aerodynamic coefficients versus the rarefaction parameter instead of the Knudsen number, which correlates with M/Re , to analyse trends. The reason is that in this flow regime close to continuum, the boundary layer effects are still significant for the overall flow field.

Since hypersonic flow is usually connected to the occurrence of high temperatures, two more similarity parameters are usually considered, the Stanton number St and the Damköhler number Da . The Stanton number relates the heat transferred into an object to the thermal capacity of the fluid and becomes relevant when thermal analyses are performed, see (2-5). Q is the integral heat transfer per area in $[W/m^2]$, ρ is the fluids density, u its velocity, cp the specific heat at constant pressure, and $T_{aw} - T_w$ the difference between the adiabatic wall temperature and the actual wall temperature.

$$St = \frac{Q}{\rho * u * cp * (T_{aw} - T_w)} = \frac{Nu}{Re Pr} \quad (2-5)$$

The Stanton number is strongly depending on the geometry of the object and the position where it is determined. It can be described as the ratio of Nusselt number Nu to Reynolds number and Prandtl number Pr . The Nusselt number represents the ratio of convective to conductive heat transfer, while the Prandtl number is defined to be the ratio of the viscous diffusion rate to the thermal diffusion rate.

The Damköhler number describes in general the ratio of time scales. In the context of aerothermodynamical analyses, it is commonly applied to describe the ratio of reaction rate to convective mass transport. In other words the Damköhler number correlates the flow time scale to the chemical time scale and is a measure whether chemical reactions are in equilibrium, non-equilibrium or frozen and whether they have to be considered for an analysis or not.

These similarity parameters and the chemically changing gas composition play an important role for hypersonic flight. During ground tests, however, it is practically impossible to match all in hypersonic flow relevant similarity parameters and chemical processes at once such that, depending on the research focus, only the most dominant similarity parameters and chemical processes are simulated. For investigating aerodynamic force coefficients in hypersonic rarefied flow, the Knudsen number, Mach number and Reynolds number are found to be the most dominant similarity parameters. A simulation of these similarity parameters can be performed in cold hypersonic wind tunnels without simulating the caloric gas properties and flow chemistry. Although Mach number and Reynolds number can be correctly simulated in cold hypersonic wind tunnels, the flow velocities to be generated are lower compared to real re-entry flight due to the lower required free stream temperatures. Further the gas composition is known due to the absence of chemical reactions, like dissociation or ionisation, which simplifies comparisons to numerical results. For investigations of aerothermodynamical effects, cold hypersonic wind tunnels are not sufficient and the caloric gas properties and the flow chemistry have to be simulated.

The desired dimensionless force coefficients relate then the measured aerodynamic forces to the dynamic free stream pressure $1/2 * \rho * u^2$ and a selected reference area such that the aerodynamic coefficients become independent from the free stream flow, and different flight configurations with different sizes and can be compared.

2.4 Mach Number Independence Principle

As this study aims at investigating aerodynamic coefficients at hypersonic Mach numbers, a brief discussion on the Mach number independence principle of Oswatitsch is important. [4], [15], [27], [63], [64], [86] The principle describes that above a certain Mach number, usually at about $M = 5$, some aerodynamic coefficients, like e.g. lift, drag and pitching moment, become asymptotically independent from the flight Mach number, such that there is no pronounced Mach number dependency determinable. This is illustrated in Fig. 14 for the drag coefficient of a sphere and a cone-cylinder.

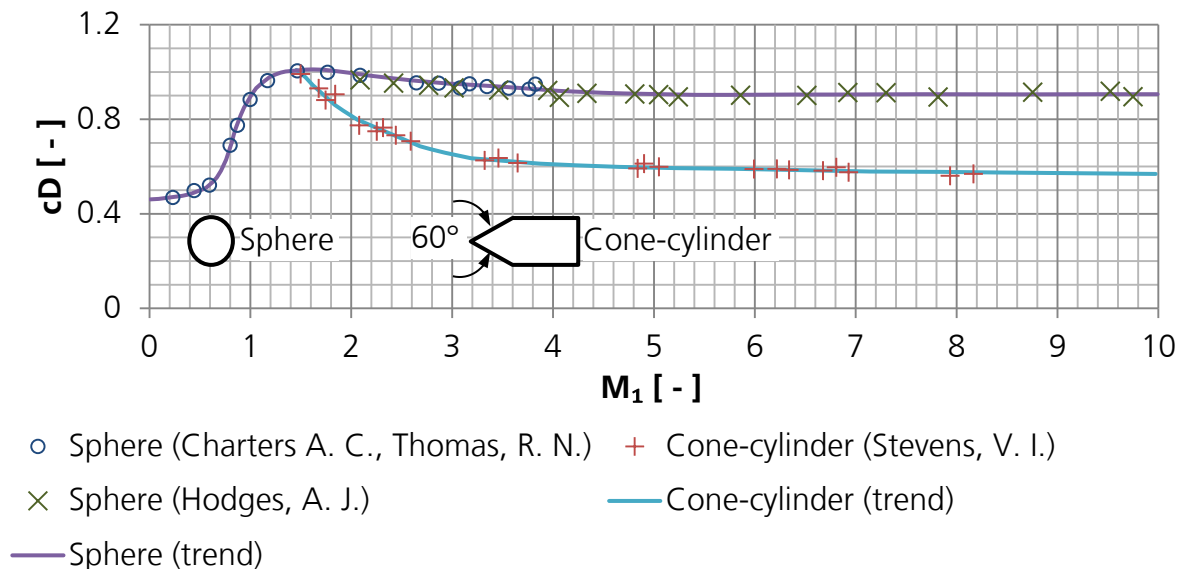


Fig. 14: Drag coefficient for a sphere and cone cylinders gathered and compared by Anderson [4] from [15], [27], [86]

It can be seen that in case of the sphere there is no Mach number dependence of the drag coefficient identifiable above $M = 5$. In case of the cone cylinder the Mach number dependency of the drag coefficient decreases from 4.1% between $M = 5$ and $M = 10$ to 1.6% between $M = 8$ and $M = 10$. Due to the asymptotic trend, it is expected that the Mach number dependency reduces further at higher Mach numbers.

The principle is derived for a calorically perfect gas and inviscid flow only. Results from a theoretical and numerical study by Kliche [30] showed the applicability of the Mach number independence principle for blunt bodies in viscous laminar flow. Due to low Reynolds numbers ($2.5 * 10^3$ to $2.5 * 10^4$ built with total body length) caused by very low densities of about 10^{-4} to 10^{-6} kg/m^3 , the flow field past the test articles is mainly laminar in the conducted experiments. Hayes et al. [23] showed that the Mach number independence principle applies to rarefied and free molecular flow as well when the configuration is blunt.

At hypersonic speeds the boundary layer thickness is inordinately increasing with Mach number squared (2-6). This causes, in particular for slender geometries, a significant change of the inviscid flow outside the boundary layer, such that the configuration appears aerodynamically blunter.^[4] Due to the viscous interaction, the surface pressure, especially in the nose region, is significantly greater compared to inviscid flow and is possibly affecting the applicability of the Mach number independence principle in case of slender configurations. This is addressed in chapter 6.1.4.

$$\delta \propto \frac{M^2}{\sqrt{Re}} \quad (2-6)$$

Applying the Mach number independence principle to the present investigation yields the consideration, that changes of aerodynamic coefficients between measurements performed at a constant Reynolds number are interpretable as a pure effect of rarefaction since solely the Mach number is varied at $M > 10$, see (2-4).

Compared to slender vehicles, blunt bodies tend to approach Mach number independence at lower Mach numbers.^[4] Since the present investigations are conducted at Mach numbers between $10 < M < 26$ the Mach number independence principle can be applied without restrictions for the blunt flight configuration. In case of the slender flight configuration, the applicability of the Mach number independence principle cannot be clarified at this point and is discussed during the analysis of the results.

3 Test Facility V2G

3.1 Operating Principle

V2G is the 2nd test section of the Hypersonic Vacuum Wind Tunnel Göttingen (VxG) of the German Aerospace Centre (DLR) in Göttingen, see Fig. 15 (top). It is a continuously running wind tunnel with theoretically unlimited test time simulating a flow with high Mach numbers between 10 and 26 at high atmospheric altitudes from 70 to 120 km. The first test section V1G^{[31], [32], [33], [34]} is a similar designed vacuum wind tunnel with a smaller test section diameter of 25 cm and higher reservoir pressures and temperatures, whereas the third test section V3G is a free jet facility connecting to the same pump assemblies. An overview about the VxG components (see Fig. 112), a reduced figure containing V2G relevant components only (see Fig. 113), and an overview about the specifications (see Table 7) can be found in Appendix A. The three test sections of the VxG facility became operational between 1964 and 1970 to investigate the transition regime between continuum and free molecular flow.

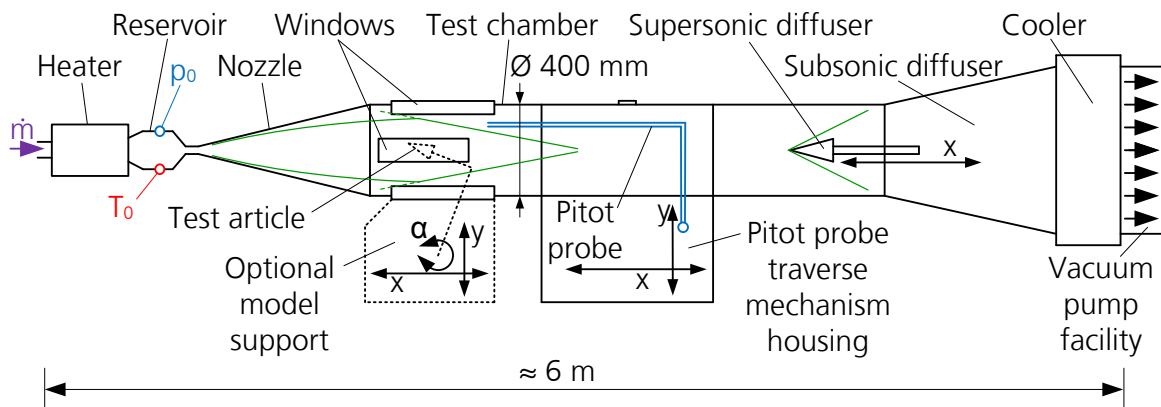


Fig. 15: V2G side view (top) and V2G sketch with roughly, in green sketched test rhombus (bottom)

The V2G, sketched in Fig. 15 (bottom), expands high pressure gas, usually Nitrogen, with up to 10 MPa through a convergent-divergent nozzle to very low pressures. With pressure ratios of 10^{-5} to 10^{-8} between test section and reservoir it is possible to accelerate the test gas to high Mach numbers at low densities. Due to the extreme expansion, the gas must be heated in advance to up to 1,500 K to prevent condensation. Downstream the nozzle, the hypersonic flow passes through the cylindrical test chamber with a diameter of 400 mm and a length of 600 mm. Two small and two large flanges are equally spaced around its circumference to allow attaching different types of model supports. By default the flanges are closed by Plexiglas

windows, see Fig. 15 (top). To provide some distance to the combined supersonic-subsonic diffuser and, hence, to avoid the influence from disturbances generated downstream, two 800 mm long cylindrical wind tunnel parts are connected downstream the test chamber. At the streamwise position of the supersonic diffuser, the test gas is already decelerated from hypersonic to supersonic Mach numbers by the oblique compression shocks generated by the impinging nozzle flow on the cylindrical test chamber. The supersonic diffuser decelerates then the supersonic flow to high subsonic speeds before the test gas is further decelerated by the subsonic diffuser. The task of the diffuser is the pressure recovery and to prepare the flow to be pumped by the further downstream following vacuum pump facility.

Further downstream the gas passes a heat exchanger cooled by water before it is finally continuously pumped out by a multistage vacuum pump facility, see Fig. 16, which is the actual centrepiece of the facility. The pump facility consists of three individual pump assemblies with a total maximum pump speed of $62.5 \text{ m}^3/\text{s}$ in the pressure range of 0.1 Pa to 133 Pa. During wind tunnel operation the pump facility keeps the static pressure as low as 1 Pa. After passing the vacuum pumps the test gas is exhaust into the atmosphere. Besides the standard test gas Nitrogen, it is also possible to operate V2G with dry air or other gases as for example noble gases. However, since the facility design does not provide a recycling of the test gas, it is uneconomic to use expensive noble gases. Except for the test chamber and the cylindrical tunnel part where the Pitot traverse mechanism housing is attached all parts of the V2G are water-cooled during operation.



Fig. 16: Picture of vacuum pump facility in cellar with 21 pumps (left), picture of biggest vacuum pump in front compared to 2 m high door (right)

Despite the heating the static temperatures decrease during the expansion down to low two-digit values. The isentropic expansion relations^[18] predict temperatures between 8 K to 15 K. Therefore, the wind tunnel flow has to be considered as a cold hypersonic flow which differs from real hypersonic re-entry flight. The hypersonic flow at the nozzle exit is not parallel but slightly divergent. The remaining divergence of the flow results in a further expansion within the downstream cylindrical wind tunnel parts and flow gradients in stream direction. The actual usable flow field, the so called core flow, is upstream defined by nozzle boundary layer and further downstream by the oblique compression shocks, generated when the expanding nozzle flow impinges on the cylindrical walls of the test chamber, see green lines in Fig. 15 (bottom). As further upstream limit the nozzle exit plane is defined since the axial flow gradients increase strongly in the heavily expanding nozzle flow. Though the flow gradients can be quantified, a correction of the measured integral forces is difficult to realise, see chapter 5.3. Due to the thick boundary layers occurring in the hypersonic low Reynolds number

flow, the maximum test article size is limited to about 10 cm. The boundary layer thicknesses can cover more than 50% of the wind tunnel diameter. Since the boundary layer thickness and, hence, the core flow dimensions are strongly depending on the operating conditions, it would be possible to use larger test articles at some operating conditions, however, simultaneously the variety of possible operating conditions is reduced further. At the given test article size, the Reynolds numbers are between $2,000 < Re < 30,000$ and the Knudsen numbers reach from about $5 * 10^{-4}$ to about 10^{-2} . An extension to higher Knudsen numbers is possible by using smaller test articles, though, simultaneously with decreasing test article size, the force measurements become even more challenging. Due to lower measurable signals, the signal-to-noise ratio decreases and less force components can be resolved.

V2G is mainly used for investigating flow problems on models of flying objects and space vehicles, typically operating at altitudes from 70 to 120 km, and for basic research in the field of rarefied gas flows to disturbed molecular flows at high Mach numbers. [13], [14], [16], [35], [36], [37], [38], [39], [40], [41], [42], [43], [49], [60], [75], [83], [84] With the V2G measurement technique, it is possible to conduct force, pressure, and heat transfer measurements on models and qualitative flow visualisation by radio frequency discharge. For the flow characterisation, the test section contains a permanently installed Pitot tube on a traversing mechanism, see Fig. 15 (bottom), movable axially and perpendicularly to the flow direction. The traversing mechanism is installed in a housing attached to the first cylindrical wind tunnel part downstream the test chamber and provides space, that the Pitot probe can be retracted if not in use. Measuring the Pitot pressure and the reservoir conditions allow the determination of the remaining flow properties using equations presented in NACA1135 [18]. The equations are derived for high speed compressible flow. The report provides relations for continuous one-dimensional flow and for normal and oblique shock waves as well as Prandtl-Meyer expansions for perfect gas.

For the attachment of the test article, different model supports are available, e.g., a model support allowing movements in two axes and rotations around two axes, and also test article injection systems to accurately control the exposure time for heat transfer measurements. The model supports can be connected to the two large flanges at the test chamber.

Measuring aerodynamic forces is the main research task in V2G. Over many years various studies are performed on both re-entry vehicles and simple shaped bodies. [13], [14], [16], [35], [36], [37], [38], [40], [41], [42], [49], [60], [83], [84], [96] Via suitable scaling of the forces and moments to flight conditions, this data is used to determine aerodynamics of the actual flight vehicle. Due to the rarefaction of the flow, the aerodynamic forces and moments acting on the vehicle are quite small (< 0.1 N) and the measurement of them is a non-trivial task. Fig. 17 shows a lifting configuration analysed with the re-established force measurement technique in V2G.

After many years of operation, the VxG were practically put out of service for about twenty years. The second test section V2G was then reactivated for new force measurements on re-entry vehicles in 2009. Within this reactivation the measurement technique, the motion control software, and the data acquisition system were

substantially revised. The main focus was on the re-establishment and optimisation of a V2G force measurement technique described in chapter 3.4 and 3.5.



Fig. 17: V2G force measurements (test article with the 3-component force balance located in water-cooled housing)

3.2 Standard Measurement Technique

The flow properties in the test section of V2G are determined by measuring the reservoir pressure, the reservoir temperature, mass flow and Pitot pressure profiles in the test section. The traversing directions of the Pitot tube are sketched in Fig. 18 (left). The origin of the coordinate system is at the intersection between nozzle exit plane and nozzle symmetry axis, see Fig. 19. The Pitot tube coordinate system is shown in Fig. 18 (right).

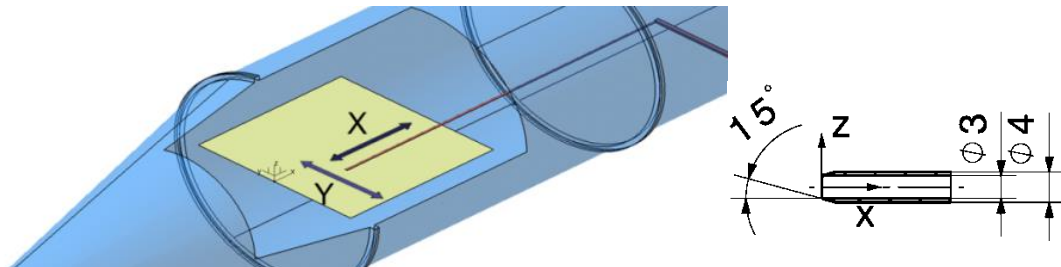


Fig. 18: Pitot tube test regime $0 \leq x \leq 449$ mm, $-187 \leq y \leq 187$ mm, $z = 0$ mm (left), Pitot tube coordinate system and CAD drawing (right)

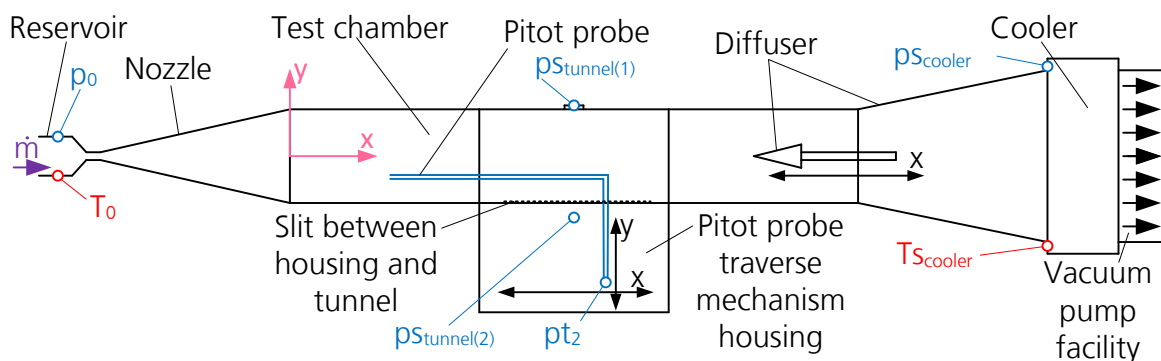


Fig. 19: Standard surveillance measurement device positions and movable mechanics at V2G, tunnel coordinate system origin located at intersection between nozzle exit plane and tunnel axis

In order to guarantee proper operation of the wind tunnel, mass flow, reservoir pressure, reservoir temperature, Pitot pressure, cooler temperature and different static pressure measurements ($p_{S_{\text{tunnel}(1)}}$, $p_{S_{\text{tunnel}(2)}}$ and $p_{S_{\text{cooler}}}$) are measured at different positions of the wind tunnel (Fig. 19). Temperature gauges are highlighted in red, pressure gauges in blue and mass flow measurement devices in purple. While reservoir pressure, reservoir temperature, mass flow and Pitot pressure are used to ensure a proper adjustment of the operating conditions, the other measurement devices are used to evaluate the general tunnel operation and effects caused by the backpressure as, for example an asymmetric flow field.

As pressure gauges only temperature-controlled Baratrons are used for the low pressure range. For p_0 sensotec pressure transducers are available with measurement ranges of 0 - 20 bar and 0 - 100 bar. The Pitot tube is also utilized during the performance of force and moment measurements to monitor the Pitot pressure in the free stream, in order to allow the comparison with the pressure obtained during the free stream calibration at the same corresponding position. For this purpose the Pitot probe is moved to a position where a mutual interference with the test articles is impossible.

Each time before the wind tunnel flow is started, the tunnel pressure is measured to ensure that a static pressure of less than 10^{-3} mbar can be reached to keep disturbances due to too high back pressure to a minimum. For this procedure $p_{S_{\text{tunnel}(1)}}$ and $p_{S_{\text{tunnel}(2)}}$ are used because they have the best accuracy in this pressure range. During operation the pressure at $p_{S_{\text{tunnel}(1)}}$ can increase to about 10^{-1} mbar and indicates how much the back pressure is affecting the flow field. The $p_{S_{\text{tunnel}(2)}}$ device is not directly connected to the tunnel flow, but to the housing of the Pitot tube traverse mechanism^[79], and is used for monitoring the pressure in the large housing cavity. Due to the long slit (480 mm long and 30 mm wide) between the housing and the tunnel, it is possible that disturbances can spread further upstream via the cavity of the housing, and in the thick boundary layer when the back pressure is not low enough. The measurement gauge at the cooler monitors the flow properties before the gas enters the cooler. This information can be used to evaluate the diffuser efficiency when it is related to the Pitot pressure.^[24] Exact measurement device positions are shown in a CAD drawing in^[79].

At the utilized reservoir temperatures between 400 K and 1,400 K, the vibrational modes of the nitrogen molecules are partially excited. From Anderson^[4] follows that for a diatomic gas the vibrational excitation starts above 600 K and reaches full excitement at about 2,000 K. However, in V2G the vibrational relaxation process freezes upstream of the nozzle throat.^[93] This analysis is performed for the V2G conical nozzle, but is also applicable to the currently utilised contoured nozzle due to similar nozzle throat diameters and almost equal expansion rates. Consequentially, the assumption of a calorically perfect gas is justified for the nozzle and test section flow, such that the ratio of specific heats is for the test gas nitrogen considered to be constantly $\gamma = 1.4$.

3.3 Supplemental Measurement Devices and Test Article Support

In addition to the permanently installed Pitot tube, it is possible to attach a test article support at the four test chamber flanges instead of a window, see Fig. 15 (bottom), to

conduct, e.g., heat transfer measurements on a copper sphere, see Fig. 20. The purpose of these heat transfer measurements is to gain further information about the flow field. This measurement technique is used to determine the possible operating conditions explained in chapter 4.3 and is here touched briefly for the sake of completeness.

The sphere is solid and has a diameter of 25 mm with a thermocouple implemented in the centre point. The position of the sphere stagnation point is invariable at 298 mm downstream the nozzle exit. By default the sphere is located in its parking position in a cavity outside the cylindrical tunnel flow. The support allows that the sphere can be quickly injected in the centre of the core flow and pulled out of the test chamber flow (indicated by red arrow in Fig. 20). In parking position the sphere is located directly behind a metallic pipe (see blue arrow in Fig. 20) which is connected to ambient air and which can be manually controlled to cool the sphere by blowing it with highly expanded ambient air.

By attaching a model support, the test chamber is changed due to the large attached cavity. A numerical analysis, simulating the cavities with the hydraulic diameter, showed that there is a further expansion due to the cavities in the test chamber, although the effect on the magnitude of the Pitot pressure is rather small.^[78]

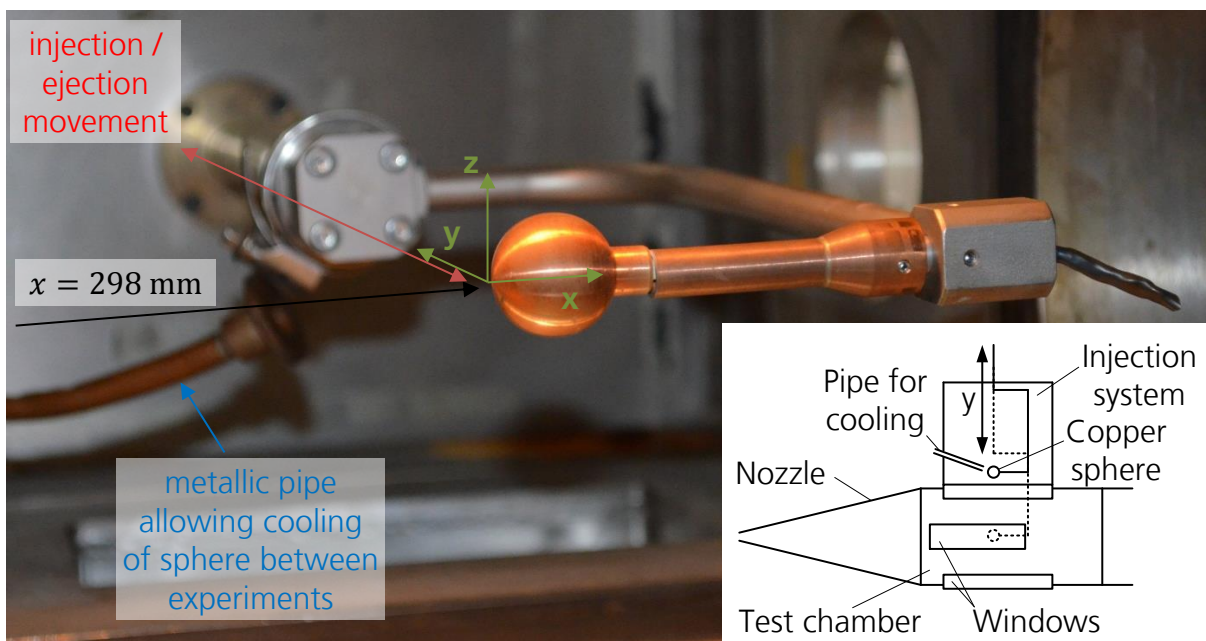


Fig. 20: Sphere for heat transfer measurements (located in V2G core flow)

3.4 Force Balance

3.4.1 Requirements and Design Limitations

For the present investigation a 3-component force balance is re-established in an optimised version. The detailed design, construction and calibration are described in^[77] and are here only briefly explained to understand the measurement capabilities and limitations. The new implemented force measurement technique is established and used within the frame of the EU FAST20XX project.^[75]

The re-establishing of the force measurement technique at V2G is accompanied by many constraints. On one hand the connection between balance and test article has to stay unchanged to allow experiments with former test articles. On the other hand it is desired to use as much as possible components from the existing water-cooled model support which enables to change the angle of attack and yaw angle of the test article and to adjust its position in V2G. Although the movable model support required some repair works and exchange of components, it could be made operational with acceptable effort, compared to a complete re-design and construction. Due to usage of the existing infrastructure, the installation size of the new balance is limited. Based on an exchange of assessments with experienced former staff about the peculiarities of conducting force measurements in V2G, it is decided to use the principle and similar design of former strain gauge balances with some optimisations explained later.

The setup of the force measurements including test article, balance, model support and wind tunnel is sketched in Fig. 21. The geometric dimensions of the balance housing are shown in [79]. It can be seen that the balance is located inside the cylindrical part of the test section and is shielded from the free stream flow. Due to the hollow test article design, the balance is partially covered by the test article and further downstream by the water-cooled balance housing. The balance is able to measure normal and axial forces as well as the pitching moment. For the evaluation of the force components the forces are afterwards transferred into the aerodynamic system. A sketch of the V2G force balance and the strain gauge positions is presented in Fig. 22.

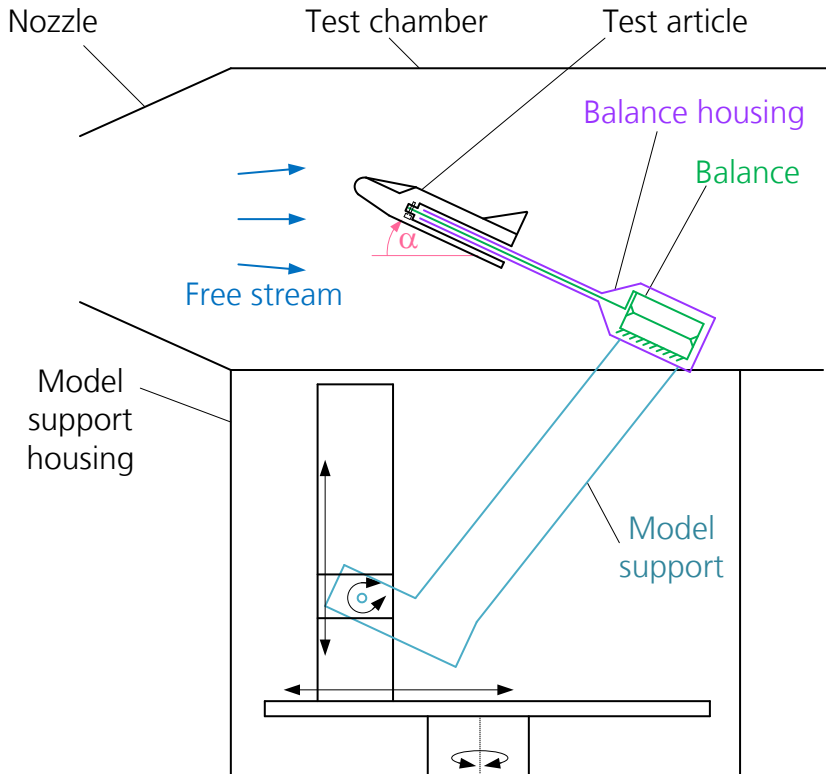


Fig. 21: Sketch of force measurement setup in V2G (top view), weight forces act normal to the drawing plane

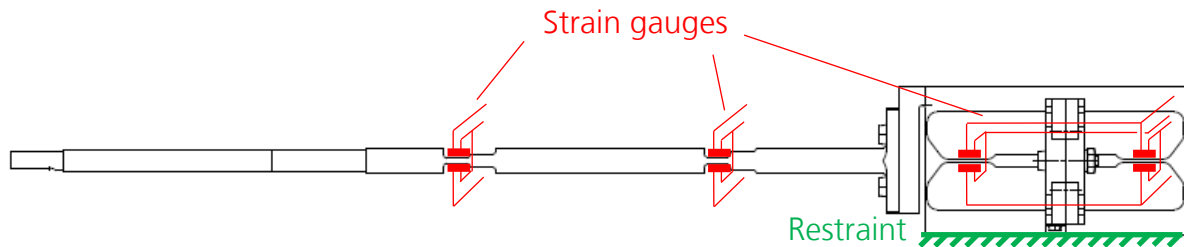


Fig. 22: Sketch of V2G force balance

3.4.2 Load Determination

The magnitude of the aerodynamic forces for the present configurations can be easily estimated from the various force measurements in V2G in the past, e.g. ^[83]. Due to the rarefaction the aerodynamic forces acting on the test article are as low as 1 mN and their measurement is challenging. Considering a test article size of 10 cm, the maximum aerodynamic force is about 100 mN. Without available data another approach would have to be used. A possibility is to consider the free molecular and continuum results theoretically, numerically or experimentally to estimate the loads in the transition regime. Wuest ^[95] describes in detail an analytical approach for the free molecular and continuum condition for simple shaped bodies.

Due to the balance principle, the test article must be as light as possible. The desired force measurement is based on the difference of two measurement signals (strain gauges along the beam, see Fig. 22) which are both proportional to the sum of aerodynamic loads and dead weight of the test article. Since the test articles dead weight acts as a high pre-load, which is with 30 g to 40 g commonly three to four times higher than the aerodynamic loads, the desired signal can easily drop below the noise level when the test article becomes heavier. However, the potentials to achieve a further weight reduction are already nearly exploited. For typical test article dimensions of 10 cm, the test article wall is only about 0.2 mm thick and very fragile. The test article accommodates only the structure necessary for the attachment onto the balance, see disassembled test article in Fig. 23. For assembling the inner structure is inserted, with the balance attachment in front, into the hull and screwed together with the hull at the back plane.

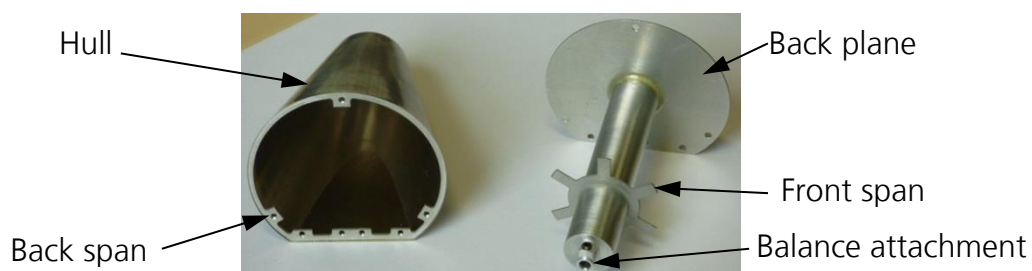


Fig. 23: Light weight COLIBRI test article, hull (left), inner structure (right)

Since the pre-load caused by the test article weight, is the weight multiplied with its lever length, it can be reduced additionally by decreasing the lever length. The lever length is measured from the strain gauge positions on the bending beam (see Fig. 22) to the centre of gravity of the test article. Due to the small test article size it is technically not possible to place the balance completely inside the test article. It is though possible to shift the balance attachment position into the test article by up to 80% of the test article length.

Despite lightweight construction the high body weight compared to the aerodynamic forces demands a rigid balance design. This rigidity in turn leads to small signals and thus to a necessity for amplification factors as high as 10,000 if output signals of up to 5 V for the maximum design load are required. Using amplification factors of this magnitude means that even small perturbation effects can easily become large enough to significantly influence or even exceed the desired force measurement signal. Especially the long-term zero point drift becomes an enormous problem due to the long test times of V2G experiments and is addressed in detail in chapter 4.7. An effective thermal shielding and an accurate calibration and monitoring of the balance temperature by sensors close to each pair or strain gauges are indispensable. For that reason the protective housing of the force and moment balance is water-cooled and designed to ensure that the wind tunnel flow cannot directly impact the balance. Additionally, already in the design phase of V2G force measurement test articles, the heat transfer from test article to the balance has to be considered and kept as low as possible. In detail this is described in chapter 3.5.

3.4.3 V2G Strain Gauge Balance Principle

The operating principle of the strain gauge force and moment balance is that a mechanical load causes a bending deformation in a deliberately designed structure and consequently a stretching or respectively a compression on the sides where the strain gauges are fixed (Fig. 24, left). Due to the fixed connection between the strain gauges and bending structure, the strain gauges are stretched or compressed and change their resistance accordingly and supply a measurable signal. This principle process is sketched for a typical foil strain gauge in Fig. 24 (right) where the strain gauge grid is stretched. Strain gauges do not only measure bending deformation, but also pressure, tensile stress and are very sensitive to temperature changes. These undesirable effects have to be compensated or taken into account for the analysis of the signals.

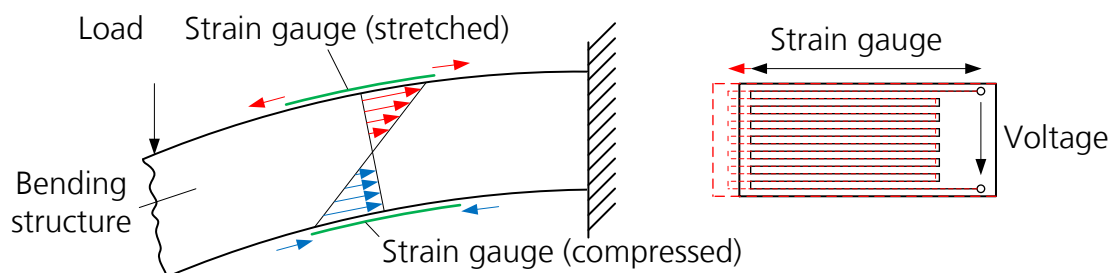


Fig. 24: Strain gauge measurement principle (left), foil strain gauge (right)

The strain gauge does not measure directly the applied force, but rather the deformation resulting from the applied force. Within the materials elastic range, the relation between applied force and resulting deformation is linear as Hooke's law states.

On the one hand it is essential that there is a measurable deformation in the balance but on the other hand a deformation is undesirable since the test article deviates from the adjusted position and attitude in the wind tunnel during the experiment. For these reasons the overall structure is designed rather rigid with a pliable narrowing, where the strain gauge is positioned, see Fig. 25. Thus, the overall deformation is reduced to a minimum, while having measurable deformations at the strain gauge position at the

same time. For the re-designed force balance, the angular deformation is ensured to be lower than 0.5° , and the lateral deformation lower than 1 mm for the maximum design load of 0.5 N which is the sum of 0.1 N aerodynamic load and 0.4 N zero loads of balance and model weight in the FAST20XX campaign.

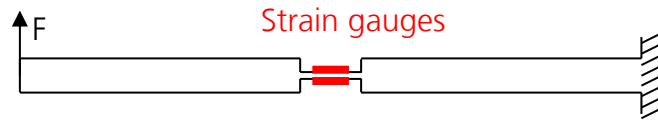


Fig. 25: Narrowing for strain gauge attachment

3.4.4 Design & Concept

Fig. 26 shows that the chosen design of the V2G balance consists of two balance transducers, the normal force and pitching moment transducer, denoted as normal force transducer (blue) and tangential force transducer (red). The green parts are hollow adapter pieces with a wall thickness of 0.2 mm to reduce the heat transfer from the test article into the balance. As adapter pieces several designs are available. The long adapter piece containing the test article holding fixture is always used, while the shorter adapter is only used if no rolling moment transducer is implemented to ensure a constant balance length.

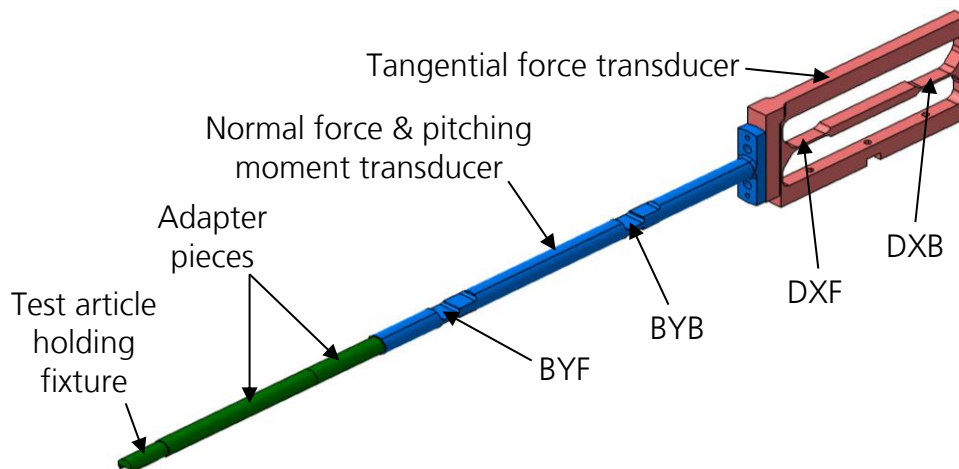


Fig. 26: 3-component balance (normal and tangential force transducer)

In opposite to earlier versions of the balance, the thickness of the narrowing at BYF and the narrowing at BYB are not equal. The thickness is rather designed that a load applying at the position where the normal force transducer ends is resulting in an equal bending deformation in both narrowings. The measurement range of the balance is larger compared to versions with equal notch thicknesses. The disadvantage is that the measured signals cannot be directly related to normal force, axial force and pitching moment, but require a more complex calibration first, see chapter 3.4.6.

3.4.5 V2G Strain Gauge Circuitry

The strain gauges change their resistance due to the applied strain caused by the local deformation. They cannot distinguish between deformations caused by a mechanical

load or temperature changes. Compensating this fact requires several strain gauges at one measurement position. The circuitry of the V2G balance strain gauge elements is carried out in both full and half Wheatstone bridge circuits which increases the signal output by simultaneously compensating strain in undesirable directions, and due to thermal expansion. The normal force components are wired in half bridges, while for the tangential force component a full bridge circuit is used. From Fig. 27 it can be seen that theoretically temperature changes affect the output signal only if the temperature is not changing uniformly for all strain gauge elements. Otherwise the bridge voltage remains unchanged. For the half bridge circuitry all strain gauges have to face the same temperature, while for the full bridge either the two on top and the two on the bottom, or the two on the sides have to have the same temperature change. Since a non-uniform temperature change results in a zero point drift, the strain gauges are usually fixed very close to each other. Zero point drift can be defined as “a gradual change of the indicated zero offset with no input signal” [28] and can normally be “specified as a function of time and/or temperature” [28]. Because of small differences in the thermal characteristics of the strain gauges and slightly different temperature distribution in the balance frame, it is usually not possible to compensate the thermal effects completely by using Wheatstone bridge circuitry. Consequently, the strain gauges should be kept at a constant temperature.

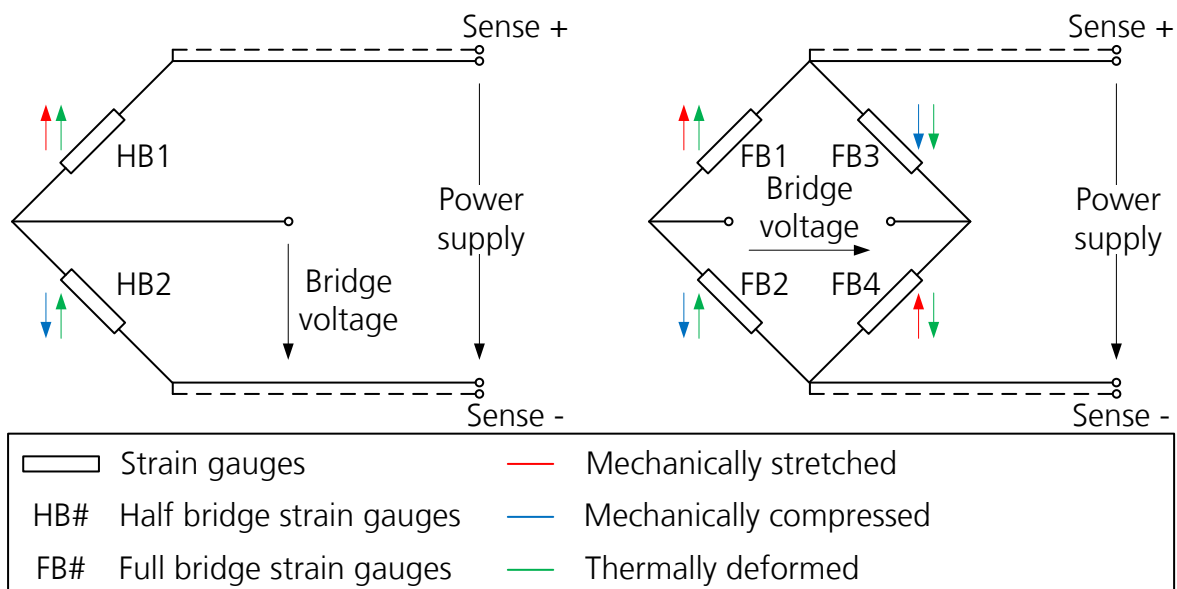


Fig. 27: Wheatstone bridge circuitry, half bridge (left), full bridge (right)

The undesirable effect of the cable resistance can be compensated if the Wheatstone bridges are wired with a five-wire connection for the half bridges, and with a six-wire connection for the full bridges respectively. [28] In particular an additional sense-wire is installed in parallel to both power supply wires (see Fig. 27). The supply unit is thus able to measure and adjust the voltage directly at the connection between the supply and sense wire.

Based on Fig. 27 for a voltage feed bridge supply, the bridge voltage can be calculated with (3-1) and (3-2) for the half and for the full bridges respectively.

$$U_{bridge(half\ bridge)} = U_{supply} * \frac{R_{FB2}}{R_{FB1} + R_{FB2}} \quad (3-1)$$

and

$$U_{bridge(full\ bridge)} = U_{supply} * \frac{R_{FB2} * R_{FB3} - R_{FB1} * R_{FB4}}{(R_{FB1} + R_{FB2})(R_{FB3} + R_{FB4})} \quad (3-2)$$

Very important for a high measurement quality is the use of carrier frequency amplifiers, because of the very low measurement signals and correspondingly high required gains of 10,000. Carrier frequency amplifiers have the advantage that constant voltage offsets, as they can occur, e.g., as a result of electromagnetic interference, or temperature changes within the cables, are not affecting the measured signal. [77]

3.4.6 V2G Force Measurement Technique

Based on the obtained signals the actual applied forces and moments can be derived.

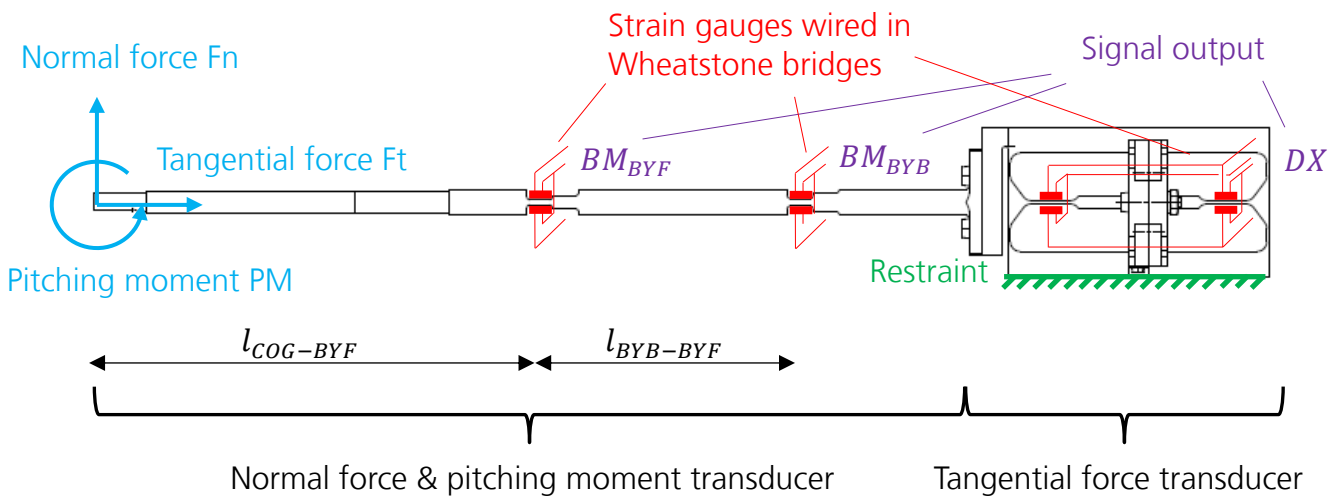


Fig. 28: V2G force balance sketch (BM: bending moment signal, BYF, BYB: stain gauge positions, DX: axial drag signal, COG: centre of gravity)

From Fig. 28 the following system of equations can be set up for the force determination by considering equilibrium of forces at BYF and BYB each:

$$BM_{BYF} = PM - Fn * l_{COG-BYF} \quad (3-3)$$

$$BM_{BYB} = PM - Fn * (l_{COG-BYF} + l_{BYB-BYF}) \quad (3-4)$$

Combining equation (3-3) and (3-4) yields

$$Fn = \frac{(BM_{BYB} - BM_{BYF})}{l_{BYB-BYF}} \quad (3-5)$$

$$PM = BM_{BYB} - \frac{(BM_{BYB} - BM_{BYF})}{l_{BYB-BYF}} * (l_{COG-BYF} + l_{BYB-BYF}) \quad (3-6)$$

and hence

$$PM = BM_{BYB} * \left(1 - \frac{l_{COG-BYF} + l_{BYB-BYF}}{l_{BYB-BYF}}\right) + BM_{BYF} \left(\frac{l_{COG-BYF} + l_{BYB-BYF}}{l_{BYB-BYF}}\right) \quad (3-7)$$

The distance $l_{BYF-BYB}$ is a body-fixed value, while the distance $l_{COG-BYF}$ is the distance from the strain gauge positions BYF to the centre of gravity or force reference point of the test article and depends on the test article geometry as well. This value has to be determined for each configuration of balance and test article. The relation between the bending moments and the mechanical loads is established by the calibration described in chapter 4.7. The required geometric dimensions are listed in Table 1. With an equal thickness of both narrowings, it would be possible to solve (3-5) and (3-6) before applying the calibration. The advantage would be that the characteristic of normal force and pitching moment could be easily determined during the measurement process.

The relation between the tangential force and the DX strain gauge circuit signal is a linear calibration described in chapter 4.8. There is no further calculation necessary as for the normal force and pitching moment.

In the last step the forces and moments have to be transformed from the balance coordinate system into the aerodynamic coordinate system using (3-8) and (3-9), see Fig. 29. Since the reference point remains at the centre of gravity, the Pitching moment remains unchanged. Fig. 30 shows a picture of the V2G force balance.

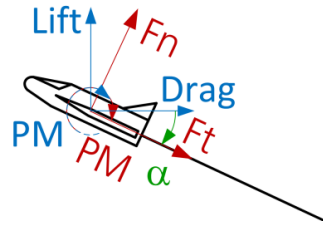


Fig. 29: Coordinate system transformation from balance to aerodynamic system

$$F_L = F_n * \cos(\alpha) - F_t * \sin(\alpha) \quad (3-8)$$

$$F_D = F_n * \sin(\alpha) + F_t * \cos(\alpha) \quad (3-9)$$



Fig. 30: Picture of V2G force balance

Table 1: Geometrical data of V2G force balance

Length	
Distance BYF – BYB	[mm] 40
Distance balance tip – BYF	[mm] 60.5

3.4.7 Analytical Approach

For the dimensioning of the balance, both force transducers are analytically calculated. Fig. 31 shows the separation of the normal force transducer in eight Macauley^[51] ² integration regimes together with the applied loads. The separation becomes necessary since the moment of area of the normal force transducer varies. The dead weight of the balances cannot be neglected and has to be taken into account for the whole frame. The influence of additional weight and stiffness of strain gauges, adhesive and circuitry is neglected, as well as the tiny radii between the different beam cross sections. The weight forces of the normal force transducer are applied as distributed load and is depending on the angle of attack. The normal force and the pitching moment are applied at the balance tip. Since the balance and the test article are mounted upside down, the weight force has the same sign as the normal force. Tangential forces are neglected for the calculation since the bending angle is with below 0.5° very small. The assumption of small deformation angles simplifies the equations because it can be assumed that $\sin(\alpha) = \alpha$ and $\cos(\alpha) = 1$. Due to the changing moment of area, a second reference model, a bending beam composed of beam parts with constant cross sections each, is applied where, starting from left, the forces and deformations for each regime (na till nh in Fig. 31) are calculated. During calculation the reference model is assumed to be rigidly restraint on the right. The resulting bearing loads are calculated and serve as reaction force (with the opposite sign) for the load applied in the next step. Since the total bending angle is small, it is assumed that the applied force acts consistently normal to the beam for all integration regimes. The bending angle and the deflection within a regime are calculated for each loop as well. l is the distance in x direction where $l = 0$ in each regime is the left side of the bending beam reference model.

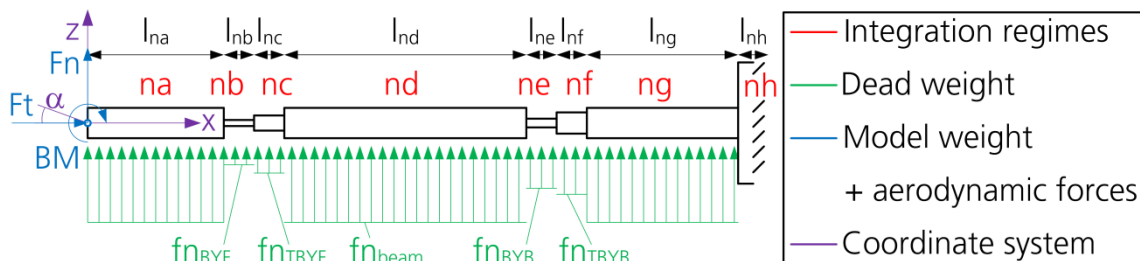


Fig. 31: Normal force transducer reference model with applied loads

Equations (3-10) to (3-14) show the necessary integration exemplarily for the integration regime na. Equation (3-10) contains the distributed loads. The integration of (3-10) yields the normal force equation (3-11) with the applied normal loads as integration constant. With a further integration the bending moment equation (3-12) is obtained with applied moments as integration constant. Integrating further and multiplying with Young's modulus and the moment of area yield the bending angle equation (3-13). The angle at the restraint on the right side corresponds to the integration constant c_1 . The final integration leads to the bending deformation equation (3-14) with the integration constant c_2 as deformation at the restraint on the right side. The two integration constants $c_{1_{na}}$ and $c_{2_{na}}$ can be calculated from the boundary conditions.

² in German referred to Föppl^[20]

$$fn_{na(l)} = fn_{na} \cos(\alpha) \langle l \rangle^0 \quad (3-10)$$

$$-Fn_{na(l)} = fn_{na} \cos(\alpha) \langle l \rangle^1 + Fn \langle l \rangle^0 \quad (3-11)$$

$$-BM_{na(l)} = \frac{1}{2} fn_{na} \cos(\alpha) \langle l \rangle^2 + Fn \langle l \rangle^1 + BM \langle l \rangle^0 \quad (3-12)$$

$$EJ_{na} \phi_{na(l)} = \frac{1}{6} fn_{na} \cos(\alpha) \langle l \rangle^3 + \frac{1}{2} Fn \langle l \rangle^2 + BM \langle l \rangle^1 + c1_{na} * EJ_{na} \quad (3-13)$$

$$EJ_{na} \eta_{na(l)} = \frac{1}{24} fn_{na} \cos(\alpha) \langle l \rangle^4 + \frac{1}{6} Fn \langle l \rangle^3 + \frac{1}{2} BM \langle l \rangle^2 + l * c1_{na} * EJ_{na} + c2_{na} * EJ_{na} \quad (3-14)$$

For the determination of the deformation and deformation angle at the left side, it is necessary to setup and integrate primarily the force equations (3-10) to (3-12) from the integration regimes na to nh to obtain the overall forces and moments accumulating at the integration regime nh. Since there the restraint deformation and angle is known to be zero, the integration constants can be inserted. For the determination of the deformations on the left side the deformation equations (3-13) and (3-14) have to be solved backwards for all integration regimes from nh to na.

The dimensioning of the tangential force transducer is calculated with the same scheme but it is far more complex since the frame structure is a closed beam structure which is statically multiple-indeterminate and has changing cross sections, see Fig. 32 (left). Therefore, the deflections are derived for a reference model sketched in Fig. 32 (right).

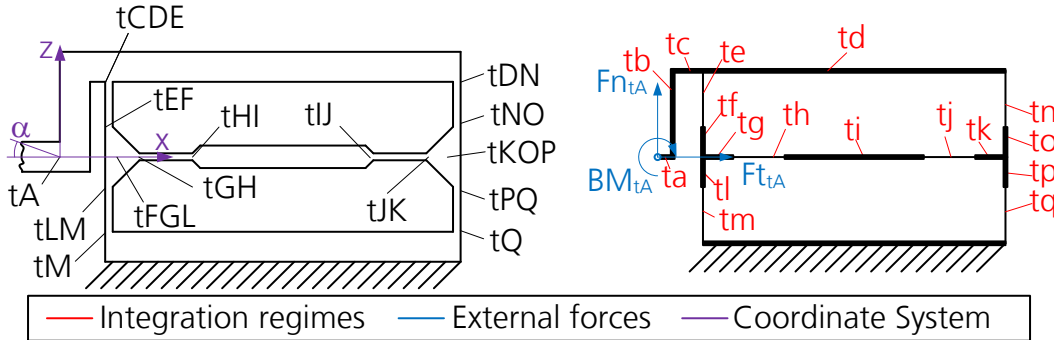


Fig. 32: Reference model of tangential force transducer (left), simplified and subdivided (right)

It can be seen that the whole structure has to be subdivided into seventeen integration regimes (ta to tq) shown in Fig. 32 (right). The system can be simplified if all thick drawn integration regimes are assumed to be rigid. They have a thickness of at least a factor of ten higher, compared to the thin marked integration regimes (te, th, tj, tn, tm, tq), and a moment of area which is higher by more than a factor of thousand. With this assumption the resulting loads in point tCDE, for example, can be directly calculated with forces and moment in tA, the weight forces in ta, tb and tc, and the corresponding lever lengths in x and z-direction. Further the dead weight of the thin-drawn beams can be neglected because of their small thickness, while the others have to be taken into

account. As for the normal force transducer, the influence of additional weight and stiffness of strain gauges, adhesive and circuitry is neglected.

To solve a statically indeterminate closed beam structure, the structure has to be broken up in a statically determinate one, see Fig. 33 (left). Instead of the previous restrictions external forces and moments with an unknown sign and magnitude are applied. The framework can then be calculated. After the force, moment, bending angle and bending deformation distributions are obtained, the additionally applied external forces can be determined.

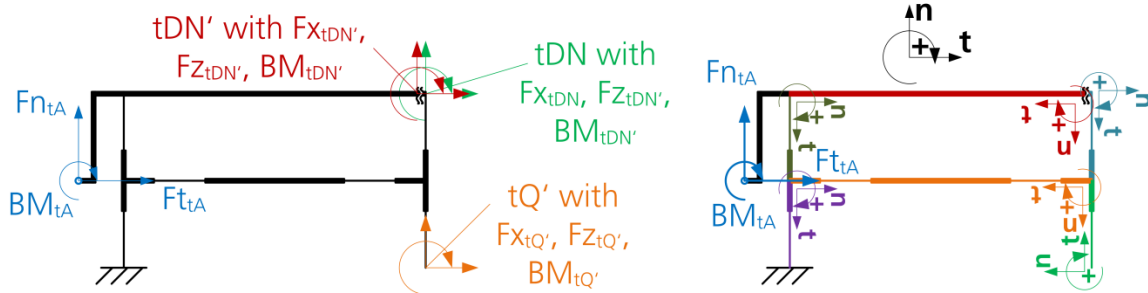


Fig. 33: Statically determined tangential force transducer (left), together with local coordinate systems (right)

The further boundary conditions, bending angle and deformation are set to:

$$\phi_{tDN'} = \phi_{tDN} \quad (3-15)$$

$$\eta_{tDN'} = \eta_{tDN} \quad (3-16)$$

$$\eta n_{tDN'} = \eta n_{tDN} \quad (3-17)$$

$$\phi_{tQ'} = 0 \quad (3-18)$$

$$\eta_{tQ'} = 0 \quad (3-19)$$

$$\eta n_{tQ'} = 0 \quad (3-20)$$

That means for the forces and moments that:

$$F_{tDN'} = \begin{pmatrix} Fx_{tDN'} \\ Fz_{tDN'} \end{pmatrix} = \begin{pmatrix} -Fx_{tDN} \\ -Fz_{tDN} \end{pmatrix} \quad (3-21)$$

$$BM_{tDN'} = -BM_{tDN} \quad (3-22)$$

$$F_{tQ'} = \begin{pmatrix} Fx_{tQ'} \\ Fz_{tQ'} \end{pmatrix} = \begin{pmatrix} -Fx_{tQ} \\ -Fz_{tQ} \end{pmatrix} \quad (3-23)$$

$$BM_{tDN'} = -BM_{tDN} \quad (3-24)$$

The dead weight of the balance frame is not shown in Fig. 33 (left) for clarity, however, except for the bending beams themselves (te, th, tj, tn, tm and tq) it is included in the calculation. The local coordinate systems are sketched in Fig. 33 (right).

The six equations (3-15) to (3-20) are building a system of equations in which the equations (3-10) to (3-14) for each tangential force transducer integration regime have to be inserted. The six unknown force and moment components in tDN and tQ are presented in equation (3-21) to (3-24). The difficulty is here not the solving of the equation system but the setup, the inserting of equations and their simplification. Since the equations of all integration regimes have to be inserted into each other, the equations become far too big for typical math programs, as e.g. MAXIMA. However, a numerical solution by SCILAB, for example, becomes only possible when the equations are manually simplified and structured in a matrix format.

Solving this equation system yields the forces, moments, deformation angles, and deformations in all integration regimes. Fig. 34 gives an overview of the deformation due to normal and tangential forces as well as pitching moment, resulting from the calculation reference model. By adding the deformations in the tangential force transducer to the normal force transducer, the overall deformations at the balance tip can be obtained. It can be seen that the normal force transducer (beam to the left in Fig. 34) measures normal forces and bending moments, while the tangential force transducer (rectangular structure on right side) independently measures the applied tangential forces. Based on the calculation reference model, the deformations can then be superposed on the actual geometry, see Fig. 35. The forces applied in Fig. 34 and Fig. 35 are far higher than the maximum allowed forces and are only chosen for better visualisation.

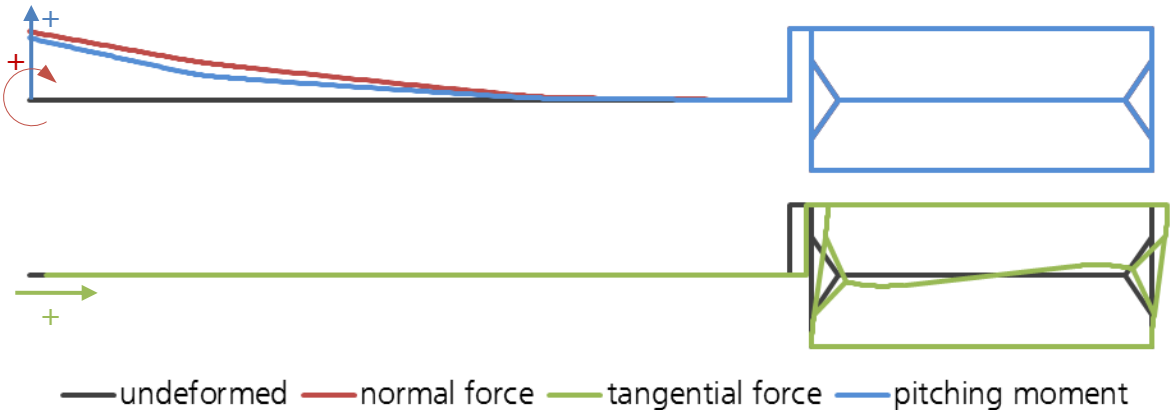


Fig. 34: Balance deformation caused by applied normal- and tangential loads and pitching moments

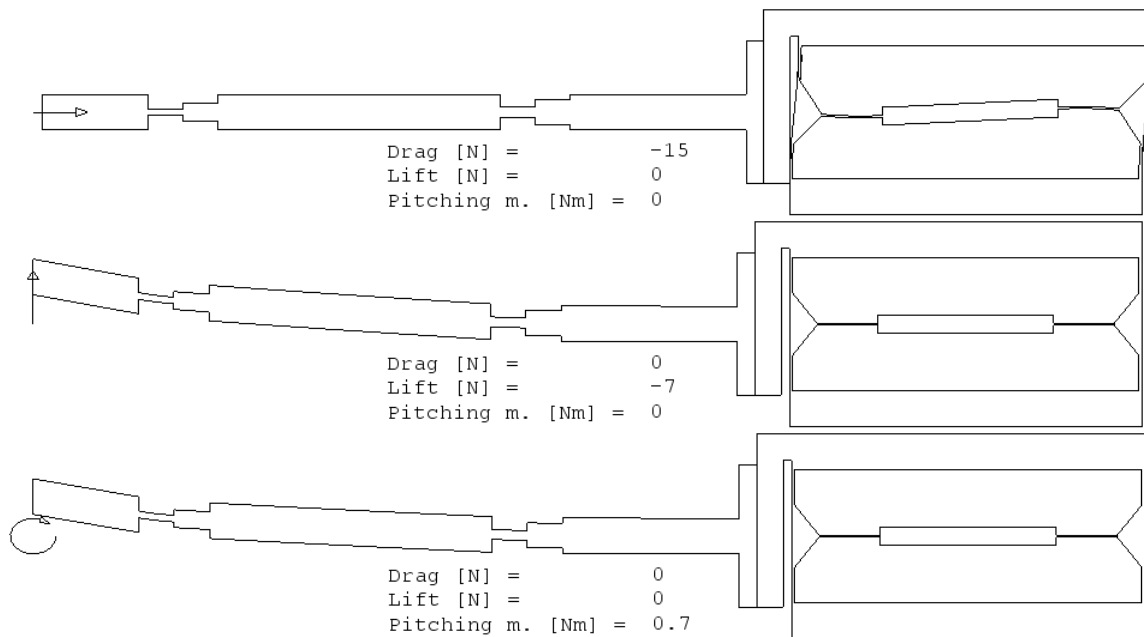


Fig. 35: Deformations shown on balance geometry

Since the calibration of the force balance requires more information about further conducted optimisations, it is treated at the end of the preparation of experiments in chapter 4.8.

3.5 Test Article Design

There are two limitations defining the size of the test articles. The maximum size is defined by the core flow diameter in V2G which strongly depends on the selected operating condition. Flow characterisations showed that at nearly all operating conditions a core flow diameter of about 10 cm is achievable. The restriction for the minimum size is not as well defined but the used force balance yields the best signal / noise ratio when the aerodynamic forces are high. Smaller test articles yield accordingly lower aerodynamic forces, and it becomes difficult to distinguish between measured signal and noise. For the best force measurement results V2G models are usually designed to be near the upper size limit.

To obtain a very lightweight test article, as described in chapter 3.4.2, the wall thicknesses have to be very thin, and the test article can only contain the necessary infrastructure to fix the test article on the balance but, e.g., no additional measurement devices. A typical hull thickness for V2G test articles is 0.2 mm. A thicker wall would increase the weight unnecessarily, while a thinner wall would complicate the handling of the test article even further due to less stiffness.

This design restriction limits the possible construction methods. As in the past, today the hull of the test articles can be manufactured only galvanoplastically. In co-operation with the Fraunhofer Institute for Manufacturing Engineering and Automation (IPA), the hull of the SHEFEX III test article is manufactured by electrolytic metal separation on a positive core, see Fig. 36.

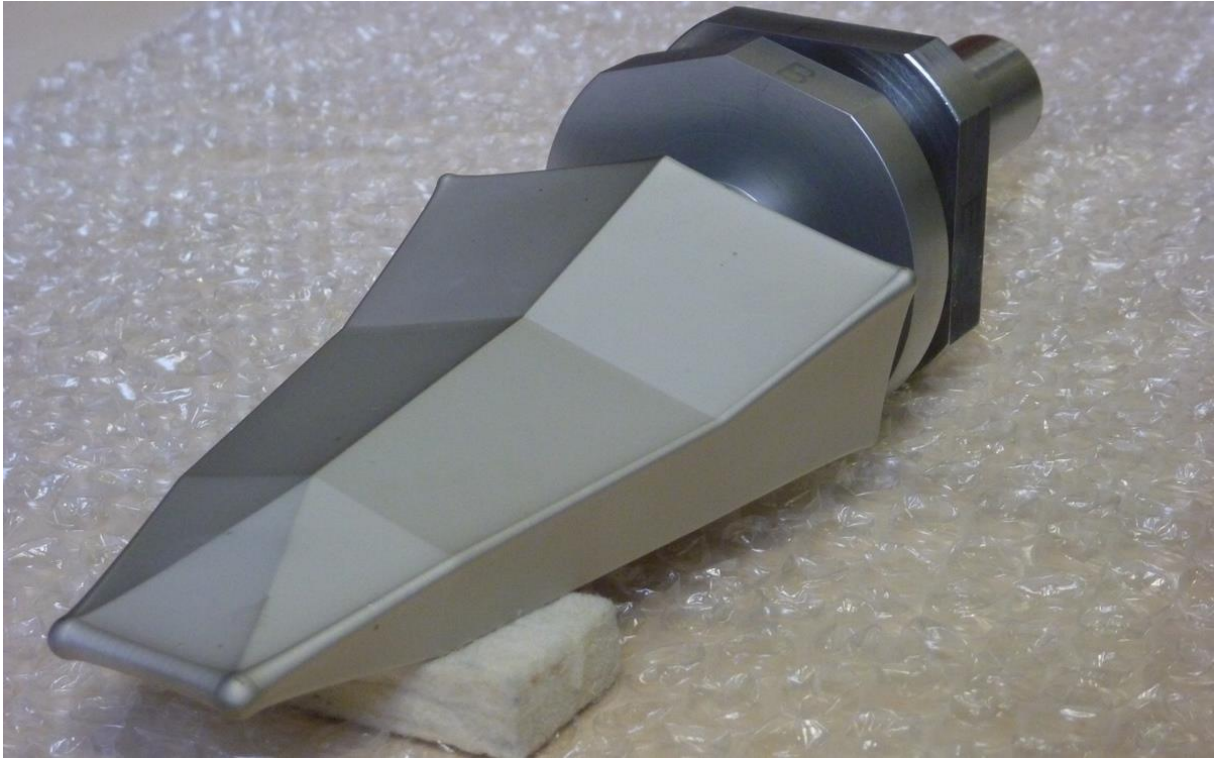


Fig. 36: Electrolytic metal separation on a positive core of SHEFEX III with adjustment planes for post-processing at the support structure in the background

The electrolytic metal separation is conducted until the metal layer reaches more than 0.5 mm. While the hull is still on the positive core, the outside has to be cut to the nominal values with a wire cut machine to keep the tensions and temperatures as low as possible. Machining the hull with a milling machine would increase the risk that the hull is locally separating from the core and being destroyed during the process. Only after the complete machining including polishing is finished, the hull can be separated from the core by cooling both parts in liquid nitrogen and subsequently heating-up the hull. After demoulding and polishing off the nickel remainders, the core could be used for another test article. However, due to several times of polishing, the core dimensions become slightly smaller which is significantly increasing the wall thickness and the weight and limits the number of re-uses.

Approaches to construct the test article hull via 3D metal moulding are not promising at the current stage of development since the surface roughness is comparably bad and requires much polishing effort. Due to the lack of a temporary support structure inside, this method is considered as inappropriate. The same applies to a material change from nickel to titanium which has much better material properties at first sight. However, titanium chemically reacts with the decelerated hot nitrogen flow in the wind tunnel to titanium nitride with unpredictable results.

The inside structure of the test articles is usually designed in differential construction, see Fig. 37 for the SHEFEX III test article. During a further improvement the inside structure, except front span and heat shield, could be built with 3D metal moulding by simultaneously reducing the weight of the structure by 25% for both COLIBRI and SHEFEX III configurations.

To reduce the lever lengths from the strain gauges to the force application point, the balance is usually placed as far as possible into the test article, see Fig. 37. The water cooled-housing reaches almost to the attachment point. This overlapping is simultaneously shielding the balance from facing the decelerated hot wind tunnel flow behind the shock. The strain gauges on the balance are extremely temperature sensitive, so that the heat transfer onto the balance has to be reduced as much as possible. Since the test article operates in a vacuum environment, the heat can be transferred to the balance by heat transfer via the hull, by radiation from the hot stagnation point area, but not by convection due to the very low-density. Due to construction limitations the material cannot be changed but the distance from the hot stagnation point to the balance can be extended. The idea is to design the front span very thin and fragile, so that the major part of the heat transfer has to take the long distance via the hull, the backplane, and back to the front via the cylindrical tube before it reaches the attachment point and then the balance, see Fig. 37 (attachment point painted in light green, covered by heat shield painted in semi-transparent red). Additional, the tip of the balance is protected by a heat shield in the front section see Fig. 37. Together with short time measurements of about 3 min test time, which finish before the temperature at the strain gauges is significantly increasing, the temperature depending error becomes nearly negligible and can be compensated. After a test cycle the test section has to be ventilated to allow a quick heat equalisation within test article and balance. To prevent measurement errors by temperature changes in the cooling water, the water temperature is controlled and kept at a constant temperature of 29°C.

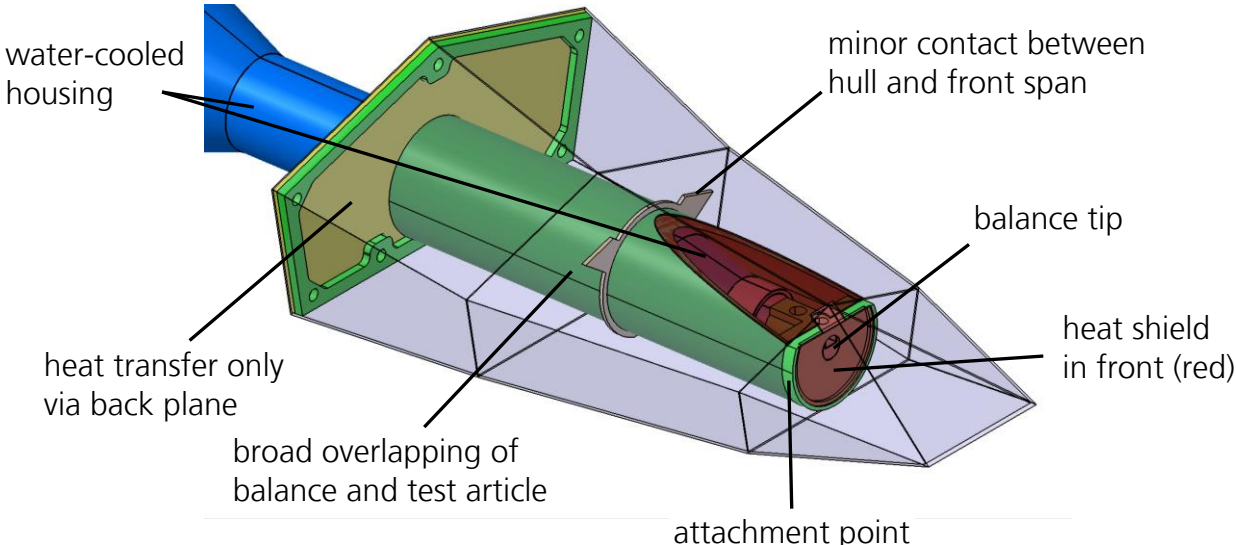


Fig. 37: CAD drawing of V2G SHEFEX III test article

Parallel to the performance of the experiments, an improved internal structure for both test articles is designed and constructed for further measurements at higher angles of attack in a following measurement campaign, see cut drawings in Fig. 38 and Fig. 39 respectively. The updated version contains internal heat shields for both configurations.³ Additionally, the weight of the internal structures could be significantly reduced (25%) due to a new construction method using Selective Laser Sintering (SLS). Both test articles are already successfully tested at the last measurements of this test campaign.

³ In contrast to the SHEFEX III test article the original version of the COLIBRI test article is not equipped with a heat shield.

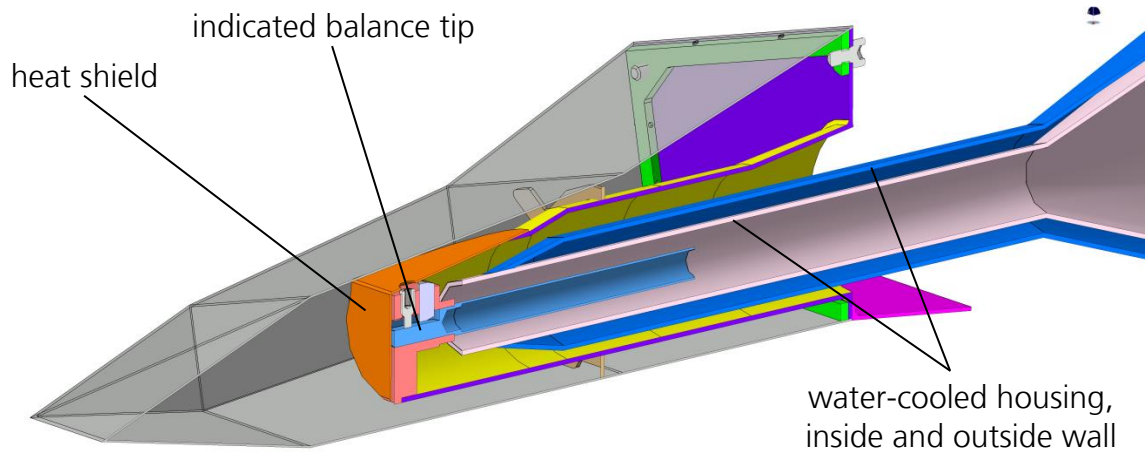


Fig. 38: CAD cut drawing of revised SHEFEX III test article

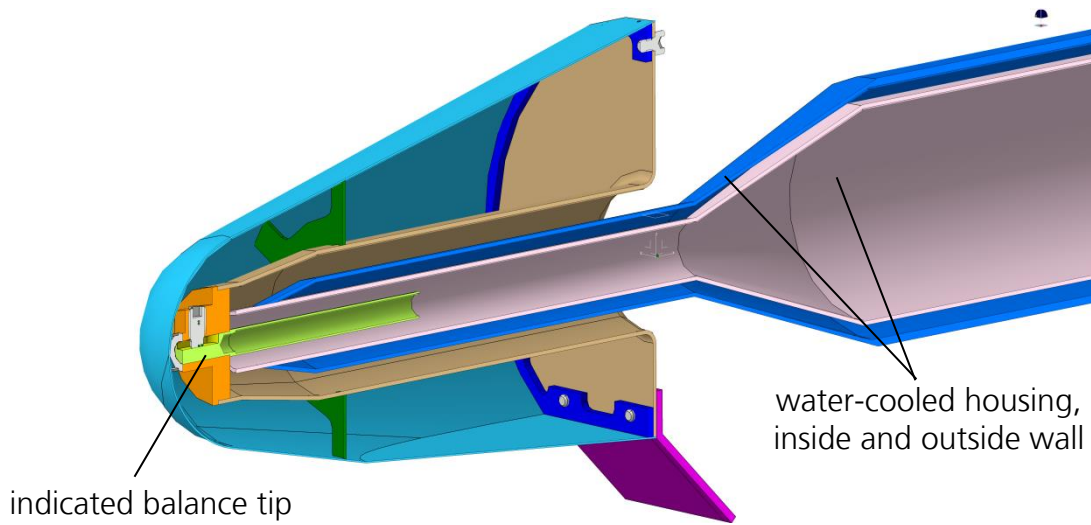


Fig. 39: CAD cut drawing of revised COLIBRI test article (heat shield not displayed)

4 Preparation of Experiments

4.1 Facility Setup

As approach to improve the flow homogeneity by means of smaller radial flow gradients in the test chamber, the present experiments are conducted using the new contoured nozzle instead of the conical nozzle used during the low-density tests within FAST20XX. Detailed geometric data of the nozzle is published in [78]. The experiments are performed with the standard test gas nitrogen.

To obtain a variation of the Knudsen number at a constant Reynolds number, the Mach number has to be varied, see (2-4). Adjusting reservoir pressure and temperature yields only minor variations in the Mach number so that the nozzle throat diameter has to be adjusted. Due to the modular design of V2G, the inner so called “nozzle core” part, containing reservoir chamber, nozzle throat and the first part of expansion to a diameter of 34 mm, can be easily exchanged, see Fig. 40.



Fig. 40: Nozzle core parts with 2 mm and 10 mm throat diameter

The V2G is designed for nozzle throat diameters between 2 and 10 mm which corresponds to nominal Mach numbers of 24 to 13. Nominal Mach numbers are calculated by the NACA1135 equations [18] using the geometric dimensions. For the data evaluation the actual Mach numbers are determined by the ratio of Pitot pressure to reservoir pressure, such that the effect of a reduced area ratio due to thick boundary layers is accommodated. For the present analysis nozzle throat diameters of 2, 3, 5, 7 and 10 mm are used to obtain a good resolution at one Reynolds number. The characterisation of the test chamber using the V2G contoured nozzle [46], [78] is concomitantly analysed numerically as well at selected conditions. [52], [80] The complete flow characterisation is described in detail in [78] and is here only briefly explained.

4.2 Test Article Selection

For the analysis of blunt and high lift / drag configurations, the aim is to use possible flyable configurations instead of basic geometries as sphere and flat plate. The two different test article configurations COLIBRI (Concept of a Lifting Body for Re-entry Investigations) [92], [97], a blunt, capsule-like shape with a flattened lower surface, and SHEFEX III (Sharp-Edge-Flight-Experiment) [5], a sharp-edged, slender vehicle, are investigated representatively, see Fig. 41 for CAD drawings.

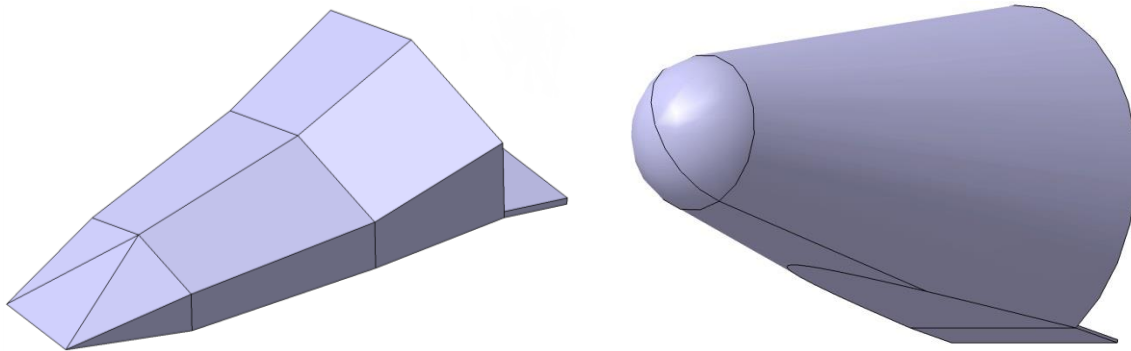


Fig. 41: CAD drawing of SHEFEX III (left) and COLIBRI (right)

COLIBRI was a project of the Institute of Space Systems (IRS) at the University of Stuttgart in the 1990s. In this time the DLR in Göttingen was commissioned to build a wind tunnel model and to perform force measurements in V2G. However, the program was stopped after the test article was operational but before the wind tunnel experiments could be conducted.

SHEFEX III in turn is the third version of a DLR flight configuration concept with the aim to increase the aerodynamic efficiency, i.e. lift / drag ratio, by simultaneously develop cheaper and simpler thermal protections system designs. SHEFEX I, the first flight test configuration in this development line, was launched on the 27th of October 2005 from the Andøya Rocket Range in Norway. SHEFEX II was launched from the same launch site seven years later on 22nd of June, 2012. SHEFEX III was considered as a potential flight test configuration and was designed as a small scale model of the DLR REX Free Flyer Prototype, a proposed flying test bed for zero gravity experiments. However, within the reorientation of DLR's space research activities the SHEFEX III project was stopped in 2014.



Fig. 42: SHEFEX Development Strategy^[17]

Both concepts COLIBRI and SHEFEX III are chosen representatively as blunt and slender, sharp-edged configuration. The COLIBRI is selected because it represents the classical capsule-shaped configuration, and a corresponding V2G test article still existed from earlier projected wind tunnel tests in the 1990s. SHEFEX III in turn represents the group of future re-entry vehicles with high lift / drag ratios and simplified geometric shapes for geometrically less complex thermal protection systems. While the test articles for this work were selected, SHEFEX III was planned as flight configuration.

Due to slightly different test article lengths, the COLIBRI test article is 18% shorter, the analysis at equal flow conditions yields slightly different Reynolds numbers and Knudsen numbers. This has to be taken into account when the test articles are directly compared with each other. Both test articles are equipped with a 7° body flap.

Koppenwallner distinguished the definition of slenderness into a geometric and an aerodynamic shape criterion.^[44] For the geometric slenderness the projected frontal area is compared to the wetted area, i.e. the total surface, while in case of the aerodynamic slenderness the flow behaviour is decisive. Accordingly, there are geometric shapes which result always in a blunt configuration, as e.g. sphere-like configurations like the COLIBRI test configuration. On the other hand there are geometric slender configurations which can be aerodynamically blunt or slender depending on their angle of attack, e.g. configurations close to a flat plate and likely the sharp edged faceted SHEFEX III test configuration. Due to that definition the COLIBRI configuration can be always considered as blunt, while the bluntness of the high lift / drag SHEFEX III configuration is depending on the angle of attack.

For the test articles to be analysed within this work, the area ratios are presented in Fig. 43 for configurations with and without a 7° body flap. Additionally, results for a flat plate and a sphere are shown since they represent the two extreme cases.

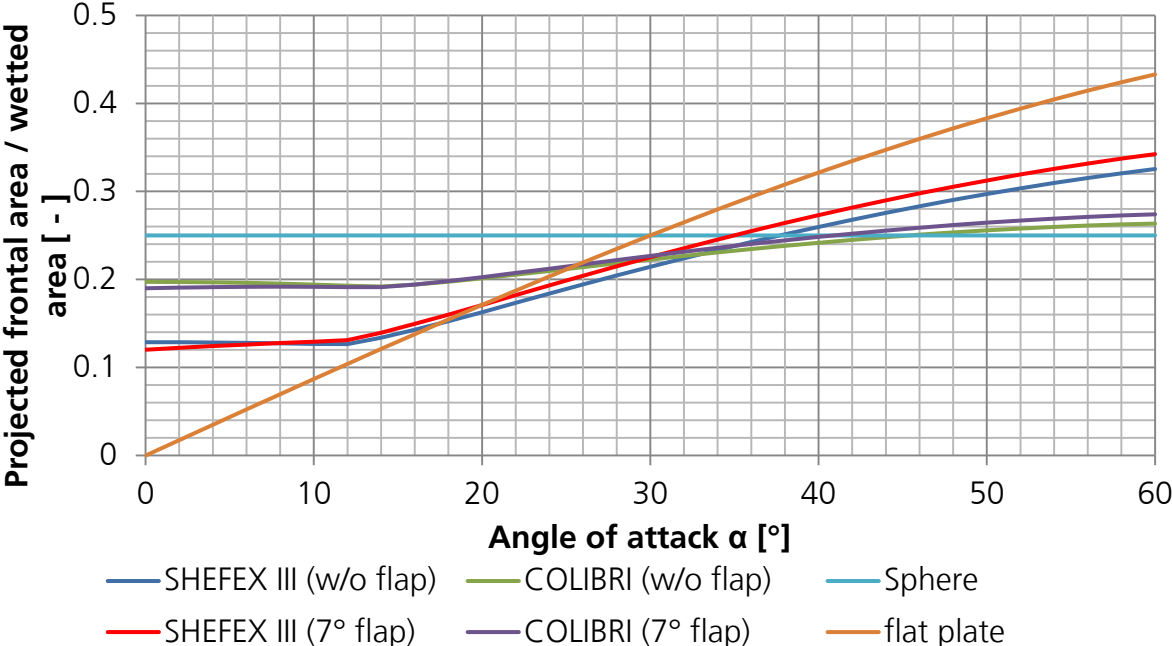


Fig. 43: Ratio of projected area / wetted area of test articles and reference configurations

A sphere has a constant ratio of 0.25 over all angles of attack, while the flat plate ratio changes from 0 at $\alpha = 0^\circ$ to 0.5 at $\alpha = 90^\circ$. In case of both tested configurations, the ratios of projected frontal area to wetted area are for low angles of attack almost constant or even slightly decreasing and start to increase significantly at angles of attack of more than 12° in case of the SHEFEX III configuration, and more than 14° in case of the COLIBRI configuration, respectively. As expected, the SHEFEX III configuration is closer to the flat plate area ratio, while the COLIBRI is closer to the area ratio of a sphere for high angles of attack.

The aerodynamic slenderness is more difficult to determine. An approach is to use the ratio of the velocity components $u_z/u_x \ll 1$ and refer to the corresponding small disturbances of the flow field, see sketch in Fig. 44.^[4] For more complex vehicle configurations, this becomes challenging, especially because it changes with the angle of attack. An accurate determination when the SHEFEX III configuration becomes blunt is, therefore, not easily possible. The idea is to evaluate the results and determine based on their characteristics at which angles of attack the configuration is rather slender or rather blunt. In between there is a transition regime where the configuration is neither aerodynamically slender nor aerodynamically blunt.

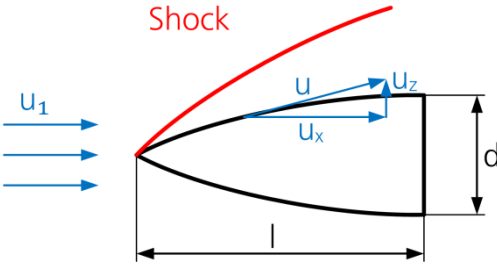


Fig. 44: Sketch for the explanation of slenderness of flight configurations^[4]

The geometric data for both test articles is given in^[79]. The analysis is conducted at angles of attack between $0^\circ \leq \alpha \leq 34^\circ$ with a 2° resolution, see Fig. 45.

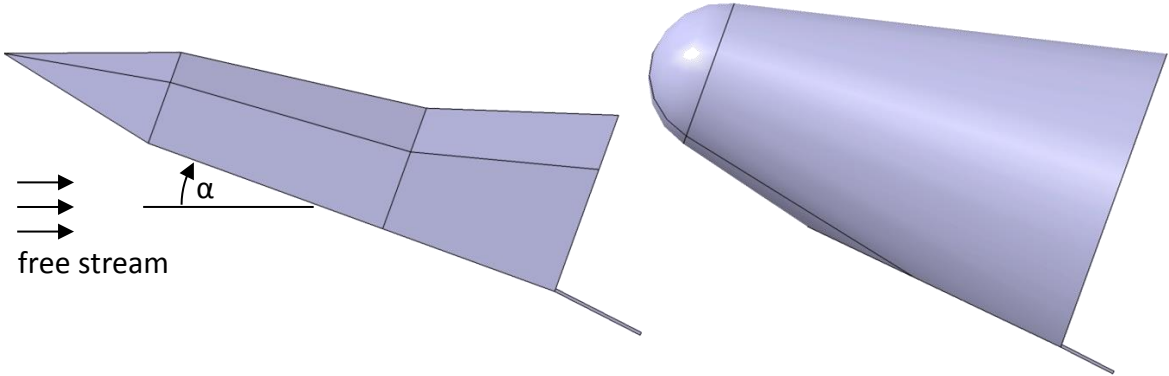


Fig. 45: Side view of CAD drawing of SHEFEX III (left) and COLIBRI (right)

4.3 Determination of Operating Conditions

Since it is desired to cover as much as possible of the rarefied flow regime within this analysis, it is important to take full advantage of the possible V2G operating range. The first step is to determine and approach the operating limits. As Fig. 46 qualitatively

shows, the V2G operating range is defined by multiple hard and soft limitations. Hard limitations are, e.g., the maximum reservoir pressure, maximum mass flow or room temperature. These limits are unchangeable connected with the facility design. In opposite, there are soft limitations which vary with the facility setup and operating conditions, as e.g., the minimum reservoir pressure, boundary layer thickness, the heater limit, or the condensation onset, so that they have to be analysed separately for each nozzle throat insert. The heater limit, i.e., the maximum reservoir temperature for a certain reservoir pressure and nozzle throat diameter, is more a question of economic feasibility since the abrasion of the heater is strongly increasing above a certain reservoir temperature, so that the life span of a heater can decrease from more than a year of measurements to few minutes or even less. Due to the variety of parameters, there are no tables for recommendations. With the experience of experimenter and wind tunnel operator, it is in the end an approach of carefully trying. For the present analysis the criteria is that the heater should at least last for several hours to allow time-consuming flow characterisations.

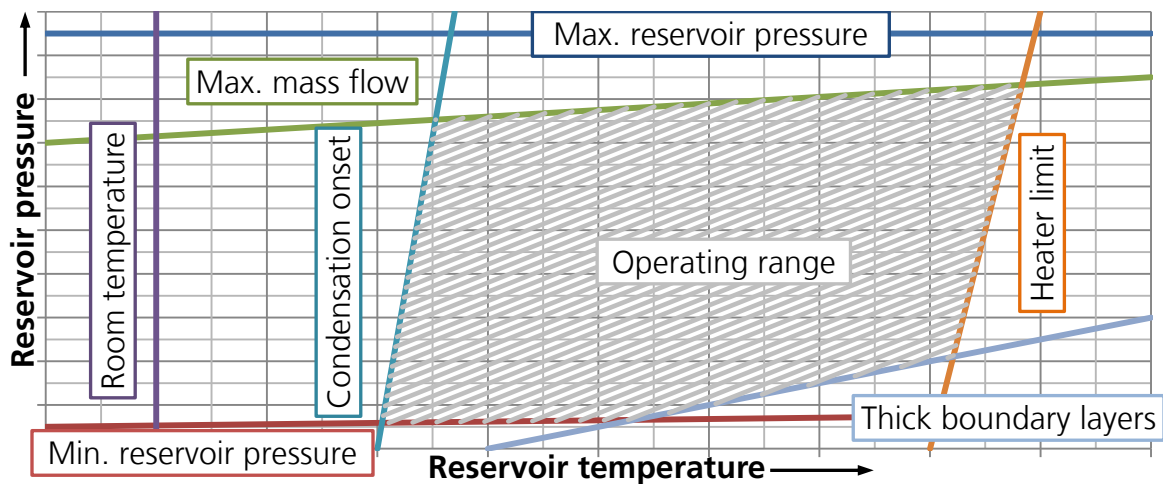


Fig. 46: Qualitative V2G operating ranges

Whether a V2G operating condition within the hard limitations is suitable for the investigation of a hypersonic flight configuration or not, has to be experimentally investigated for each operating condition separately. At V2G there are currently two experimental methods established which indicate the condensation onset. One method uses the permanently installed Pitot tube, while the other method uses the heat transfer measurement on a copper sphere. In both cases initially a reservoir pressure is set. Subsequently the reservoir temperature is gradually increased from ambient temperature, while the Pitot pressure or heat transfer respectively is measured. For the present analysis a step size of 20 K is selected which corresponds roughly to the V2G reservoir temperature adjustment accuracy. As described in^[78] the expected accuracy of the condensation onset prediction via the heat transfer measurement is less than with the Pitot probe, so that they are used for few reference measurements only. Both methods have the disadvantage that they are able to prove the existence of condensation, but they are unable to confirm that there is no condensation in the flow field, which is more important. The reason is that between compression shock and surface the decelerated hot flow has some time to re-evaporate. To make sure there is only negligible condensation in the identified operating range, a temperature safety margin is implemented. When the condensation onset is sharply determinable by a

steep pressure increase, the chosen safety margin is 20 K, i.e., one reservoir temperature step size away from the Pitot pressure change. In cases of a blurred pressure increase the chosen margin is larger, to accommodate the inaccurate determination of the condensation onset.

By using the method with the Pitot tube one takes advantage of the fact that the Pitot pressure suddenly in- or decreases when condensation becomes significant at high Mach numbers.^[55] Although the same applies to the even more sensitive static pressure^[21], it is far more complex to investigate the condensation onset with a static pressure probe due to very long settling times in the rarefied flow and due to the adjustment sensitivity of the static pressure probe.

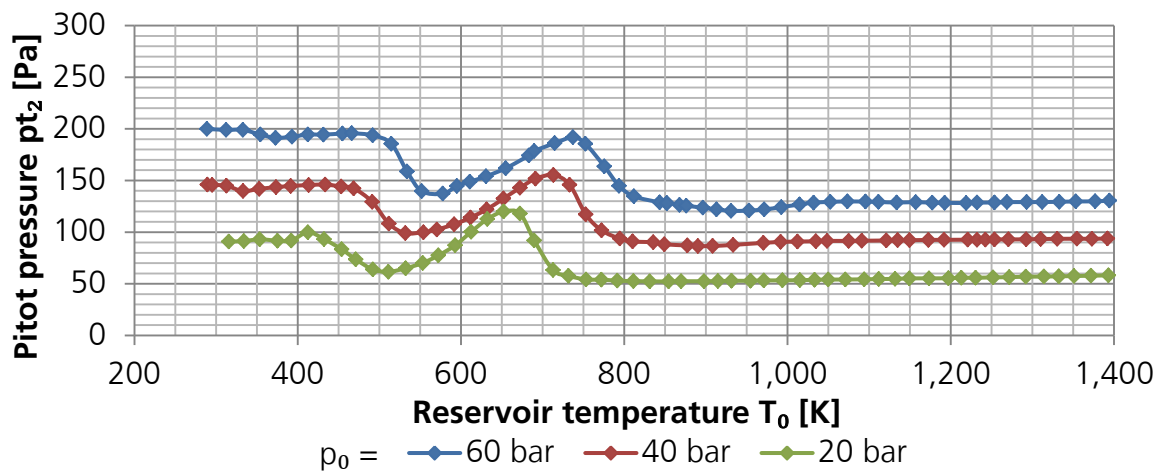


Fig. 47: Pitot pressure condensation measurements, $d^* = 2$ mm, Pitot tube at $x = 448$ mm, $y = 0$ mm

Fig. 47 shows the condensation caused change in the Pitot pressure distribution for selected reservoir pressures between 20 and 60 bar which covers almost the total investigated range. Starting with 40 bar condition (red), with the Pitot tube positioned at 448 mm downstream the nozzle exit on the tunnel axis, the Pitot pressure is independent of the reservoir temperature for reservoir temperatures above 950 K. Below that temperature the Pitot pressure slightly decreases and increases, before at about 800 K a sudden and strong increase in Pitot pressure follows. After that increase the Pitot pressure reaches a local maximum before it decreases similarly strong, to nearly reach the original pressure level and increases finally again to reach and remain at a roughly 50% higher pressure level. Hefer^[24] explained that the initial sudden pressure increase is caused by the released heat of condensation. He assumed that the Pitot pressure oscillation during a further reservoir temperature decrease is related to flow inhomogeneities caused by condensation. Additionally, Reynolds number effects within the changing gas-droplet-mixture, as well as vaporisation effects, could further be responsible for the observed oscillation. Since the condensation always starts at the lowest expansion velocities, the condensation onset is expected to start far downstream of the test chamber and to move upstream with decreasing reservoir temperature. Therefore, the analysis is performed in the downstream end of the test section at $x = 448$ mm. Comparing different operating conditions it can be observed that the condensation onset moves to higher reservoir temperatures when the reservoir pressure is increased. A higher reservoir pressure yields a thinner boundary layer and a larger effective area ratio of nozzle throat to test chamber and, therefore, a corresponding

stronger expansion. The result is that the expansion reaches further beyond the nitrogen saturation line and the risk of condensation rises. Operating conditions with higher reservoir pressures require thus higher reservoir temperatures to avoid condensation.

It is unlikely that condensation occurs during force measurements, unless condensation is detected during the flow characterisation when no test article is installed. Due to the bow shock in front of the test article, the flow in the vicinity of the test article is compressed compared to the pure free stream and a lower risk for condensation exists.

4.4 Radial and Axial Pitot Pressure

After the condensation free operating range is determined (see grey area in Fig. 9), the core flow can be characterised. The aim is to analyse the flow field and check if the core flow is sufficiently large to cover the available test article size and to determine radial and axial flow gradients. In opposite to free flight, there are almost always flow gradients in wind tunnel experiments as described in chapter 3.1. For an interpretation of force measurements, these flow gradients have to be quantified. Further, it is investigated if there are any compression shocks occurring in the flow field.

For that purpose the flow properties in the test section are investigated. Pitot pressure profiles are measured in streamwise direction between $0 \leq x \leq 448 \text{ mm}$ and in radial direction between $-160 \leq y \leq 160 \text{ mm}$ with the single Pitot tube described in chapter 3.2. The origin of the coordinate system is at the intersection between nozzle exit plane and nozzle symmetry axis, see Fig. 19. The radial profiles are resolved in 5 mm steps and are recorded every 50 mm in flow direction from 0 mm to 448 mm . Additionally, one axial Pitot pressure profile is measured in the range of $0 \leq x \leq 448 \text{ mm}$ with a 5 mm resolution on the wind tunnel axis at $y = 0 \text{ mm}$. For both radial and axial directions a staggered measurement procedure is used here, i.e., if for example a 5 mm spaced radial profile is considered between $\pm 160 \text{ mm}$, on the forward sweep the values from -160 to $+160 \text{ mm}$ are determined in steps of 10 mm , while on the backward sweep the remaining values are recorded. At each Pitot probe position $5,000$ values are measured within one second and averaged to reduce measurement noise.

In the following the results of the flow field characterisation are explained exemplarily for one selected operating condition. The full set of plots and data tables for all investigated operating conditions is presented in^[78]. Fig. 48 shows the results of the radial Pitot pressure profiles at different positions downstream the test chamber for the 2 mm nozzle throat diameter insert with $p_0 = 40 \text{ bar}$ and $T_0 = 980 \text{ K}$.

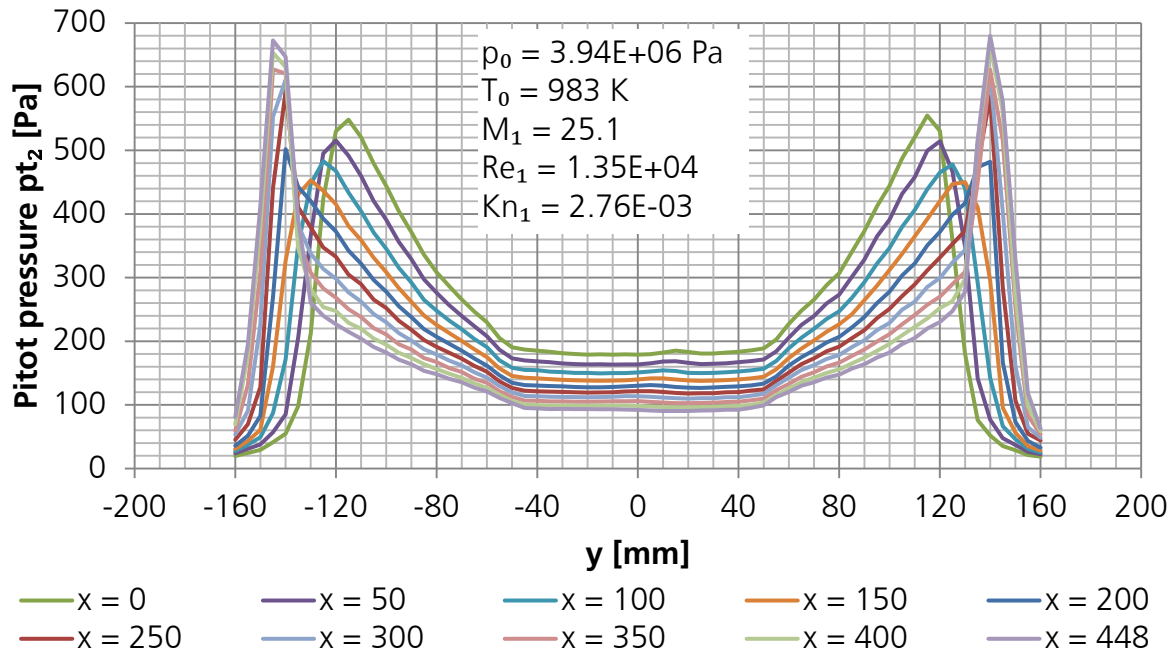


Fig. 48: Pitot pressure radial profile for cond. no. 3, see Table 3 or in detail^[79] (M_1 , Re_1 , Kn_1 based on data at $x = 150 \text{ mm}$, $y = 0 \text{ mm}$, ref. length = 100 mm)

In Fig. 48 primarily noticeable is that all radial profiles have a distinct plateau in the centre where the Pitot pressure is almost independent of the radial position. Outside this plateau the Pitot pressure is increasing when moving further away from the centreline. The position of the increase is strongly depending on the operating condition and is hardly changing in stream direction.

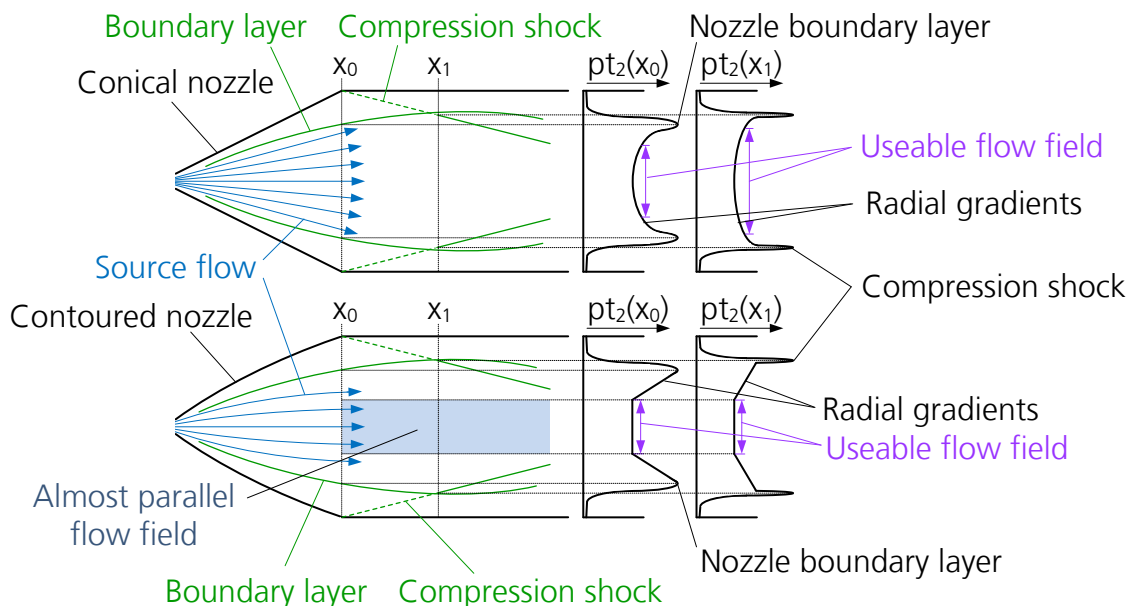


Fig. 49: Sketch of V2G flow field and radial Pitot pressure profiles for both conical (top) and contoured nozzle (bottom)

The increase is caused by two different effects, see Fig. 49. The radial profiles close to the nozzle exit are limited by the expansion of the nozzle wall boundary layer. This can be tracked downstream in Fig. 48 by following the broad small amplitude peak at either

side of the profiles, which is moving outwards. Parallel to the outwards moving peaks, the pressure plateau in the centre is decreasing with growing distance to the nozzle exit, showing the further downstream expansion of the flow. Further downstream the core flow is limited by the shock angle of the inward targeting oblique compression shocks, generated when the expanding flow impinges on the cylindrical wind tunnel wall, see Fig. 49. These oblique compression shocks can be identified by narrow peaks with high amplitude. The differences are highlighted in Fig. 50 where the foremost and the furthest downstream measured radial profiles are shown. The Pitot pressure peaks generated by the oblique compression shocks on the left and right side differ for some operating conditions in amplitude and position. The main reason is an insufficient spatial resolution of the Pitot pressure measurements (radial spacing of 5 mm). However, for the determination of the core flow properties the determination of the positions of the oblique compression shocks are sufficient.

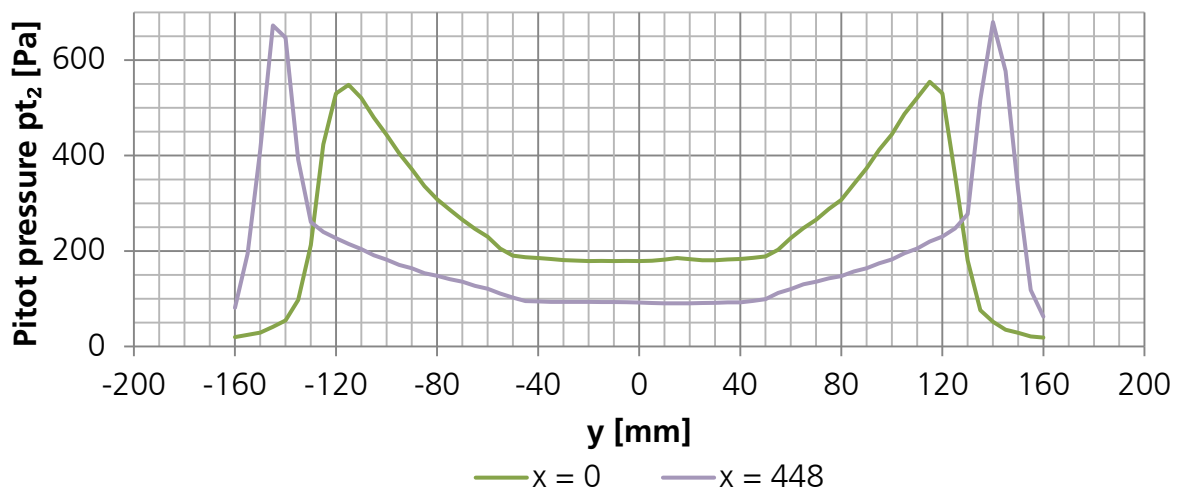


Fig. 50: Selected Pitot pressure radial profiles of Fig. 48 (contoured nozzle cond. no. 3, see Table 3 or in detail ^[79])

The shape of the Pitot pressure profiles between the peaks, caused by nozzle boundary layer or oblique compression shocks, depends on the nozzle contour as Fig. 49 visualises. In case of a conical nozzle, the radial flow gradients cause a smooth Pitot pressure increase which begins on the wind tunnel axis. The experimenter has to decide which radial gradient is tolerable for the research question and defines the useable flow for the operating conditions. In opposite to the smooth Pitot pressure increase in case of the conical nozzle, the contoured nozzle is designed to generate an almost parallel flow field within the centre region. The useable flow field is usually limited to the region with the almost parallel flow field since the radial gradients outside the plateau occur abruptly and are stronger compared to those of a conical nozzle at this position. The reason is that the position and magnitude of the Pitot pressure maximum, due to nozzle boundary layer or oblique compression shocks, are almost the same for the available conical and contoured nozzles since they are primarily depending on reservoir conditions, wall temperature, nozzle area ratio, and length of the nozzle. Only in few exceptions where the radial gradients outside the parallel flow field are also acceptably small, it is possible to use bigger test articles which exceed the parallel flow region. Within the present experiments the contoured nozzle is used only.

The already mentioned Pitot pressure decrease in stream direction is visualised in Fig. 51. The blue line is based on a separately measured axial profile, while the coloured dots are taken from the radial profiles. It can be seen that the axial gradient is stronger close to the nozzle exit and decreases in stream direction. In the region of the test article, which is located between $x = 110 \text{ mm}$ and $x = 220 \text{ mm}$, the axial gradient is for this operating condition -0.2 Pa/mm . This corresponds to a Pitot pressure decrease of 14.6 % over the test article length referred to the test article nose position at about $x = 110 \text{ mm}$. The axial Pitot pressure gradient is not negligible and is discussed in the evaluation of the results in chapter 5.3. The dynamic pressure of all used operating conditions is listed in [79].

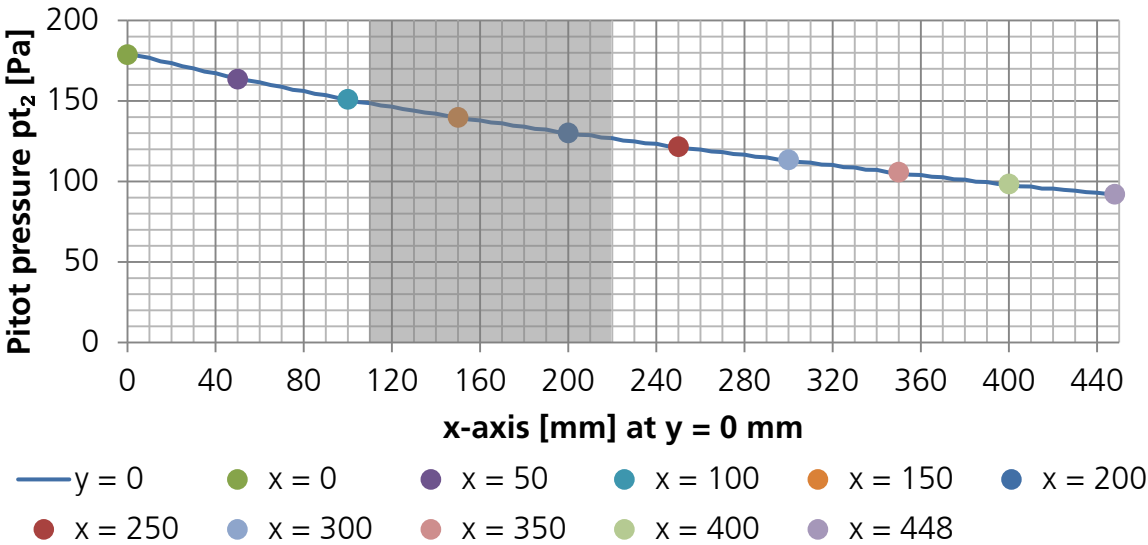


Fig. 51: Pitot pressure axial profile for cond. no. 3 with test article location (grey), see Table 3 or in detail [79]

For some operating conditions an inhomogeneity can be identified within the centre of the core flow region, i.e., the Pitot pressure is locally increasing or decreasing on the tunnel axis. Responsible for this are discontinuities in the second derivative of the nozzle contour and tiny junctions between the nozzle parts. [78] Both lead to inward moving expansion and compression waves inside the core flow region where they interfere on the wind tunnel axis and cause the Pitot pressure inhomogeneities.

Due to the earlier explained forward / backward Pitot tube sweeps and slightly fluctuating operating conditions, a little zigzag pattern might become noticeable in some Pitot pressure profiles, when they are plotted in their geometric order and not in the order they are recorded. Since the reason is known and their magnitude small, they are neglected.

Based on the measured Pitot pressure and reservoir conditions, the remaining flow properties can be determined using NACA1135 [18]. The viscosity, which is required for the determination of the Reynolds number, is here determined using the Lennard-Jones potential [26] in a simplified and extrapolated version for V2G applications [10]. Based on Mach number and Reynolds number, the Knudsen number is determined using (2-1). The similarity parameters are evaluated based on the flow field data at $x = 150 \text{ mm}$, $y = 0 \text{ mm}$, the average test article location, and on the typical test article length of

10 cm. Later the individual test article length of the blunt and slender flight configuration is used for the final evaluation.

After the determination of the radial and axial Pitot pressure profiles the test matrix can be set up for the selected test article size. Fig. 52 shows the operating conditions and indicates the different nozzle throat diameters with different colours.

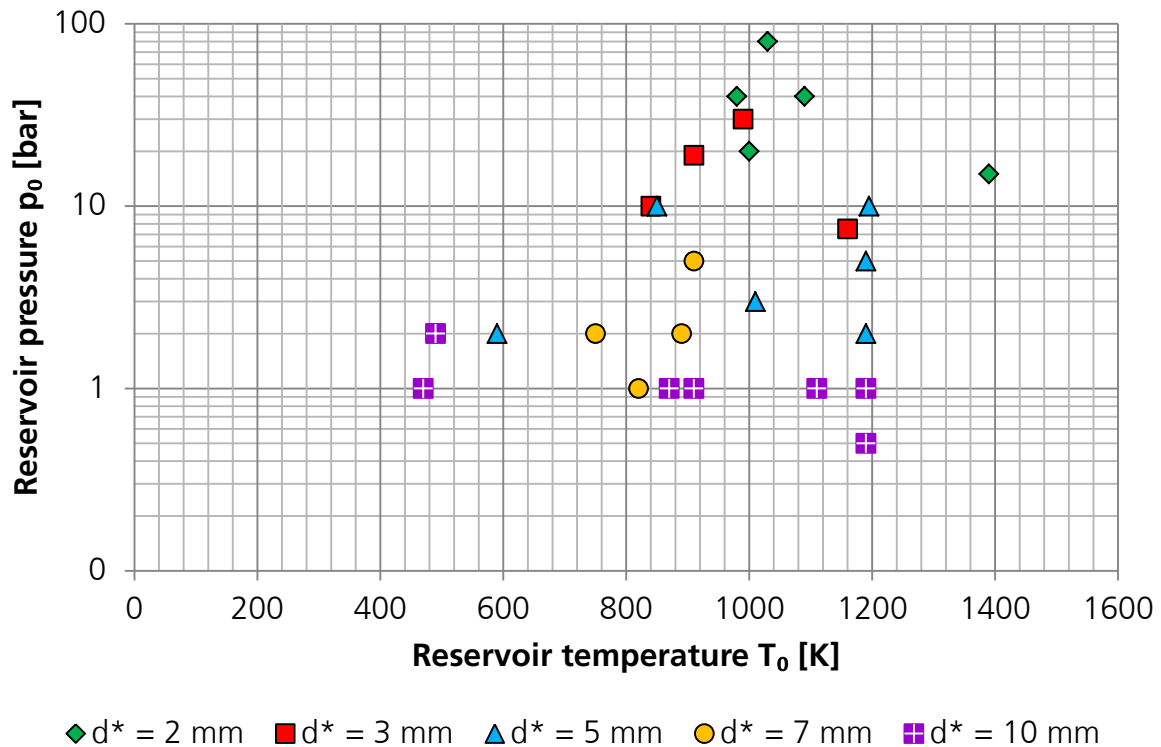


Fig. 52: V2G operating conditions

4.5 Test Matrix Definition

In a prior study within the EU funded “Future High-Altitude High-Speed Transport 20XX” project (FAST20XX), a 3-component force measurement technique for the V2G was re-established by the author of this study^[77]. It was used to investigate the effect of rarefaction on the aerodynamic coefficients lift, drag and pitching moment of a selected lifting configuration (HERMES), shown in Fig. 53, at six different flow conditions, see Table 2^[74]. The aim was to investigate the effect of rarefaction on the aerodynamic coefficients of a lifting configuration at a high and a low altitude, hence, at a low and a high Reynolds number and three different nominal Mach numbers with a conical wind tunnel nozzle. The used operating conditions are related to the rarefaction parameters introduced by Schaaf & Chambré^[73], see Fig. 53, to allow a classification of the experimentally investigated flow regime. The rarefaction parameter, distinguishing the free molecular flow, is determined from the ratio of Mach number and Reynolds number, while the other rarefaction parameters determined from the ratio of Mach number and square root of Reynolds number.

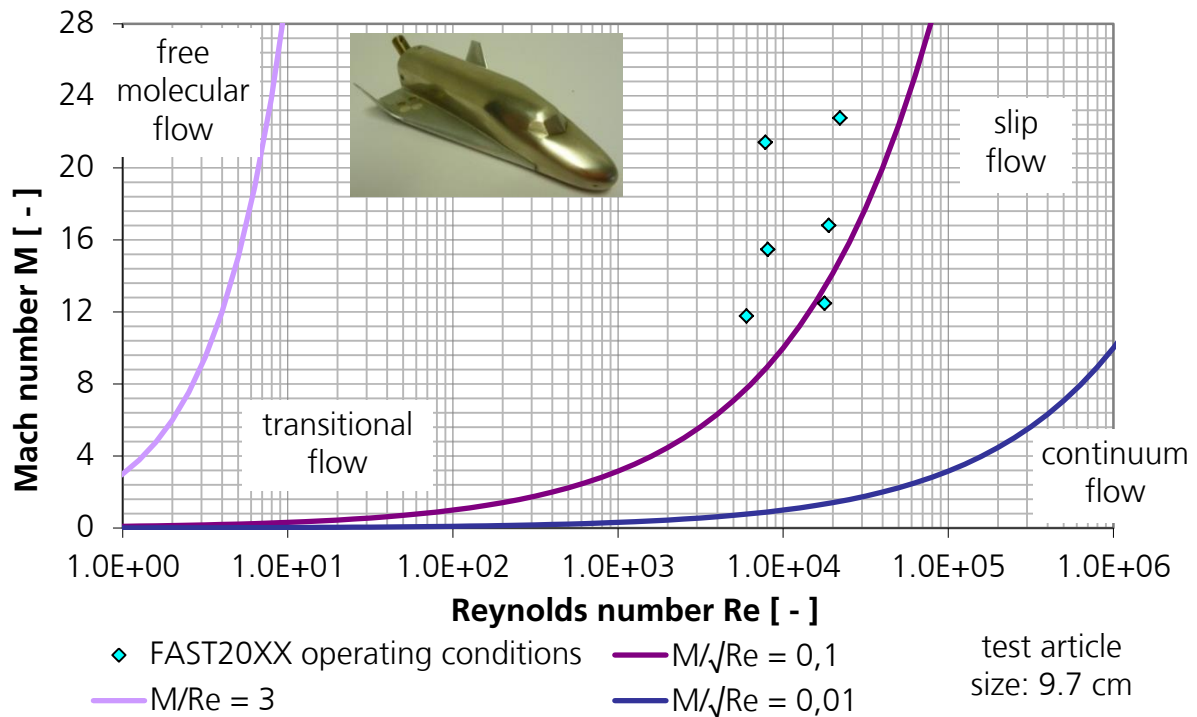


Fig. 53: FAST20XX operating conditions vs. rarefaction parameters introduced by Schaaf & Chambré^[73] shown with lifting body test article HERMES

Table 2: FAST20XX test matrix with nominal V2G operating conditions (similarity parameters calculated by isentropic expansion for perfect gas^[18])

Cond. no.	Re_1 (9.7 cm) [-]	M_1 [-]	Kn_1 (9.7 cm) [-]	Altitude* [km]
1	6.0E+03	11.8	2.9E-03	93
2	1.8E+04	12.5	1.0E-03	88
3	8.1E+03	15.5	2.9E-03	93
4	1.9E+04	16.8	1.3E-03	89
5	7.8E+03	21.4	4.1E-03	95
6	2.2E+04	22.8	1.5E-03	90

* related by Knudsen number (ratio of mean free path to test article / vehicle length) and scaling of test article length to re-entry vehicle length

As lifting configuration served an already existing test article of the European HERMES project, investigated in the late 1980s and early 1990s^[83], see test article in Fig. 53. Most of the original data was preserved so that the re-established force measurement technique could be compared to the results of the former force measurements.^{[75], [90]} It turned out that the re-established force measurement technique was able to achieve more accurate results than the results performed in the early 1990s. Within the project the results were used by CIRA to compare CFD and DSMC predictions and to create bridging functions.^{[76], [90], [91]}

During FAST20XX it turned out that there are some distinct effects of rarefaction visible in the characteristics of the aerodynamic coefficients in the analysed flow regime. The lift coefficient is decreasing with increasing Knudsen number.^[66] In case of the drag coefficient the effect of rarefaction becomes even more significant. The drag coefficient characteristics of all investigated conditions are shifted to higher values with increased

Knudsen number. Since the drag coefficient approaches its maximum in free molecular flow^[11], this trend is plausible. Due to the changing lift and drag coefficient, the aerodynamic efficiency is affected as well, resulting in decreased lift / drag ratios with increasing Knudsen number, as qualitatively described by Koppenwallner^[43]. It is observed that the pitching moment becomes more positive with increasing rarefaction.

The key result of the low-density experiments in FAST20XX^[75] is that the rarefaction effects on the aerodynamic coefficients are strong and clearly measurable in the investigated, comparably narrow and near continuum, flow regime between Knudsen numbers of $1.0 \cdot 10^{-3}$ to $4.1 \cdot 10^{-3}$. Considering that the rarefied flow regime in total covers from 10^{-3} to 1 about three orders of magnitude of Knudsen numbers, a Knudsen number increase, from e.g. $1.0 \cdot 10^{-3}$ to $4.1 \cdot 10^{-3}$, reduced the lift coefficient already by 6% and increased the drag coefficient by 10% for an angle of attack of 26° . The corresponding aerodynamic efficiency thus experiences a reduction of 15%, while the pitching moment coefficient is modified such that the trim point is shifted to higher angles of attack, from $\alpha = 8^\circ$ at $Kn = 1.0 \cdot 10^{-3}$ to 16° at $Kn = 2.9 \cdot 10^{-3}$.

Due to the Reynolds number variation within the FAST20XX experiments, there is an ambiguity whether the determined effects are caused by a change in Reynolds and Knudsen number or solely by a change in Knudsen number. Because of this further experiments are conducted, during which the Reynolds number is kept constant within the adjusting precision of V2G, by solely varying the Mach number for the adjustment of different Knudsen numbers, to ensure that only one setting parameter is varied, i.e. $Re = const., Kn = f(M)$. Within the present investigation the force measurements are conducted at constant Reynolds numbers, by solely varying the Mach number to obtain different Knudsen numbers, see test conditions on dotted lines and V2G operating range in Fig. 54.

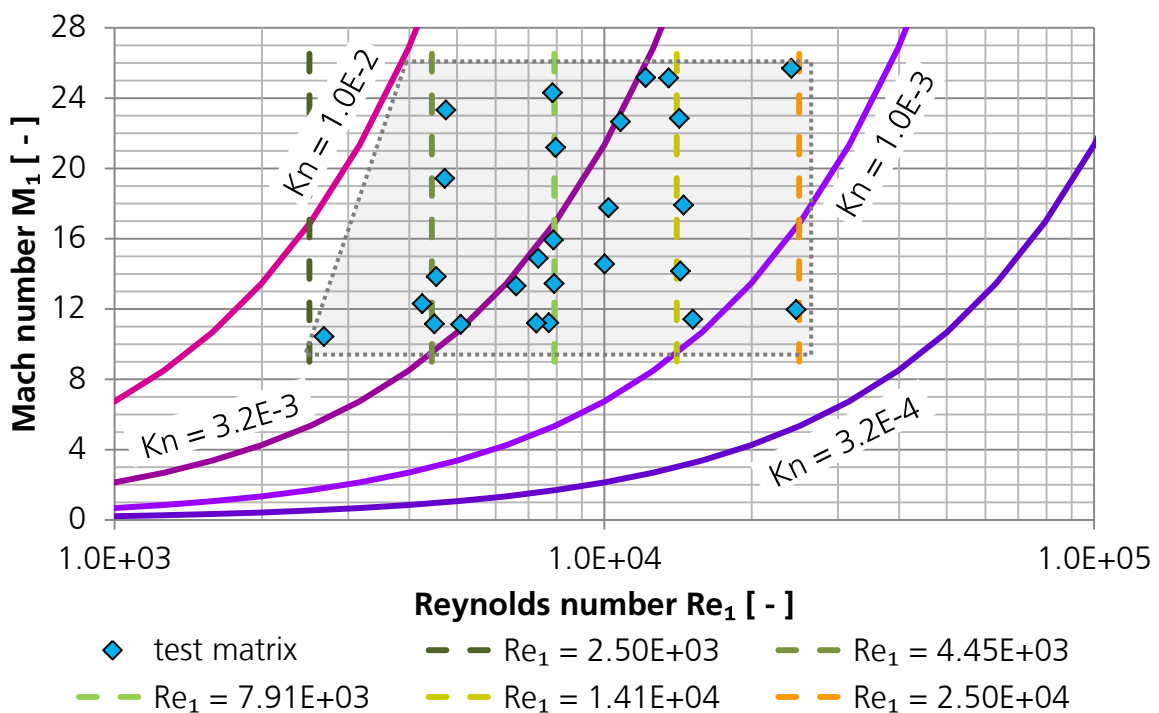


Fig. 54: Test matrix of constant Reynolds number analysis with V2G operating range (shaded grey)

Since the adjustable Mach numbers at V2G ranges from about $M = 10$ to $M = 25$, the possible Knudsen number variation at a constant Reynolds number is slightly more than a factor of two. This is little compared to the ranges of the rarefied flow regime, which covers more than three orders of magnitude. For that reason the constant Reynolds number analysis is repeated at several constant Reynolds numbers, covering the whole regime which can be simulated using a typical 10 cm test article in V2G. Instead of the six investigated operating conditions during FAST20XX, the present investigation is performed at 26 operating conditions for a more detailed analysis. All investigated operating conditions are listed briefly in Table 3 and in detail in [79]. Additionally, few other force measurements are performed, while keeping the Knudsen number constant at $3.2 * 10^{-3}$ and varying the Mach and Reynolds number, i.e. $Kn = const., M = f(Re)$.

Table 3: Operating conditions used for constant Reynolds number analysis

Cond. no.	Re_1^* [-]	M_1 [-]	Kn_1^* [-]	Cond. no.	Re_1^* [-]	M_1 [-]	Kn_1^* [-]
1	4.75E+03	23.33	7.28E-03	14	1.45E+04	17.92	1.83E-03
2	7.84E+03	24.31	4.60E-03	15	1.02E+04	17.77	2.59E-03
3	1.35E+04	25.15	2.76E-03	16	4.25E+03	12.30	4.29E-03
4	1.21E+04	25.18	3.08E-03	17	7.90E+03	13.45	2.53E-03
5	2.41E+04	25.69	1.58E-03	18	6.61E+03	13.32	2.99E-03
6	4.72E+03	19.44	6.10E-03	19	1.43E+04	14.16	1.47E-03
7	7.96E+03	21.20	3.95E-03	20	2.68E+03	10.44	5.79E-03
8	1.08E+04	22.66	3.11E-03	21	1.52E+04	11.42	1.12E-03
9	1.42E+04	22.85	2.38E-03	22	7.71E+03	11.22	2.16E-03
10	1.00E+04	14.57	2.16E-03	23	7.26E+03	11.21	2.29E-03
11	4.54E+03	13.84	4.53E-03	24	5.09E+03	11.13	3.24E-03
12	7.33E+03	14.89	3.01E-03	25	4.50E+03	11.16	3.68E-03
13	7.87E+03	15.93	3.00E-03	26	2.46E+04	11.97	7.21E-04

* reference length 10 cm

4.6 Model Support

For the force measurements the V2G is equipped with a water-cooled model support, able to change the angle of attack and yaw angle and to adjust the position of the test article, see Fig. 21. The movements are controlled by SCMV^[50], a LabView program developed in the DLR Spacecraft Department in Göttingen, which is also responsible for the control of the data acquisition system. The water-cooled housing of the balance replaces the white dummy shown in Fig. 55 left. The model support is designed such that angle of attack changes can be realized, while the test article position is kept at a constant position, by simultaneously compensating movements in x and z-direction (Fig. 55 right). The centre of rotation can be changed by adjusting the geometric parameters in the control software. Currently, there are two support frames available, one for low angles of attack (see Fig. 56) and one to realise high angles of attack of up to 60° by pre-setting the angle of attack. The model support is later mounted horizontally to the side of the wind tunnel, so that the movement for a variation of the angle of attack is solely in the horizontal plane. This has to be done to avoid changing dead loads on the balance transducers due to shifting of the gravity force vector relatively to the balance fixed coordinate system.

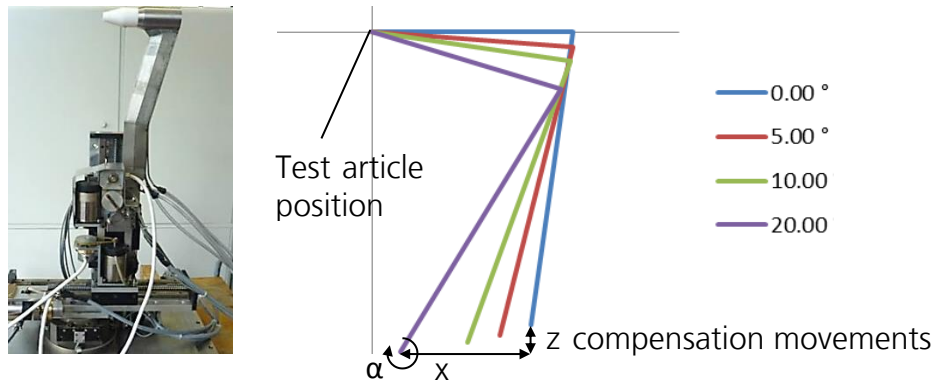


Fig. 55: Model support (left), angle of attack adjustment (right)

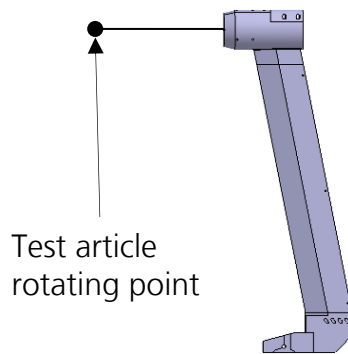


Fig. 56: Support frames allowing pre-setting of the angle of attack

4.7 Balance Improvements

In preparation of the present experiments, the force balance and the measurement process are optimised, compared to former measurements within FAST20XX between 2009 and 2012. The optimisation focus is on a reduction of the balance zero point drift which is found to be the dominating negative effect. As explained in 3.4.5 the zero point drift is a function of temperature and time. Hence, the zero point drift can be reduced by keeping the temperature as much as possible constant, and by reducing the test time to a minimum. To obtain best results several measures are taken to reduce both temperature change and test time. The approaches are presented in the following.

The thermal effects are theoretically compensated within a bridge circuit, however, it turned out that the slight differences in thermal characteristics, even within strain gauges from a single product batch, are sufficient to strongly influence the measured signal. The temperature changes due to evacuation, hence, decreasing convective heat transfer, due to operation of vacuum pumps, and of course due to the hot wind tunnel flow.

It is found that a major effect is caused by the cooling water supplying the balance housing and keeping the balance at low temperatures during the wind tunnel operation. Originally, simply tub water was used. However, its temperature is changing, amongst others, with local weather conditions and season. Additionally, the tub water has usually a temperature below 15°C, while the equilibrium temperature of the balance in a vacuum environment is, due to its electrically supplied strain gauges, at about 28°C.

Cooling the balance housing with low tub water temperatures causes strong and unpredictable thermal gradients in the whole balance, which results in poor zero point stability. For the present approach the tub water is preheated to about 29°C by a heat exchanger, while the temperatures are monitored at the inflow and outflow of the vacuum region.

A further step aiming at a lower temperature change is taken in the new test article design. Few of the former test articles were already designed to reduce the heat transfer from the hot nose to the balance by a structure where the heat is mainly transferred via the test article backplane and then back to the front. Additionally, using this design the test article shields the small gap between balance housing and test article and impedes the balance from a direct impact of free stream flow through that gap.

Different is that the newly designed sharp-edged slender test article is equipped with an additional internal heat shield which protects the balance tip from a direct impact of radiation from the hot leading edge, see Fig. 37. In case of the sharp-edged slender configuration, this is of particular importance since the expected heat loads at the leading edge are much larger than the heat loads occurring at the nose of the blunt configuration due to its smaller nose radius, see (1-1). Due to the larger bluntness and the lower absolute heat flux, the existing blunt configuration is not upgraded with a similar internal heat shield in front of the balance tip. Nevertheless, the redesigned internal structure of the COLIBRI configuration included a heat shield. The differences between the tests performed with the new and the original internal structure showed no differences based on the error margin of the experiments.

To reduce time influence of the zero point drift, the force measurement process is optimised to decrease the time between the zero load measurement in the beginning of a test cycle, described in chapter 5.1, and the end of the measured force measurement profile. As already conducted in former experiments, the test articles are shielded during the wind tunnel start-up and shut-down phase, to reduce the exposure time of the test article and, hence, to decrease the aerodynamic heating.

Apart from the balance zero point drift, electric and electromagnetic noise plays an important role. Since the unamplified balance signals are very low, down to 10^{-7} V, the force measurement technique is very susceptible to all kinds of electric or electromagnetic perturbations, while at the same time during wind tunnel operation, large vacuum pumps and wind tunnel heater generate excessive electric and electromagnetic noise. Therefore, all openings of the balance housing and connectors are thoroughly closed with several layers of aluminium tape. Challenging is additionally, that it is with justifiable effort hardly possible to implement pre-amplifiers directly on the balance with the aim to transmit already amplified signals. The space within the water-cooled balance housing is limited, and the pre-amplifiers would have to withstand the environmental conditions, as e.g. vacuum and, hence, almost no cooling effect by convection is present. As explained, the amplification is conducted with carrier frequency amplifiers described in 3.4.5. Due to the very low signals, it is essential that the balance calibration is performed with the complete measurement chain.

The result of the taken measures is exemplarily shown in Fig. 57 for the BYB balance component. Although the test article, nozzle type, and operating condition are

different, the improvement due to the taken measures is clearly identifiable. As in case of the Pitot probe measurements, see chapter 4.4, the force measurements are conducted with forward / backward sweeps as well, to unveil possible hysteresis effects. Especially in the case of the FAST20XX measurements, it can be seen that the connecting lines deviate slightly between the forward and the backward sweep. This deviation is caused by thermal zero point drift. In case of the measurements of the present analysis, the results of the forward and backward sweep are that close together that the connecting line appears almost as one thicker line. The difference is more clearly when the connecting line is compared to the regime between $\alpha = 0^\circ$ and $\alpha = 2^\circ$, where only one line is shown.

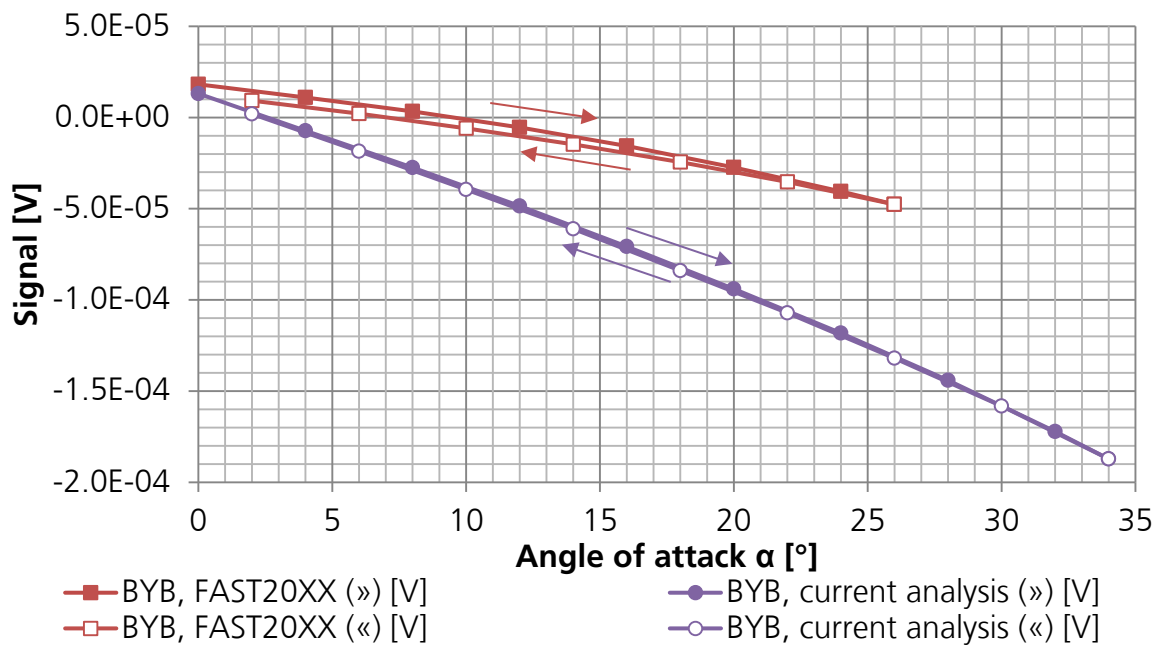


Fig. 57: Improvement in reducing zero point drift for BYB, comparison of (») forward and («) backward sweep (FAST20XX cond. no. 5, $d^* = 2$ mm, $p_o = 10$ bar, $T_o = 778$ K, HERMES and present analysis cond. no. 4, $d^* = 2$ mm, $p_o = 40$ bar, $T_o = 1090$ K, SHEFEX III)

After successfully implementing the measures, the remaining zero point drift magnitude is small compared to the measured signal, such that compensation would not be necessary but nevertheless it is performed routinely. The small drift magnitude allows a compensation assuming a linear zero point drift over the measured values. For that purpose the signals at $\alpha = 2^\circ$ are calculated with the Newtonian 2nd degree interpolation equation using the values at $\alpha = 0^\circ$, 4° and 8° from the forward sweep measurements, see (4-1).^[62] Since the zero point drift is very sensitive to temperature gradients between the strain gauges of one bridge circuit, it is not possible to measure accurately the temperature gradient without affecting the balance sensitivity. During the balance design four temperature sensors are installed, one in close vicinity to each strain gauge pair. Although the temperatures at the different positions of the balance can be monitored, it is impossible to analyse temperature gradients within a strain gauge pair. Therefore, the zero point drift has to be estimated. Assuming a linear thermal zero point drift over the short time period of 3 min and assuming that the movements between the angles of attack taking similarly long, the drift can be linearly compensated, by using (4-2) at each angle of attack. The equation is designed that the initial measured value at

$\alpha = 0^\circ$ remains unchanged, while for all others a fraction from the determined deviation between the calculated and measured value at $\alpha = 2^\circ$ is subtracted depending on the order they are recorded. The final value at $\alpha = 2^\circ$ is compensated to reach the interpolated value.

$$f_{\alpha=2^\circ} = f_{\alpha=0^\circ} + \frac{f_{\alpha=4^\circ} - f_{\alpha=0^\circ}}{\alpha_{4^\circ} - \alpha_{0^\circ}} (\alpha_{2^\circ} - \alpha_{0^\circ}) + \left(\frac{f_{\alpha=8^\circ} - f_{\alpha=4^\circ}}{\alpha_{8^\circ} - \alpha_{4^\circ}} - \frac{f_{\alpha=4^\circ} - f_{\alpha=0^\circ}}{\alpha_{4^\circ} - \alpha_{0^\circ}} \right) \frac{(\alpha_{2^\circ} - \alpha_{0^\circ})(\alpha_{2^\circ} - \alpha_{4^\circ})}{\alpha_{8^\circ} - \alpha_{0^\circ}} \quad (4-1)$$

$$f_{\alpha_{compensated}} = f_{\alpha_{measured}} - (f_{\alpha=2^\circ_{interpolated}} - f_{\alpha=2^\circ_{measured}}) * \left(\frac{N_{number\ of\ measured\ AoA} - 1}{N_{total\ number\ of\ measured\ AoA} - 1} \right) \quad (4-2)$$

Compared to the measurements performed in FAST20XX^[75], the zero point stability is now in average more than one order of magnitude better, especially for the signals BYF and BYB on the balance normal force transducer where the effect of the improved test article design becomes strongly noticeable. The results obtained in FAST20XX in turn were, however, already much better than the experiments conducted with the former force measurement technique in the late 1980s^[83], where the pitching moment results are hardly interpretable (Fig. 58).

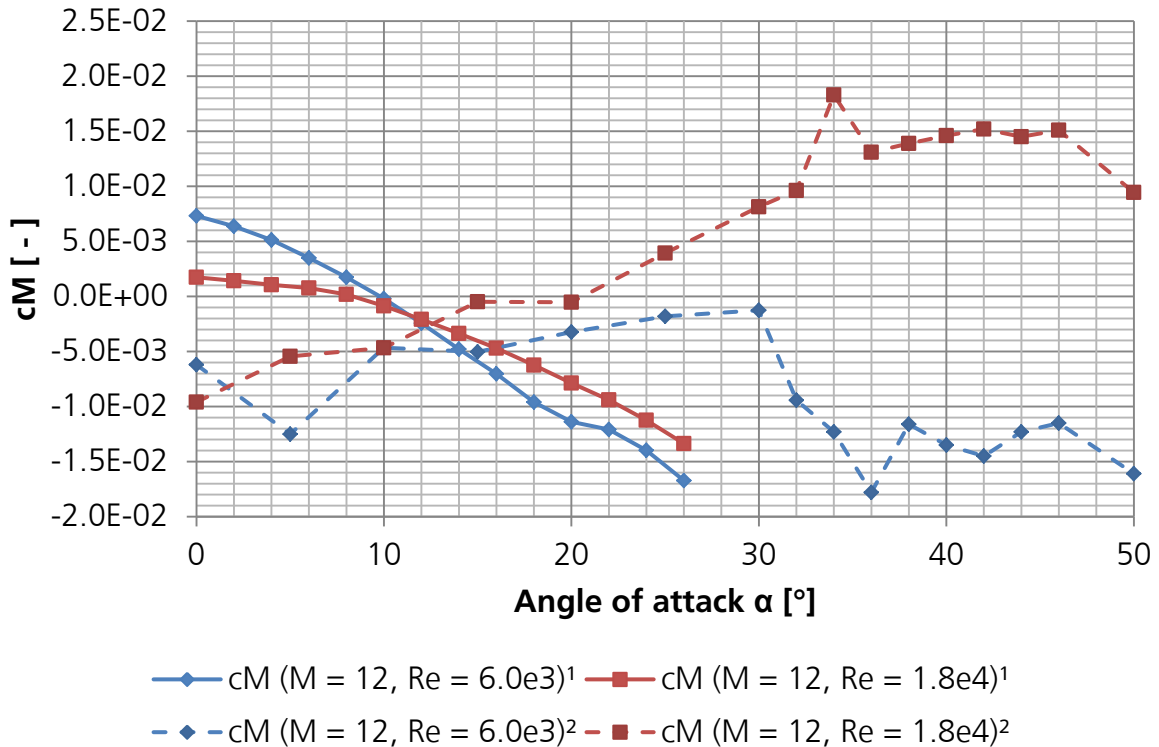


Fig. 58: Pitching moment measurements at selected operating conditions: 1: FAST20XX results, 2: results of former test campaign in late 1980s

Fig. 60 and Fig. 61 show the calibration results to applied normal and tangential loads. There is a linear relation between applied forces and recorded bridge voltage. Thereby, only the gradient of the relation is important. The signal-intercept of the linear calibration can be arbitrarily shifted within the elastic range of the balance frame by balancing the Wheatstone bridge. Pre-loads, as e.g., the dead weight of the balance and different test article weights can be compensated.

Additionally to the calibration Fig. 60 and Fig. 61 show the regression lines with their functional equation and the standard deviation σ of the measured signal. The standard deviation refers to the absolute signal deviation of the measured values to the regression line and is determined by subtracting the regression line from the measured values. For the transducer signal DX in Fig. 60, the regression line fits the data well as the standard deviation of the measurements to the regression line shows. The response of the normal force transducer elements at the positions BYF and BYB show nearly no influence except the noise. The data related to BYF and BYB fall on top of each other in Fig. 60, and are inseparable. The response of the balance to an applied normal calibration load is shown in Fig. 61. The recorded values for the bending moments at BYF and BYB show here a linear characteristic and have also a low standard deviation. The DX characteristic shows in this plot only noise and no mutual component dependence.

The balance resolution can be determined considering that the maximum design forces are of a magnitude of 0.1 N, see chapter 3.4.2. According to the data sheet of the used analogue digital converter, the smallest possible resolution is about 5 mV for the maximum input voltage range of ± 10 V. This allows to determine the minimum resolvable force (see Table 4).

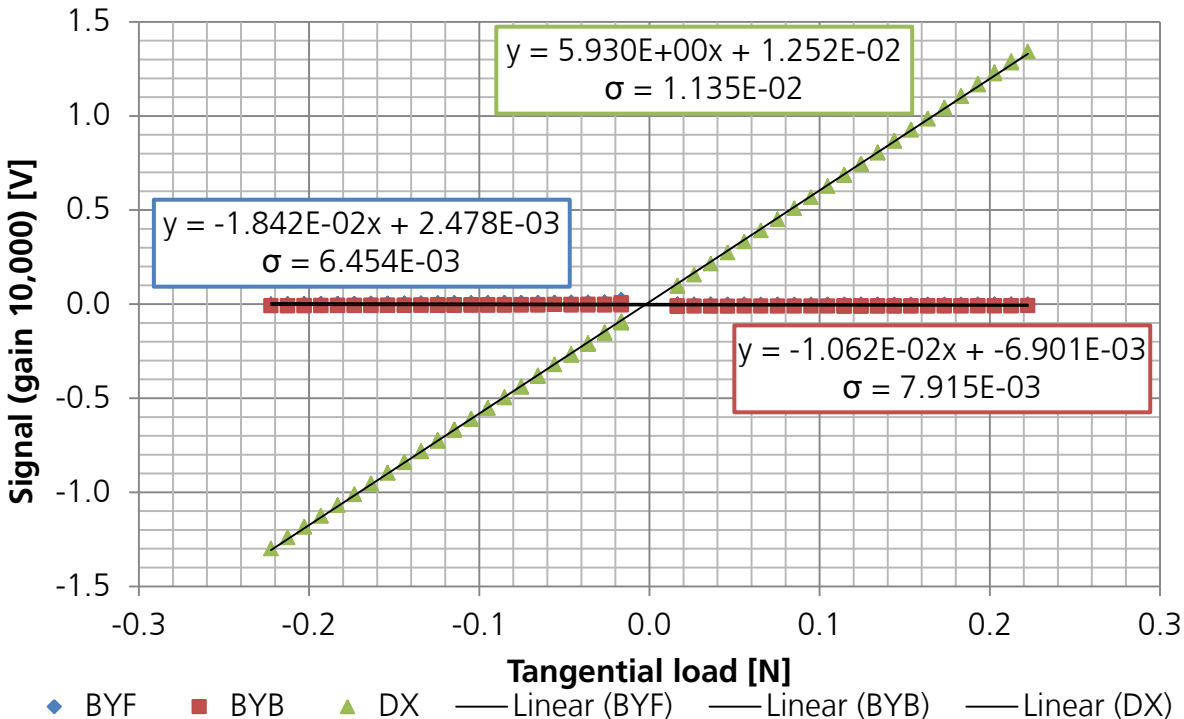


Fig. 60: Balance response to a defined tangential load (y and σ in [V])

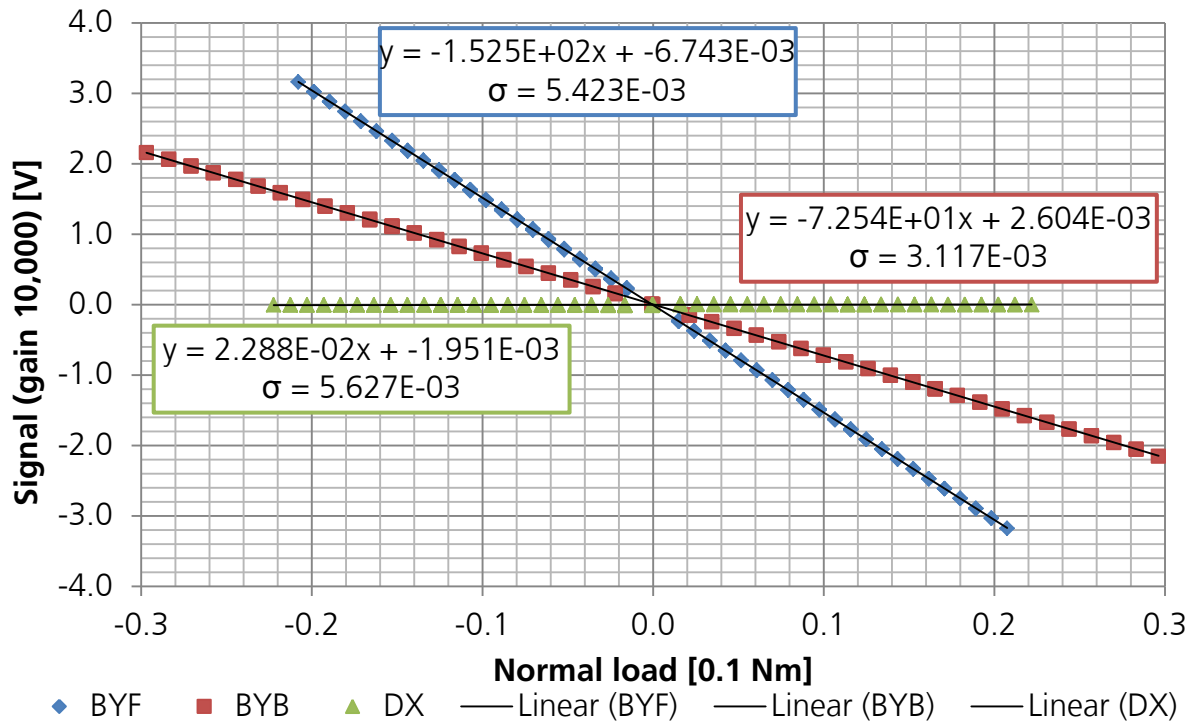


Fig. 61: Balance response to a defined normal load (y and σ in [V])

Table 4: Force and moment balance resolution

Transducer component	Minimum resolvable force / moment
BYF	$\sim 3.5 * 10^{-4}$ [Nm]
BYB	$\sim 5.0 * 10^{-4}$ [Nm]
DX	$\sim 6.5 * 10^{-4}$ [N]

5 Performance of Force Measurements

5.1 Procedure

At this point all preparations for the experimental investigations are completed. The desired operating conditions are selected, and their flow fields are characterised. The V2G measurement technique, containing balance but also test article design and measurement procedure, is further improved, compared to the measurements performed within FAST20XX. From the calibration of the V2G balance, the linear relation from applied load to obtained signal is known. Further, V2G lightweight test articles are available for the sharp-edged, slender (SHEFEX III) and for the blunt (COLIBRI) configuration so that it is now possible to start with the actual force measurements.

The V2G force measurement process follows an optimised sequence to reduce the error caused by temperature related zero point drift. Amongst others the zero point drift is a function of time, and if the exposure time of the balance to the flow is reduced, the drift during the test sequences is reduced as well. The duration of one test cycle defines the maximum uncertainty due to zero point drift.

Before the wind tunnel flow is started, the amplifiers are balanced and the zero load signals, i.e., the remaining sensor unbalance of all force components is measured. This allows a later removal of signal offsets from the force measurements which are too small to be removed by hardware balancing via the amplifiers.

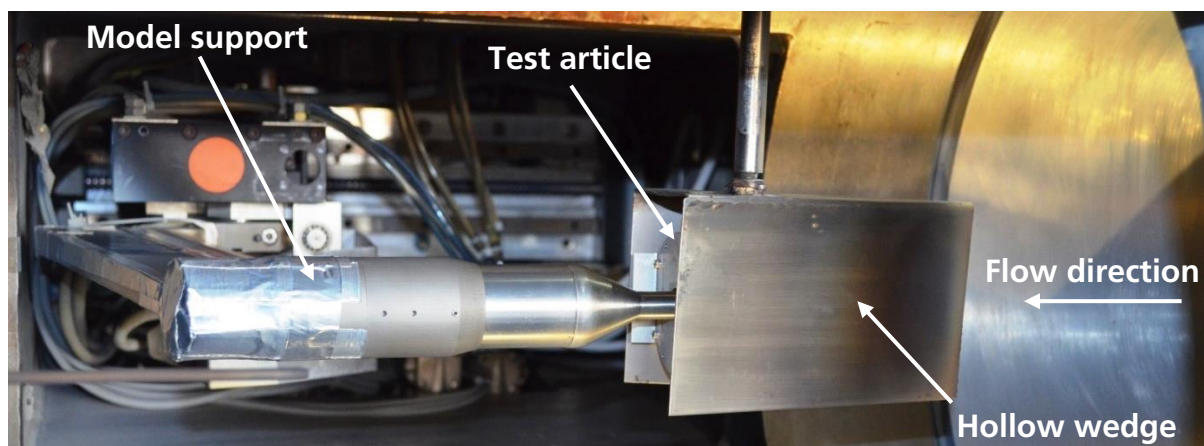


Fig. 62: Shielded test article during facility start-up and shut-down

While the flow is started and the desired operating condition is setup, the test article is moved to a parking position where it is shielded by a hollow wedge (see Fig. 62) to reduce the aerodynamic heating. After the desired flow condition is established, the shield is removed and the test article is moved to the desired position in the test section via SCMV the movement control and data acquisition software. For each operating condition a complete angle of attack profile (SHEFEX III: $0^\circ \leq \alpha \leq 34^\circ$, COLIBRI: $0^\circ \leq \alpha \leq 30^\circ$, step size 4°) is performed in a forward and a backward sweep, see chapter 4.7, to reach a final resolution of 2° steps. Fig. 63 shows both test articles during the experimental force measurements with an angle of attack of 30° .

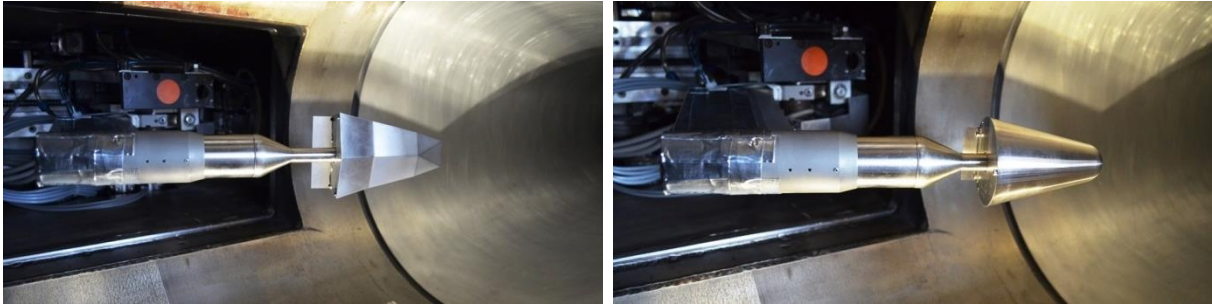


Fig. 63: Test articles during experimental analysis: SHEFEX III (left), COLIBRI (right)

Due to the different lengths of the test articles, it is necessary to use the model support to position the shorter COLIBRI test article further upstream, such that the nose of both test articles is located at $x = 112 \text{ mm}$ downstream the nozzle exit. In case of the COLIBRI test article, the model support has less remaining travelling distance left, so that translational movements, caused by varying angles of attack, could be compensated in x and z -direction up to 30° only.

After the experimental data is recorded, the test article is moved back to the parking position and is again shielded during the shut-down of the facility, followed by ventilating the tunnel to allow a quick heat equalisation in the test article and balance. The shielding during shut-down of the facility prevents the test article from further aerodynamic heating and reduces the time to cool down and the time to the next test cycle.

At each position 5,000 values are recorded within one second and averaged in the evaluation, to remove dynamic elements within the measurement signal, e.g., due to electric noise or mechanic vibrations. Higher frequencies are already removed within the amplifiers by using a 1 kHz low pass filter. Together with the sampling rate of 5 kHz and the low pass filter cut-off frequency, the procedure complies with the Nyquist–Shannon sampling theorem. Due to the facility design and the experimental setup, currently only steady-state analyses can be conducted. Although the balance design allows transient analyses, the results have to be averaged to smooth the scattering caused by the mechanical and electrical noise of the large vacuum pumps, see Fig. 64 and Fig. 65.

Although the actual measurements take only about 3 min, the total test cycling including force measurement, shut down of wind tunnel flow, ventilation, heat equalisation, evacuation, and start of the subsequent operating condition sums up to at least 30 min. The effort is rewarded with temperature related drifts such small, that they could be even neglected for some operating conditions.

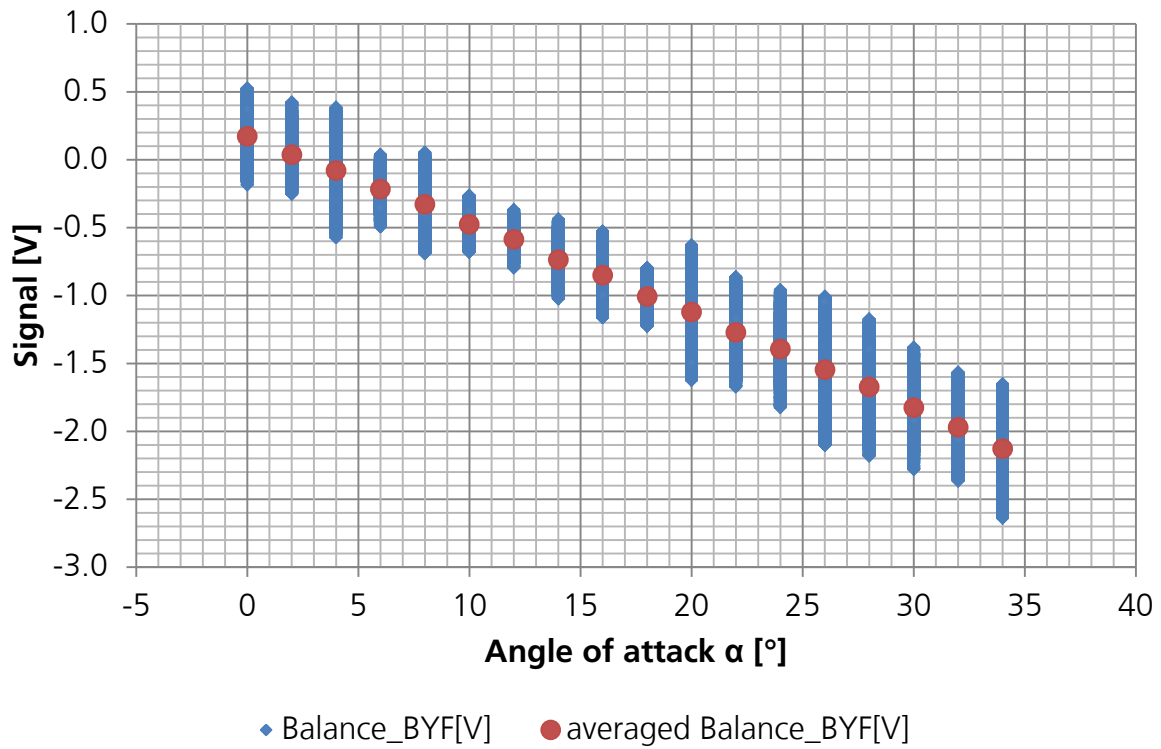


Fig. 64: Raw signal and averaged values (cond. 4)

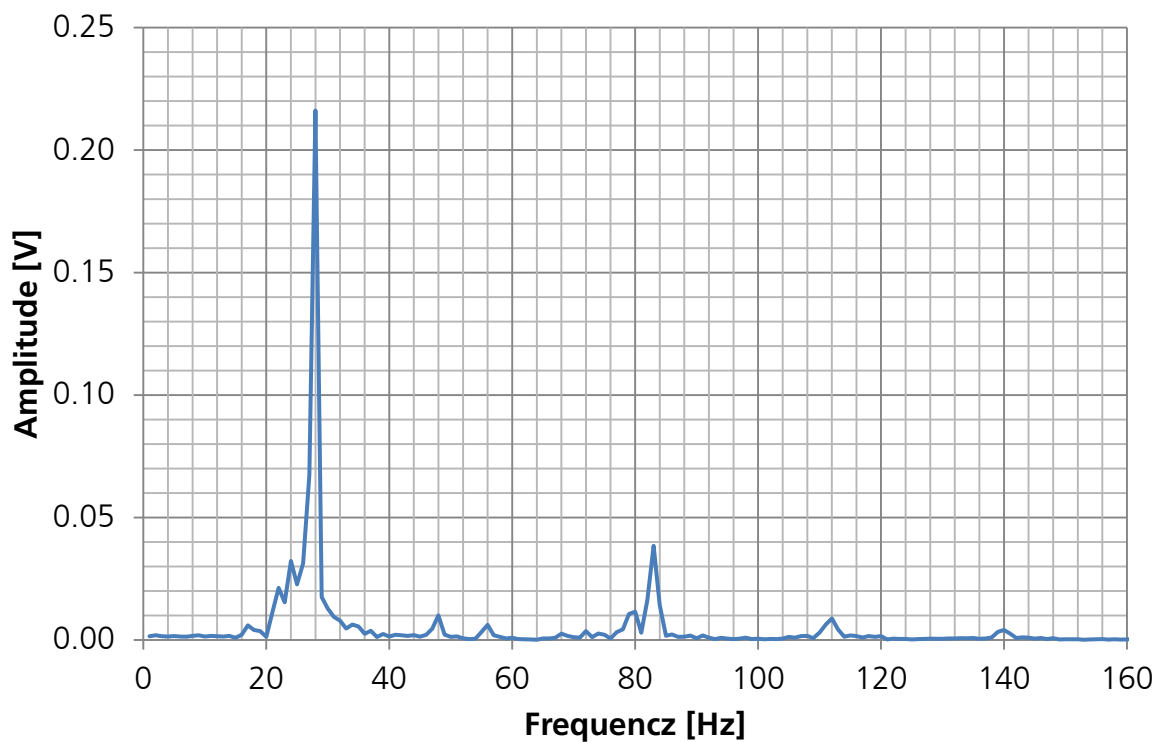


Fig. 65: Frequency spectrum between 1 Hz and 160 Hz of raw signal (cond. 4, $\alpha = 0^\circ$)

5.2 Measurements

The measurements and the processing of the data from raw data to the aerodynamic coefficients lift, drag and pitching moment is exemplarily explained for the operating condition no. 4, using the 2 mm nozzle throat diameter with 40 bar reservoir pressure and 1090 K reservoir temperature. At this condition the Knudsen number is $Kn = 3.2 \cdot 10^{-3}$, the Reynolds number is $Re = 1.22 \cdot 10^4$ and the Mach number is $M = 25.2$. The processing is the same for all force measurements. The figures and tables containing the aerodynamic coefficients are shown in [79]. The data processing procedure for the determination of the aerodynamic coefficients is visualised as flow chart in Fig. 114 in Appendix A.

Within the so called signal quick check, the data is visualised in an early stadium of evaluation. Directly after the pre-evaluation, where remaining sensor unbalances, i.e., the zero load signals are subtracted and the signals are divided through the gains, the signals are plotted versus the angle of attack, see Fig. 66. The results of the forward / backward sweeps are very close together that they appear rather as one thick line. The result of the linear zero point drift compensation (chapter 4.7) is shown in Fig. 67.

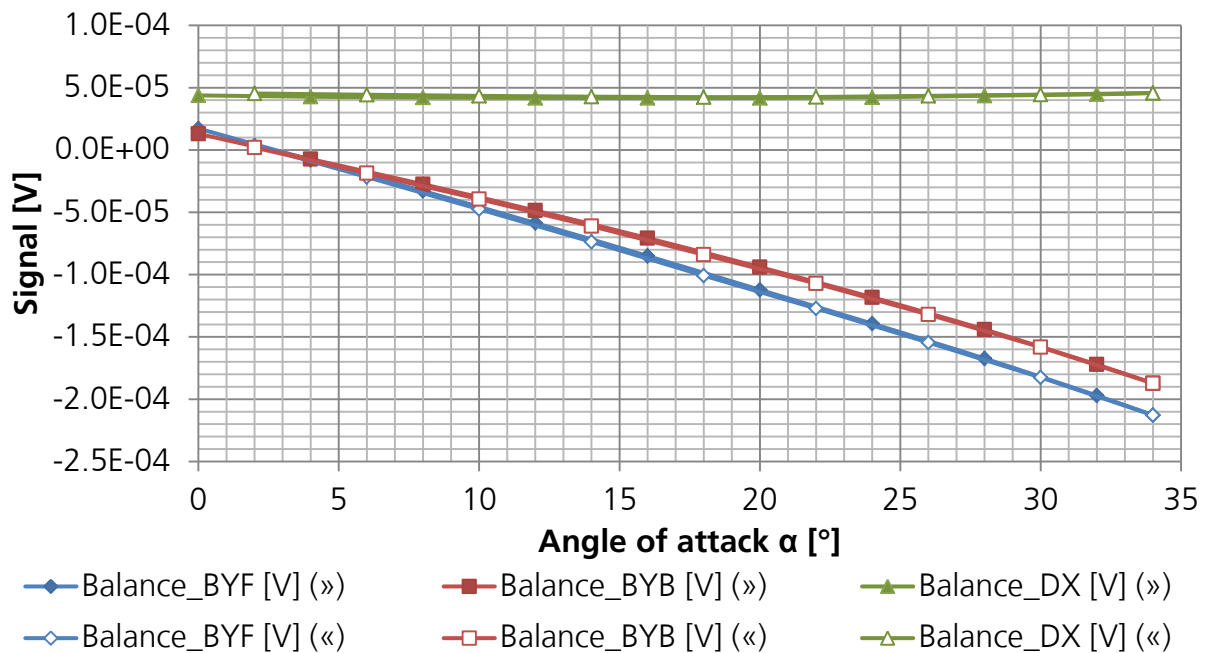


Fig. 66: Signal quick check for cond. no. 4, SHEFEX III, (») forward sweep («) backward sweep (see Table 3 or in detail [79])

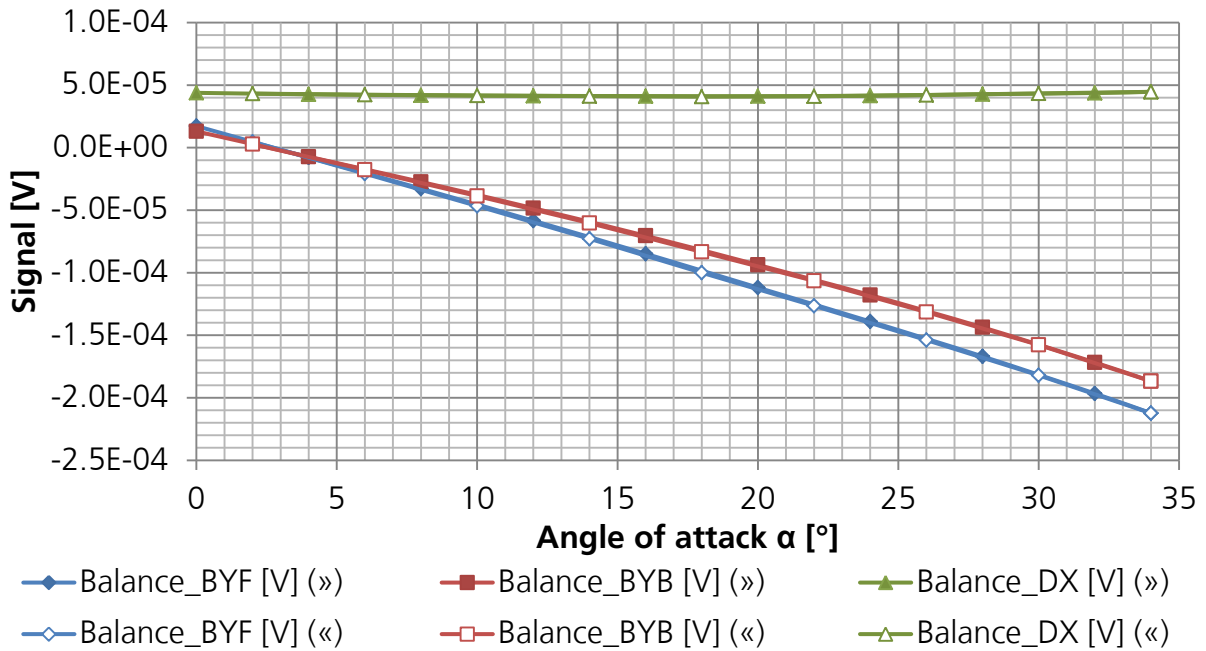


Fig. 67: Compensated thermal zero point drift for cond. no. 4, SHEFEX III, (») forward sweep («) backward sweep (see Table 3 or in detail [79])

5.3 Evaluation

The first evaluation step is to apply the calibrations of the sensors BYF, BYB and DX to the thermally compensated data. For the two Wheatstone half bridges BYF and BYB, located on the normal force transducer, it is important to use the correct geometrical dimensions listed in Table 1. The unit of BYF and BYB is Nm, while the unit of DX is N.

The next step is the determination of the forces and moments in the balance coordinate system by applying (3-5) and (3-7). Subsequently, using (3-8) and (3-9) the force components are then transformed into the aerodynamic coordinate system of the test article, see Fig. 69. The physical meaning of the characteristics of the aerodynamic forces is explained in the next step where the aerodynamic coefficients are determined. There the results can be directly compared between both test articles.

It can be seen that the maximum aerodynamic loads exceed 0.1 N where the balance is originally designed for, see chapter 3.4.3. Due to a horizontal fixing of the model support to the wind tunnel side, the test article weight acts on the balance as side force. Since it is neither affecting the normal force, nor the tangential force, nor the pitching moment, see Fig. 68, the balance can be used for aerodynamic forces up to 0.5 N, while remaining in its designed total range, see Fig. 21.

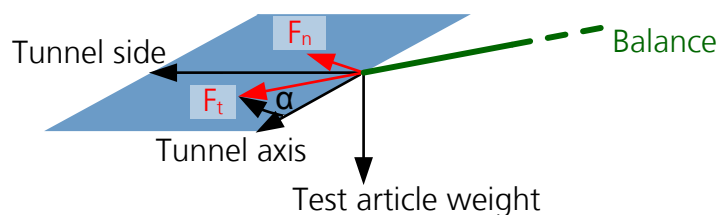


Fig. 68: Measurement plane (blue) and normal acting test article weight

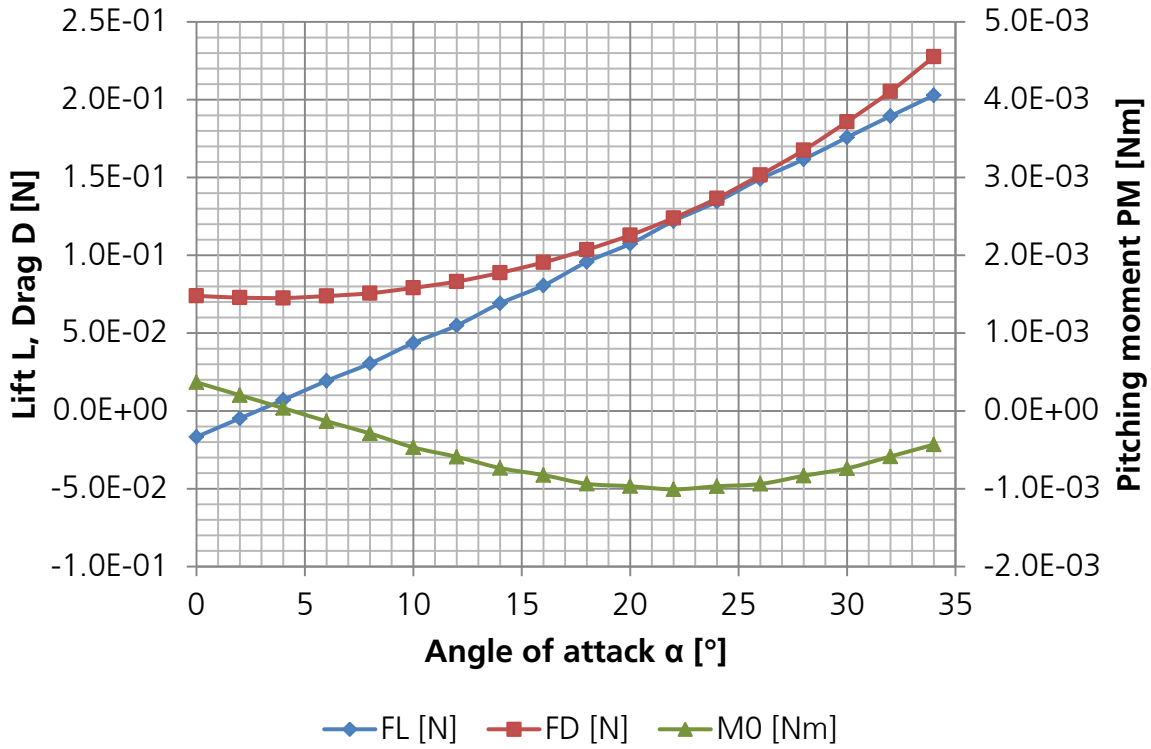


Fig. 69: Forces and moments in aerodynamic coordinate system for cond. no. 4, SHEFEX III, (see Table 3 or in detail ^[79])

The aerodynamic coefficients are then obtained with (5-1), (5-2) and (5-3). As dynamic pressure an averaged value of the region where the test articles are located is used. The detailed procedure is explained in ^[79]. The reference area is defined to be the projected test article planform area, i.e., the in the horizontal plane projected cross section of the test article at $\alpha = 0^\circ$. The reference length is defined to be the total length of the test article without body flap. The pitching moment is built around the centre of gravity. The quantities of the test article reference area A_{ref} , the reference length l_{ref} and the position of the centre of gravity are taken from ^[79].

$$c_L = \frac{F_L}{qp_1 * A_{ref}} \quad (5-1)$$

$$c_D = \frac{F_D}{qp_1 * A_{ref}} \quad (5-2)$$

$$c_M = \frac{PM}{qp_1 * A_{ref} * l_{ref}} \quad (5-3)$$

Fig. 70 and Fig. 71 show finally the aerodynamic coefficients for lift, drag and pitching moment, together with the aerodynamic efficiency for both the SHEFEX III and COLIBRI test article configuration for the selected condition number 4. The full data set and full set of plots is shown in ^[79].

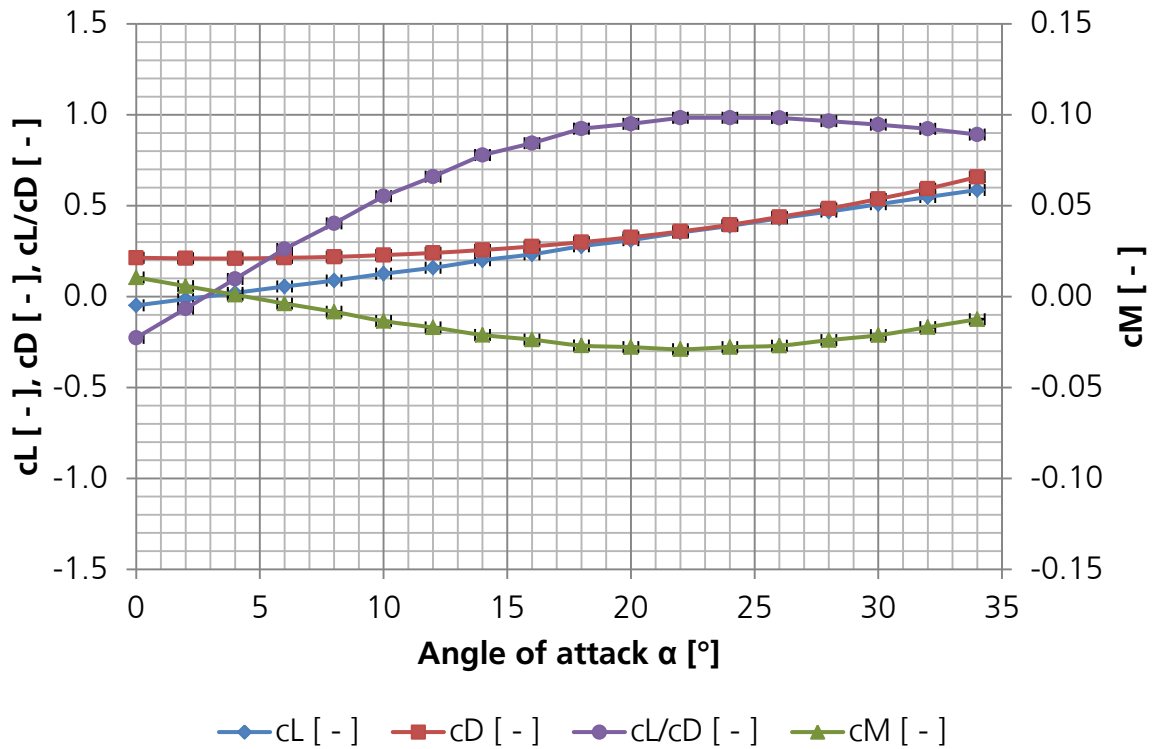


Fig. 70: Force and moment coefficients in aerodynamic coordinate system for cond. no. 4, SHEFEX III, (see Table 3 or in detail ^[79])

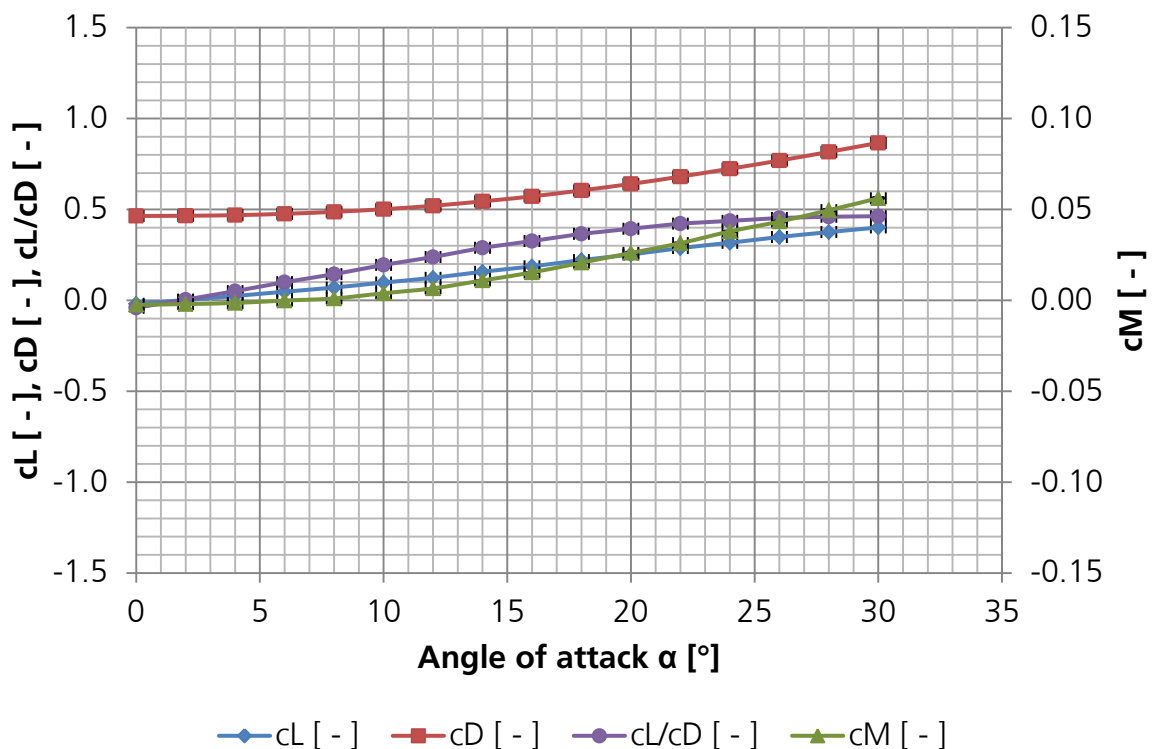


Fig. 71: Force and moment coefficients in aerodynamic coordinate system of cond. no. 4, COLIBRI, (see Table 3 or in detail ^[79])

Starting with the SHEFEX III configuration, see Fig. 70, it can be seen that the lift coefficient starts at $\alpha = 0^\circ$ with a negative value and is increasing with increasing angle

of attack to nearly 0.59 at $\alpha = 34^\circ$ at this operating condition. The zero crossing is at $\alpha \approx 3^\circ$. The drag coefficient starts at $\alpha = 0^\circ$ with a value of about 0.21 and initially decreases with increasing angle of attack to a local minimum at $\alpha = 3^\circ$, before the drag coefficient starts to increase with increasing angle of attack. At the maximum measured angle of attack of $\alpha = 34^\circ$, the drag coefficient reaches almost 0.66. Based on the lift and drag coefficient characteristics, the maximum aerodynamic efficiency c_L/c_D can be determined. At an angle of attack of $\alpha \approx 24^\circ$, the lift / drag ratio reaches a local maximum where the aerodynamic efficiency approaches almost 1.0.

The pitching moment coefficient shows primarily a decreasing characteristic with increasing angle of attack. That means if an aerodynamic force pushes the vehicle away from its originally trimmed flight attitude, a counter acting pitching moment is generated which moves the vehicle back to its original flight attitude, i.e., the vehicle is aerodynamically statically stable. However, the pitching moment approaches at $\alpha \approx 22^\circ$ a local minimum before the trend is reversed. That means that the vehicle becomes statically unstable at angles of attack larger than 22° at this operating condition. It can also be seen that the intersection point between the pitching moment characteristic and the x-axis, the so called trim point, is located at $\alpha \approx 4^\circ$ for this operating condition.

Turning towards the COLIBRI configuration, see Fig. 71, the lift coefficient has a similar characteristic as the SHEFEX III configuration. It can be seen that the lift coefficient starts at $\alpha = 0^\circ$ also with a negative value and is increasing with increasing angle of attack. Though the starting value is not as negative as for the SHEFEX III configuration, and the slope of the pitching moment seems to decrease at high angles of attack, indicating a nearby local maximum. At the highest measured angle of attack of the COLIBRI configuration at $\alpha = 30^\circ$, the lift coefficient is 21% lower than in case of the SHEFEX III configuration. The zero crossing is close to $\alpha \approx 2^\circ$. The COLIBRI drag coefficient has also a similar characteristic but with a local minimum close to $\alpha = 0^\circ$ and far higher values. The drag coefficient starts at $\alpha = 0^\circ$ already with a value of about 0.46 and increases with increasing angle of attack to almost 0.87 at $\alpha = 30^\circ$. The aerodynamic efficiency is correspondingly far lower and reaches only 0.46 at this angle of attack. The decreasing slope of the aerodynamic efficiency at high angles of attack indicates that the maximum value is nearby $\alpha = 30^\circ$ and that the maximum value is not significantly higher.

The pitching moment coefficient is continuously increasing with increasing angle of attack, contrary to the characteristic of the SHEFEX III configuration. This pitching moment characteristic shows statically unstable behaviour and indicates that the body flap is too small for the position of the centre of gravity. Detailed measurements of the COLIBRI showed that the used body flap is indeed 2 mm, i.e. 17%, too short, compared to the test article scale. This difference can be the reason for the statically instable flight attitude. However, there are no restrictions for the significance of the regarded analysis of rarefaction effects.

For the error discussion the measurement errors are distinguished in random errors and systematic simulation errors^[28]. Random errors can change from measurement to measurement and are defining the preciseness of the reproducibility. The systematic errors in turn describe the deviations of the measured results from the true values. The systematic errors can only be determined by comparing the results to other investigation methods, as e.g. numerical predictions, and are only described and estimated.

The error bars shown in Fig. 70 and Fig. 71 correspond only to the random error. Since the random errors are very small, they are presented for one case in a detailed view in Fig. 72.

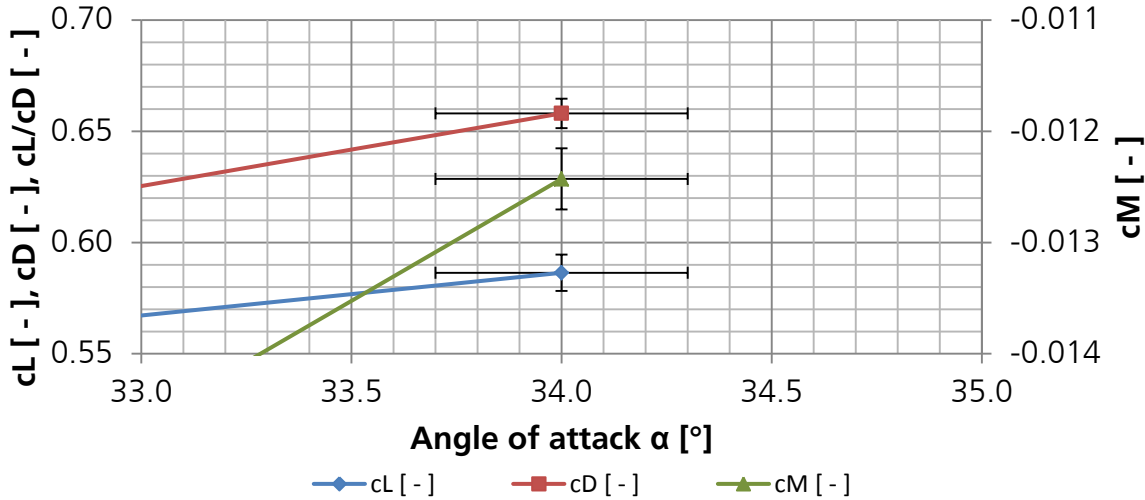


Fig. 72: Detail of force and moment coefficients in aerodynamic coordinate system for cond. no. 4, SHEFEX III

The angle of attack error is determined to be below $\alpha < 0.3^\circ$ by adding the balance deformation and the adjustment accuracy of the model. It is lower than the requested balance accuracy of $\alpha < 0.5^\circ$, see chapter 3.4.3. The reason is that the maximum balance loads are strongly reduced by mounting the model support horizontally, such that the test article weight loads are not applied on the balance signal. Since only aerodynamic loads are applied, the total balance deformation is much smaller. Concerning the systematic error, the angular deviation increases with increasing normal forces based on the balance principle and, therefore, with increasing angle of attack.

The error bars of the aerodynamic coefficients are determined by selecting the minimum of the single standard deviation determined during the balance calibration, and the absolute error due to the minimum balance resolution. Errors related to averaging raw data (Fig. 64) are not considered. The error bars of the aerodynamic efficiency are larger than the other shown error bars as a result of error propagation. The systematic error based on the inhomogeneity of the flow field, i.e. flow gradients in the free stream, is not included. Instead the distribution of the dynamic pressure, used for the determination of the aerodynamic coefficients, is listed in [79]. Further the standard deviation of the averaged dynamic pressure is listed for each experiment together with the corresponding aerodynamic coefficients in [79].

Due to the inhomogeneity of the dynamic pressure, i.e. its decrease in flow direction, the pitching moment can be stronger affected than the dynamic pressure [79]. The reason is that, opposed to lift and drag coefficients, the pitching moment coefficient is very sensitive to the location where the resulting force of the dynamic pressure attacks. The variation of the dynamic pressure along the test article generates an additional raising pitching moment as indicated in Fig. 73. For a detailed quantification of the pitching moment sensitivity, a detailed analysis of local flow properties along the test article surface is required. This information cannot be determined from the conducted experiments where only integral forces and moments are measured. Instead the detailed

flow field data along the surface should be determined numerically, after gaining confidence by comparing integral forces between experimental and numerical results.

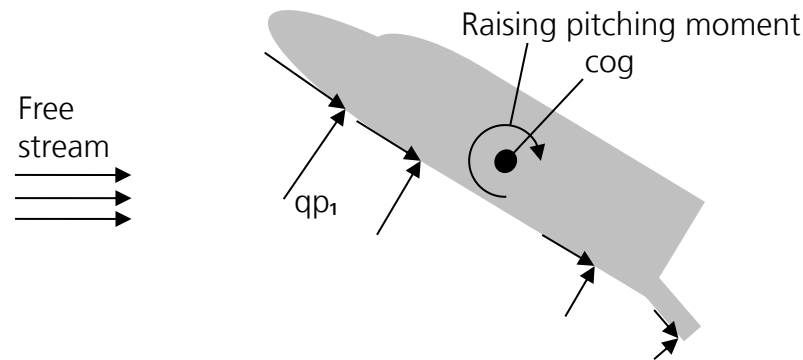


Fig. 73: Pitching moment distortion due to inhomogeneous dynamic pressure

The pitching moments measured in a further expanding wind tunnel flow are always more positive than the pitching moments in a homogeneous flow field. The magnitude of the influence is depending on the operating condition and on the angle of attack.⁴ In the present analysis the projected test article length in stream direction decreases with $1 - \cos \alpha$ and yields maximum decreases of 17% for the SHEFEX III configuration ($\alpha_{max} = 34^\circ$) and of 13% for the COLIBRI configuration ($\alpha_{max} = 30^\circ$), see Fig. 74. That means that with increasing angles of attack the influence of axial flow gradients becomes less. Since the test articles are rotated around their centre of gravity ($\sim 60\%$), the change of the averaged value remains in the magnitude of 0.05%.

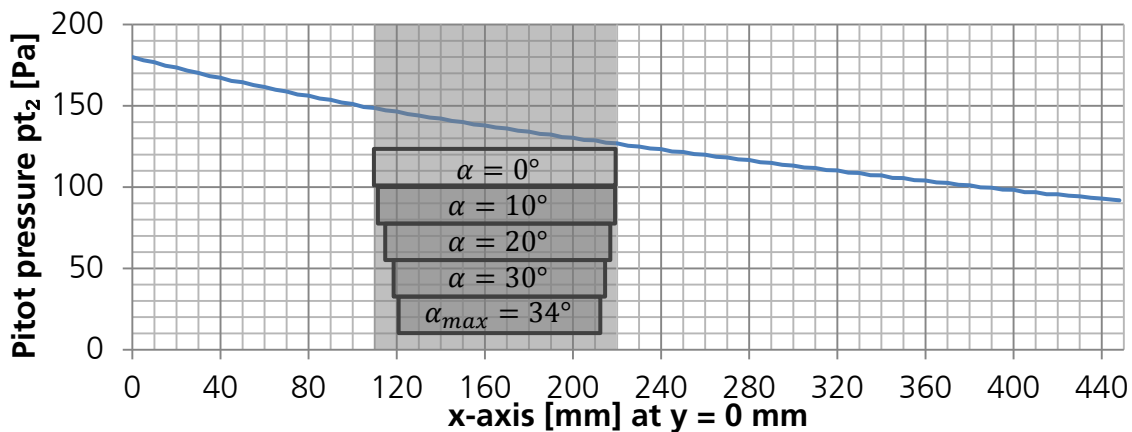


Fig. 74: Pitot pressure axial profile for cond. no. 3 with test article location (SHEFEX III) at different angles of attack (grey)

An approach to compensate the axial flow gradients with simple engineering methods is not possible and yields quickly to a full numerical simulation. The reasons are that the detailed flow field behind the compression shock and in the boundary layer is unknown, and that the processes are taking place in a flow regime where the friction forces become significant so that the “history” of the flow has to be taken into account. It is expected, that the rarefaction effects on the pitching moment coefficient are, therefore, difficult to distinguish from other changes caused by different flow gradients.

⁴ The magnitude of the influence is independent from the angle of attack for a sphere shaped test article.

The error values for each experiment are listed together with the aerodynamic coefficients in^[79].

At this point the data set of aerodynamic coefficients is available covering all 26 tested operating conditions with both test article configurations at angles of attack of $0^\circ \leq \alpha \leq 34^\circ$ in case of the sharp-edged, slender SHEFEX III configuration, and of $0^\circ \leq \alpha \leq 30^\circ$ in case of the blunt COLIBRI configuration, respectively. Thus, now 52 diagrams are available^[79] to investigate the behaviour of the aerodynamic coefficient characteristics at different degrees of rarefactions. Considering 18 angle of attack positions for the SHEFEX III configuration and 16 angle of attack positions for the COLIBRI configuration, it sums up to a database of about 900 experimentally investigated test cases.

6 Rarefaction Effects

The effects of rarefaction are analysed by comparing the aerodynamic coefficients at operating conditions with different Knudsen numbers. The first step is here to compare only operating conditions at a constant Reynolds number each, to make sure that there is a pure effect of rarefaction. For an extension of the effect this analysis is repeated at different Reynolds numbers. In a second step aerodynamic coefficients of the single constant Reynolds number comparisons are compared to quantify the Reynolds number effect. As countercheck of the rarefaction effects on the aerodynamic coefficients, the results of operating conditions at one single Knudsen number are then compared in a third step. The results of step one and two can also be used to check the applicability of the Mach number independence principle in case of the slender configuration at low angles of attack, by comparing the results of both test configurations.

Since the test article sizes are slightly different, their reference lengths for the similarity parameters are different as well, such that the Reynolds numbers and the Knudsen numbers of the COLIBRI test configuration are slightly deviating from the SHEFEX III test configuration, although they are analysed at the same operating conditions. The similarity parameters of both test configurations share, however, a large overlapping range where a direct comparison is possible.

The variation of the Knudsen number between the operating condition closest to continuum and the most rarefied operating condition is always in the range of a factor of 2 at one constant Reynolds number, due to the direct relation of Knudsen number, Reynolds number and Mach number and the limited Mach number adjustment range in V2G experiments.

6.1 Comparison at Constant Reynolds Number

6.1.1 Aerodynamic Coefficients versus Angle of Attack at Constant Reynolds Numbers

The aerodynamic coefficient characteristics, showing the aerodynamic coefficients versus the angle of attack, are plotted as explained by means of Fig. 70 for each test configuration and operating condition. As mentioned in chapter 5.3 now 52 diagrams are available. Based on these diagrams the four aerodynamic coefficients of lift, drag, pitching moment, and lift / drag ratio are separated into four diagrams. To evaluate the rarefaction effects, aerodynamic coefficients determined at equal Reynolds numbers are plotted in one figure with Knudsen number as parameter. Simultaneously with the Knudsen number, the Mach number varies as well but due the Mach number independence principle there is no dependency expected at these operating conditions in case of the blunt configuration and in case of the slender configuration at high angles of attack. Based on the comparison of the behaviour at low angles of attack between both test configurations, the applicability of the Mach number independence principle for the slender configuration at low angles of attack can be assessed.

The effects for both test configurations are exemplarily described at one large and one small constant Reynolds number, see Fig. 75 to Fig. 78. The whole set of figures

showing all constant Reynolds number investigations is presented in Appendix B from Fig. 115 to Fig. 124.

Starting with the SHEFEX III test configuration and the operating conditions close to continuum, i.e., the operating conditions with the largest Reynolds number, it can be seen that in case of the lift coefficient characteristics the values of both experiments are nearly indistinguishable on top of each other, see Fig. 75. The maximum difference is below $1.5 * 10^{-2}$.

In opposite a distinct difference can be observed in the drag coefficient characteristics where the drag coefficient increases already with increasing rarefaction. The increase is constant over the full analysed variation of the angle of attack. In percent the increase is varying from 26% at $\alpha = 0^\circ$ to only 8% at $\alpha = 34^\circ$. The corresponding random measurement errors at these angles of attack are for both experiments below 1.1%. The standard deviation of the dynamic pressure of the flow field is 5.9% for the rarefied operating condition and 3.6% for the operating condition close to continuum.

In case of the pitching moment, the rarefaction seems to slightly affect the pitching moment coefficient characteristic by rotating it around the pitching moment coefficient value at about $\alpha = 7^\circ$, such that the pitching moment becomes more negative with increasing rarefaction for $\alpha > 7^\circ$.

The characteristic of the aerodynamic efficiency, i.e., the lift / drag ratio, shows also a dependence on the Knudsen number. Due to the almost constant difference in the drag coefficient over the analysed angle of attack range and an unaffected lift coefficient, the characteristic for the more rarefied condition becomes flatter. The intersection is located at a lift / drag ratio of 0.2 and an angle of attack of $\alpha = 5^\circ$. The maximum aerodynamic efficiency decreases already by 13%, while simultaneously the angle of attack with the best aerodynamic efficiency tends to shift slightly from about $\alpha = 20^\circ$ to about $\alpha = 22^\circ$ and, hence, to higher angles of attack. Due to the measurement resolution of 2° the actual shift cannot be resolved.

Looking at the results of the second smallest Reynolds number a slight effect of rarefaction becomes noticeable in the lift coefficient characteristic, see Fig. 76. Although the effect is still small, it can be observed that the slope of the lift coefficient decreases with increasing rarefaction.

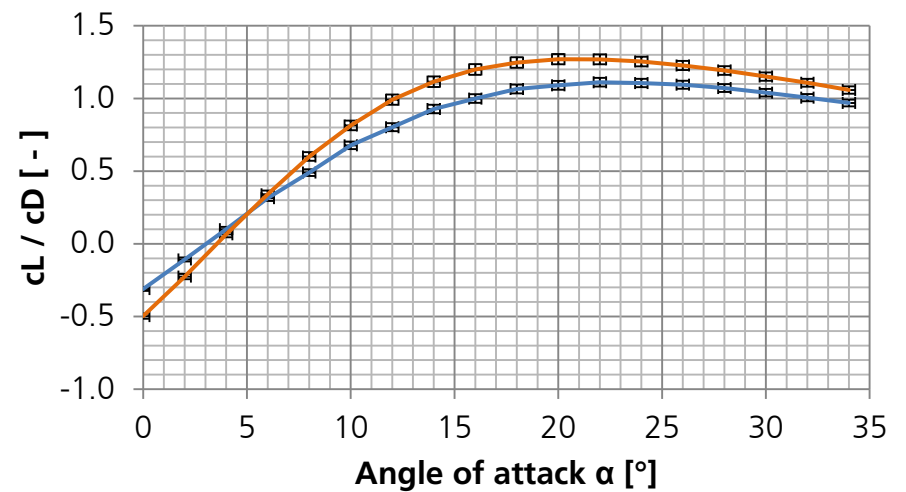
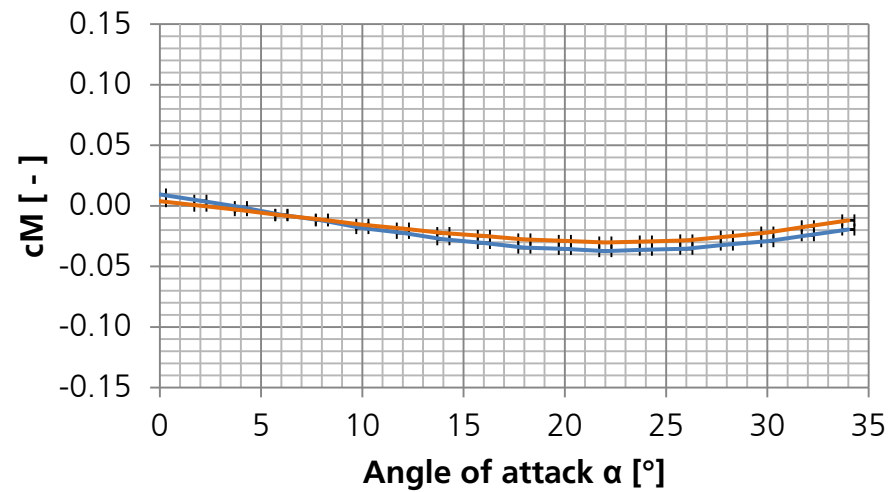
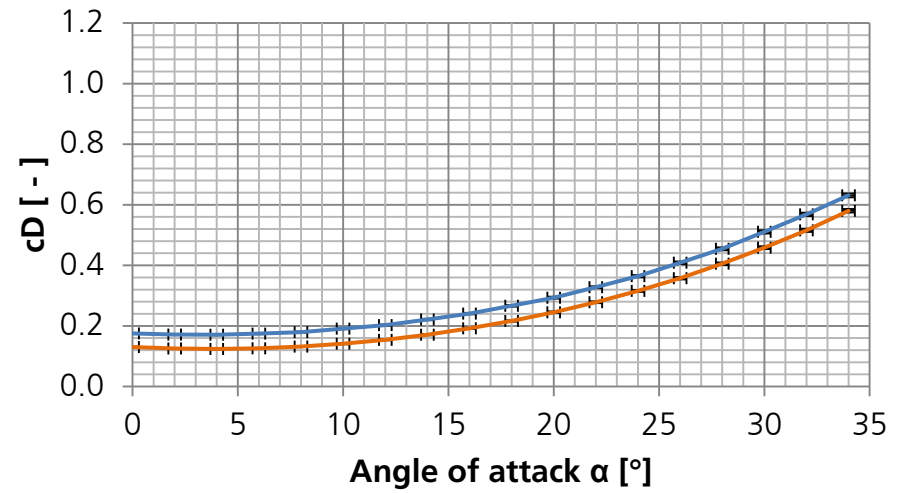
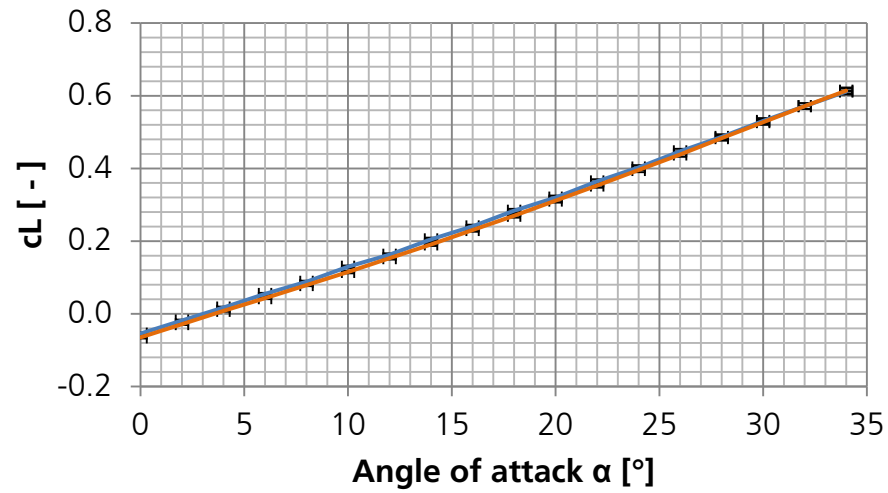
Turning towards the drag coefficient, it can be seen that the effect of increasing drag with increasing Knudsen number is intensified. The increase is also constant over most of the analysed variation of the angle of attack as well but increases slightly more at high angles of attack. In percent the increase is varying from 38% at $\alpha = 0^\circ$ to 21% at $\alpha = 34^\circ$.

The pitching moment coefficient is at this degree of rarefaction significantly affected. Fig. 76 indicates that the pitching moment becomes more positive with increasing rarefaction and is, hence, directly opposed to the previously explained high Reynolds number results. As a direct consequence of the pitching moment change, the vehicles trim point is shifted to higher angles of attack at an unchanging flap deflection, in this case from 3° to about 13° .

As in the earlier explained case, the aerodynamic efficiency of the SHEFEX III test configuration decreases with increasing rarefaction. The loss in aerodynamic efficiency is in case of the more rarefied condition already 23%, compared to the operating conditions close to continuum at $Re = 4.6 * 10^3$. A shift of the angle of attack with the best aerodynamic efficiency cannot be observed or rather be resolved here.

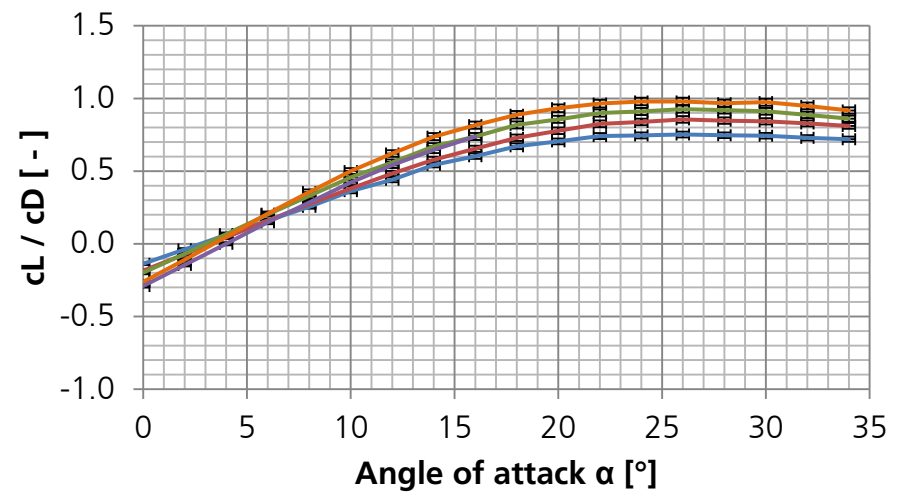
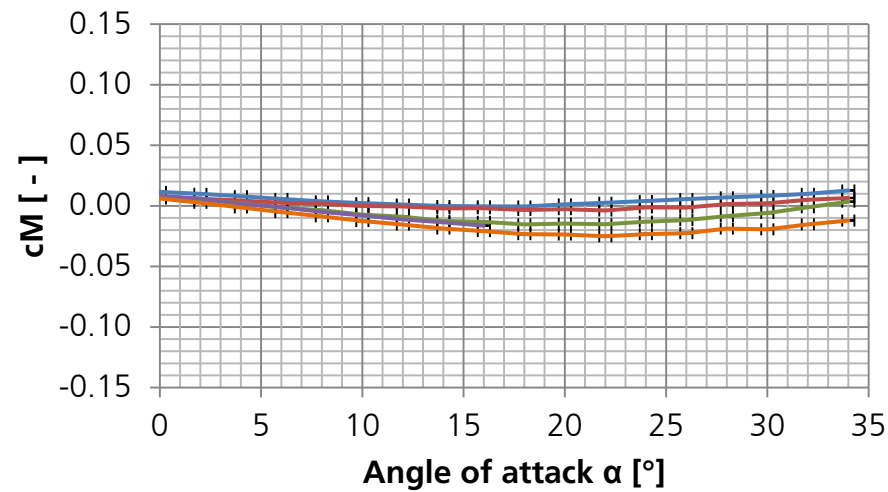
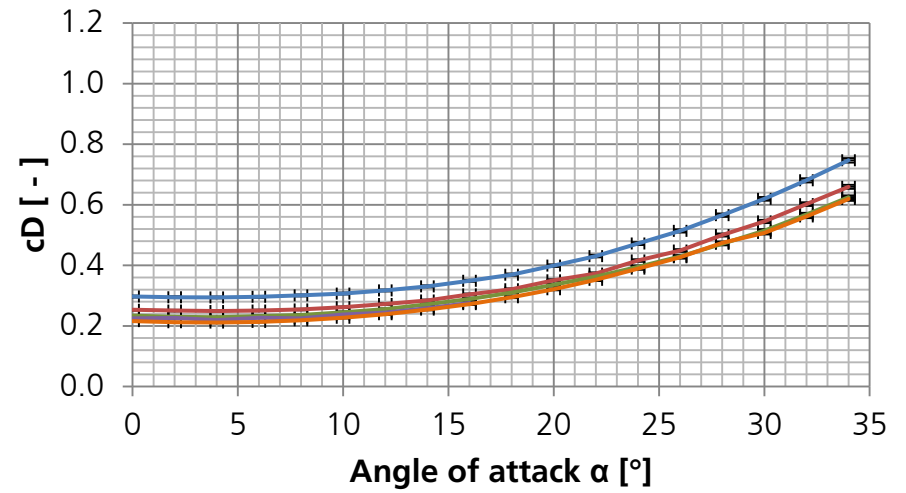
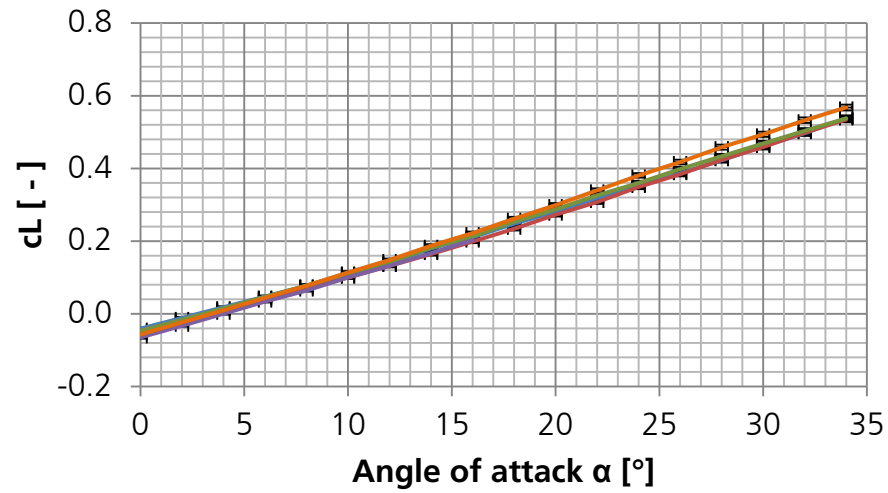
Comparing the results of the SHEFEX III test configuration to the COLIBRI test configuration, it can be seen that the effects of rarefaction are similar in both cases, but differ in a few aspects. As in case of SHEFEX III, both lift coefficient characteristics of the COLIBRI test configuration are almost superimposable in case of the largest Reynolds number, see Fig. 77. Also the rarefaction effect on the drag coefficient characteristic is similar and decreases from 21% at $\alpha = 0^\circ$ to only 10% at $\alpha = 30^\circ$. Apart from the fact that the COLIBRI pitching moment shows a complete instable behaviour, the influence due to rarefaction effects is similar to the SHEFEX III results. The aerodynamic efficiency is also decreasing with increasing Knudsen numbers. The maximum lift / drag ratio is reduced by 11% and the angle of attack with the best aerodynamic efficiency is shifted from 28° to 30° .

At the second lowest Reynolds number, see Fig. 78, there is already a significant decrease in the lift coefficient characteristic of the COLIBRI configuration noticeable. At the highest analysed angle of attack of $\alpha = 30^\circ$, the maximum lift is decreased by 24%. In case of the drag coefficient, again the constant offset between the different characteristics can be observed but the drag coefficient decreases even further from 27% at $\alpha = 0^\circ$ to only 17% at $\alpha = 30^\circ$. The pitching moment becomes more positive with increasing rarefaction and is directly opposed to the high Reynolds number results, which agrees to the results of the SHEFEX III configuration. The maximum lift / drag ratio in the measured range is reduced by 35% at $\alpha = 30^\circ$. The aerodynamic efficiency characteristic indicates that the angle of attack with the best lift / drag ratio is larger than $\alpha = 30^\circ$ and not in the analysed range.



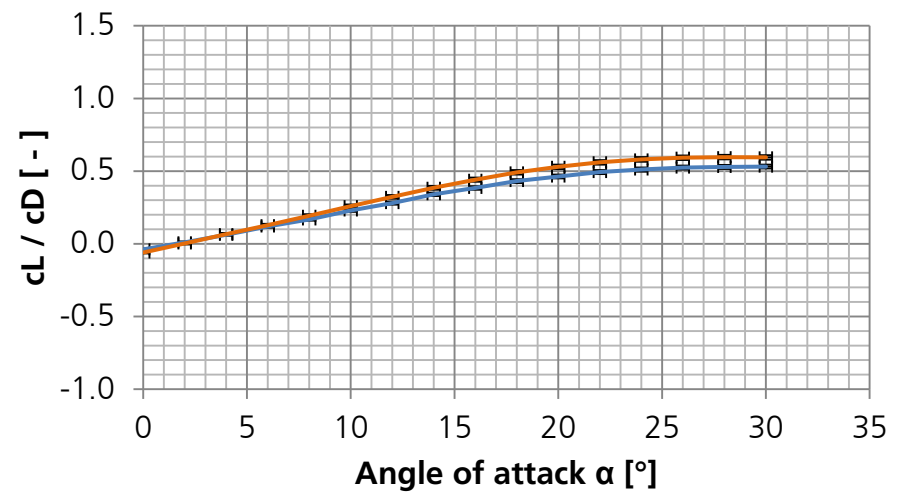
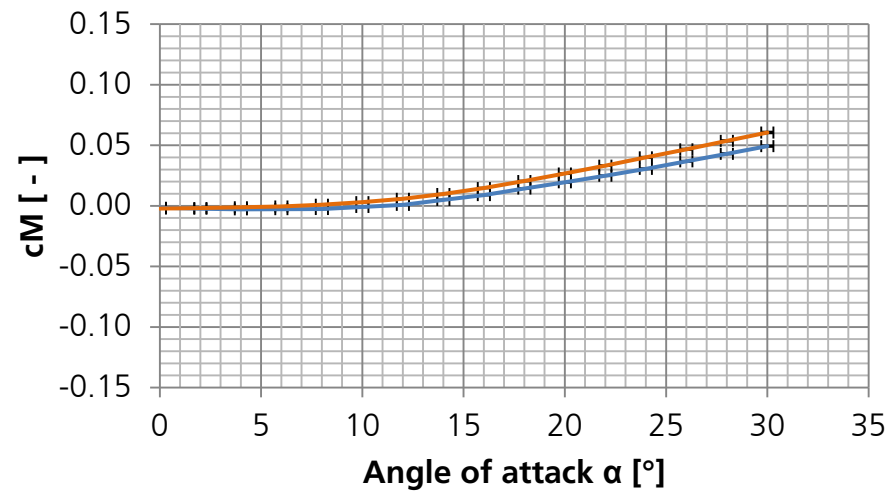
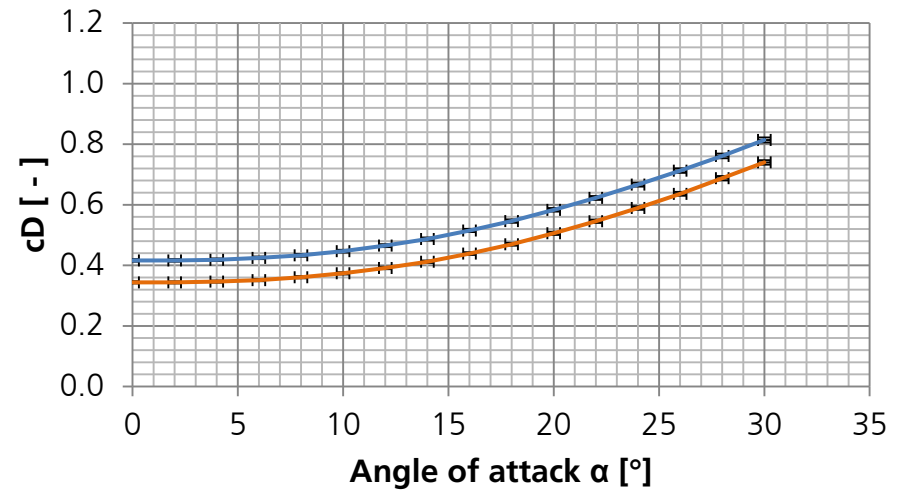
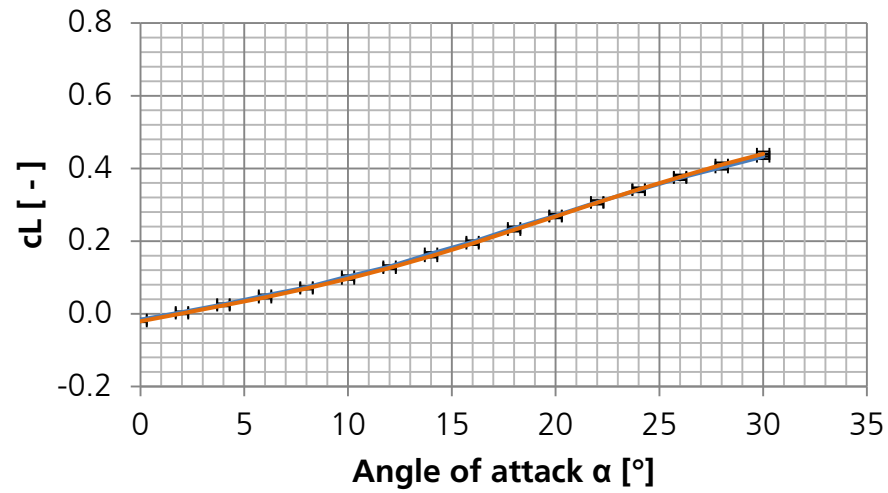
— $Kn_1 = 1.57E-3,$ — $Kn_1 = 7.16E-4,$
 $M_1 = 25.7$ $M_1 = 12.0$

Fig. 75: Rarefaction effects on aerodynamic coefficients ($Re_1 = 2.5e+4$, SHEFEX III)



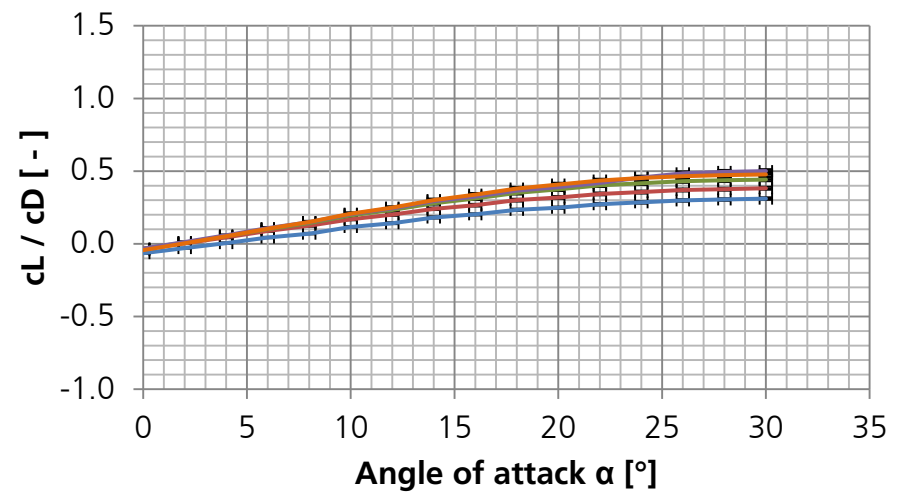
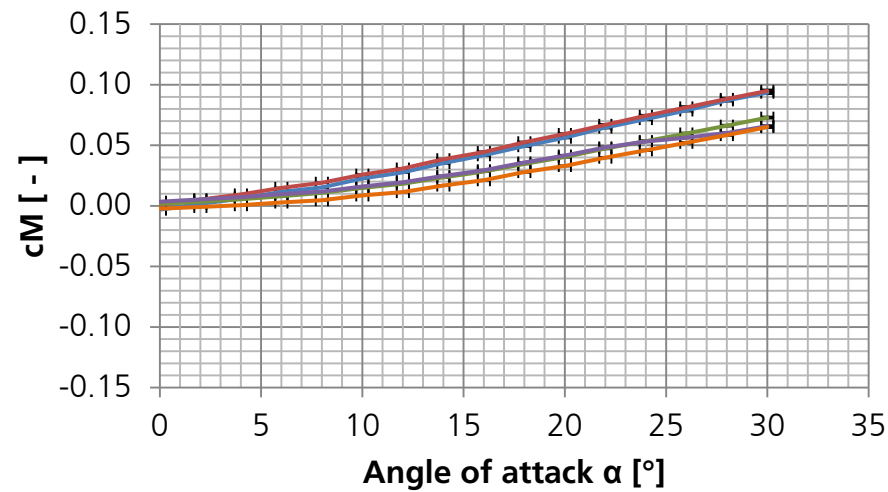
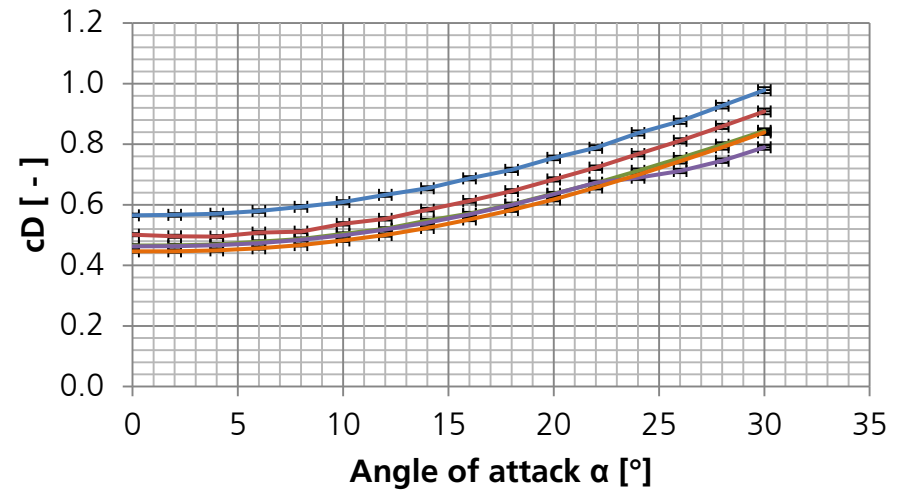
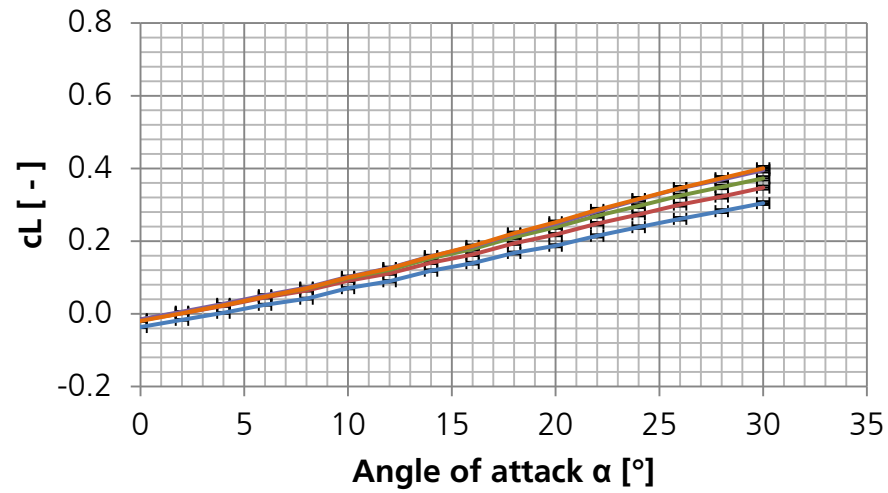
— $Kn_1 = 7.23E-3,$ $M_1 = 23.3$
— $Kn_1 = 6.06E-3,$ $M_1 = 19.4$
— $Kn_1 = 4.49E-3,$ $M_1 = 13.8$
— $Kn_1 = 4.26E-3,$ $M_1 = 12.3$
— $Kn_1 = 3.65E-3,$ $M_1 = 11.2$

Fig. 76: Rarefaction effects on aerodynamic coefficients ($Re_1 = 4.6e+3$, SHEFEX III)



— $Kn_1 = 1.92E-3,$ — $Kn_1 = 8.75E-4,$
 $M_1 = 25.7$ $M_1 = 12.0$

Fig. 77: Rarefaction effects on aerodynamic coefficients ($Re_1 = 2.0e+4$, COLIBRI)



— $Kn_1 = 8.84E-3, M_1 = 23.3$
 — $Kn_1 = 7.41E-3, M_1 = 19.4$
 — $Kn_1 = 5.49E-3, M_1 = 13.8$
 — $Kn_1 = 5.21E-3, M_1 = 12.3$
 — $Kn_1 = 4.47E-3, M_1 = 11.2$

Fig. 78: Rarefaction effects on aerodynamic coefficients ($Re_1 = 3.8e+3$, COLIBRI)

6.1.2 Aerodynamic Coefficients versus Knudsen Number at Constant Angles of Attack

To quantify the effect of rarefaction, it is convenient to plot the aerodynamic coefficients versus the Knudsen number for selected angles of attack. Fig. 79 to Fig. 86 show the results of both test articles at selected angles of attack of 0° , 10° , 20° and 30° . Since Koppenwallner^{[37], [38], [40], [41], [42]} formerly used mainly the rarefaction parameter M/\sqrt{Re} as basis for the evaluation of the V2G experiments in rarefied flow, another set of plots is added where the investigated aerodynamic coefficients are shown based on the rarefaction parameter. Both approaches are compared in chapter 6.1.3. In both approaches, aerodynamic coefficients determined at a constant Reynolds number are connected with solid lines, while the line is disconnected when the Reynolds number is changing, see detail in Fig. 79. In the detailed view the process is illustrated for the case of the lift / drag ratio. Connected solid lines belong to one Reynolds number denoted from Re_1 to Re_5 . The corresponding Knudsen numbers are denoted from $Kn_{\#1}$ to $Kn_{\#5}$ where # refers to the subscript of the corresponding Reynolds number. Since there is only one measurement at Re_5 , it is not connected to any other operating condition and is not regarded in this diagram type.

The plots allow an overview of all experiments performed for the constant Reynolds number analysis by simultaneously highlighting the values obtained at a constant Reynolds number. Although some aerodynamic coefficients show a large scattering especially at larger angles of attack, a clear trend is visible. The question about the Reynolds number influence, which arose from the results of the former measurements performed within FAST20XX, see chapter 1.4, can be answered by analysing these diagrams and is discussed in this chapter.

Fig. 79 shows the aerodynamic coefficients and the lift / drag ratio for the SHEFEX III configuration at an angle of attack of $\alpha = 0^\circ$. For all analysed aerodynamic coefficients a general trend is visible not only within one constant Reynolds number but over the total analysed Knudsen number range from $7.2 \cdot 10^{-4}$ to $7.2 \cdot 10^{-3}$. Although the Reynolds number effect cannot be denied, the Knudsen number is clearly dominating the general behaviour.

As described previously the lift coefficient at $\alpha = 0^\circ$ seems to be hardly influenced by rarefaction effects. Regarding the change of the lift coefficient absolute value at the large Knudsen number condition related to the small Knudsen number condition in percent, however, it turns out that there is a decrease of about 37%. Due to the low absolute value of the lift coefficient compared to, e.g., the drag coefficient, this is not clearly visible. Therefore, the differences of the aerodynamic coefficients between the large Knudsen number and the small Knudsen number are briefly summarised in Table 5.

The drag coefficient significantly increases by 128% with increasing Knudsen number. The absolute value of the lift / drag ratio, which decreases by 72%, is, therefore, dominated by the larger drag increase. The pitching moment change is in percent even more severe and increases by more than 200%.

At higher angles of attack ($\alpha = 10^\circ$), the lift coefficient is in the positive range and shows only a slight decrease with increasing Knudsen number. The behaviour of the drag coefficient is almost unchanged compared to the $\alpha = 0^\circ$ attitude, see Fig. 80. Due to less changes of the lift coefficient, the lift / drag ratio loss decreases to 55%. In Fig. 80 the changes in pitching moment coefficient become clearly visible as it becomes even more positive with increasing Knudsen number.

The trend explained at $\alpha = 10^\circ$ continues at higher angles of attack as Fig. 81 and Fig. 82 for $\alpha = 20^\circ$ and $\alpha = 30^\circ$ show. The values of the lift and drag coefficient are continuously rising with increased angle of attack. Their ratio seems to have a maximum somewhere between $\alpha = 10^\circ$ and $\alpha = 30^\circ$. This is a very rough localisation and is refined in chapter 6.1.5. At high angles of attack of $\alpha \geq 20^\circ$, it can be observed that especially in case of the pitching moment strong interferences occur. The suspicion is that despite of constant Reynolds numbers, determined each at the reference position at 150 mm downstream the nozzle exit on the tunnel axis, the flow gradients are responsible for these strong variations. The effect of the flow gradients is explained in chapter 5.3 and is analysed in detail in chapter 6.3.

The same behaviour can be observed in case of the COLIBRI configuration where a Knudsen number range from $8.8 * 10^{-4}$ to $8.8 * 10^{-3}$ is covered. At low angles of attack, see Fig. 83 for $\alpha = 0^\circ$, the lift coefficient is still in the negative region and experience there, regarded in absolute values, an increase, see Table 5. Responsible is the negative deviation of the lift coefficient at the largest Knudsen number where the consideration is based on.

A clear effect of rarefaction is particularly visible in Fig. 83. The drag coefficient increase reaches here 64%, which is the half of the change, the SHEFEX III configuration experiences at the same angle of attack. However, the absolute COLIBRI drag coefficient values are at $\alpha = 0^\circ$ and the small Knudsen number already more than a factor of two larger than in case of the slender SHEFEX III configuration. The absolute drag coefficient increase of both tested configurations is similar.

The lift / drag ratio at $\alpha = 0^\circ$ remains almost constant at $5 * 10^{-3}$ over the whole analysed Knudsen number range from $8.8 * 10^{-4}$ to $8.8 * 10^{-3}$. The pitching moment coefficient is in this Knudsen number range also nearly unchanged.

Moving on to the $\alpha = 10^\circ$ diagram presented in Fig. 84, it can be seen that the lift coefficient is in the positive range and decreases with increasing Knudsen number. The drag coefficient has over the whole analysed Knudsen number range slightly higher values, while the absolute increase is almost unchanged compared to $\alpha = 0^\circ$. Based on the change in lift and drag coefficient, the aerodynamic efficiency, i.e., the lift / ratio, shows a significant decrease of about 55% within the regarded Knudsen number range, related to the lowest analysed Knudsen number. Concerning the pitching moment coefficient, it can be observed that aside from the increased scattering it becomes more positive over the Knudsen number range.

As in the case of the SHEFEX III configuration, the explained trends for the COLIBRI configuration are continuing to higher angles of attack too. Especially in case of the pitching moment coefficients, but also in case of the other aerodynamic coefficients, the

scattering increases with increasing angle of attack, see $\alpha = 20^\circ$ and $\alpha = 30^\circ$ in Fig. 85 and Fig. 86 respectively.

From that it can be found that the percentage effect of rarefaction on the aerodynamic coefficients for both test configurations is, except the COLIBRI $\alpha = 0^\circ$ condition, always larger in case of the drag compared to the lift at the investigated angles of attack of $\alpha \leq 30^\circ$. The trend indicates a change at higher angles of attack, since the percentage lift coefficient change increases, while the percentage drag coefficient change decreases with increasing angle of attack, see Table 5.

Table 5: Changes of aerodynamic coefficients between maximum (2) and minimum (1) Knudsen number

α	SHEFEX III				COLIBRI			
	$cL_2 - cL_1$	$cD_2 - cD_1$	$cM_2 - cM_1$	$(cL_2/cD_2) - (cL_1/cD_1)$	$cL_2 - cL_1$	$cD_2 - cD_1$	$cM_2 - cM_1$	$(cL_2/cD_2) - (cL_1/cD_1)$
0°	2.4E-02 -37%	1.7E-01 128%	7.8E-03 203%	3.6E-01 -72%	-1.6E-02 77%	2.2E-01 64%	-8.3E-04 37%	-4.5E-03 8%
10°	-3.8E-03 -3%	1.7E-01 117%	1.8E-02 -115%	-4.5E-01 -55%	-2.6E-02 -27%	2.4E-01 63%	2.0E-02 637%	-1.4E-01 -55%
20°	-3.0E-02 -10%	1.5E-01 63%	3.0E-02 -104%	-5.7E-01 -45%	-8.1E-02 -30%	2.5E-01 49%	3.0E-02 111%	-2.8E-01 -53%
30°	-6.7E-02 -13%	1.6E-01 35%	3.0E-02 -138%	-4.1E-01 -35%	-1.4E-01 -31%	2.4E-01 32%	3.3E-02 54%	-2.8E-01 -48%

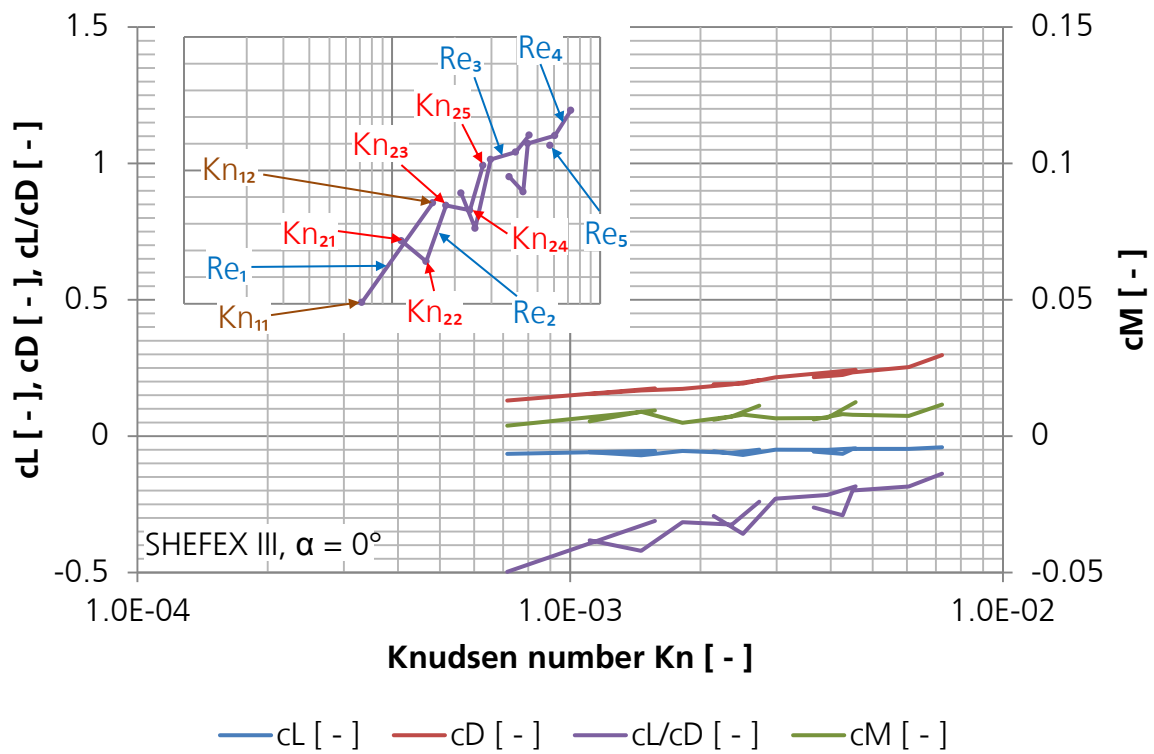


Fig. 79: Rarefaction effects on aerodynamic coefficients shown vs. Knudsen number (SHEFEX III, $\alpha = 0^\circ$)

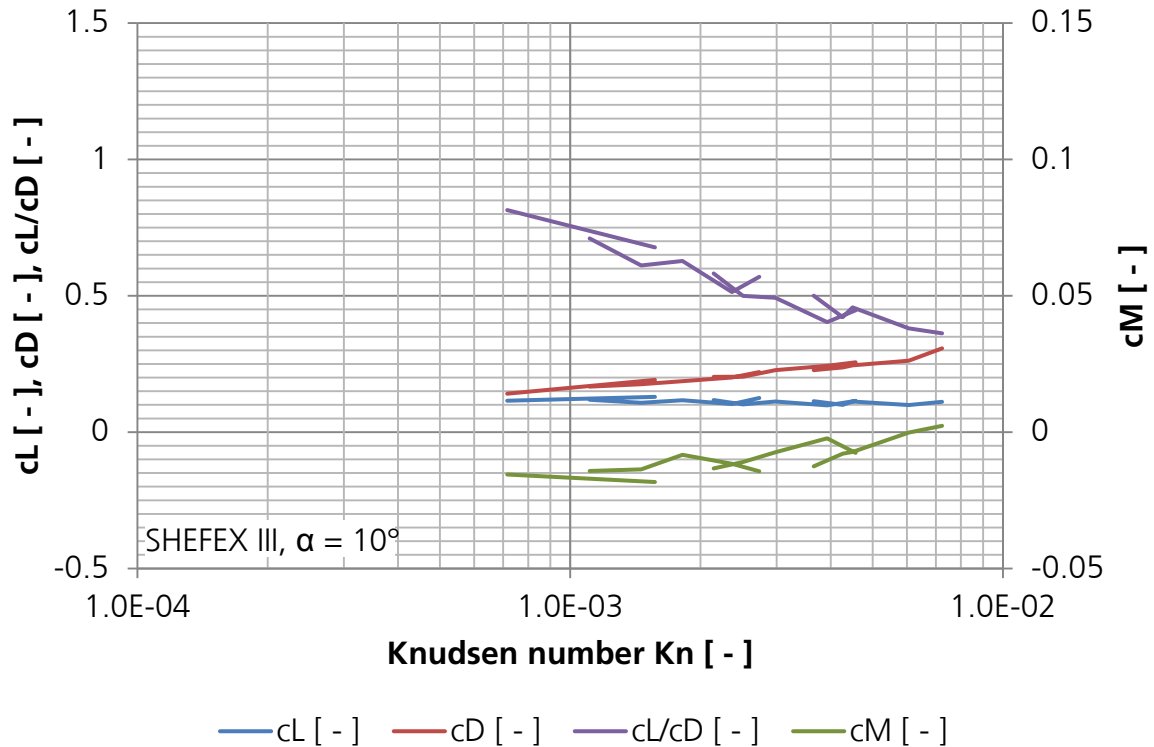


Fig. 80: Rarefaction effects on aerodynamic coefficients shown vs. Knudsen number (SHEFEX III, $\alpha = 10^\circ$)

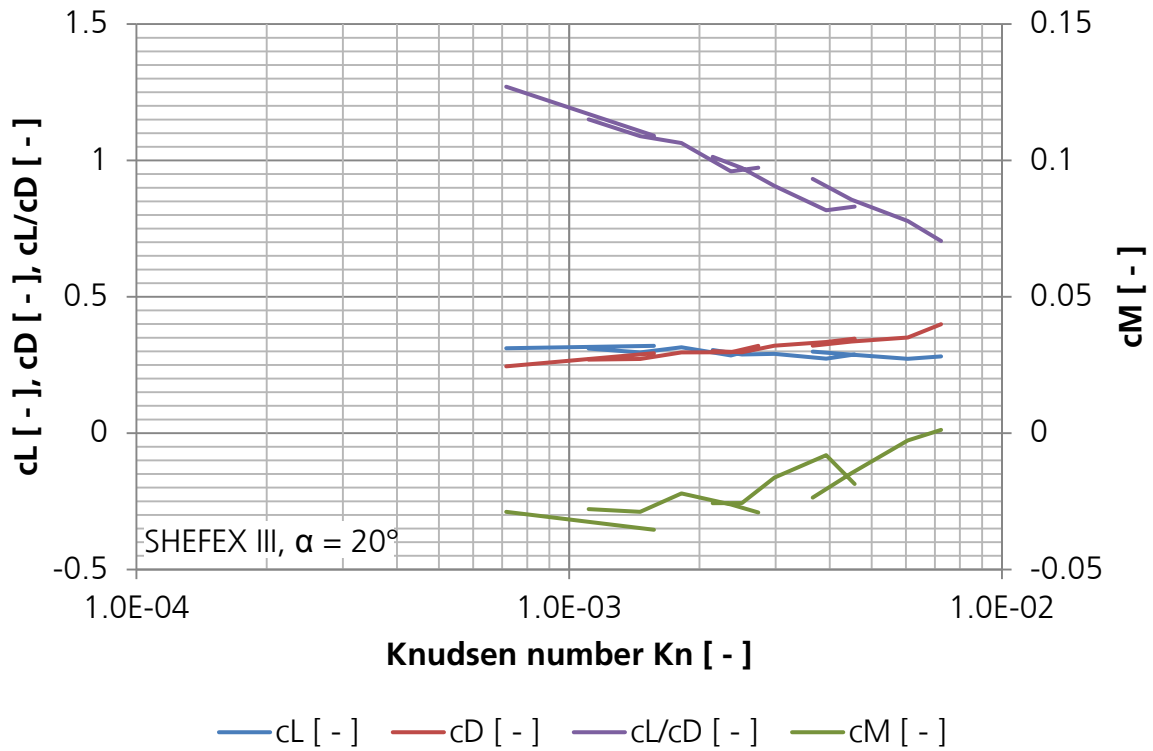


Fig. 81: Rarefaction effects on aerodynamic coefficients shown vs. Knudsen number (SHEFEX III, $\alpha = 20^\circ$)

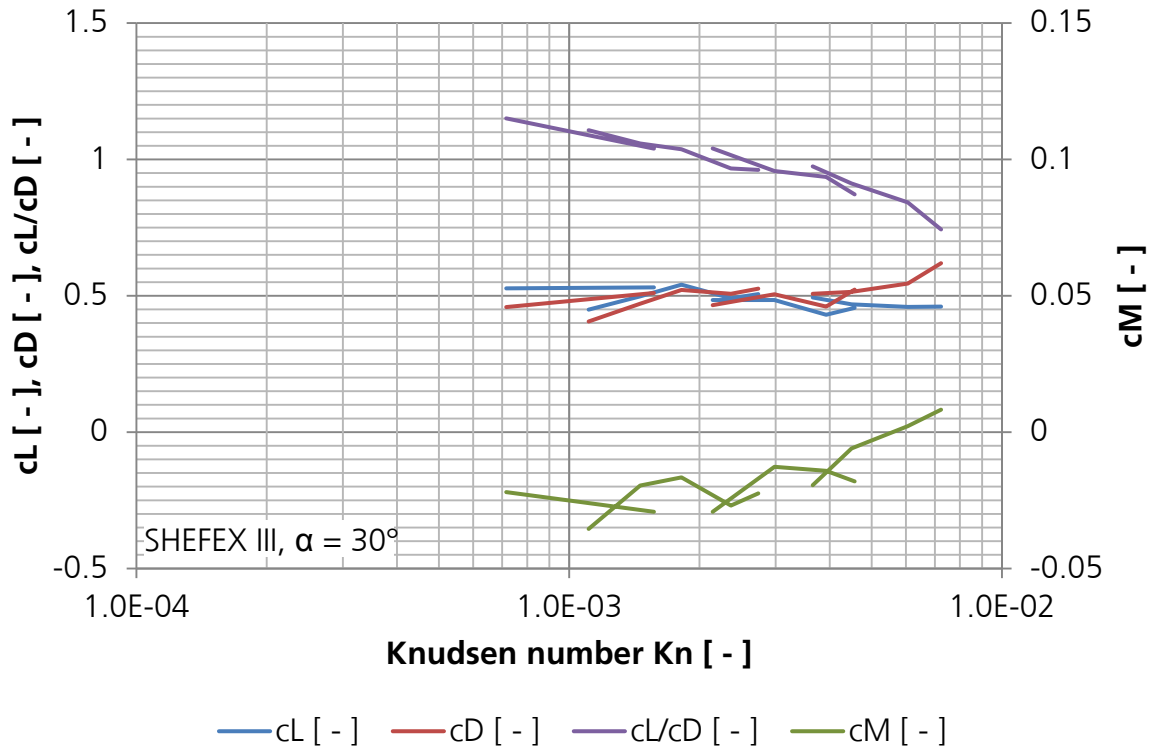


Fig. 82: Rarefaction effects on aerodynamic coefficients shown vs. Knudsen number (SHEFEX III, $\alpha = 30^\circ$)

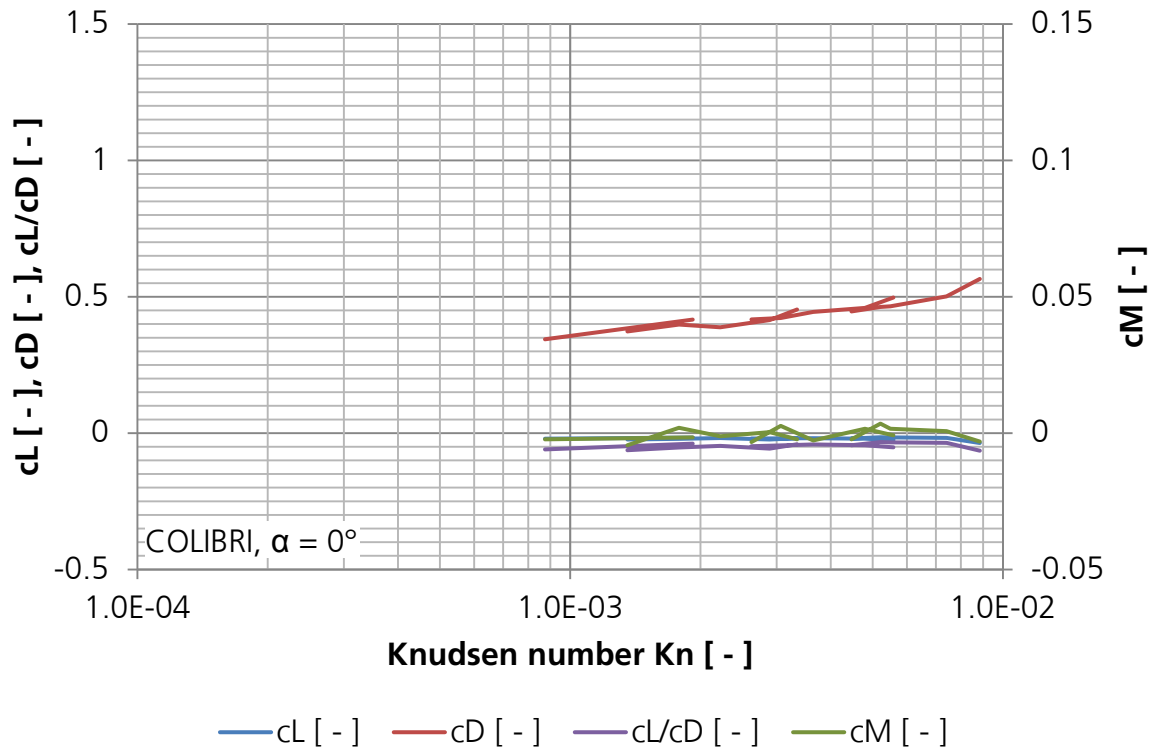


Fig. 83: Rarefaction effects on aerodynamic coefficients shown vs. Knudsen number (COLIBRI, $\alpha = 0^\circ$)

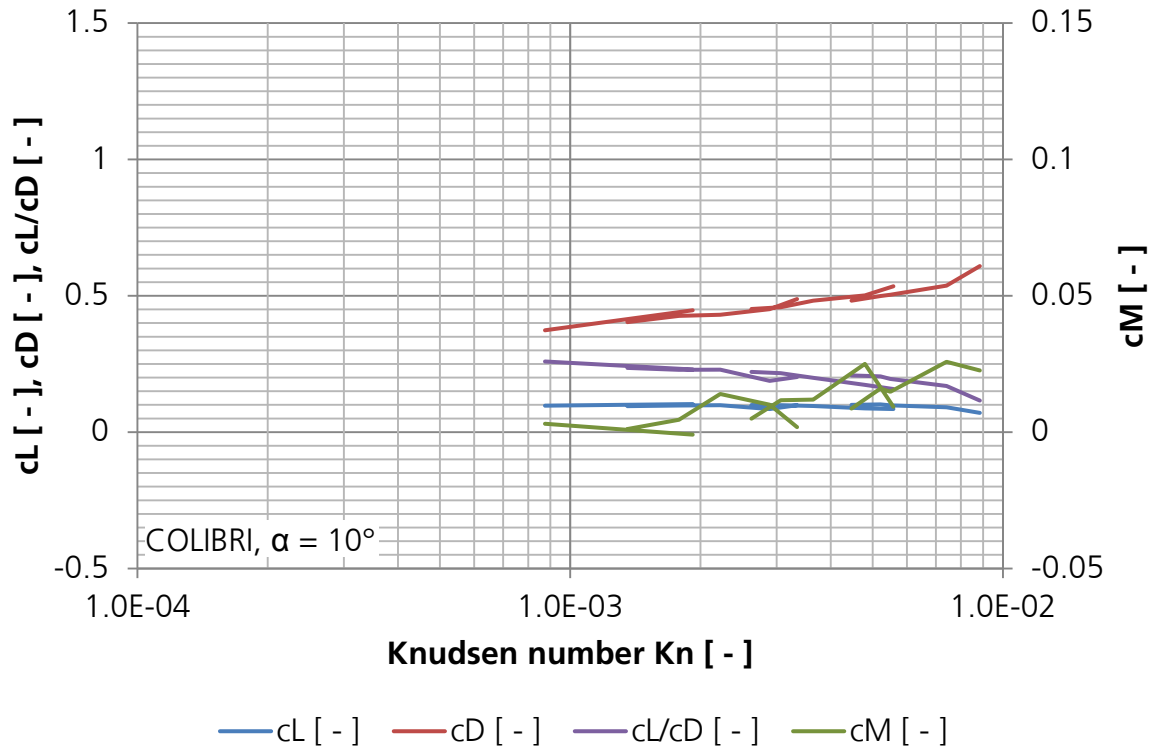


Fig. 84: Rarefaction effects on aerodynamic coefficients shown vs. Knudsen number (COLIBRI, $\alpha = 10^\circ$)

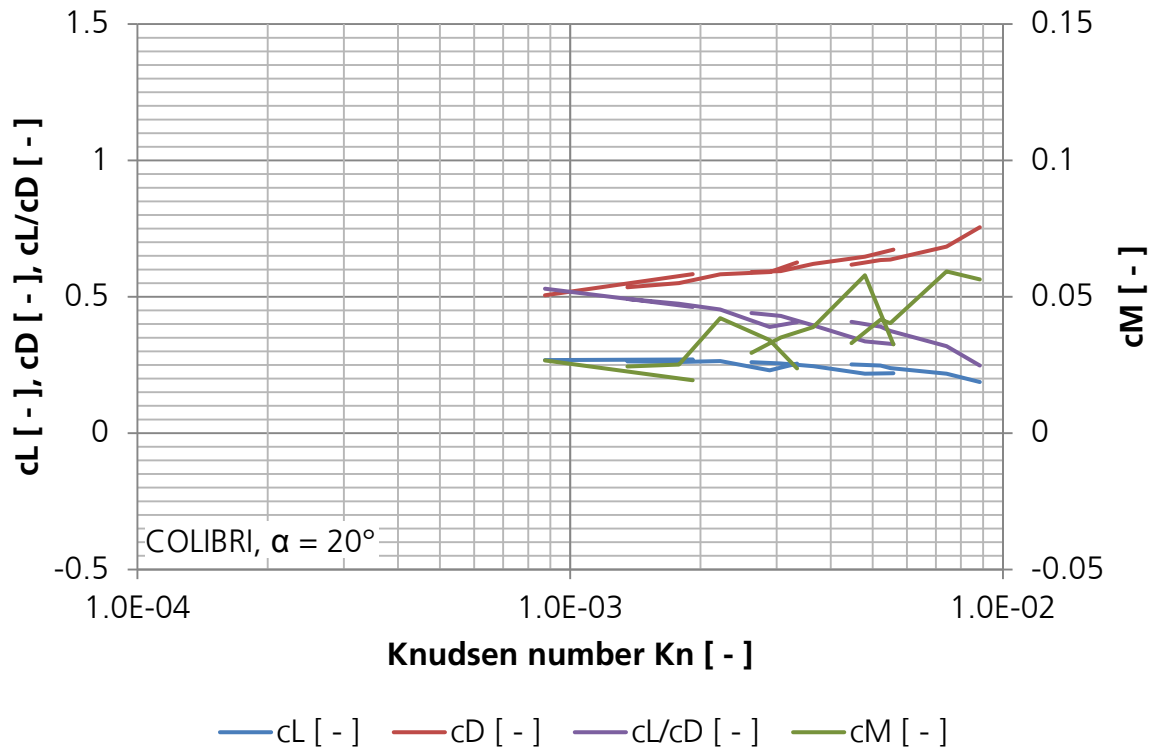


Fig. 85: Rarefaction effects on aerodynamic coefficients shown vs. Knudsen number (COLIBRI, $\alpha = 20^\circ$)

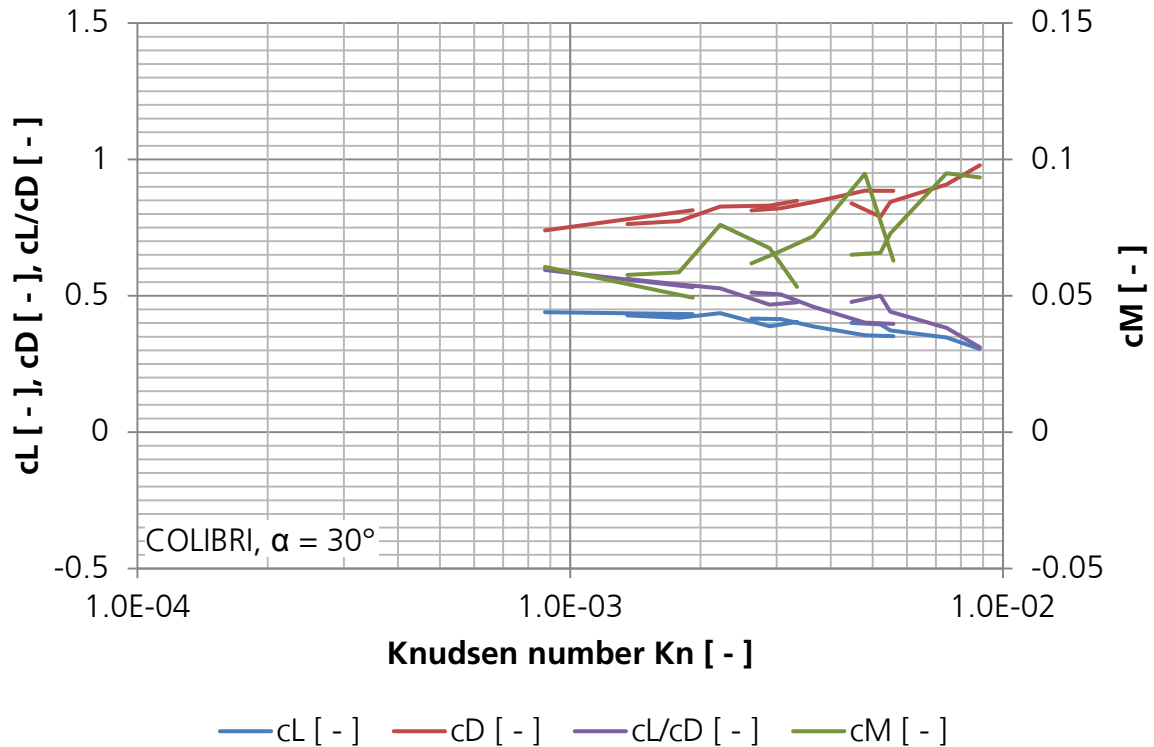


Fig. 86: Rarefaction effects on aerodynamic coefficients shown vs. Knudsen number (COLIBRI, $\alpha = 30^\circ$)

Summing up it can be stated that for both test configurations:

1. at low angles of attack ($0^\circ \leq \alpha \leq 10^\circ$), the rarefaction effect on the drag coefficient in percent is larger, compared to the effect on the lift coefficient (see Table 5 and compare almost constant lift coefficient versus increase in drag coefficient in Fig. 79 / Fig. 80 and Fig. 83 / Fig. 84).
2. at high angles of attack ($20^\circ \leq \alpha \leq 30^\circ$), the rarefaction effect on lift and drag coefficient in percent become more similar and indicate, that for $\alpha > 30^\circ$ the lift coefficient might be even more affected by rarefaction (see Table 5 and Fig. 81 / Fig. 82 and Fig. 85 / Fig. 86)

This constellation indicates that rarefaction is affecting pressure and friction forces differently. To illustrate this consideration lift and drag forces are separated into normally F_n and tangentially F_t acting forces, i.e. pressure and friction forces respectively, see Fig. 87.

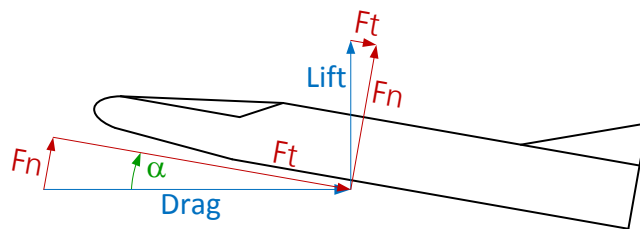


Fig. 87: Normal and tangential fractions of lift and drag (at the wall)

While the drag is composed of a pressure part from the projected frontal area and a friction part from the tangential forces at the wall, the lift is strongly dominated by the pressure part and has an almost negligible friction part at low angles of attack. At higher angles of attack where the friction part on the lift becomes noticeable, the effect is not as strong anymore.

The stronger rarefaction effect on the drag coefficient compared to the lift coefficient at already low Knudsen numbers is attributed to less decrease of friction forces, compared to the stronger decreasing pressure forces. Since the friction part of the drag is in percent larger for slender configurations, it is expected that the effects are stronger for the slender SHEFEX III compared to the blunt COLIBRI. This is true and is discussed in chapter 6.1.5. Koppenwallner^[41] explains the percentage increase of drag forces with an increased viscosity effect when $M/\sqrt{Re} > 0.01$ which is true in all investigated cases.

An explanation can be found when regarding the gas molecule body surface interaction. In practice, usually the diffuse reflection is observed.^[45] Since in the continuum limit, the molecule-molecule interaction is far greater than the molecule-wall interaction, the average reflection behaves like a mirrored reflection. This leads to the Newtonian pressure distribution where the momentum is solely dependent on the surface angle. In free molecular flow in contrast, the molecule-wall interaction becomes more and more dominant and the single molecule reflections have to be treated independently. Consequently, the diffuse reflection becomes dominant. Due to the adsorption, the whole momentum of the molecules is transferred to the surface which explains the increased ratio of friction to pressure forces with increasing rarefaction. Since only integral forces on the test configuration are measured within this work, a separation in drag and friction force fractions during the evaluation is not possible. This question should be addressed numerically where a separation of drag and friction forces is easier possible.

6.1.3 Aerodynamic Coefficients versus Rarefaction Parameter at Constant Angles of Attack

Turning towards the plots showing aerodynamic coefficients versus the rarefaction parameter, it can be seen that both approaches lead to similar characteristics. In case of the rarefaction parameter based plots, the results of different Reynolds numbers appear more compressed due to larger overlapping along the diagram's x-axis.

In case of the slender SHEFEX III configuration at $\alpha = 0^\circ$, the results of the drag coefficient show a better agreement between different Reynolds numbers when plotted versus the Knudsen number (see Fig. 79) instead of the rarefaction parameter (see Fig. 88) where slight offsets are visible. In turn when regarding the lift / drag ratio, the plot versus the rarefaction parameter shows a slightly clearer trend. The lift and pitching moment coefficients show no significant difference. At higher angles of attack at $\alpha = 10^\circ$ (compare Fig. 80 with Fig. 89) and $\alpha = 20^\circ$ (compare Fig. 81 with Fig. 90), the Knudsen number based drag coefficient shows still a slightly better trend between different Reynolds numbers, however, decreases with increasing angle of attack. While lift and pitching moment coefficients show no significant difference between plots versus Knudsen number or rarefaction parameter, the rarefaction parameter based lift / drag ratio reveals large offsets between different Reynolds numbers. At the largest analysed angle of attack, at $\alpha = 30^\circ$ (see Fig. 91), the offsets in the lift / drag ratio decrease but remain larger than in plots versus the Knudsen number, see Fig. 82. Due to larger overlapping between experiments at different Reynolds numbers in the plot versus the rarefaction parameter, the pitching moment coefficient results can be rather interpreted as random scattering than along a curve.

Regarding the blunt COLIBRI configuration, the differences between the plots versus the Knudsen number and the plots versus the rarefaction parameter are not as clear as in case of the slender SHEFEX III configuration. Especially at low angles of attack at $\alpha = 0^\circ$ (compare Fig. 83 with Fig. 92) and $\alpha = 10^\circ$ (compare Fig. 84 with Fig. 93) both approaches show similar good agreements over all regarded aerodynamic coefficients. At higher angles of attack at $\alpha = 20^\circ$ (compare Fig. 85 with Fig. 94) and $\alpha = 30^\circ$ (compare Fig. 86 with Fig. 95), the plots versus the Knudsen number show, with the angle of attack increasing, offsets between the aerodynamic coefficients measured at different Reynolds numbers. Mainly the drag coefficient and lift / drag ratio are affected but also slightly the lift coefficient. The pitching moment coefficient in turn shows a more distinct trend in the plots versus the Knudsen number.

Generally, it can be summarised that the trends of how aerodynamic coefficients are affected by rarefaction are slightly more distinct in plots versus Knudsen number in case of the slender SHEFEX III configuration. In case of the blunt COLIBRI configuration, trends are visible slightly clearer when plotted versus the rarefaction parameter. This is understandable since the slender SHEFEX III configuration experiences rarefaction effects at the same operating condition earlier than the blunt COLIBRI configuration. Recalling, that Schaaf & Chambré^[73] used the rarefaction parameter to distinguish the transition regime between continuum and rarefied flow, and the Knudsen number to describe the rarefied flow, confirms the result additionally.

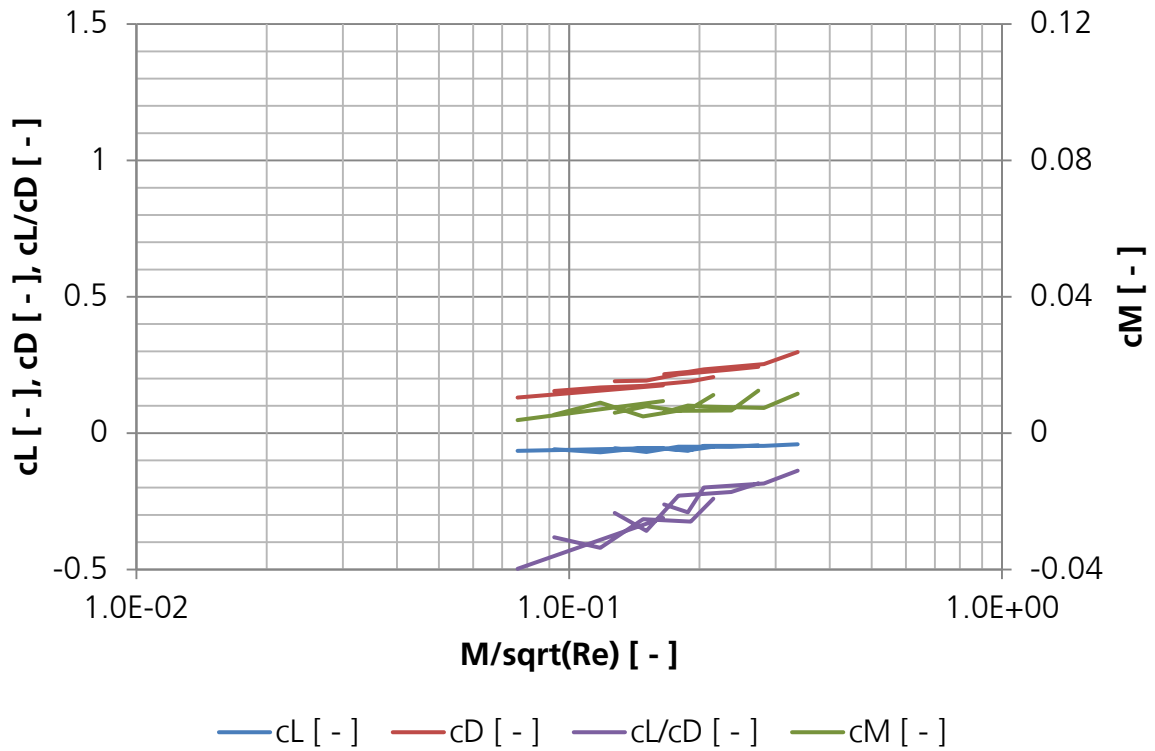


Fig. 88: Rarefaction effects on aerodynamic coefficients shown vs. rarefaction parameter (SHEFEX III, $\alpha = 0^\circ$)

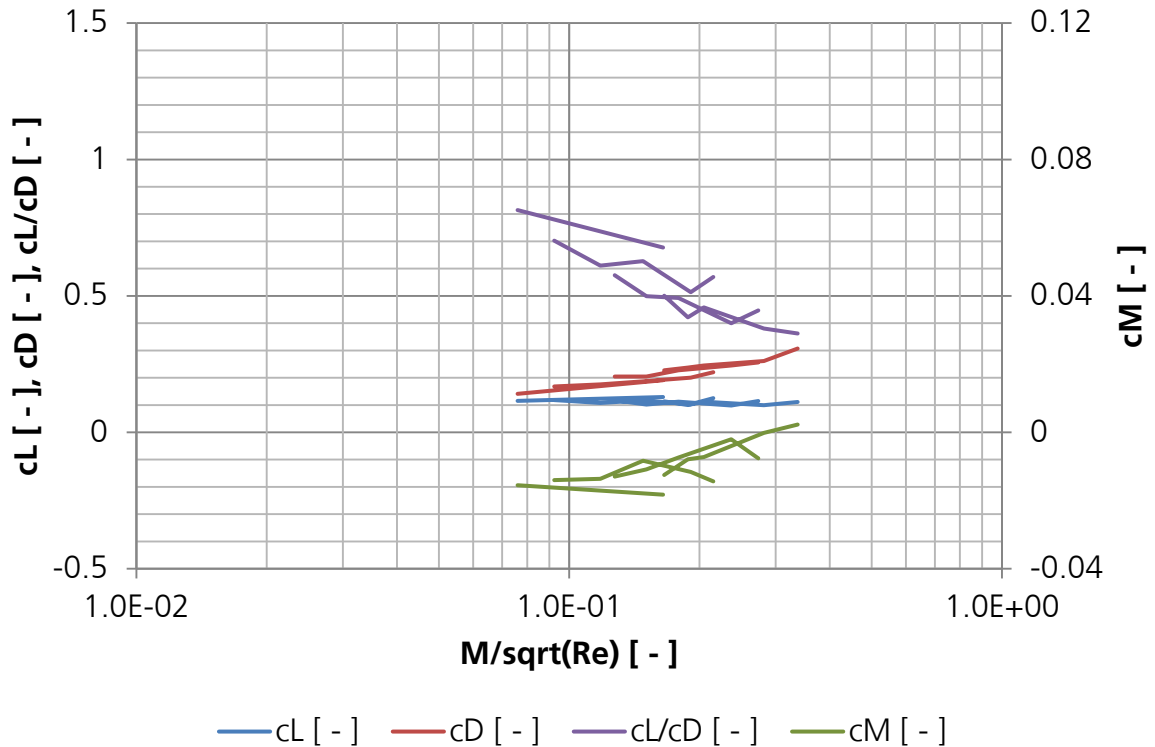


Fig. 89: Rarefaction effects on aerodynamic coefficients shown vs. rarefaction parameter (SHEFEX III, $\alpha = 10^\circ$)

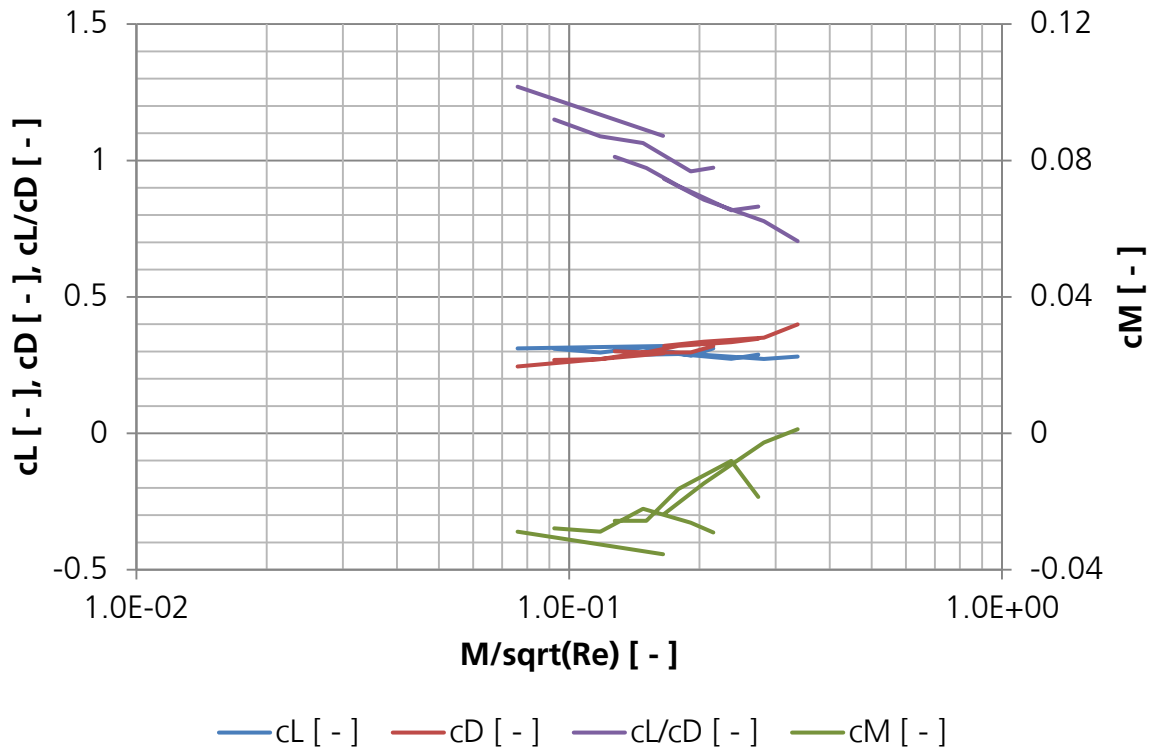


Fig. 90: Rarefaction effects on aerodynamic coefficients shown vs. rarefaction parameter (SHEFEX III, $\alpha = 20^\circ$)

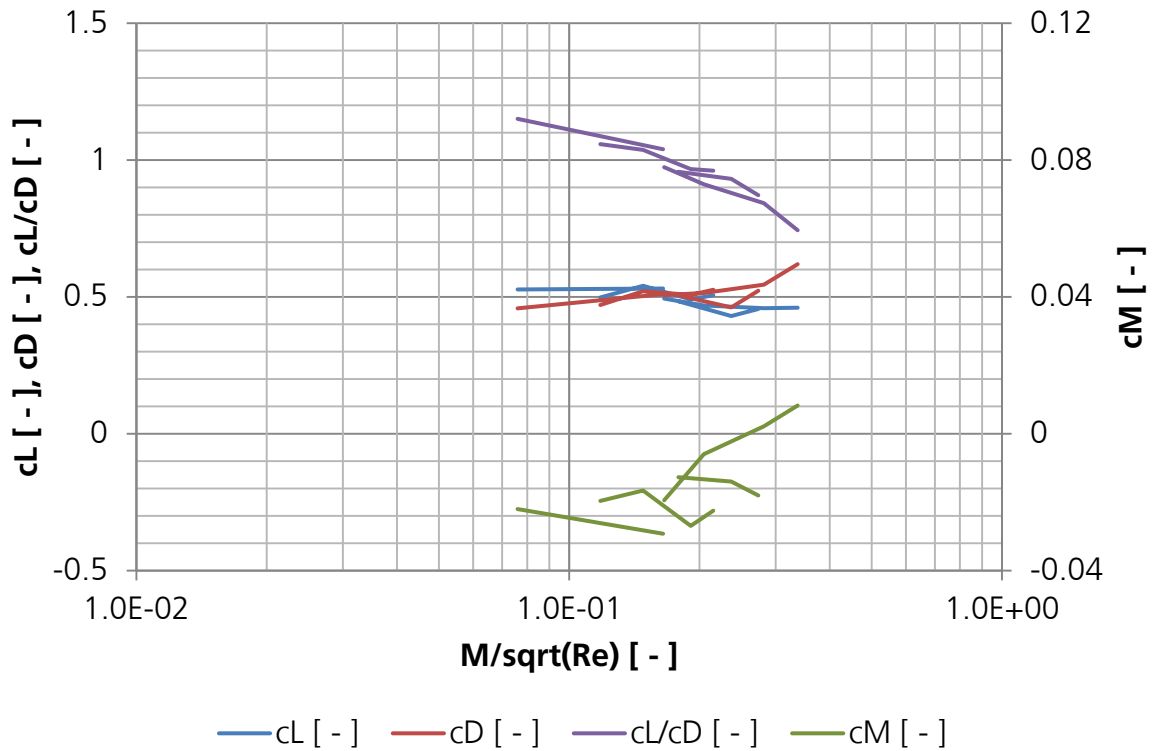


Fig. 91: Rarefaction effects on aerodynamic coefficients shown vs. rarefaction parameter (SHEFEX III, $\alpha = 30^\circ$)

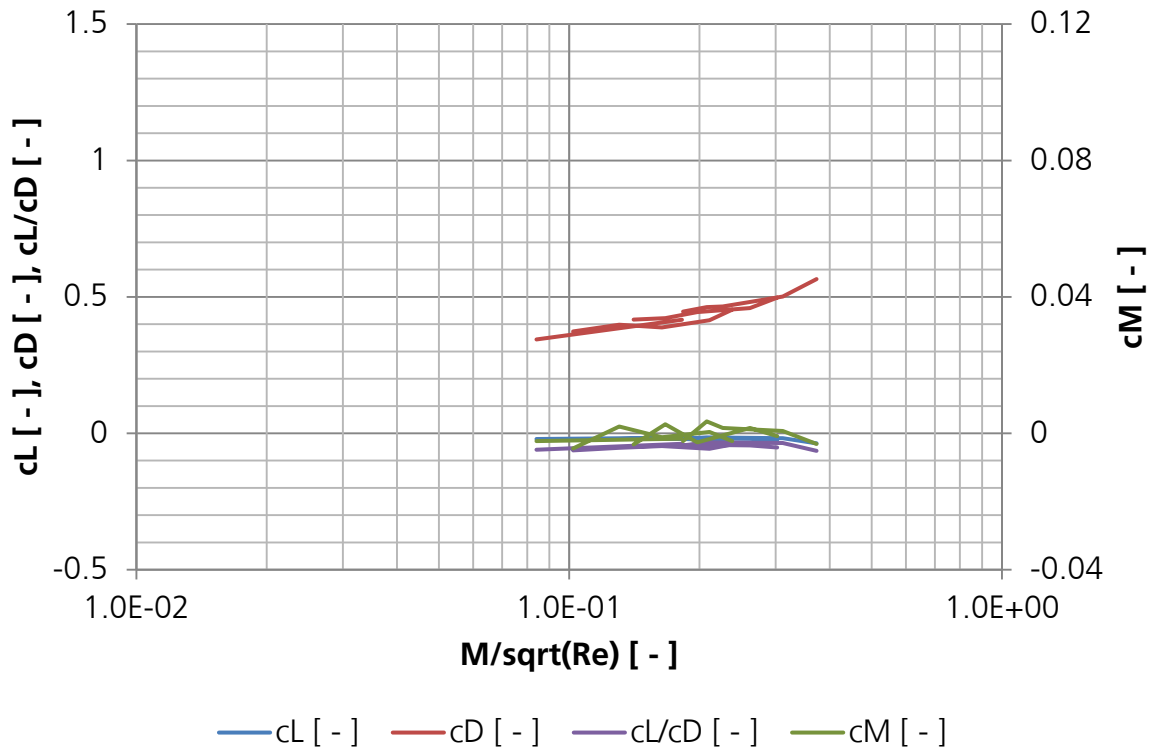


Fig. 92: Rarefaction effects on aerodynamic coefficients shown vs. rarefaction parameter (COLIBRI, $\alpha = 0^\circ$)

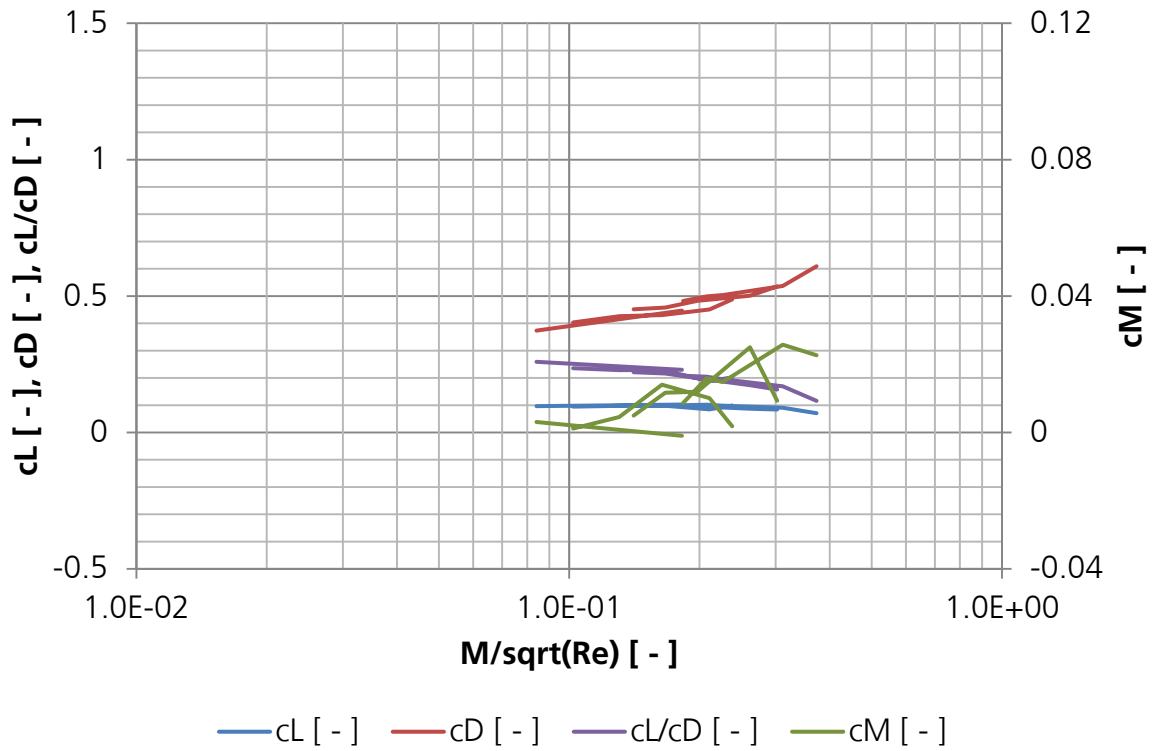


Fig. 93: Rarefaction effects on aerodynamic coefficients shown vs. rarefaction parameter (COLIBRI, $\alpha = 10^\circ$)

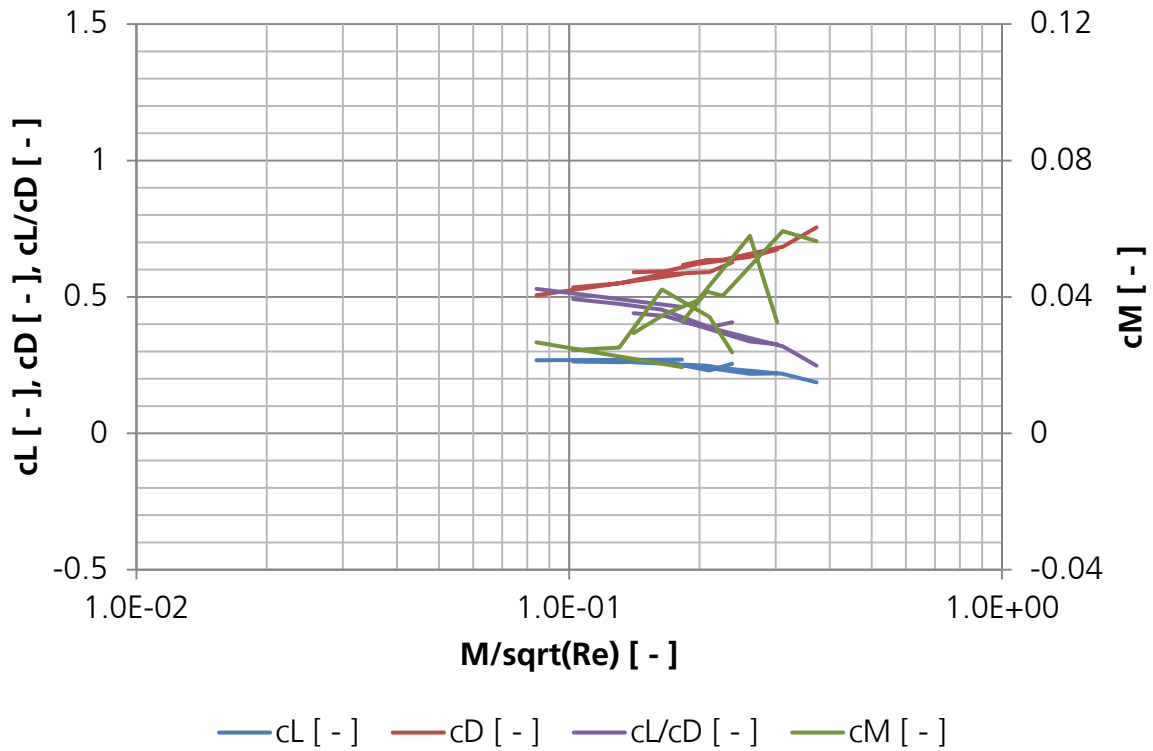


Fig. 94: Rarefaction effects on aerodynamic coefficients shown vs. rarefaction parameter (COLIBRI, $\alpha = 20^\circ$)

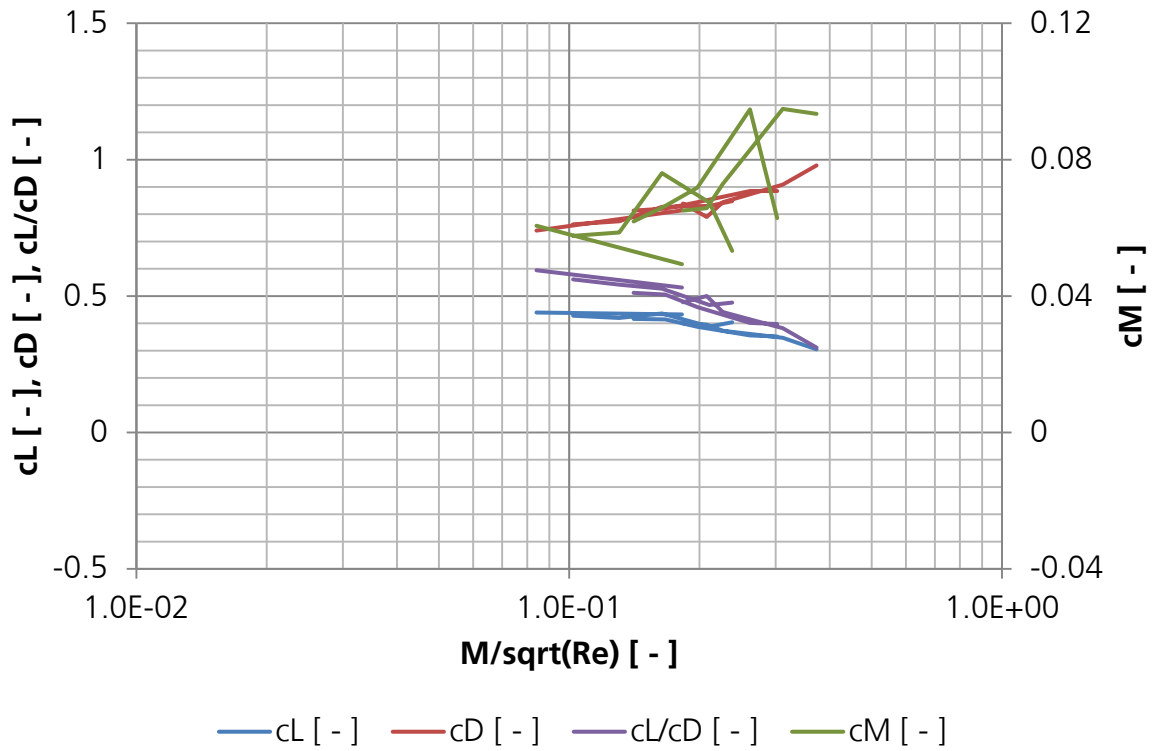


Fig. 95: Rarefaction effects on aerodynamic coefficients shown vs. rarefaction parameter (COLIBRI, $\alpha = 30^\circ$)

6.1.4 Assessing Mach and Reynolds Number Effects

The trends of the aerodynamic coefficients plotted versus both Knudsen number and rarefaction parameter yield similar good results, so that it is justified to select one parameter for both test configurations to allow a direct comparison between both test configurations. Since the applicability of the Mach number independency principle has to be assessed in case of the slender SHEFEX III configuration at low angles of attack (see chapter 2.4), the plots versus Knudsen number are selected.

The diagrams, shown in Fig. 79 / Fig. 80 and Fig. 83 / Fig. 84, are suitable to assess the Mach number effects and the applicability of Mach number independence principle in case of the slender SHEFEX III configuration at low angles of attack. For that purpose the diagram setup from Fig. 79 to Fig. 86 is used where the aerodynamic coefficients are plotted versus the Knudsen number. For this analysis, however, the aerodynamic coefficients measured at operating conditions with high Mach numbers are connected with a solid line, while the aerodynamic coefficients measured at operating conditions with low Mach numbers are connected with a dotted line, see Fig. 96 to Fig. 99. When the Mach number independence principle is not applicable or has limited applicability only in case of the slender SHEFEX III geometry, one would expect differences between the aerodynamic coefficients measured at high and low Mach numbers, hence, between solid and dotted lines, see Fig. 96 and Fig. 97, which exceed the differences between those in case of the blunt COLIBRI configuration, see Fig. 98 and Fig. 99.

Although the boundary layer thickness is inordinately increasing with Mach number squared (2-6), as explained in chapter 2.4, the results show that the differences between high and low Mach numbers are similar in case of both configurations. Therefore, the Mach number effects are considered as small, such that the Mach number independence principle can be applied to the slender SHEFEX III configuration at low angles of attack as well within the measurement accuracy. The existence of Mach number effects cannot be excluded but they are not of significant importance in the performed analyses.

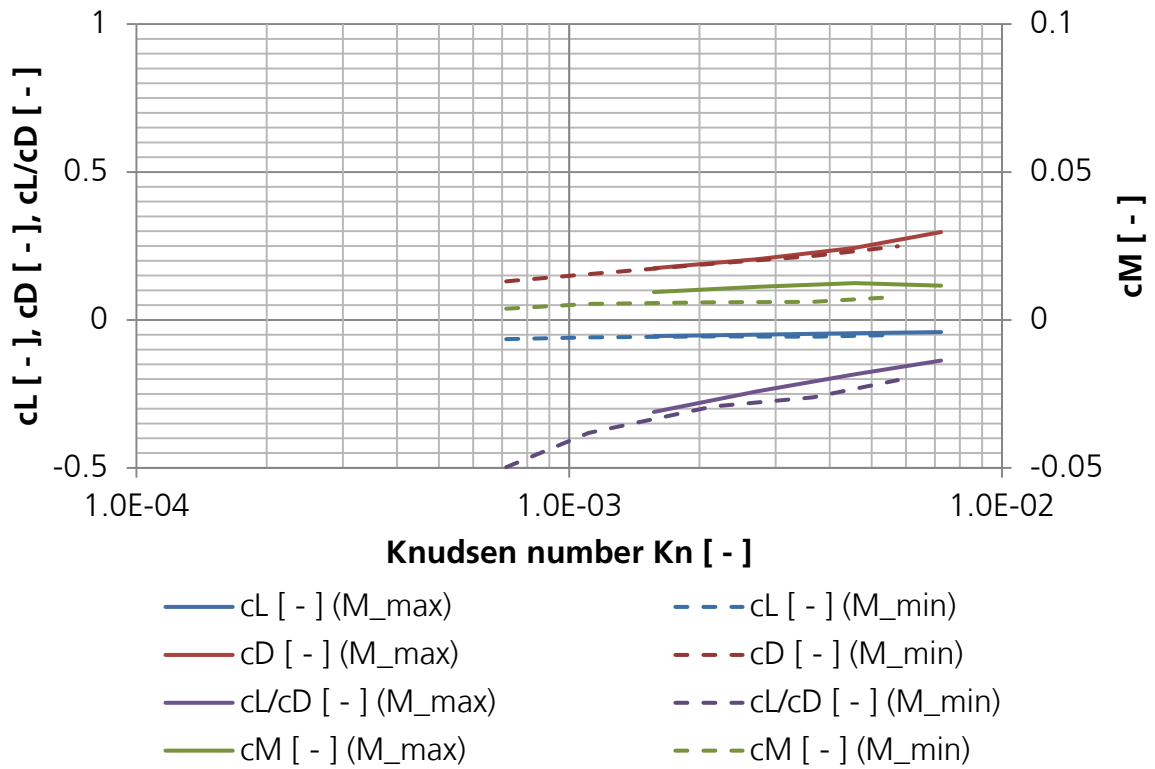


Fig. 96: Mach number effects on aerodynamic coefficients (SHEFEX III, $\alpha = 0^\circ$)

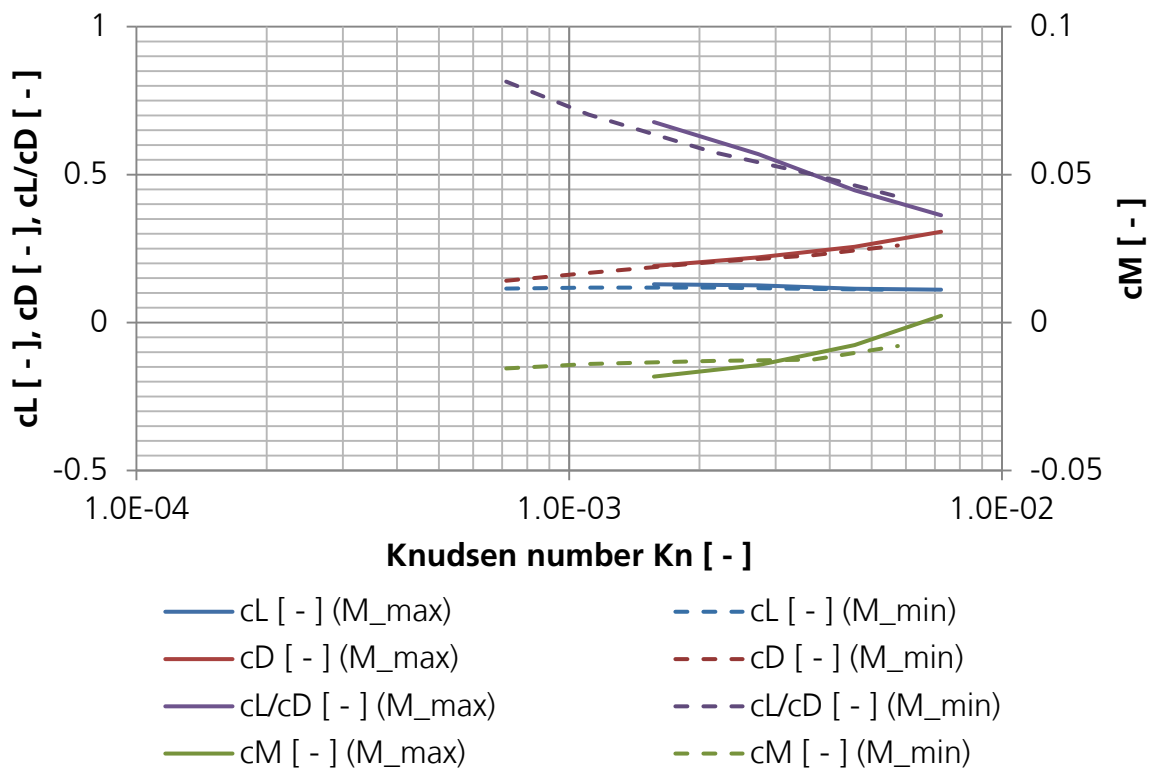


Fig. 97: Mach number effects on aerodynamic coefficients (SHEFEX III, $\alpha = 10^\circ$)

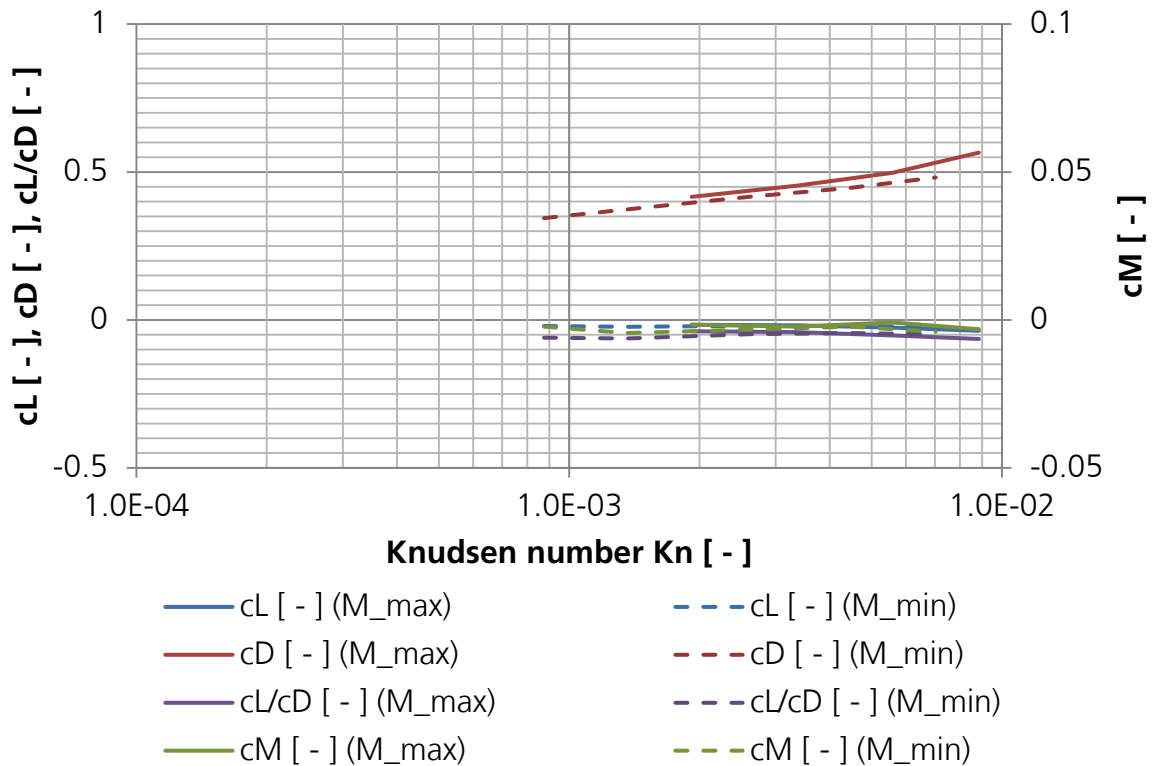


Fig. 98: Mach number effects on aerodynamic coefficients (COLIBRI, $\alpha = 0^\circ$)

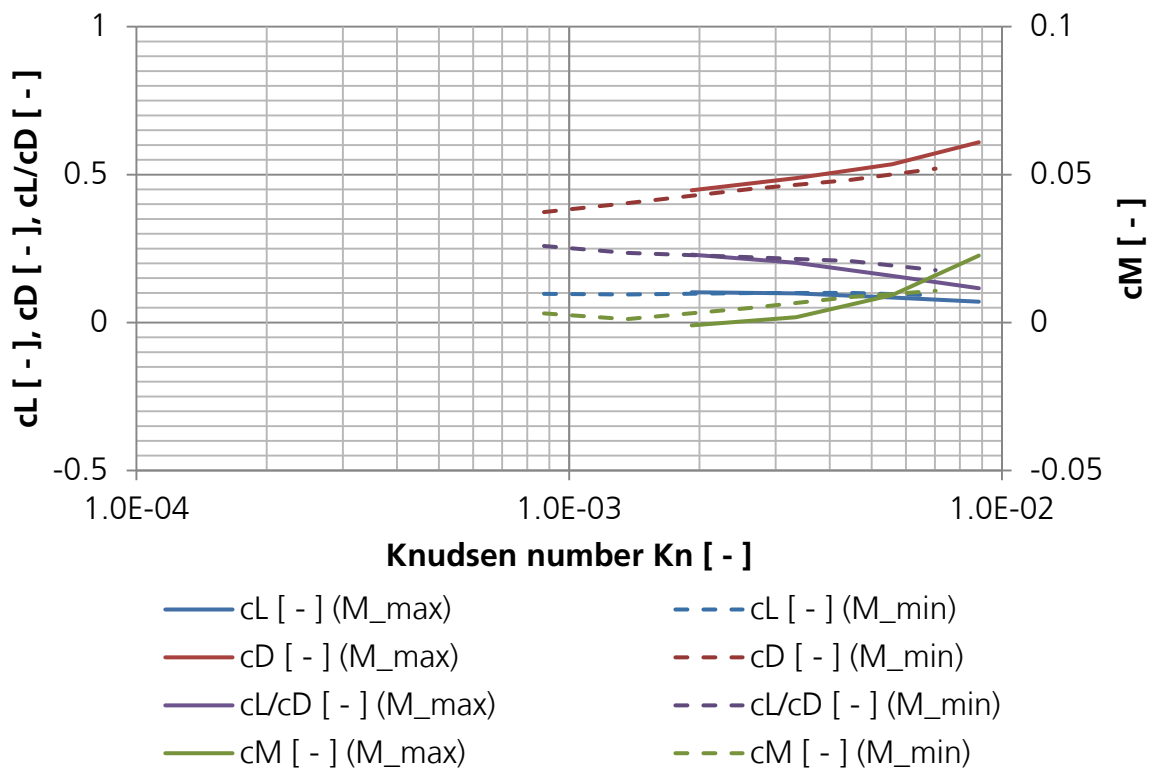


Fig. 99: Mach number effects on aerodynamic coefficients (COLIBRI, $\alpha = 10^\circ$)

Concluding it can be said that in all presented figures (Fig. 79 to Fig. 86) the effect of the Reynolds number influence, i.e., the scattering between connected points related to the trend, see Fig. 100, is visible but it is small compared to the Knudsen number influence. With increasing angle of attack this effect increases. An exception are here the pitching moment coefficients at higher angles of attack where the overlaying effects of Reynolds number influence and axial flow gradients are rising significantly for both test configurations. However, for a clear assignment numerical investigations are essential. Due to the uneven characteristics, probably caused by flow gradients within one constant Reynolds number analysis which are based on up to five points only, it is not possible to compensate the effect based on the present data. Further experiments adding more data to the defined Reynolds numbers would increase the resolution in the diagrams and could allow a compensation of the Reynolds number effects. Complementary numerical investigations can help here significantly to distinguish the source of the observed effects.

It can be seen that the analysis of the COLIBRI test configuration covers slightly higher Knudsen numbers from $8.8 \cdot 10^{-4}$ to $8.8 \cdot 10^{-3}$, compared to $7.2 \cdot 10^{-4}$ to $7.2 \cdot 10^{-3}$ for SHEFEX III due to its lower reference length. However, in the major part both Knudsen number ranges are overlapping. In both cases the aim to analyse a full order of magnitude in Knudsen number could be realised.

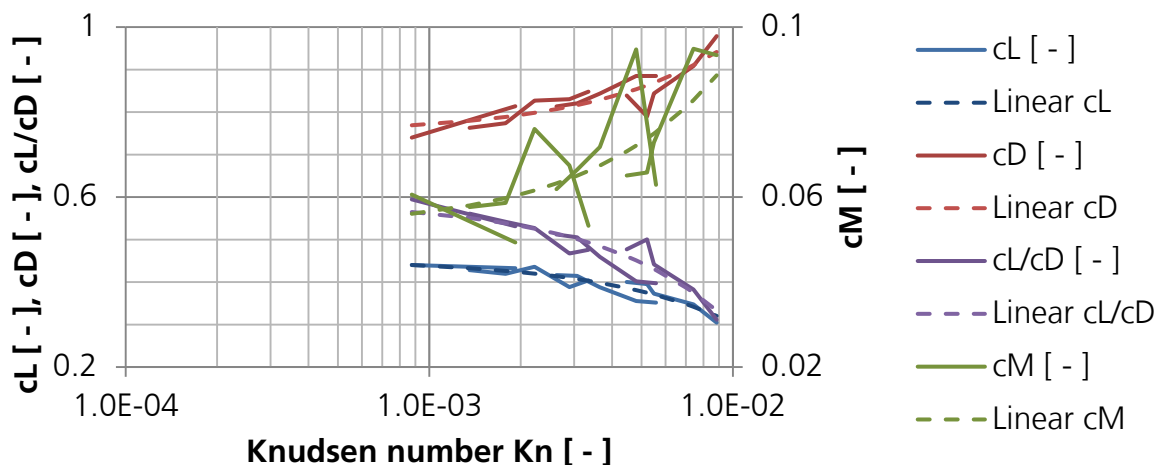


Fig. 100: Rarefaction effects on aerodynamic coefficients approximated with linear regression line for COLIBRI, $\alpha = 30^\circ$

6.1.5 Comparing Effects of Rarefaction of Both Test Configurations

In a further step it is now possible to analyse how much the aerodynamic coefficients are affected by increasing rarefaction. For that purpose the results shown in Fig. 79 to Fig. 86 are primarily approximated with a linear regression line, see Fig. 100. Subsequently, the values are calculated at the highest and lowest analysed Knudsen number. The ratio of the aerodynamic coefficients, determined at the maximum analysed Knudsen number to the aerodynamic coefficients determined at the minimum measured Knudsen number, is visualised in Fig. 101 to Fig. 104, i.e., the shown change corresponds to rarefaction effects over one order of magnitude of Knudsen number, for

SHEFEX III from $7.2 * 10^{-4}$ to $7.2 * 10^{-3}$ and for COLIBRI from $8.8 * 10^{-4}$ to $8.8 * 10^{-3}$ respectively. The black chain line indicates the factor of one and, hence, no effect.

For these plots the whole available data set is used to obtain the initially measured resolution in 2° steps, while only selected angles of attack are shown in Fig. 79 to Fig. 86. If the ratio is larger than one it describes that the aerodynamic coefficient is increasing with increasing Knudsen number, if it is smaller the aerodynamic coefficient is respectively decreasing. A value of one means no effect of rarefaction. Except for the drag coefficient ratio, there is a strong oscillation in the range between $0^\circ \leq \alpha \leq 10^\circ$ visible, which is caused by aerodynamic coefficients close to zero. Since the linear trend is a rough approximation, it is difficult to interpret the ratio when the aerodynamic coefficients become close to zero, especially when the scattering is large.

Concerning the lift coefficient, presented in Fig. 101, it can be seen that beyond the oscillation region at low angles of attack, the ratio is at angles of attack of $6^\circ \leq \alpha \leq 30^\circ$ nearly at a constant level below one in case of both test article configurations. Obviously that means that there is a distinct rarefaction influence on the lift coefficient which is small and difficult to visualise in the earlier presented plots. The rarefaction influence on the lift coefficient of the blunt COLIBRI configuration is consistently lower, between 20% and 30%, and, hence, decreasing slightly stronger, see Fig. 101. In case of the slender SHEFEX III configuration the reduction is between 10% and 20%.

The rarefaction influence on the drag coefficient, shown in Fig. 102, is for low angles of attack stronger and decreases at higher angles of attack. In case of the SHEFEX III test configuration, there is almost a factor of 2 between the drag coefficients at the large and small Knudsen number condition at angles of attack of about 4° , where the configuration is aerodynamically slender. In case of the COLIBRI configuration, this factor reaches a maximum of 1.5. Above $\alpha = 4^\circ$ the rarefaction caused drag coefficient increase is reduced but remains above 20% at angles lower than $\alpha = 30^\circ$. The percentage decrease, shown in Fig. 102, is caused by the increasing drag coefficient value at increasing angles of attack, while the absolute changes remain almost constant at the same size independent of the angle of attack. Considering that the investigated Knudsen numbers are in the rarefied regime but still close to continuum, these results are particularly remarkable. Such a drag coefficient increase has a strong impact on the flight characteristics and has to be considered during the vehicle design. The resulting effect on the flight trajectory and, hence, longitudinal and cross range, is depending on how long the vehicle is flying in the rarefied regime and has to be evaluated in a mission analysis. Since the SHEFEX III configuration has lower drag coefficients the stronger rarefaction influence causes the SHEFEX III drag coefficients to increase more and approach the blunt COLIBRI drag coefficients. For $\alpha \geq 20^\circ$ where the aerodynamic bluntness of SHEFEX III increases further, the rarefaction influence on the SHEFEX III drag coefficient approaches the rarefaction influence on the COLIBRI drag coefficients, i.e. both are equally affected.

Corresponding to that the rarefaction influence on the lift / drag ratio is decreasing in both cases, see Fig. 103. Beyond the oscillation region at low angles of attack, the rarefaction effect on the COLIBRI configuration decreases the aerodynamic efficiency almost constant by 40% to 50% for angles of attack of $\alpha \geq 8^\circ$. In case of the SHEFEX III configuration the decrease is stronger and can cause a reduction of 60% between

$6^\circ \leq \alpha \leq 12^\circ$. The decreasing effect is weakening at higher angles of attack, such that there is a decrease of only 30% at $\alpha = 34^\circ$. Summarising, it can be stated that below an angle of attack of about 17° the effect is stronger for the slender SHEFEX III configuration. At higher angles of attack, the effect becomes more dominant for the blunt COLIBRI test configuration, such that the lift / drag ratio characteristics of both test configurations are differing further with increased rarefaction. Independent of the rarefaction effect, the aerodynamic efficiency of SHEFEX III is always better between a factor of 2 to 4 in the analysed flow regime.

For the pitching moment coefficient, the assumption of a linear trend line does not fit as well as in case of the other investigated aerodynamic coefficients due to its strong dependence on the pressure gradients in the flow. Since simultaneously the pitching moment coefficient is close to zero, the oscillation is strongly increasing and requires for the pitching moment coefficient ratio a scale twenty times larger than in case of the ratio of the other aerodynamic coefficients, see Fig. 104, and it is difficult to derive meaningful relations about the rarefaction effect on the pitching moment from this plot.

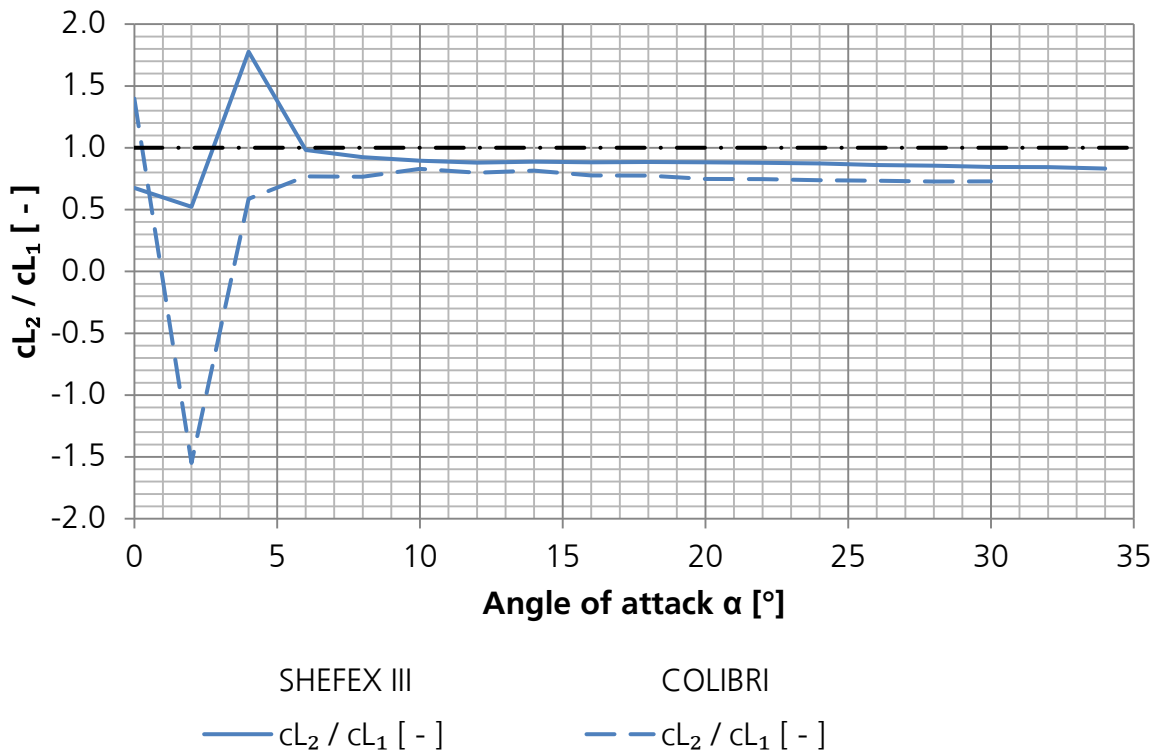


Fig. 101: Ratio of lift coefficients of high to low Knudsen numbers (calculated with linear trend line at: α_1 : minimum Knudsen number, α_2 : maximum Knudsen number)

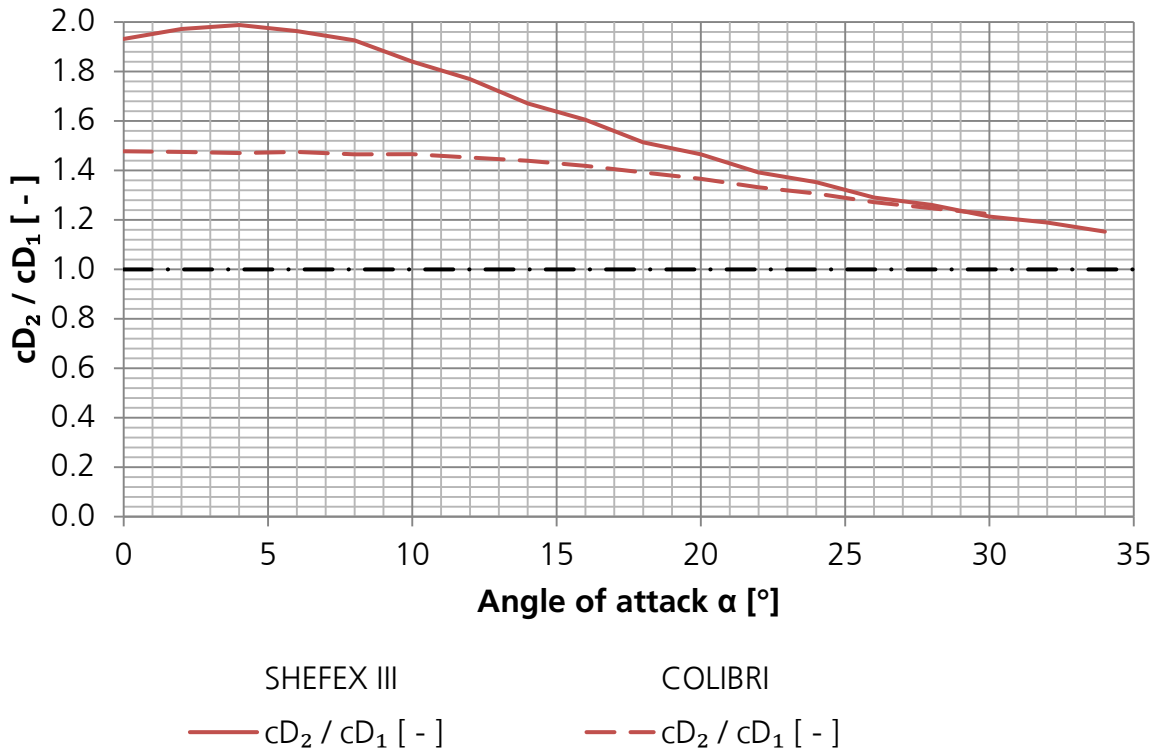


Fig. 102: Ratio of drag coefficients of high to low Knudsen numbers (calculated with linear trend line at: α_1 : minimum Knudsen number, α_2 : maximum Knudsen number)

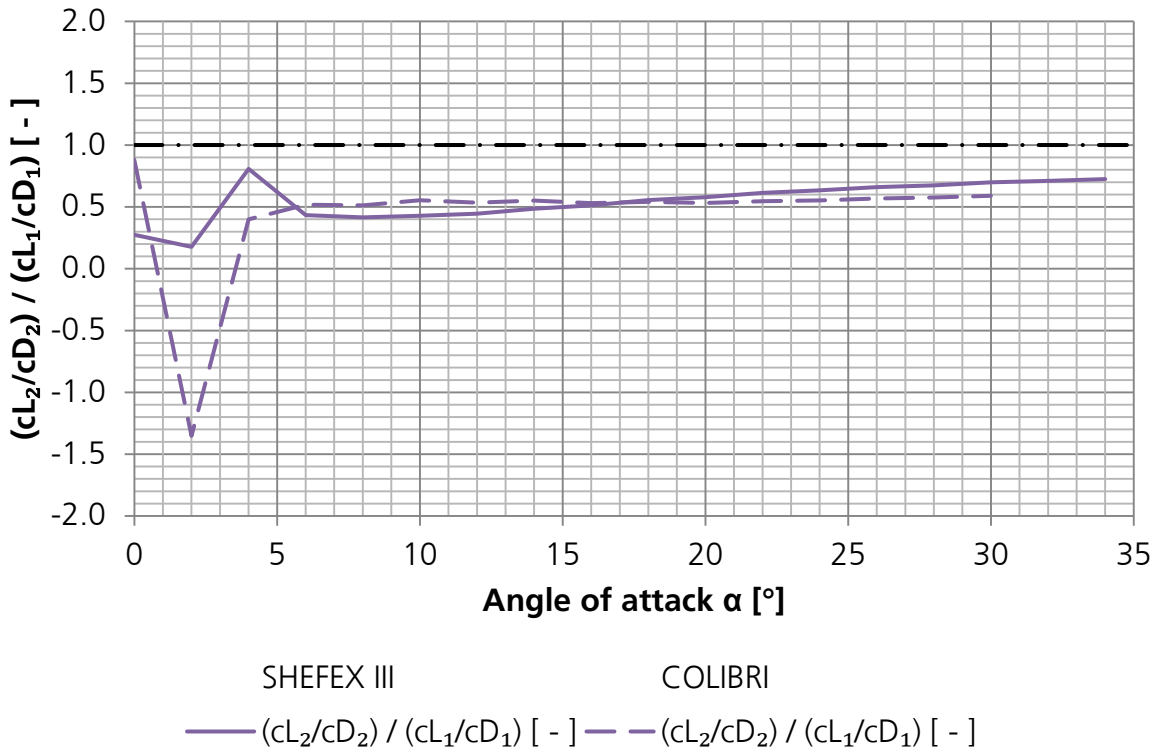


Fig. 103: Ratio of lift / drag ratios of high to low Knudsen numbers (calculated with linear trend line at: α_1 : minimum Knudsen number, α_2 : maximum Knudsen number)

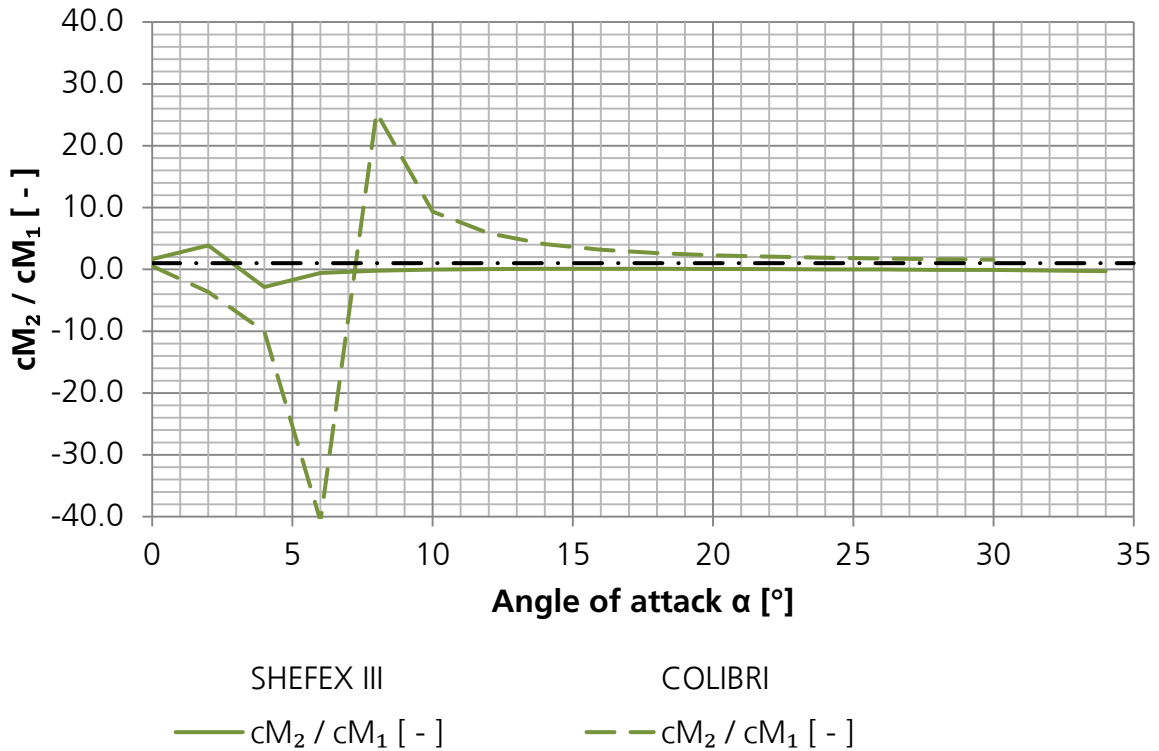


Fig. 104: Ratio of pitching moment coefficients of high to low Knudsen numbers (calculated with linear trend line at: α_1 : minimum Knudsen number, α_2 : maximum Knudsen number)

6.2 Comparison at Constant Knudsen Number

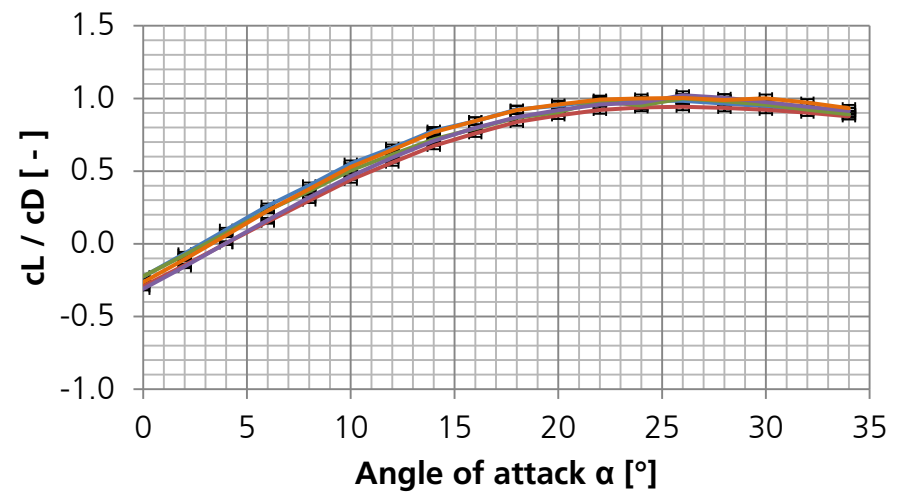
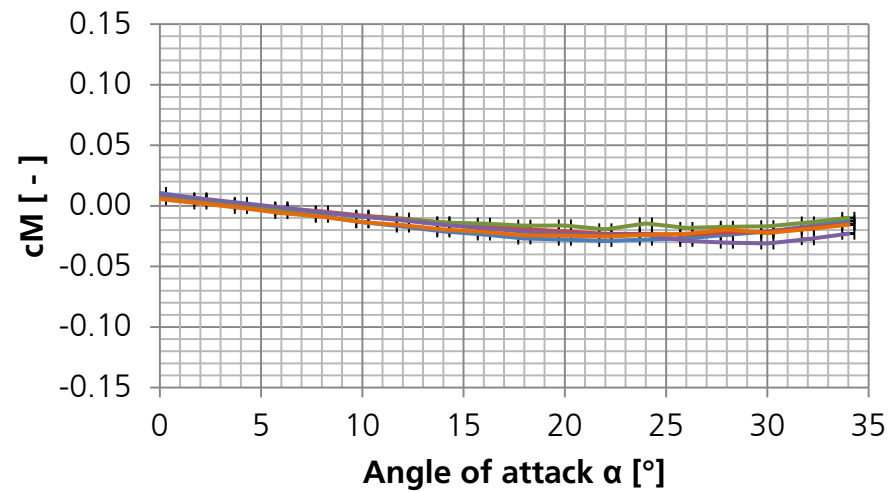
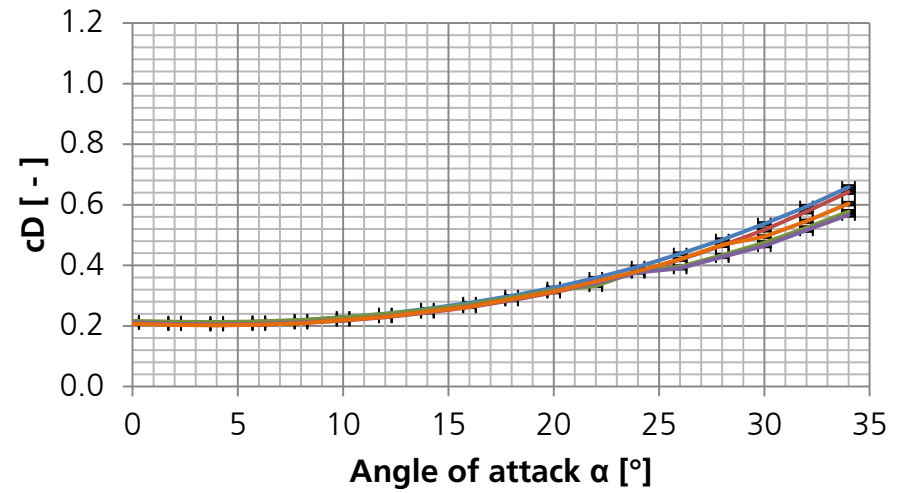
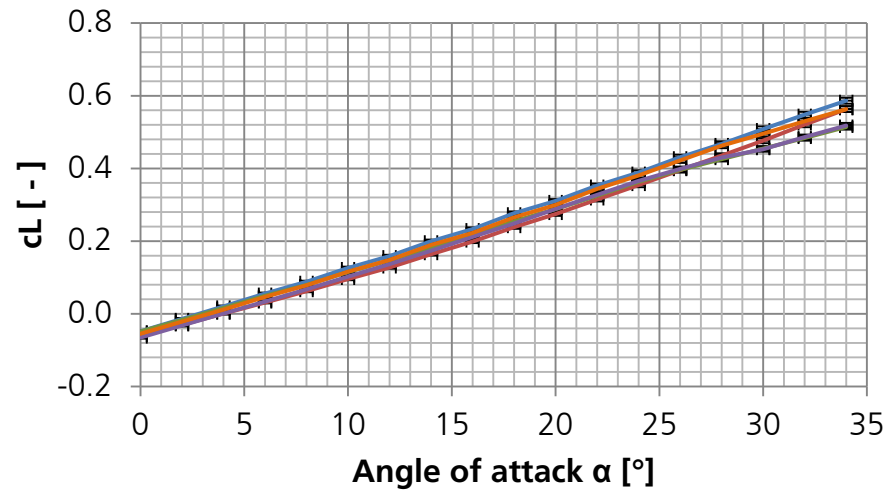
To evaluate the Reynolds number effect directly, five experiments are performed with both test configurations at a constant Knudsen number of $Kn = 3.1 \cdot 10^{-3}$ in case of the SHEFEX III configuration, see Fig. 105, and of $Kn = 3.8 \cdot 10^{-3}$ in case of the COLIBRI configuration, see Fig. 106. Based on the relation between Knudsen number, Mach number and Reynolds number (2-4), it means that if the Reynolds number, e.g. increases, the Mach number has to decrease with the same factor so that the ratio of Mach number to Reynolds number remains constant. For the analysis at a constant Knudsen number, only one Knudsen number is selected which limits the analysable range to the maximum V2G Mach number variation of about a factor of 2.

Concerning the lift coefficient the results of both test configurations show deviations over the Mach number and Reynolds number variation. Based on the previous chapter, where the Mach number influences are determined as small, the major reason for the deviation is attributed to the Reynolds number variation.

The Reynolds number caused change in drag coefficients is visible but is clearly lower than the rarefaction effect determined in the constant Reynolds number analysis. In case of the SHEFEX III configuration, the effects is almost indistinguishable for low angles of attack and increases at angles of attack of $\alpha \geq 24^\circ$. The reason for this sudden increase is not found yet and requires further investigations.

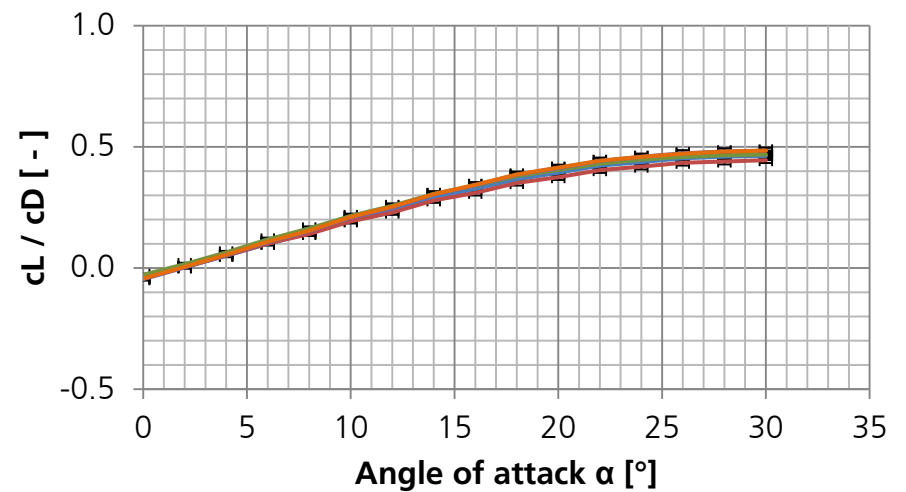
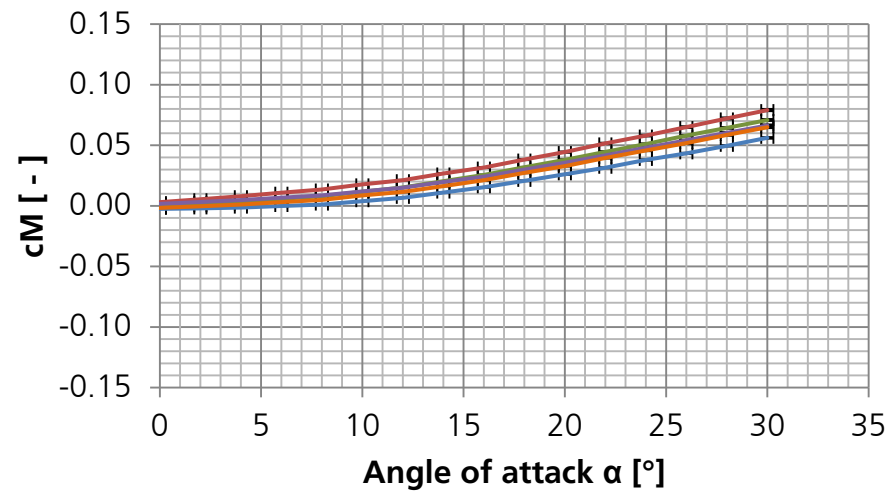
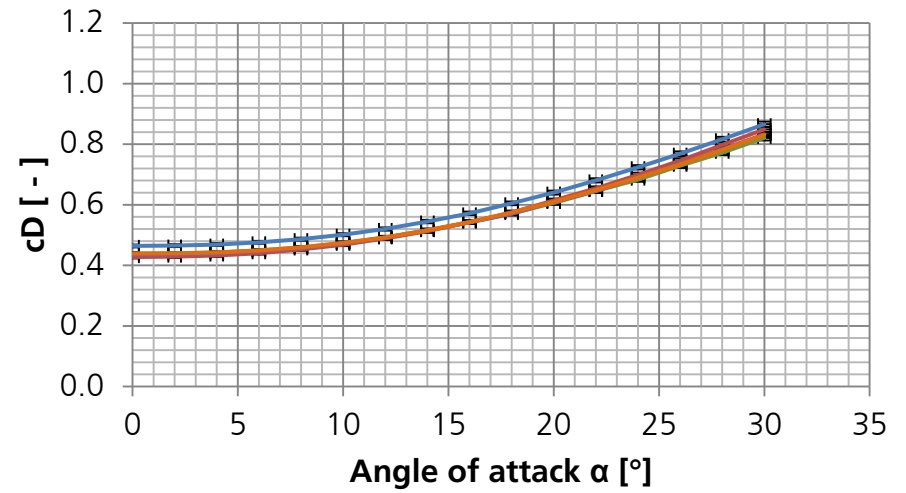
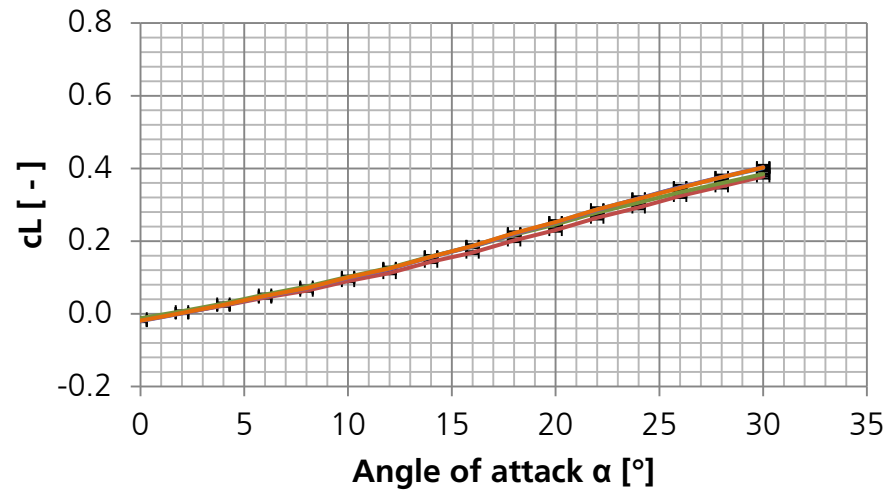
The pitching moment coefficient shows a distinct overlaying deviation in the magnitude of the previously analysed rarefaction effect. However, evidence that this deviation is based solely, or to a certain extent, on the Reynolds number variation cannot be provided on basis of the conducted experiments. The cause is the lacking ability to distinguish between effects caused by Reynolds number variations, and effects caused by flow inhomogeneities.

Based on the low influence on lift- and drag coefficient their ratio is almost not affected by the Reynolds number variation. The robustness against Reynolds number variations is stronger for the blunt COLIBRI configuration.



— $Re_1 = 1.22E+4,$ $M_1 = 25.2$
— $Re_1 = 1.09E+4,$ $M_1 = 22.7$
— $Re_1 = 7.38E+3,$ $M_1 = 14.9$
— $Re_1 = 6.65E+3,$ $M_1 = 13.3$
— $Re_1 = 5.13E+3,$ $M_1 = 11.1$

Fig. 105: Reynolds number effects on aerodynamic coefficients ($Kn_1 = 3.1e-3$, SHEFEX III)



— $Re_1 = 1.00E+4,$ $M_1 = 25.2$
— $Re_1 = 8.89E+3,$ $M_1 = 22.7$
— $Re_1 = 6.04E+3,$ $M_1 = 14.9$
— $Re_1 = 5.44E+3,$ $M_1 = 13.3$
— $Re_1 = 4.19E+3,$ $M_1 = 11.1$

Fig. 106: Reynolds number effects on aerodynamic coefficients ($Kn_1 = 3.8e-3$, COLIBRI)

6.3 Comparison Flow Inhomogeneity at Constant Reynolds Number

To evaluate the influence of flow inhomogeneity on the force measurement results, it is important to visualise which free stream conditions are used for the definition of Mach number, Reynolds number and Knudsen number. Based on discontinuities in the second derivative of the nozzle contour shortly downstream of the nozzle throat and tiny junctions between different nozzle parts, spatial time-independent fluctuations along the wind tunnel axis are reproducibly generated. During the concomitant numerical flow characterisation^[80], these spatial fluctuations are provoked by a slight misalignment between different nozzle parts of about 0.5 mm in stream direction, about 6 cm downstream the nozzle throat, see Fig. 107. Due to the V2G specific design larger misalignments can be excluded during experiments, since they would severely affect the required vacuum-tightness and, hence, the functional ability of V2G. However, tiny inaccuracies within the fabrication and assembling tolerance cannot be avoided.

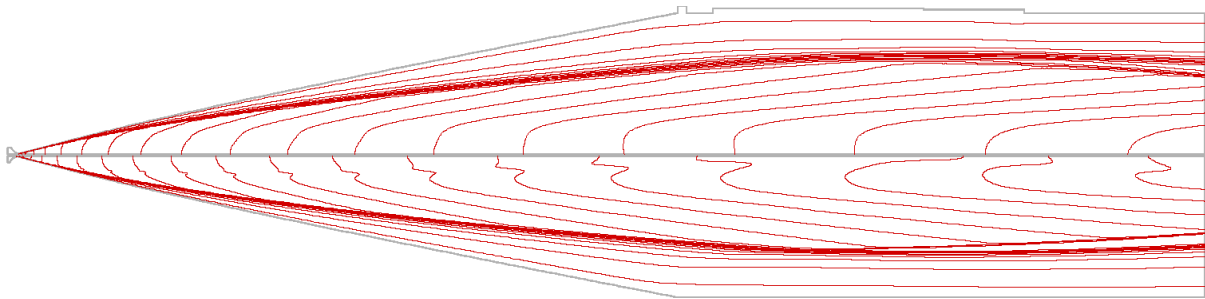


Fig. 107: Mach number isolines⁵: smooth nozzle contour (top), slight nozzle part misalignment and resulting time-independent spatial fluctuations (bottom)^[80]

Depending on the operating condition, these spatial fluctuations can cause the Pitot pressure to locally in- or decrease at the position ($x = 150 \text{ mm}$ and $y = 0 \text{ mm}$), where the values for the determination of the corresponding Mach number and Reynolds number are measured, as in Fig. 48 described. Due to these spatial fluctuations, the locally determined Reynolds numbers of two different operating conditions can be equal, while the flow field characteristics, the Mach number and, hence, the Knudsen number are different, compare condition 10 presented in Fig. 108 and condition 15 shown in Fig. 109. The aim of this analysis is to check whether the approach of using a single locally determined Reynolds number is justified to classify the whole flow field, where the test article is located. For the meaning of the constant Reynolds number analysis it is essential that the influence of the different flow fields is evaluated.

Condition 10 and 15 are selected since they showed the largest pressure peak difference of all analysed operating conditions, so that the effect of flow inhomogeneity is lower for all other cases. It is, however, not possible to perform force measurements up to the full angle of attack range at condition 10, since the core flow is too small to cover the test articles at high angles of attack. The error in Mach number or Reynolds number determination due to the spatial Pitot pressure fluctuations is evaluated by comparing it to a Mach number or Reynolds number based on an imaginary Pitot pressure distribution without spatial fluctuations in the core flow centre. Performing it

⁵ Cavity of flanges simulated with hydraulic diameter (top), cavity of flanges neglected (bottom)

for both extreme operating conditions, where maximum spatial fluctuations are provoked, showed a Mach number deviation of +1.1% for condition 10 and -2.5% for condition 15. The deviations in case of the Reynolds number are larger and reach up to -3.6% for condition 10 and +8.8% for condition 15 and correspond to Knudsen number deviations of +4.9% and -10.3%. This seems much, however, one has to keep in mind that the operating conditions are selected to generate maximum possible opposed spatial fluctuations to determine an upper and lower limit.

The aerodynamic coefficients measured at the operating conditions 10 and 15 are presented in Fig. 110 for the SHEFEX III configuration and in Fig. 111 for the COLIBRI configuration respectively. It can be seen that the aerodynamic coefficients of lift and drag and also their ratio, for both operating conditions are almost superimposable with only marginal deviations (see Table 6). The observed deviations remain in the magnitude of the measurement error, except for the pitching moment coefficient. The higher percentage value of the COLIBRI lift coefficient at $\alpha = 0^\circ$ is caused by values close to the zero-crossing. The precision of the agreement of the results is positively astonishing since the influence is expected to be stronger especially due to the large peaks in the core flow centre, see Fig. 109. Only in case of the pitching moment, some deviations are visible and cause an interference with the effects caused by rarefaction. This is plausible and expected due to the high sensitivity of the pitching moment coefficient to gradients in the flow field, see Fig. 73.

Table 6: Changes of aerodynamic coefficients between condition 15 (2) and condition 10 (1) exemplarily shown at $\alpha = 0^\circ$ and $\alpha = 10^\circ$

	$(cL_2 - cL_1)/cL_1$	$(cD_2 - cD_1)/cD_1$	$(cM_2 - cM_1)/cM_1$	$((L/D)_2 - (L/D)_1)/(L/D)_1$
SHEFEX III				
$\alpha = 0^\circ$	-0.8%	1.7%	-49.2%	-2.5%
$\alpha = 10^\circ$	2.4%	-1.4%	-19.3%	3.9%
COLIBRI				
$\alpha = 0^\circ$	7.8%	-1.4%	-51.6%	9.4%
$\alpha = 10^\circ$	1.3%	0.0%	221.6%	1.3%

However, the good agreement is contrary to what is expected when regarding the Knudsen numbers of both operating conditions. Based on the observed rarefaction effects on the aerodynamic coefficients elaborated in chapter 6.1, deviations within the determined magnitude are expected. However, the results are almost identical. Applying the Knudsen number deviations, explained in the second paragraph of this chapter, shows, that the remaining Knudsen number difference between conditions 10 and 15 is reduced to about 2.5% for both test articles. The results indicate that for the determination of similarity parameters an imaginary Pitot pressure distribution without fluctuations in the core flow centre can yield better results, than the used locally based determination ($x = 150 \text{ mm}$ and $y = 0 \text{ mm}$) on the actual measured data. Since the influence of spatial fluctuations on the flow field is for most operating conditions not clearly separable from an imaginary undisturbed Pitot pressure profile, the analysis complexity increases drastically and becomes difficult to reproduce. Additionally, the error of locally determined similarity parameters is small and within the previously determined limits, such that this simpler approach is selected for this work.

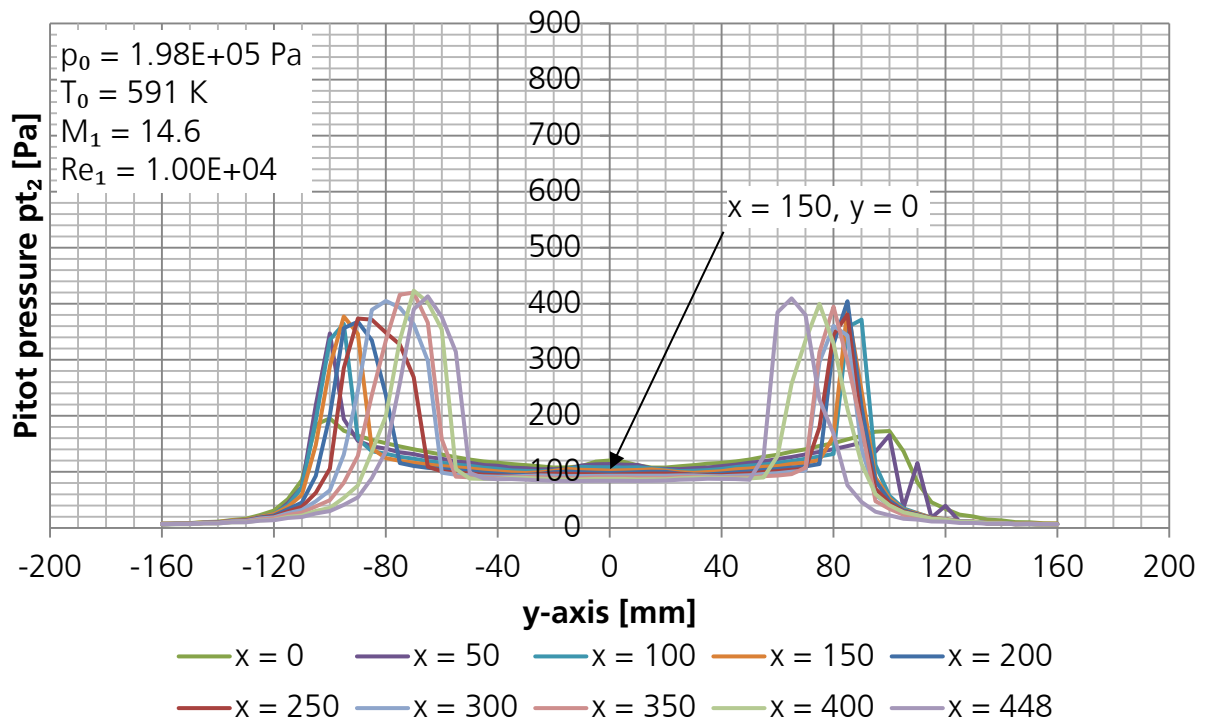


Fig. 108: Pitot pressure profiles with positive pressure peaks in core flow centre (cond. 10)

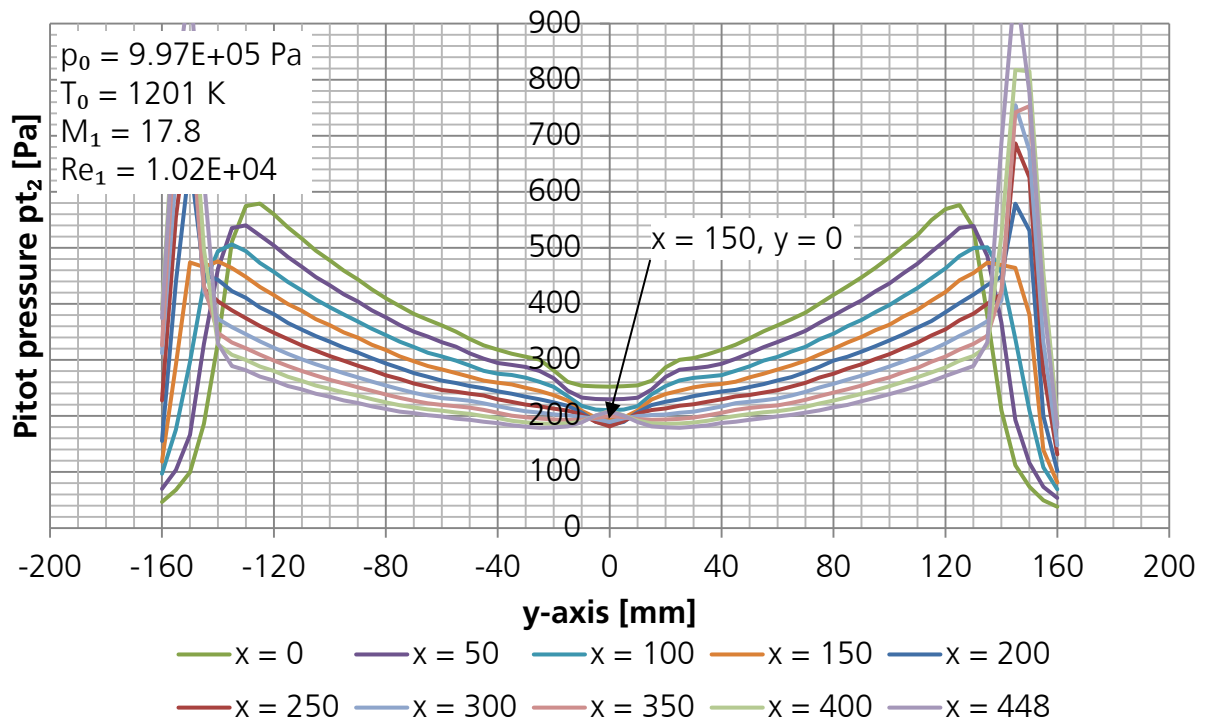
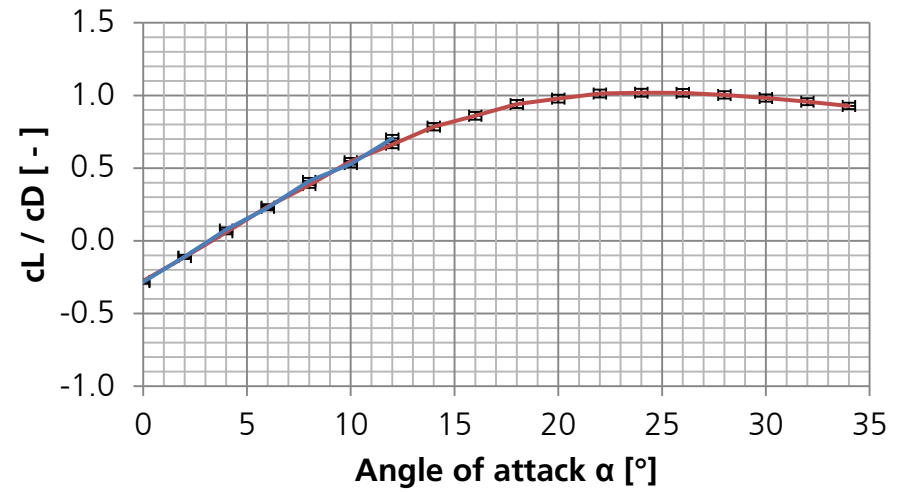
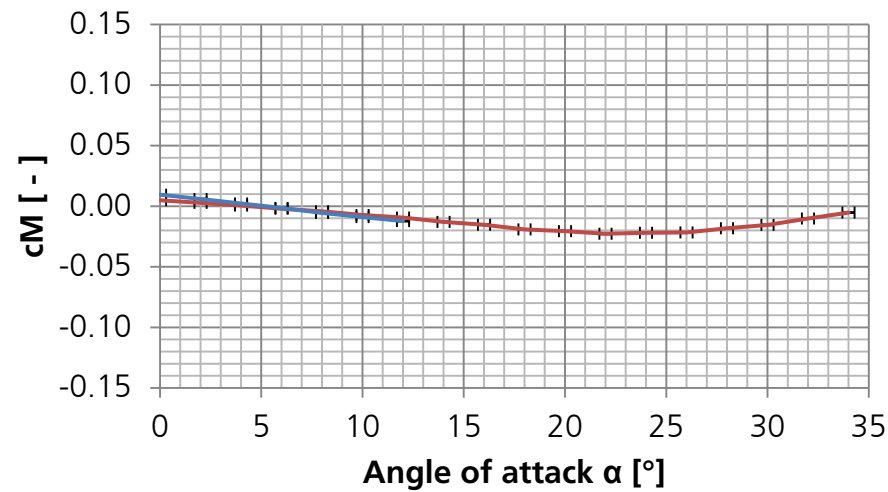
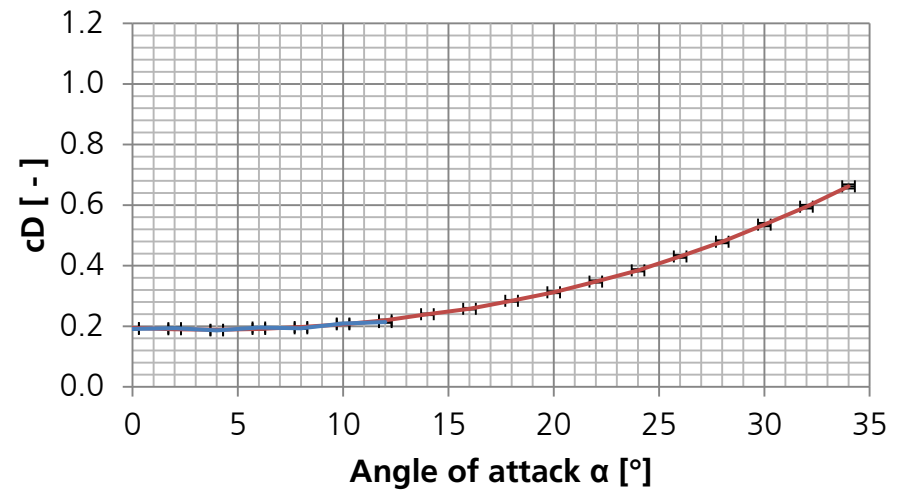
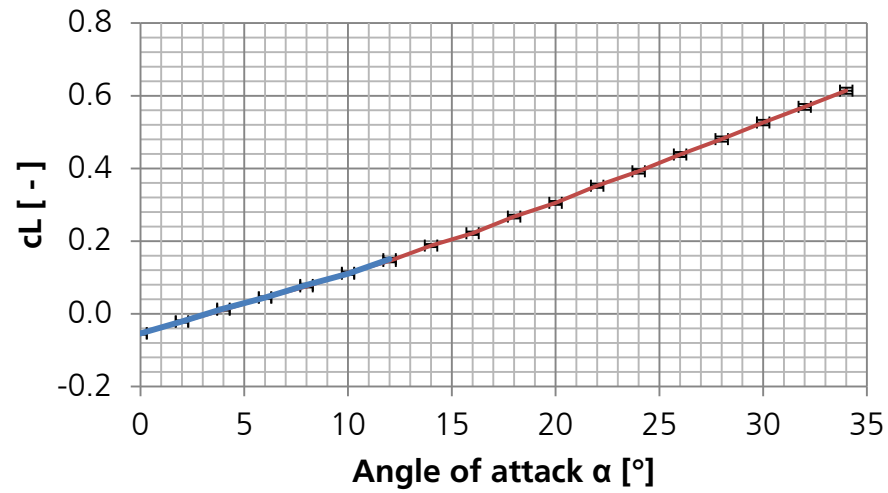
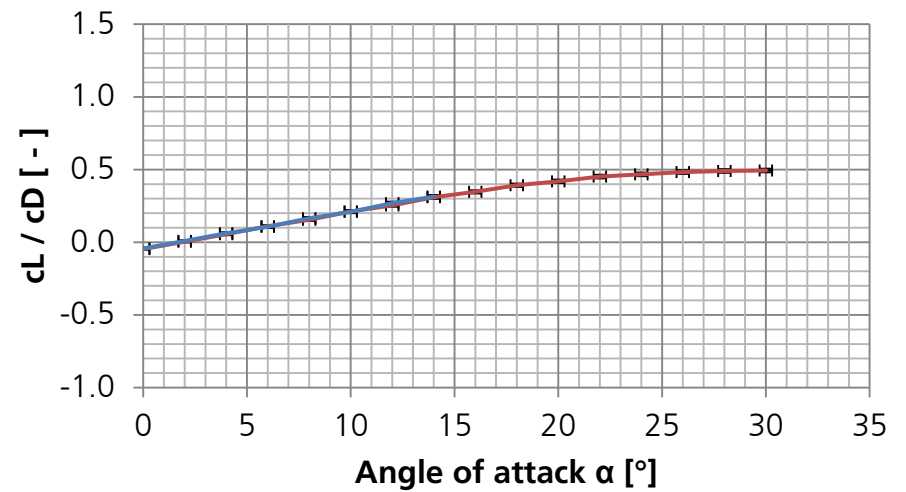
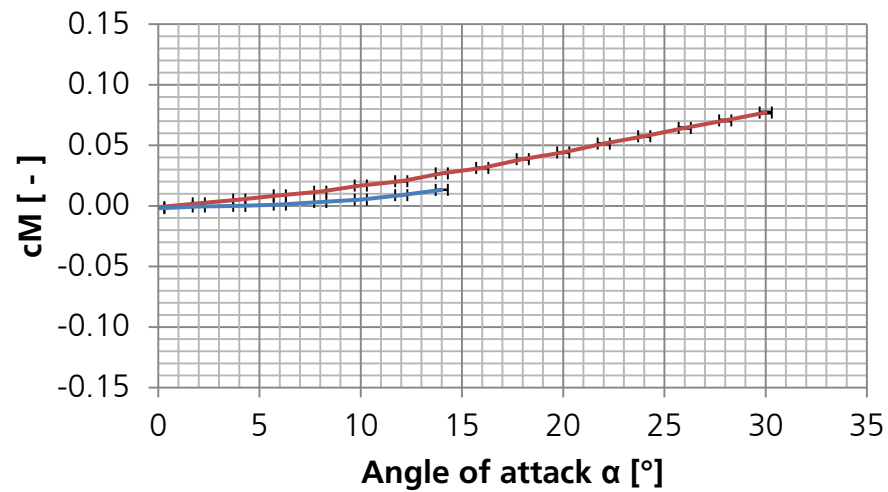
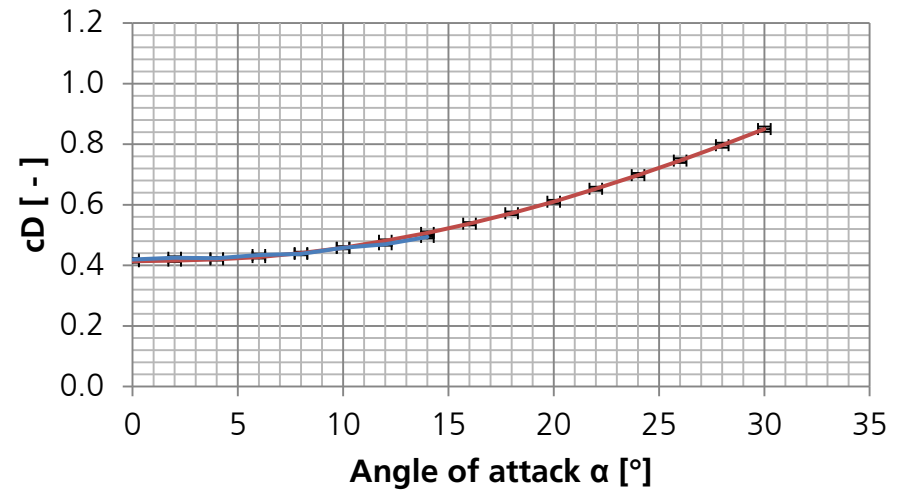
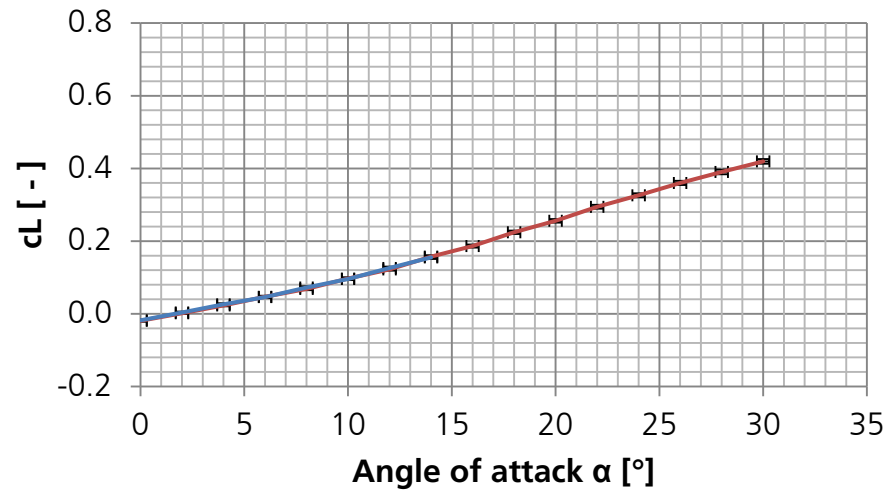


Fig. 109: Pitot pressure profiles with negative pressure peaks in core flow centre (cond. 15)



— $Kn_1 = 2.14E-3,$ $M_1 = 14.6$ — $Kn_1 = 2.57E-3,$ $M_1 = 17.8$

Fig. 110: Influence of flow inhomogeneity on aerodynamic coefficients ($Re_1 = 1.02e+4$, SHEFEX III)



— $Kn_1 = 2.62E-3,$ — $Kn_1 = 3.14E-3,$
 $M_1 = 14.6$ $M_1 = 17.8$

Fig. 111: Influence of flow inhomogeneity on aerodynamic coefficients ($Re_1 = 8.33e+3$, COLIBRI)

7 Summary

This work aims at determining and evaluating the behaviour of aerodynamic coefficients of lift, drag and pitching moment of re-entry and hypersonic transport vehicles in the gas kinetic transition region between continuum and rarefied flow. Measurements performed within the FAST20XX project indicated a strong rarefaction effect, but are uncertain regarding the simultaneous potential presence of Reynolds number effects. Motivated by this the focus of this study is not on the analysis of a specific configuration and trajectory, but on the general influence of rarefaction on the aerodynamic coefficients of blunt and slender configurations. Based on the relation of Knudsen number to Mach number and Reynolds number and the goal to vary only one parameter at a time, the test matrix is setup. Assuming the validity of the Mach number independence principle, it is straight forward to vary the Mach number since the resulting effect can be interpreted as a pure effect of rarefaction. By repeating the test series at a constant Reynolds number step by step at different Reynolds numbers, it is possible to extend the Knudsen number variation.

Scaled models of the blunt COLIBRI and of the sharp-edged slender SHEFEX III configuration are selected exemplarily, to analyse the rarefaction effects on a blunt and slender vehicle type since it is expected that rarefaction effects affect blunt and slender configurations differently. Both configurations were designed as flight configurations, although they did never fly. The experiments are performed for both test articles at angles of attack between 0° and 34° with an angles of attack resolution of 2° steps. For a broad analysis experiments are conducted at 26 different flow conditions in the rarefied flow, covering one full order of magnitude in Knudsen number, in case of the SHEFEX III configuration from $7.2 \cdot 10^{-4}$ to $7.2 \cdot 10^{-3}$, and in case of the slightly shorter COLIBRI configuration from $8.8 \cdot 10^{-4}$ to $8.8 \cdot 10^{-3}$. The rarefied flow regime covers (from 10^{-3} to 1) about three orders of magnitude of Knudsen numbers and although the experimentally investigated range covers the regime close to continuum, strong rarefaction effects are observed for both test configurations.

Since the experiments are performed in the transition regime between rarefied flow and continuum, the measured rarefaction effects on aerodynamic coefficients are analysed focussing on the change versus both Knudsen number and rarefaction parameter. It turned out that the consideration versus both parameters yield similar good trends of how aerodynamic coefficients behave in rarefied flow. While the aerodynamic coefficients versus Knudsen number showed slightly better trends in case of the slender SHEFEX III configuration, the usage of the rarefaction parameter is slightly more suitable for the blunt COLIBRI configuration at high angles of attack. Recalling that the rarefied flow regime is distinguished from free molecular flow by the Knudsen number and from continuum by the rarefaction parameter, this result is plausible, because the COLIBRI configuration experiences at high angles of attack the lowest degree of rarefaction of all conducted test cases.

The experiments, performed in this work in the second test section of the DLR Hypersonic Vacuum Wind Tunnel Göttingen, provide extensive experimental data for two test configurations. For the experimental investigation a 3-component strain gauge force measurement technique, capable of simultaneously measuring lift, drag and

pitching moment, is re-established and optimised. The zero point stability, most critical for the precision of the measurements, is improved in average by one order of magnitude, compared to the earlier measurements performed within FAST20XX. At the same time the test articles are optimised to reduce the dead weight on the balance and to reduce the heat transfer onto the balance. In parallel it is attempted to minimise flow gradients by replacing the conical nozzle, which was used for the FAST20XX experiments, with a contoured nozzle.

In detail the lift coefficient of both test configurations is found to be significantly reduced over the whole analysed Knudsen number range, compared to the lowest Knudsen number, hence, the operating condition closest to continuum. Over a wide range of angles of attack $6^\circ \leq \alpha \leq 30^\circ$, the percentage reduction is almost constant between 20% and 30% for the blunt COLIBRI configuration and between 10% and 20% for the slender SHEFEX III configuration.

In case of the drag coefficient, the rarefaction effects are even stronger and can reach almost a factor of 2 for the SHEFEX III configuration, hence, an increase of 100% at low angles of attack, where the configuration is aerodynamically slender. The maximum drag coefficient increase of the blunt COLIBRI configuration is 50%. The strongest effects occur at low angles of attack of $\alpha \approx 4^\circ$ (SHEFEX III) and $\alpha \approx 0^\circ$ (COLIBRI). At higher angles of attack, the rarefaction caused drag coefficient increase is reduced, but still above 20% at angles of attack below 30° . The reason is that the absolute values of the drag coefficients increase at higher angles of attack, while the absolute changes remain almost constant independent of the angle of attack, such that the percentage effects become smaller.

As a direct consequence of the changes in lift and drag coefficient, the aerodynamic efficiency, i.e. lift / drag ratio is decreased in case of the SHEFEX III configuration by almost 60%, and, hence, more than a factor of 2, at an angle of attack of 6° . At higher angles of attack the reduction decreases to 30% at the highest analysed angle of attack of 34° . In case of the COLIBRI configuration the rarefaction caused decrease in lift / drag ratio is almost constant between 50% and 40%. Comparing the aerodynamic efficiency of both configurations, it can be found that at low angles of attack the SHEFEX III configuration experiences a stronger rarefaction effect, while at higher angles of attack from about $\alpha = 17^\circ$ the COLIBRI configuration is affected more by rarefaction. Independent of the rarefaction effect, the aerodynamic efficiency of SHEFEX III remains always between 2 and 4 times better.

Transferred onto an actual re-entry of a vehicle with high lift / drag ratio, the reduction of the aerodynamic efficiency causes the vehicle to dive deeper into the atmosphere before it is decelerated. How strong the reduced lift / drag ratio is affecting the longitudinal and cross range of a re-entry or hypersonic transport mission depends on the respective trajectory and has to be assessed in each individual case.

The pitching moment shows a tendency to become more positive with increasing Knudsen number, however, strong dependencies on, e.g., the Reynolds number and flow gradients make a non-ambiguous interpretation impossible and do not allow quantitative statements. This study shows how flow inhomogeneities affect the aerodynamic coefficients and confirms that there is a non-negligible influence on the

pitching moment coefficient. In case of the other aerodynamic coefficients, lift and drag and lift /drag ratio, there is no significant effect due to flow inhomogeneity observable.

A Reynolds number effect could be observed at nearly all operating conditions. The effect increases with the angle of attack but appears to have a smaller influence, than effects due to the change in Knudsen number. For a quantification of the Reynolds number effect, it is necessary to conduct further experiments at a constant Knudsen number, while varying the Reynolds number. To broaden the analysable regime it is recommended to repeat that constant Knudsen number analysis then at different Knudsen numbers as it is performed in this study for the different Reynolds numbers.

The results showed that the Mach number independence principle is also applicable for the slender SHEFEX III configuration at low angles of attack within the measurement accuracy. Although the SHEFEX III configuration is slender compared to other re-entry vehicles, it differs significantly from an ideal slender shape. The existence of Mach number effects cannot be denied, but they are not of significant importance in the performed analyses on the selected test configurations.

Due to the scaling via the similarity parameters Knudsen number, Mach number and Reynolds number and the usage of aerodynamic coefficients instead of aerodynamic forces the obtained results can be transferred to real hypersonic flight when the similarity parameters are equal. The aerodynamic coefficients determined in wind tunnel tests are then equal to those of the actual flight condition.

Based on the facility design and the experimental setup, currently only steady-state analyses can be conducted with the V2G force balance. Although the balance design allows transient measurements, the results have to be averaged to smooth the scattering caused by the mechanical and electrical noise of the large vacuum pumps.

8 Outlook and further Use for Numerical Comparisons

The present analyses showed the Knudsen number effect over a wide range of operating conditions for a blunt and a slender configuration at angles of attack between 0° and 34° . It is expected that at this angle of attack range, the largest effects for the analysis of the differences between blunt and slender configurations could be observed. Since typical re-entry vehicles fly at angles of attack of up to about 50° during re-entry, it is interesting to conduct further measurements in this angle of attack range and to extend the existing plots to higher angles of attack.

In further subsequent analyses it would also be useful to conduct more measurements at a constant Knudsen number and extend the investigation of the Reynolds number effect, which is briefly performed in chapter 6.2. To allow a quantification of the Reynolds number effect on the Knudsen number, a study similar to this work is recommended where the experiments are conducted at constant Knudsen numbers instead of constant Reynolds numbers as it is briefly touched in chapter 6.2.

Apart from the actual rarefaction analysis, this work provides with its extensive number of experiments valuable possibilities for numerical comparisons. The total data set necessary for numerical simulations can be found in ^[79].

It would be interesting to see how good the experimental results agree to numerical results. Due to the axial flow gradients, however, it is important that the actual flow field is simulated for a realistic comparison. If numerical and experimental results agree, then confidence is established and the numerical tool can be carefully extended to other conditions. Interesting would be whether the analysed experiments can be still simulated with continuum solvers when additional wall slip conditions are implemented, or if Direct Simulation Monte Carlo methods have to be used.

With a numerical analysis it would then be possible to approach open questions which could not be answered by the experimental analysis. In particular the treatment of flow gradients has to be addressed. For the experimenter it is here difficult to choose, which dynamic pressure or averaging method should be used, so that some advice based on numerical predictions is appreciated. A further numerical simulation of the test article in a parallel flow field would then help to evaluate the effect of flow gradients on lift drag and pitching moment coefficients.

9 Acknowledgements

First of all I want to address special thanks to Professor Klaus Hannemann, my Ph.D. supervisor, for countless fruitful discussions and helpful thoughts. His analytic expertise and his thoroughness allowed an invigorating exchange during numerous technically complex discussions.

Additionally, I want to address special thanks to the technical staff Günter von Roden and Jens Steinhoff for persistently and reliably running, maintaining and repairing the V2G facility and its measurement technique countless times and for their excellent and invaluable technical support and advice.

Further, I would like to address special thanks to Rolf-Detlef Boettcher for numerous constructive technical discussions and valuable hints during the work. His preciseness and analytic expertise is incomparable and always a role model for scientific working.

Moreover, I want to especially thank the former and mostly already retired staff, namely Herbert Berger, Professor Georg Koppenwallner, Dr. Gerhard Hefer, Carl Dankert, Dr. Hans-Dieter Speckmann and endless more for their tireless helpfulness and willingness to assist and for supporting me with help and advice even after in some cases nearly twenty years of retirement.

I want to express my special thanks also to Dr. Georg Dettleff, Dr. Tobias Ecker, Dr. Volker Hannemann and Jeremy Wolfram for thoroughly proofreading this work and many helpful thoughts during this work.

Last but not least, I would like to thank my wife, family and friends for continuously supporting me during the last years.

10 References

- [1] Allègre, J., Raffin, M., Chpoun, A., & Gottesdiener, L., *Rarefied hypersonic flow over a flat plate with truncated leading edge*, Progress in Astronautics and Aeronautics, 160, 285-285, 1994.
- [2] Allègre, J., Raffin, M., Lengrand, J. C., *Aerodynamic Forces and Moments for a Re-Entry Module*, Journal of Spacecraft and Rockets, Vol, 34, No. 2, Mar.-Apr., 1997
- [3] Allègre, J., Bisch, D., Lengrand, J. C., *Experimental Rarefied Density Flowfields at Hypersonic Conditions over 70-Degree Blunted Cone*, Journal of Spacecraft and Rockets, Vo. 34, No. 6, Nov.-Dec., 1997
- [4] Anderson, Jr., J. D., *Hypersonic and High Temperature Gas Dynamics*, McGraw-Hill Inc., ISBN 0-07-001671-2 ,1989
- [5] Barth, T., *Aerothermodynamische Voruntersuchung der REX – Free Flyer Konfiguration*, DLR-IB 124-2009 / 911, Braunschweig, 2009
- [6] Bird, G. A., *Molecular Gas Dynamics and the Direct Simulation of Gas flows*, Oxford engineering Science Series, Clarendon Press, Oxford, 1994
- [7] Bird, G. A., *The DSMC method*, Version 1.2, CreateSpace Independent Publishing Platform, ISBN 9781492112907, 2013
- [8] Blanchard, R. C., Hinson, E. W., *Rarefied-flow Pitching Moment Coefficient Measurements of the Shuttle Orbiter*, 16th ICAS Congress, Jerusalem, Israel, Aug. 28 - Sept. 2, 1988
- [9] Blanchard, R. C., Larman, K. T., Moats, C. D., *Rarefied-Flow Shuttle Aerodynamics Flight Model*, NASA Technical Memorandum 107698, February, 1993
- [10] Boettcher, R.-D., Legge, H., *A Study of Rocket Exhaust Plumes and Impingement Effects on Spacecraft Surfaces*, II. Plume Profile Analysis, Part 2: Rarefaction Effects, DFVLR-IB 222-81 A 19, Göttingen, 1981
- [11] Boettcher, R.-D., *Applicability of Bridging Methods to Hypersonic Rarefied Flow Aerodynamics of Reentry Vehicles*, Proceedings of the 1st European Symposium of Aerodynamics for Space Vehicles pp. 469-476, Noordwijk, Netherlands, 1991
- [12] Burkhardt, J., *Konzeptioneller Systementwurf und Missionsanalyse für einen auftriebsgestützten Rückkehrkörper*, Dissertation, Universität Stuttgart, Stuttgart, 2001
- [13] Bütefisch, K. A., Schöler, H., *Fünfkomponenten-Messungen am MBB-Raumflugkörper bei hypersonischen Machzahlen und kleinen Reynoldszahlen*, DFVLR-IB 063-72 H 06, 1972
- [14] Bütefisch, K. A., Schöler, H., *Windkanalmessungen an einem Raumflugkörper in verdünnter Hyperschallströmung*, DFVLR-IB 252-73 H 12, 1973
- [15] Charters, A. C., Thomas, R. N., *The Aerodynamic Performance of Small Spheres from Subsonic to High Supersonic Velocities*, Journal of the Aeronautical Sciences, vol. 12, pp. 468-476, 1945
- [16] Chun, Ch.-H. et al., *Three-Component Aerodynamic Tests of Cones in Hypersonic Rarefied Flow at Ma 20 in Vacuum Wind Tunnel (V1G) DFVLR*, Göttingen, DFVLR-IB 222-88 C 07, 1988
- [17] DLR Homepage, SHEFEX Development Strategy http://www.dlr.de/desktopdefault.aspx/tabid-728/1208_read-24147, last access: 27th May 2016
- [18] *Equations, Tables, and Charts for Compressible Flow*, NACA Report 1135 – Moffett Field, California, USA, 1953

- [19] Fay, J. A., Riddell, F. R., *Theory of Stagnation Point Heat Transfer in Dissociated Air*, Journal of the Aeronautical Sciences, vol. 25, no. 2, pp. 73-85, February 1958
- [20] Föppl, A., *Vorlesungen über technische Mechanik*, 3. Band Festigkeitslehre, Verlag von R. Oldenbourg, München und Berlin, Germany, 1944
- [21] Grossir, G., Rambaud, P., *Detection of Nitrogen Flow Condensation in a Hypersonic Wind-Tunnel using a Static Pressure Probe*, 52nd Aerospace Science Meeting, pp.10762-10776 Maryland, USA, 2014
- [22] Harvey, J. K., Jeffery, R. W., Uppington, D. C., *The Imperial College Graphite Heated Hypersonic Windtunnel*, Reports and Memoranda No. 3701, London, UK, January, 1971
- [23] Hayes, W. D., Probstein, R. F., *Hypersonic Flow Theory*, New York Academic Press, 1959
- [24] Hefer, G., *Die Zweite Messstrecke des Hypersonischen Vakuumwindkanals der AVA – Baubeschreibung und Betriebsverhalten*, DLR FB 70-42, 1970
- [25] Hirschel, E. H., Weiland, C., *Design of hypersonic flight vehicles: some lessons from the past and future challenges*, CEAS Space J (2011), DOI 10.1007/s12567-010-0004-4, 2010
- [26] Hirschfelder, J. O., Curtiss, C. F., Bird, R. B., *Molecular Theory of Gases and Liquids*, Wiley, New York, ISBN-13: 978-0471400653, 1967
- [27] Hodges, A. J., *The Drag Coefficient of Very High Velocity Spheres*, Journal of the Aeronautical Sciences, vol. 24, pp. 755-758, 1957
- [28] Keithley Instruments GmbH, *Low level measurements handbook; Precision DC current, voltage and resistance measurements*, 6th edition, Germering, Germany, <http://www.keithley.com>, 2004
- [29] Kemp, N. H., Rose, R. H., Detra, R. W.: *Laminar Heat Transfer around Blunt Bodies in Dissociated Air*, Journal of the Aerospace Sciences, vol. 26, no. 7, pp. 421-430, July 1959
- [30] Kliche, D., Mundt, C., Hirschel, E. H., *The hypersonic Mach number independence principle in the case of viscous flow*, Shock Waves (2011) , Springer Verlag, DOI 10.1007/s00193-011-0318-y, 2011
- [31] Koppenwallner, G., *Ein Hypersonischer Windkanal für kleine Gasdichten (Vakuumwindkanal) – Baubeschreibung*, AVA-Bericht 64 A 44, 1964
- [32] Koppenwallner, G., Wuest, W., *Ein hypersonischer Windkanal für kleine Gasdichten (Vakuumwindkanal); Entwurfsgrundlagen und Baubeschreibung*, AVA Bericht 64 S 02, 1964
- [33] Koppenwallner, G., *Der hypersonische Vakuumwindkanal der Aerodynamischen Versuchsanstalt Göttingen - Betriebsverhalten und erste Ergebnisse über reale Gaseffekte in Düsenströmungen*, DLR FB 66-62, 1966
- [34] Koppenwallner, G., Bütetisch, K., Kienappel, K.: *Experimentelle Untersuchung über die hypersonische Düsenströmung bei sehr geringer Gasdichte mit Schwingungsrelaxation*, DLR FB 67-69, 1967
- [35] Koppenwallner, G., *Drag and pressure distribution of a circular cylinder at hypersonic Mach numbers in the range between continuum flow and free molecular flow*, AVA-Bericht 68 A 31, 1968
- [36] Koppenwallner, G., Kienappel, K., *Untersuchung der Druckverteilung, der Klappenmomente und des Strömungsfeldes an einem Integralkörper der Firma Junkers*, AVA-Bericht 70 A 25, 1970

- [37] Koppenwallner, G., Wuest, W., *Experimental and Theoretical Investigations of Different Configurations of Lifting Re-Entry Vehicles in Hypersonic Low Density Flow*, AVA-Bericht 70 A 33, 1970
- [38] Koppenwallner, G., *Experimentelle Untersuchung der Kräfte an einfachen Flugkörpern bei verdünnter Hyperschallströmung*, BMBW-FB W 70-41, 1970
- [39] Koppenwallner, G., Legge, H., Müller, H., *Apollo Command Module Aerodynamic Simulation Test in Hypersonic Flow*, 22nd International Astronautical Congress, Bruxelles, Belgium, 20-26 September, 1971
- [40] Koppenwallner, G., *Kraftmessung an einem Modell des ERNO-Lifting-Body LB21 im Hyperschallbereich bei kleinen Reynoldszahlen*, DFVLR-IB 063-72 H 09, 1972
- [41] Koppenwallner, G., Schepers, H. J., *Typische Ergebnisse der DFVLR-Windkanaluntersuchungen an der ART-Konfiguration*, DFVLR-IB 252-74 H 08, 1974
- [42] Koppenwallner, G., *Kraftmessungen an den Versionen A und B des Wiedereintrittskörpers ART24 im hypersonischen Vakuumwindkanal*, DFVLR-IB 252-74 H 09, 1974
- [43] Koppenwallner, G., *Problems of hypersonic low Reynolds number flow in space flight*, DFVLR, IB 252-74 H 13, 1974
- [44] Koppenwallner, G., *Aerodynamics of Rarefied Gases and High-Altitude Flight*, Proceedings of the 18th International Symposium on Rarefied Gas Dynamics, pp. 75-103, Volume 160, University of British Columbia, Vancouver, British Columbia, Canada, July 26-30, 1992, ISSN 0079-6050, 1994
- [45] Koppenwallner, G., *Aerodynamik des Wiedereintritts - Aerothermodynamik des Wiedereintritts*, Lecture script, Technische Universität Braunschweig, 2004
- [46] Kuhn, T., *Strömungscharakterisierung der Hypersonischen Versuchsanlage V2G*, Student thesis, Department Spacecraft, Institute of Aerodynamics and Flow Technology, DLR, Göttingen, 2014
- [47] Lees, L.: *Laminar Heat Transfer over Blunt-Nosed Bodies at Hypersonic Flight Speeds*, Jet Propulsion, vol. 26, no. 4, pp. 259-269, 274, April 1956
- [48] Legge, H., *Kontinuierliche Hyperschallwindkanäle geringer Gasdichte*, 9. Lehrgang für Raumfahrttechnik, Versuchsanlagen IV, Göttingen 1971
- [49] Legge, H., *Force and Heat Transfer on Delta Wing from Continuum to Free Molecular Flow*, Proceedings of the 18th International Symposium on Rarefied Gas Dynamics, pp. 104-114, Volume 160, University of British Columbia, Vancouver, British Columbia, Canada, July 26-30, 1992, ISSN 0079-6050, 1994
- [50] Lerpe, A., *Implementierung einer Software für die Messdatenauswertung der Versuchsanlage CCG/STG und ihre Integration in die Datenmanagementinfrastruktur*, Diplomarbeit, Berufsakademie Mannheim, 2007
- [51] Macauley, W., H., *A note on the deflection of beams*, Messenger of Mathematics, 48, p. 129ff, 1919
- [52] Maes, V., *Thermal Coupling Simulation of the V2G Nozzle Cores using Tau and ANSYS*, Internship report, Department Spacecraft, Institute of Aerodynamics and Flow Technology, DLR, Göttingen, 2014
- [53] Maslov, A. A., Mironov, *Experimental Investigation of the Hypersonic Low-Density Flow Past a Half-Closed Cylindrical Cavity*, Fluid Dynamics, Vol. 31, No. 6, 1996
- [54] Matting, F. W., *Approximate Bridging Relations in the Transitional Regime between Continuum and Free-Molecule Flows*, Journal of Spacecraft and Rockets, Vol. 8, No. 1 pp. 35-40, 1971
- [55] Mc Bride. D., D., Sherman, P., M., *Pitot Pressure in Hypersonic Flow with Condensation*, AIAA Journal, vol. 9, no. 12, pp. 2354-2357, 1970

- [56] Mehta, U., Aftosmis, M., Bowles, J., Pandya, S., *Skylon Aerodynamics and SABRE Plumes*, 20th AIAA International Space Planes and Hypersonic Systems and Technologies Conference, Glasgow, Scotland, 2015
- [57] Messerschmid, E., Fasoulas, S., *Raumfahrtsysteme – Eine Einführung mit Übungen und Lösungen*, 2. Auflage, Springer Verlag, ISBN-3-540-21037-7, 2005
- [58] Moss, J. N., Blanchard, R. C., Wilmoth, R. G., Braun, R. D., *Mars Pathfinder Rarefied aerodynamics: Computations and Measurements*, 36th AIAA Aerospace Science Meeting & Exhibit, Reno, NV, USA, January 12-15, 1998
- [59] Moss, J. N., Glass, C. E., Greene, F. A., *Blunt Body Aerodynamics for Hypersonic Low Density Flows*, 25th International Symposium on Rarefied Gas Dynamics; 21-28 Jul. 2006; Saint Petersburg; Russia, 2006
- [60] Müller-Eigner, R., *Aerodynamische Untersuchungen an elliptischen Körpern im hypersonischen Vakuumwindkanal der DLR*, DLR-IB 222-90 A 28, 1990
- [61] Muntz, E. P., *Rarefied Gas Dynamics*, Annual Review of Fluid Mechanics, Volume 21 pp 387-422, ISSN 0066-4189, 1989
- [62] Munz, C.-D., Westermann, T., *Numerische Behandlung gewöhnlicher und partieller Differenzialgleichungen*, Springer Verlag, ISBN: 3-540-29867-3, 2005
- [63] Oswatitsch, K., *Ähnlichkeitsgesetz für Hyperschallströmung*, ZAMP, vol. II, pp. 249-264, 1951
- [64] Oswatitsch, K., *Contributions to the Development of Gasdynamics*, pp. 76-88. Vieweg Verlag, 1980
- [65] Padilla, J. F., Boyd, I. D., *Assessment of Rarefied Hypersonic Aerodynamics Modeling and Windtunnel Data*, 9th AIAA/ASME Joint Thermophysics and Heat Transfer Conference, San Francisco, CA, USA, 5-8 June 2006
- [66] Potter, J. L., *Transitional, Hypervelocity Aerodynamic Simulation and Scaling*, 20th AIAA Thermophysics Conference, pp. 79-96, Williamsburg, VA, USA, 1986
- [67] Potter, J. L., *Rarefied-flow Aerodynamics*, Final Summary Report, NASA Research Grant NAG-1-921, 1 Jan. 1989 to 31 May 1992
- [68] Rajasooria, G. P. D., Brundin, C. L., *An Experimental Investigation of the Laminar Near Wake Behind a Circular Cylinder in a Mach 6, Rarefield Air Stream*, University of Oxford, Oxford, UK, 1970
- [69] Riabov, V. V., *Rarefaction Effects in Hypersonic Aerodynamics*, Proceedings of the 27th International Symposium on Rarefied Gas Dynamics, Pacific Grove, CA, USA, July 10-15, 2010
- [70] Rose, P. H., Stark, W. I.: *Stagnation Point Heat-Transfer Measurements in Dissociated Air*, Journal of the Aeronautical Sciences, pp. 86-97, February 1958
- [71] Scaled Composites, Hangar 78 Airport, 1624 Flight Line, Mojave, CA 93501, *Space flight profile SpaceShipOne*, http://www.scaled.com/http://www.scaled.com/images/uploads/pdf/SS1_flight_profile.pdf, last access 19th August 2015
- [72] Scanlon, T. J., Roohi, E., White, C., Darbandi, M., Reese, J. M., *An Open Source, Parallel DSMC Code for Rarefied Gas Flows in Arbitrary Geometries*, Computer and Fluids, ISSN 0045-7930, 2010
- [73] Schaaf, S. A., Chambré, P. L., *Flow of Rarefied Gases*, Princeton University Press, Princeton, New Jersey, USA, 1961
- [74] Schlegat, T., Hannemann, K., *Test Matrix Definition of Low Density Experiments in V2G*, FAST20XX Project Deliverable D.3.4.1.1, Göttingen, Germany, 2010
- [75] Schlegat, T., Hannemann, K., *Experimental Investigation in V2G*, FAST20XX Project Deliverable D.3.4.1.2, Göttingen, Germany, 2012

- [76] Schlegat, T., Votta, R., Marini, M., *Bridging Functions*, FAST20XX Project Deliverable D.3.4.1.3, Göttingen, Germany, 2013
- [77] Schlegat, T., Re-design of the Strain Gauge Force Balances for the Hypersonic Vacuum Wind Tunnel Göttingen, DLR FB 2013-18, 2015
- [78] Schlegat, T., *Flow Characterisation of the DLR Hypersonic Vacuum Wind Tunnel (V2G) using the Contoured Nozzle at Nominal Free Stream Mach Numbers of 13, 15, 17, 21 and 24*, DLR-EB 224-2016 C 1, 2016
- [79] Schlegat, T., *Experimental Investigation of Rarefaction Effects on Aerodynamic Coefficients of Slender and Blunt Re-entry Vehicles*, DLR-EB 224-2017 C 18, 2017
- [80] Schlosser, A., *Numerische Untersuchung der Strömungsbedingungen im V2G-Vakuumwindkanal Göttingen*, Internship report, Department Spacecraft, Institute of Aerodynamics and Flow Technology, DLR, Göttingen, 2014
- [81] Sharipov, F., *Hypersonic flow of rarefied gas near the Brazilian satellite during its reentry into atmosphere*, Brazilian Journal of Physics, vol. 33, no. 2, São Paulo, June, 2003
- [82] Sippel, M., Schwanekamp, T., *The SpaceLiner Hypersonic System – Aerothermodynamic Requirements and Design Process*, 8th European Symposium on Aerothermodynamics for Space Vehicles, 2.3 – 6.3.2015, Lisbon, Portugal, 2015
- [83] Speckmann, H.-D., Chun, Ch.-H., *Six-Component Force and Moment Measurements on the HERMES-R Configuration in Hypersonic Rarefied Flow at $Ma = 12, 15$ and 22 in the Vacuum Wind Tunnel V2G*, DLR-IB 222-89 C 06, 1989
- [84] Speckmann, H.-D., Chun, Ch.-H., *Three Component Measurements on Cones in Hypersonic Rarefied Flows at $Ma 22$* , DLR-IB 222-90 C 18, 1990
- [85] Stemmer, C., *Hyperschallströmungen*, Lecture notes, Chair of Aerodynamic and Fluid mechanics, Department of Mechanical Engineering, Technical University of Munich, <https://www.tum.de/en/>, <https://www.aer.mw.tum.de/fileadmin/tumwaer/www/pdf/lehre/hyperschallstroem/skript.pdf>, last access 14th March 2018
- [86] Stevens, V. I., *Hypersonic Research Facilities at the Ames Aeronautical Laboratory*, Journal of Applied Physics, vol. 21, pp.1150-1155, 1950
- [87] Van Driest, E. R., *The Problem of Aerodynamic Heating*, Aeronautical Engineering Review, pp. 26-41, October 1956
- [88] Vas, I. E., Koppenwallner, G., *The Princeton University high pressure hypersonic nitrogen tunnel N-3*, Princeton University Report 690, Princeton, NJ, USA, 1964
- [89] Votta, R., Ranuzzi, G., Marini, M., Schlegat, T., Hannemann, K., *DSMC simulations in V2G conditions and comparison with measurements, conclusions on DSMC code validation*, FAST20XX Project Deliverable D.3.4.2.2, Naples, Italia, 2012
- [90] Votta, R., Ranuzzi, G., Marini, M., Morsa, L., Fels, G., Schlegat, T., Hannemann, K., *Numerical and Experimental Analysis of Low-Density Effects in Suborbital Flight of FAST20XX*, 43rd AIAA Thermophysics Conference, New Orleans, USA, 2012
- [91] Votta, R., Marini, M., Ranuzzi, G., Schlegat, T., Hannemann, K., Schwanekamp, T., Sippel, M., *Rarefied Aerothermodynamics Technology Development for Future High-Altitude High-Speed Transport (EU-FAST20XX)*, AIAA SPACE 2013 Conference & Exposition, San Diego, USA, 2013
- [92] Weiland, C., *Aerodynamic Data of Space Vehicles*, Springer Verlag, ISBN-978-3-642-54168-1, 2014

- [93] Wuest, W., Koppenwallner, G., *The Hypersonic low density wind tunnel of the Aerodynamische Versuchsanstalt Göttingen – operational behaviour and results on vibrational relaxation*, AVA-Bericht 67 A 52, 1967
- [94] Wuest, W., *Eine Hypersonische Windkanalanlage für kleine Gasdichten*, AVA-Bericht 70 A 09, 1970
- [95] Wuest, W., *Näherungsweise Berechnung von Kräften und Momenten in hypersonischer Strömung geringer Dichte*, AVA-Bericht 70 A 17, 1970
- [96] Wuest, W., *Experimentelle und theoretische Untersuchung verschiedener Konfigurationen von tragenden Wiedereintrittskörpern in hypersonischer Strömung geringer Dichte*, AVA-Bericht 70 A 33a, 1970
- [97] Zimmermann, F., Burkhardt, J., Schöttler, U. M., *Comparison of Guidance Concepts for a Semi-Ballistic Reentry Capsule*, AIAA Meeting Papers on Disc, DOI: 10.2514/6.1996-3708, 1996

Appendix A – General Facts, Specifications and Derivations

Table 7: V2G specifications

Description	Dimension	Magnitude / Range
Similarity parameters		
Mach number	[–]	10 – 26
Reynolds number	[1/m]	$10^4 – 10^6$
Mean free path (Knudsen number * ref. length)	[m]	$4 * 10^{-5} – 10^{-3}$
Geometric data		
Test chamber diameter	[cm]	40
Test chamber length	[cm]	60
Typical test article size	[cm]	10
Nozzle half angle	[°]	14.6
General data		
Test gas		mainly N ₂
Test time		several hours continuously
Reservoir pressure	[bar]	0.25 – 100
Reservoir temperature	[K]	290 – 1500
Static pressure	[mbar]	$10^{-3} – 10^{-1}$
Static temperature	[K]	7 – 35
Pump facility performance		
Three individual pump assemblies with five and seven pump stages Overall maximum pumping speed (at up to 133 [Pa] intake pressure)	[m ³ /s]	62.5
Used measurement techniques		
Force and moment measurements with 3-component strain gauge balance		
Surface pressure distribution measurements		
Heat transfer measurements		
Flow visualisation by radio frequency flow discharge		

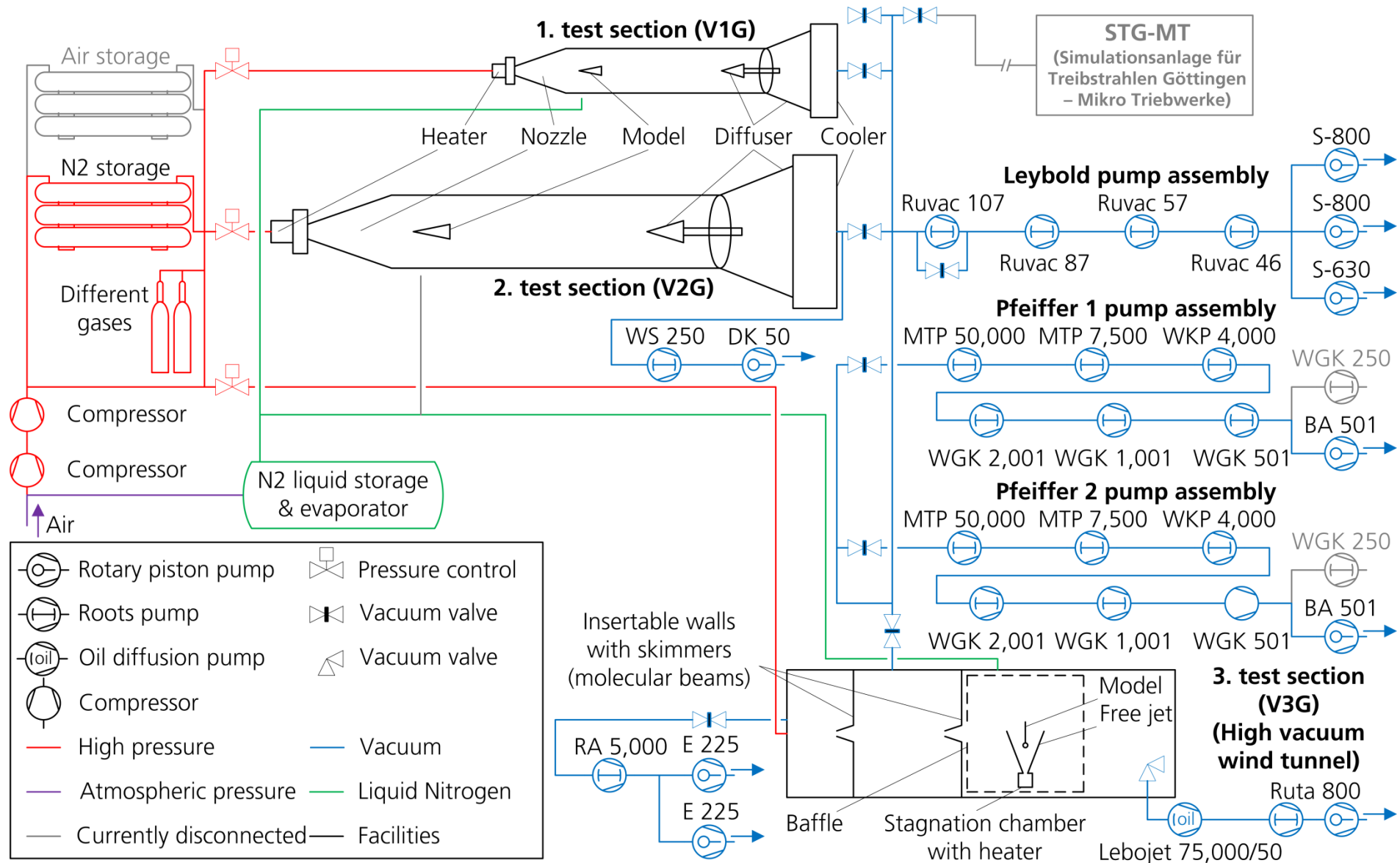


Fig. 112: Sketch of VxG facility

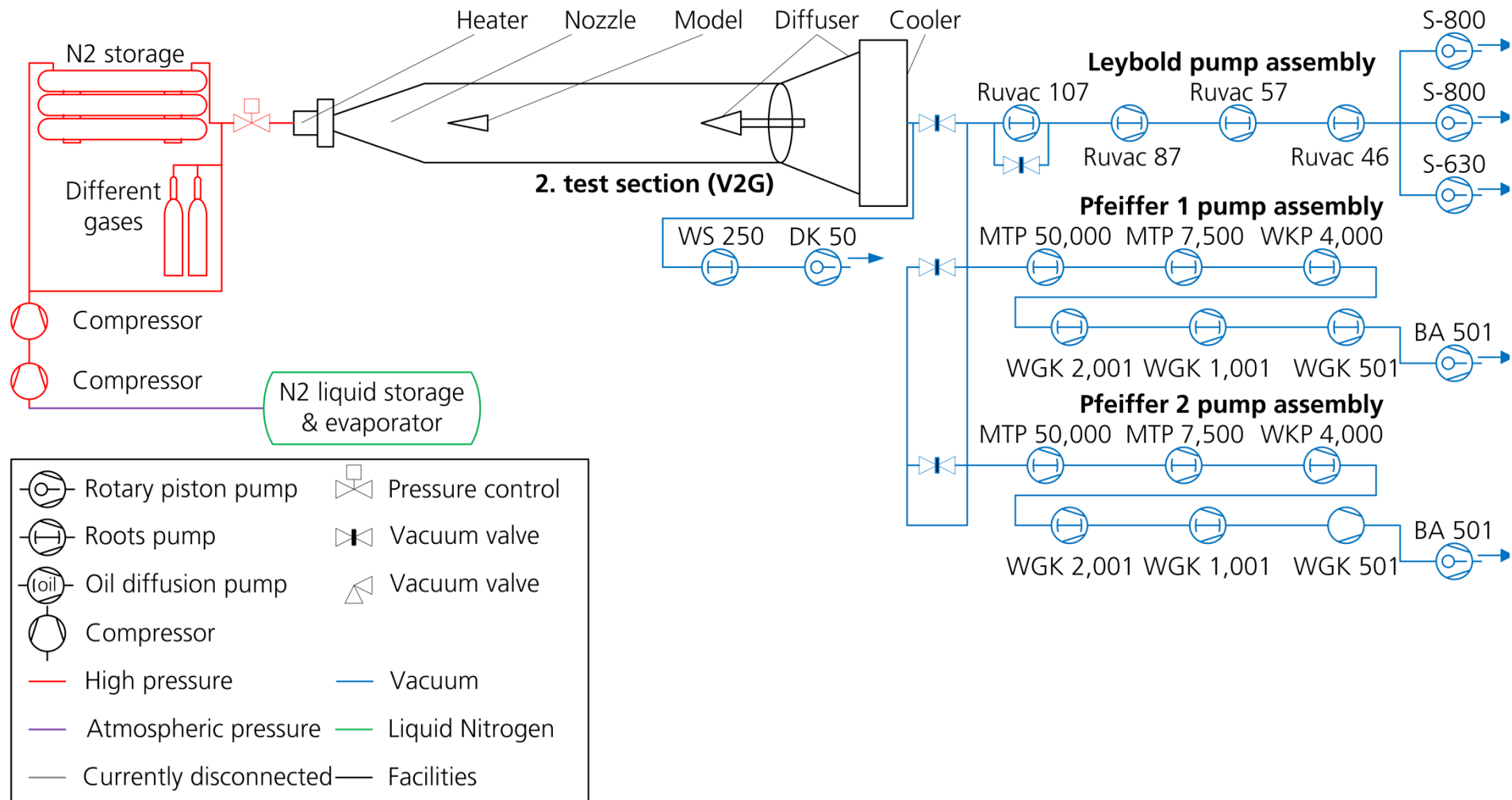


Fig. 113: Sketch of VxG facility (reduced to V2G relevant infrastructure)

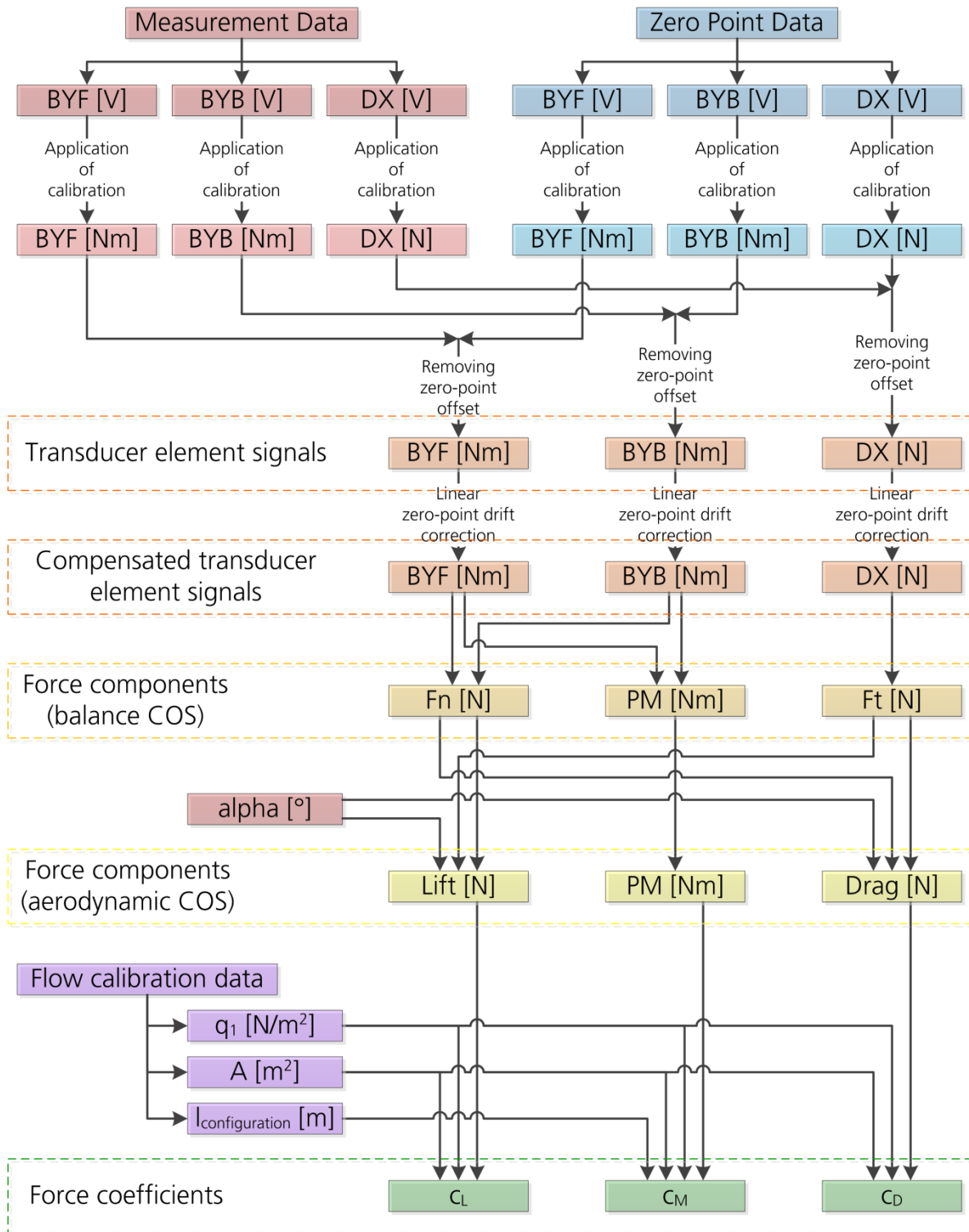
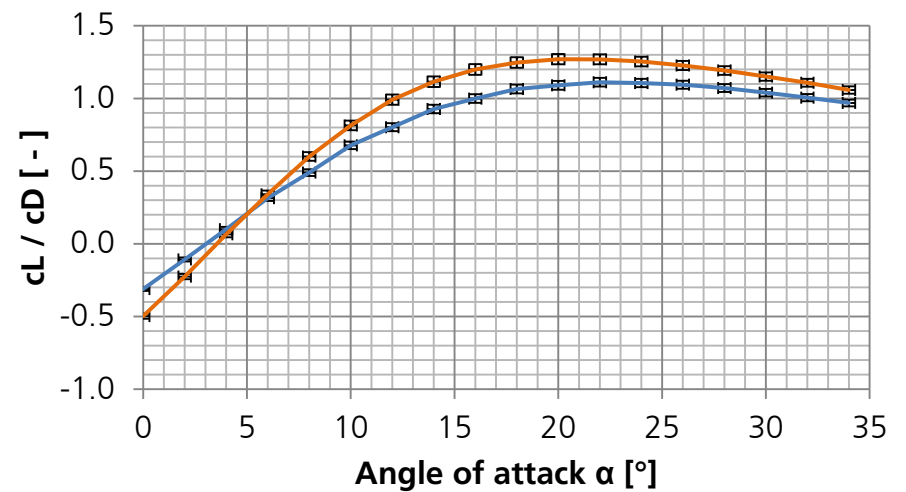
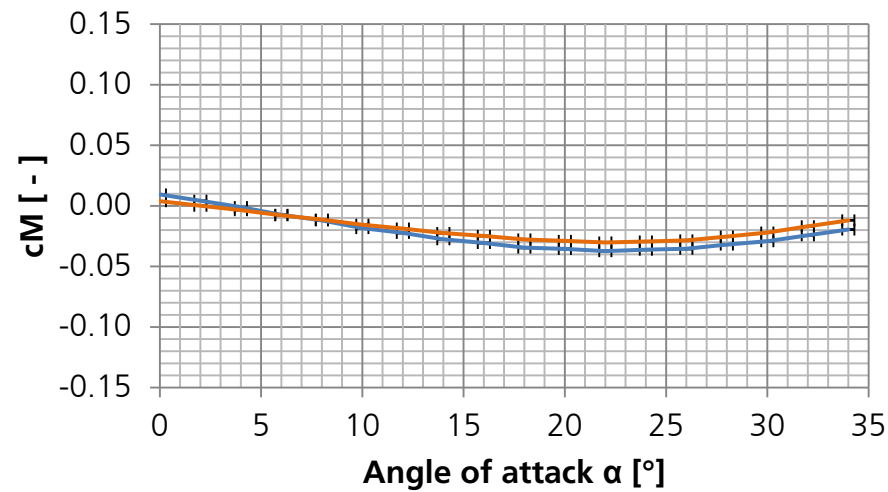
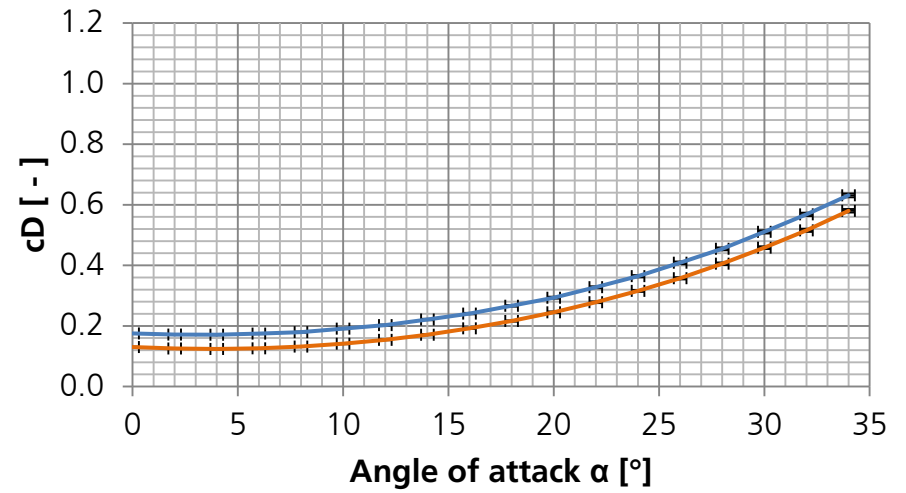
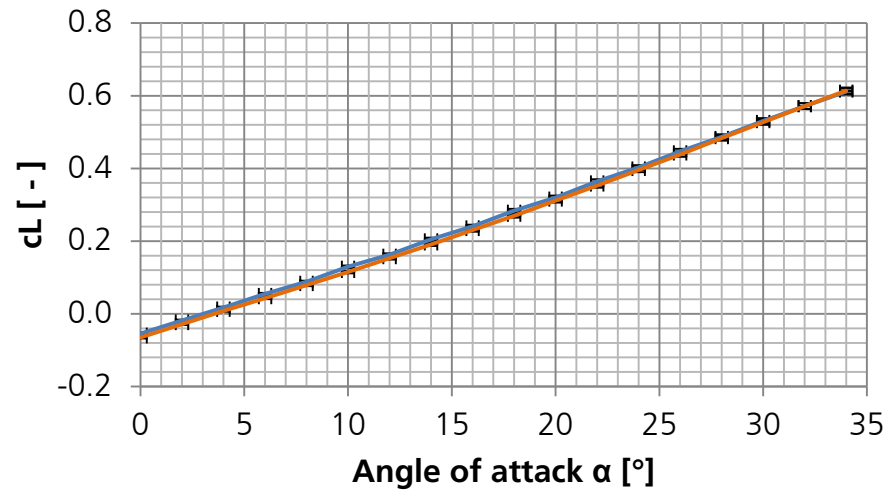


Fig. 114: Flow chart of data processing procedure^[77]

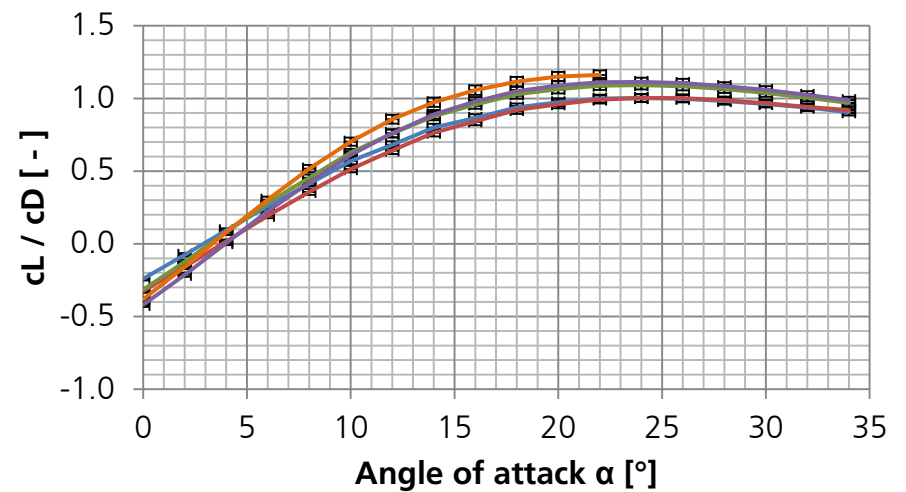
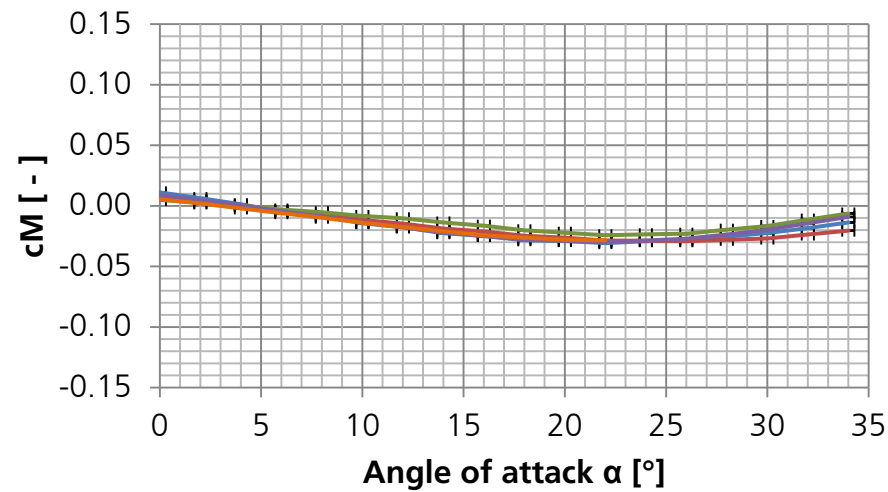
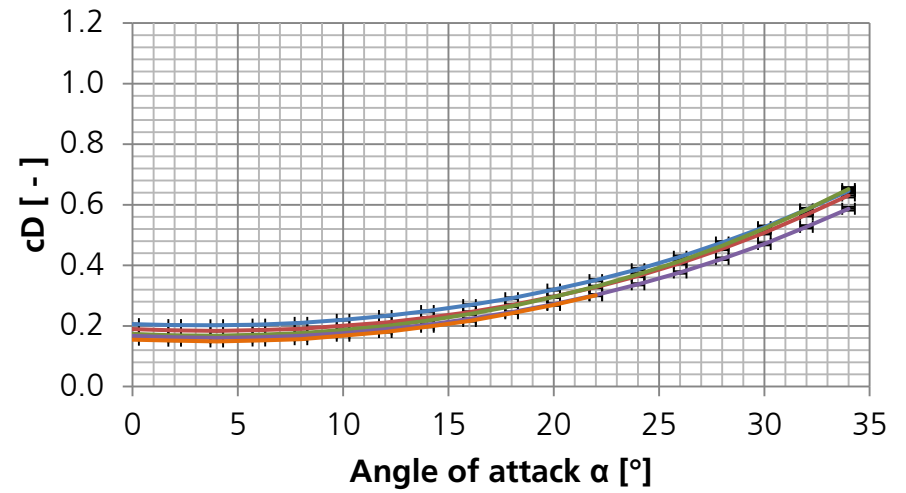
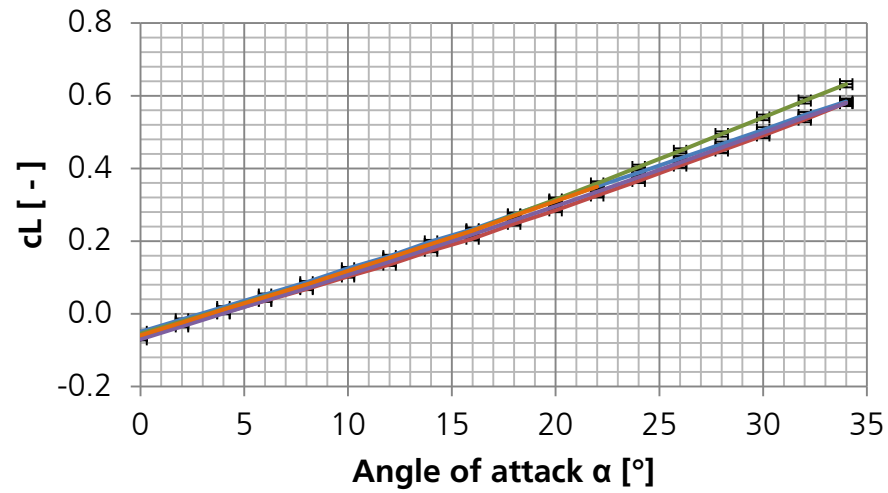
Appendix B – Rarefaction Effects

Appendix B contains the full set of plots showing the rarefaction effects.



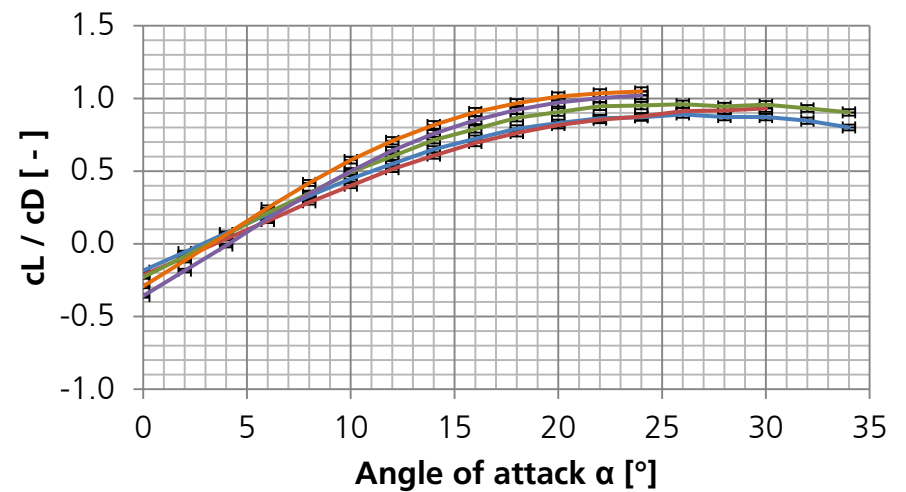
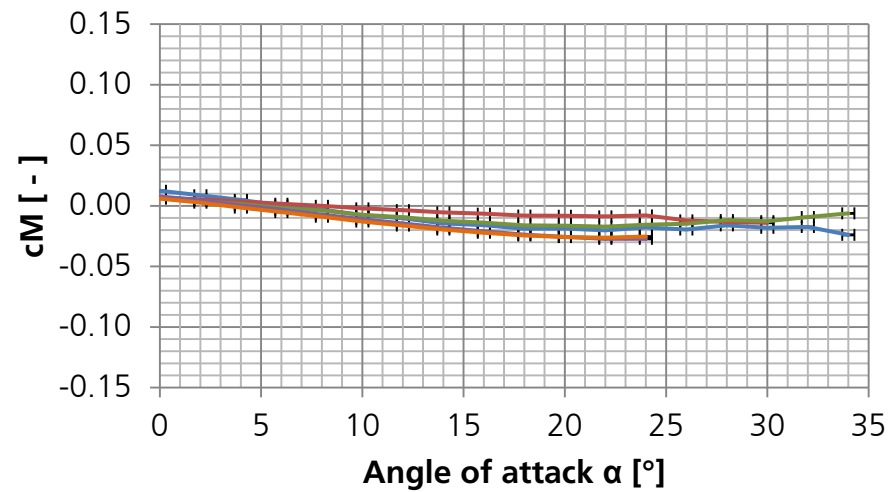
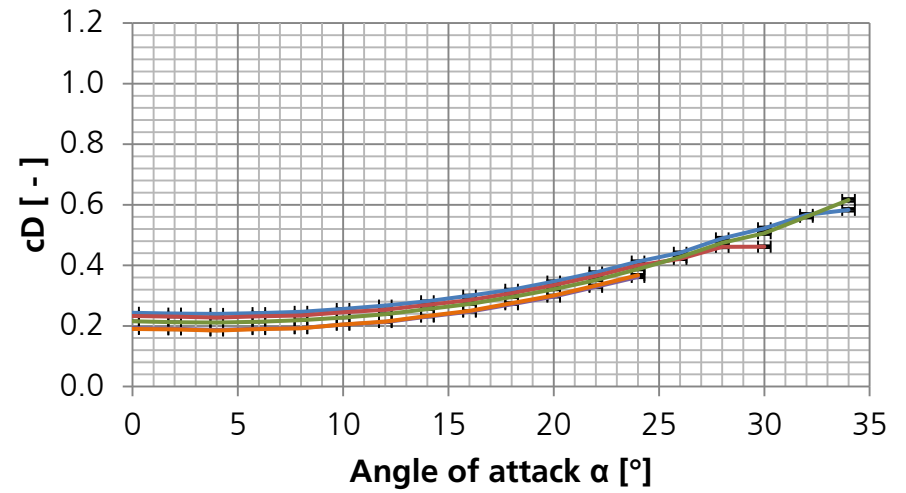
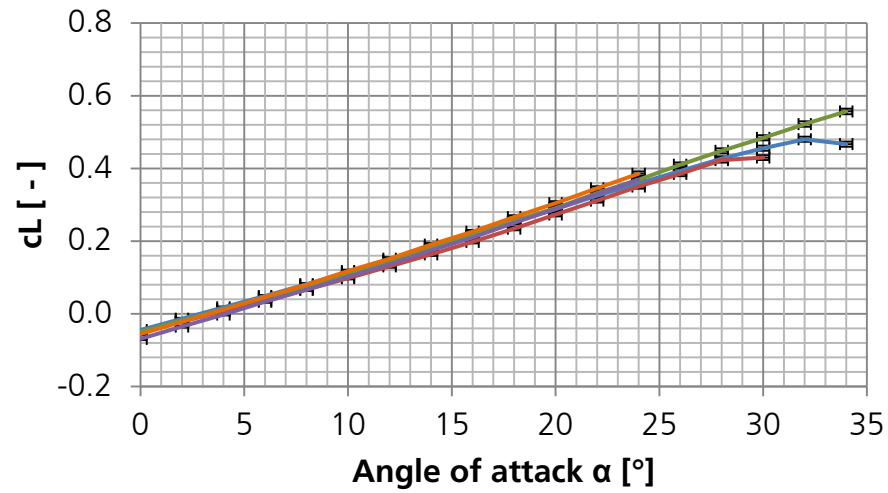
— $Kn_1 = 1.57E-3,$ — $Kn_1 = 7.16E-4,$
 $M_1 = 25.7$ $M_1 = 12.0$

Fig. 115: Rarefaction effects on aerodynamic coefficients ($Re_1 = 2.5e+4$, SHEFEX III)



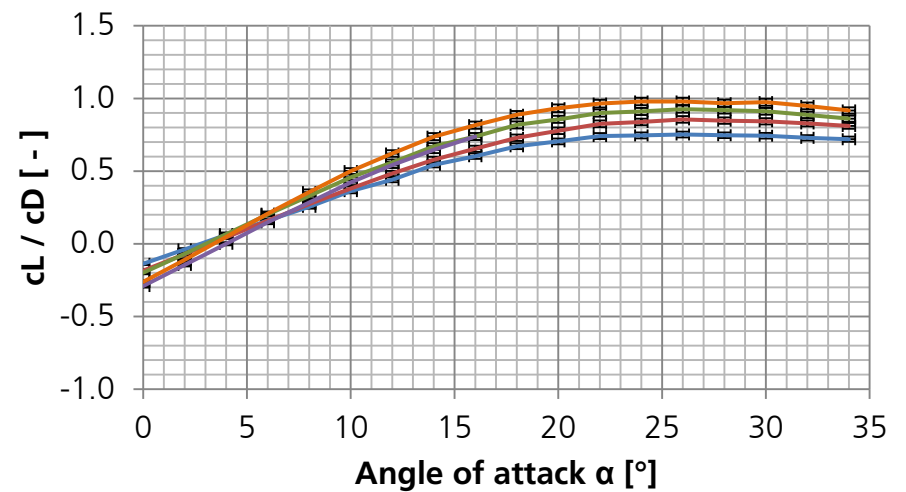
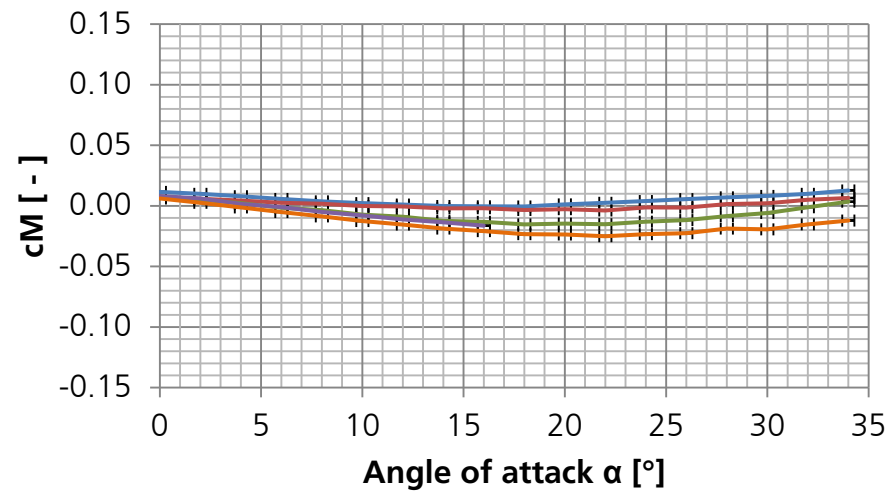
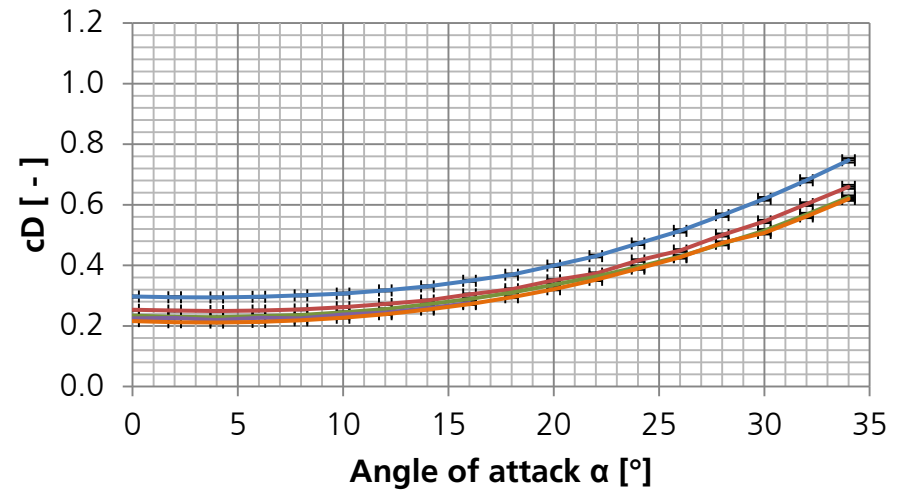
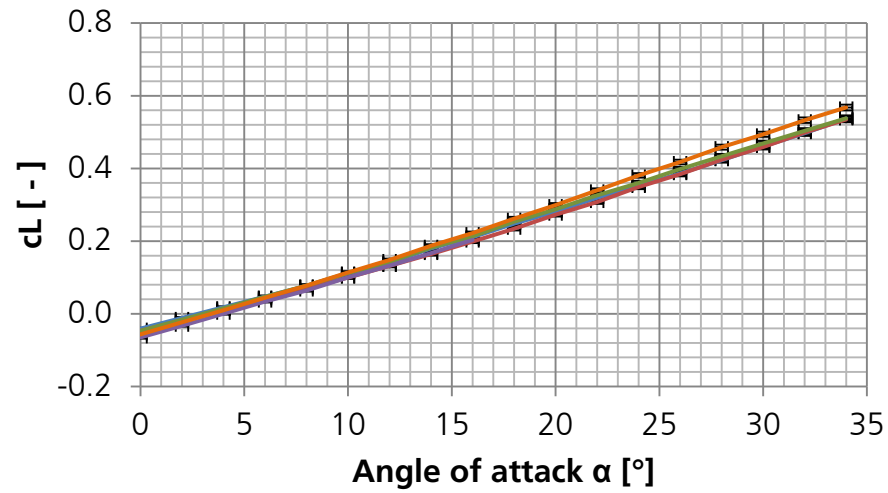
— $Kn_1 = 2.74E-3,$ — $Kn_1 = 2.37E-3,$ — $Kn_1 = 1.82E-3,$ — $Kn_1 = 1.46E-3,$ — $Kn_1 = 1.11E-3,$
 $M_1 = 25.1$ $M_1 = 22.9$ $M_1 = 17.9$ $M_1 = 14.2$ $M_1 = 11.4$

Fig. 116: Rarefaction effects on aerodynamic coefficients ($Re_1 = 1.5e+4$, SHEFEX III)



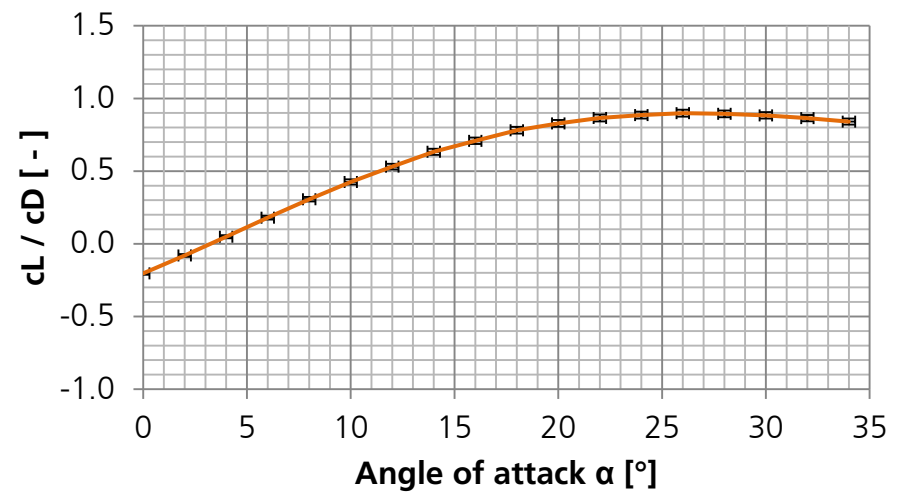
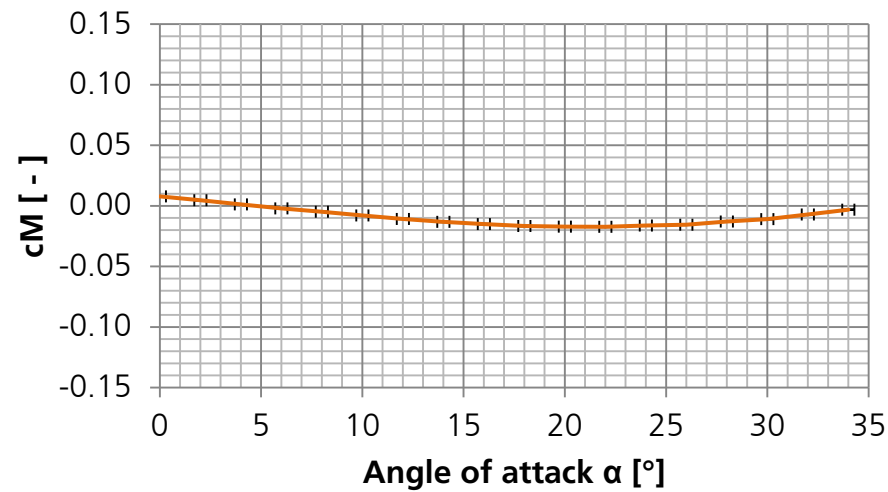
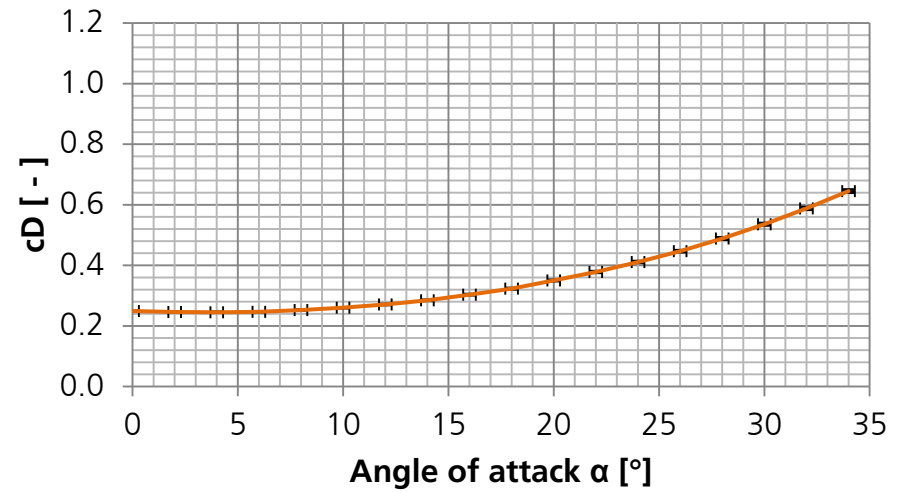
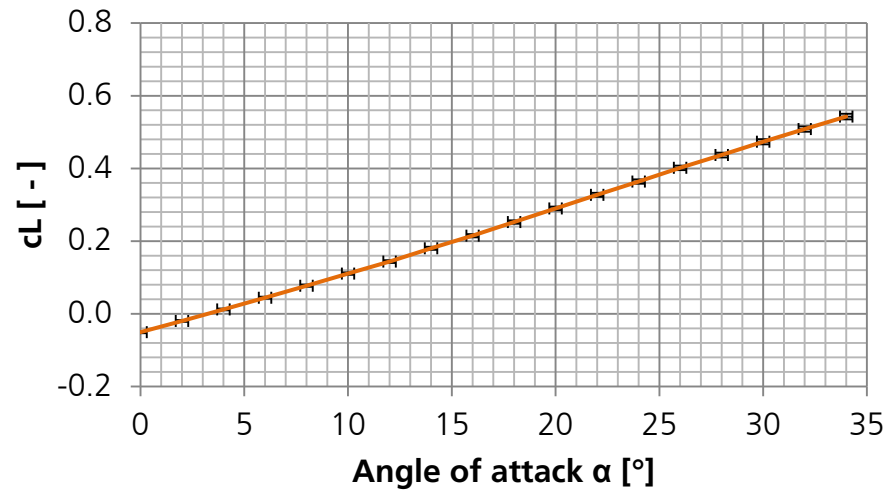
— $Kn_1 = 4.57E-3,$ $M_1 = 24.3$
— $Kn_1 = 3.92E-3,$ $M_1 = 21.2$
— $Kn_1 = 2.98E-3,$ $M_1 = 15.9$
— $Kn_1 = 2.51E-3,$ $M_1 = 13.5$
— $Kn_1 = 2.15E-3,$ $M_1 = 11.2$

Fig. 117: Rarefaction effects on aerodynamic coefficients ($Re_1 = 7.9e+3$, SHEFEX III)



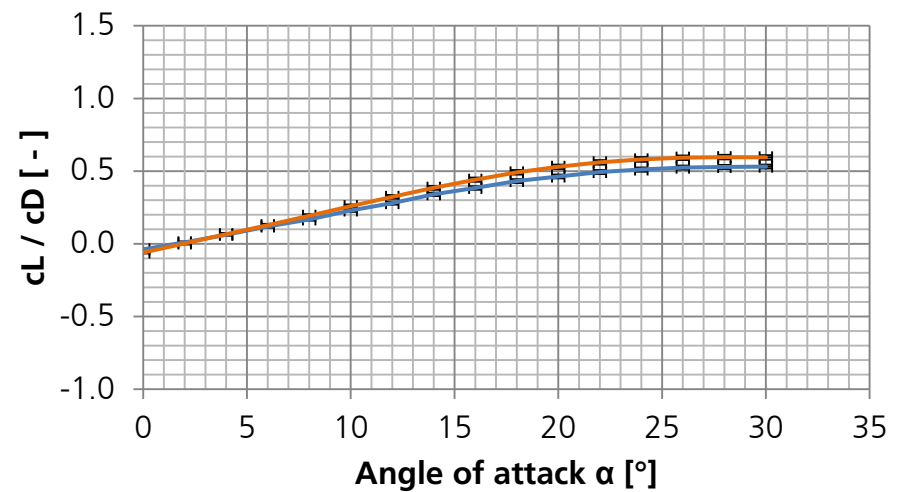
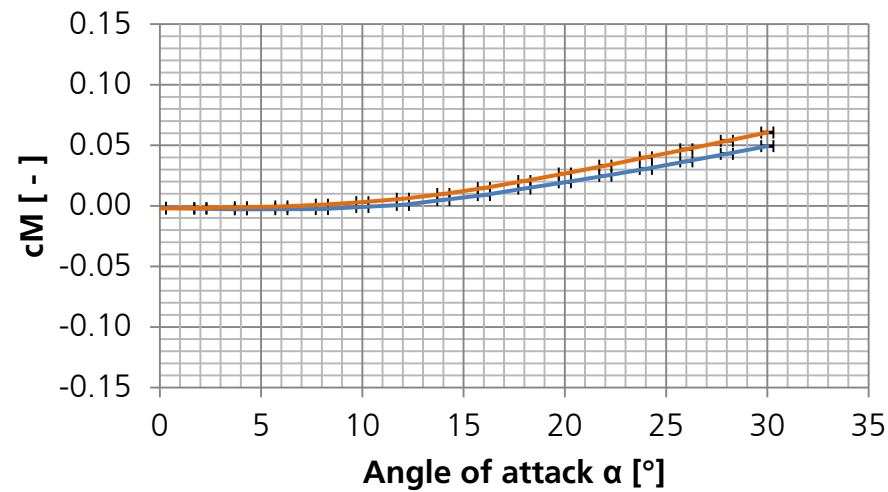
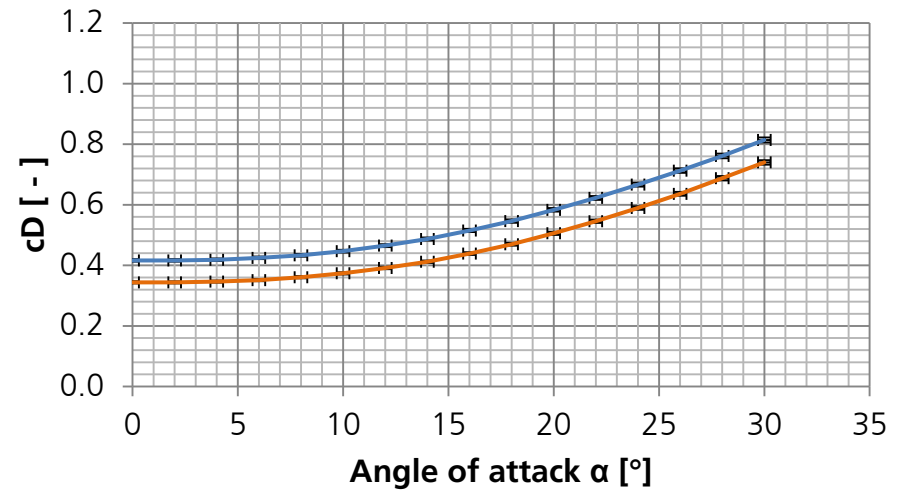
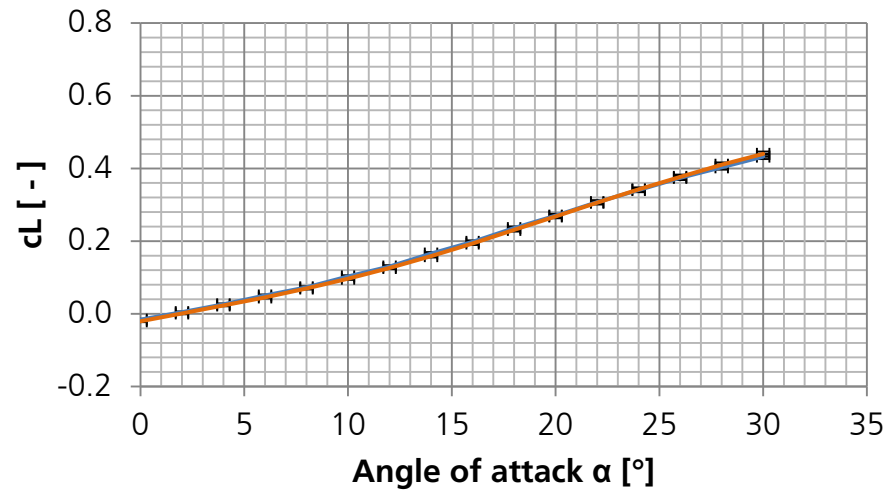
— $Kn_1 = 7.23E-3,$ $M_1 = 23.3$
— $Kn_1 = 6.06E-3,$ $M_1 = 19.4$
— $Kn_1 = 4.49E-3,$ $M_1 = 13.8$
— $Kn_1 = 4.26E-3,$ $M_1 = 12.3$
— $Kn_1 = 3.65E-3,$ $M_1 = 11.2$

Fig. 118: Rarefaction effects on aerodynamic coefficients ($Re_1 = 4.6e+3$, SHEFEX III)



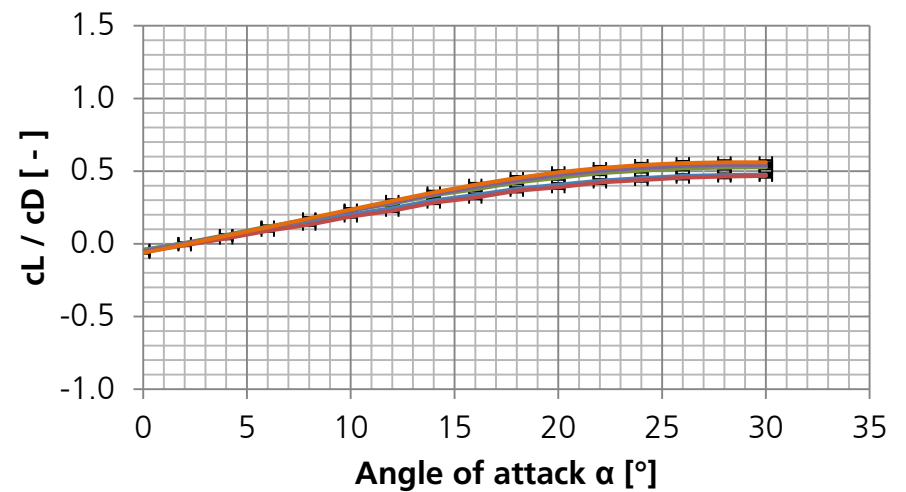
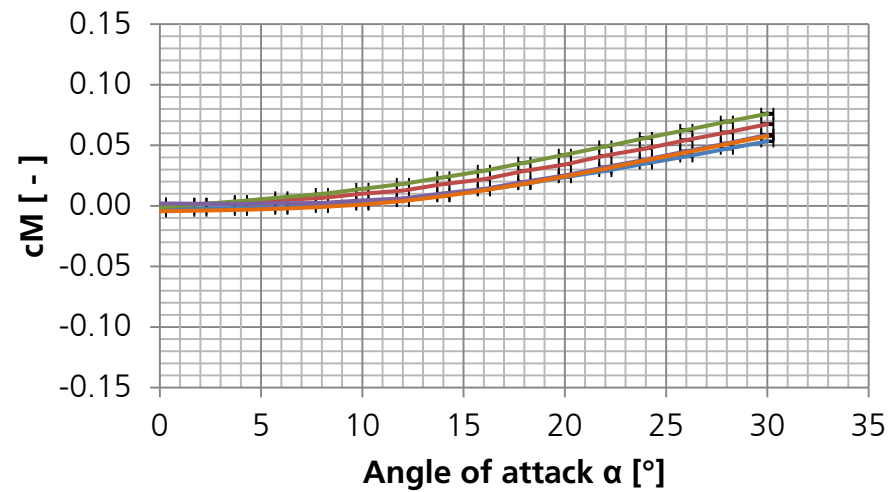
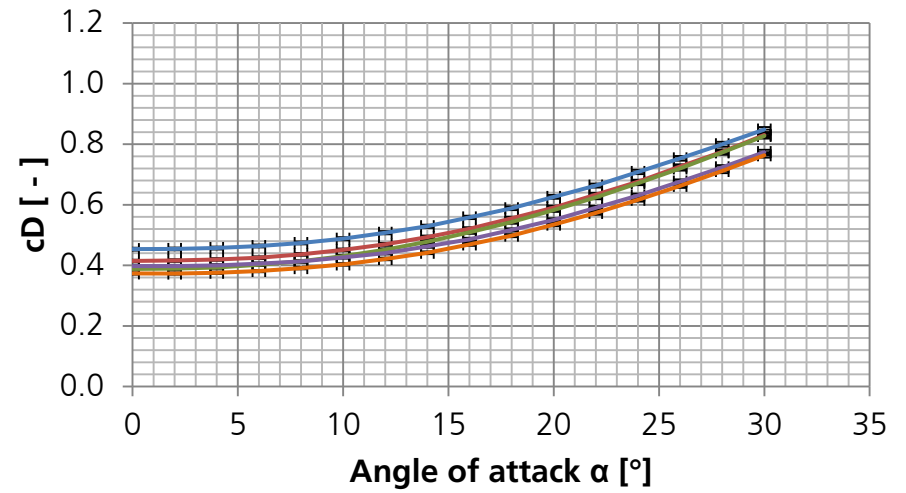
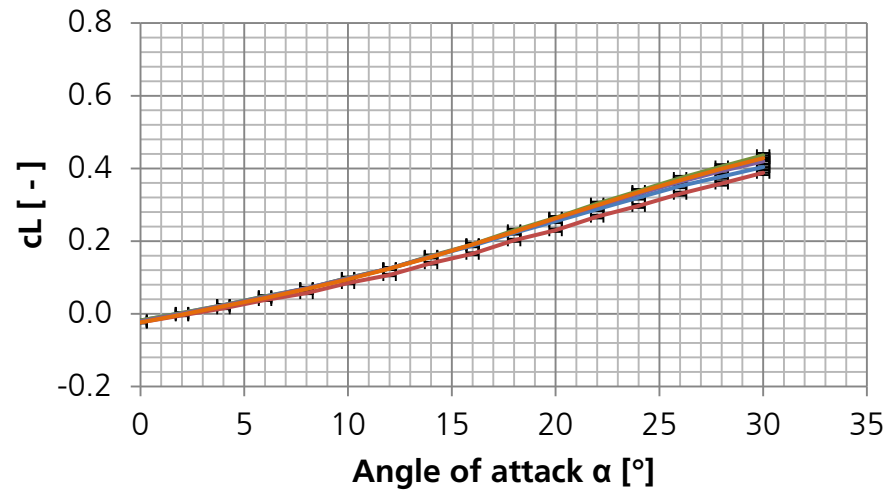
— $Kn_1 = 5.75E-3,$
 $M_1 = 10.4$

Fig. 119: Rarefaction effects on aerodynamic coefficients ($Re_1 = 2.7e+3$, SHEFEX III)



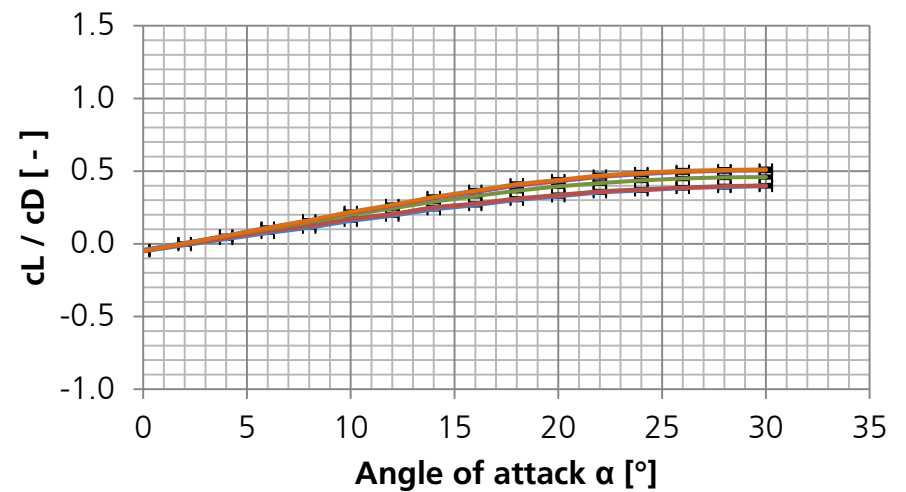
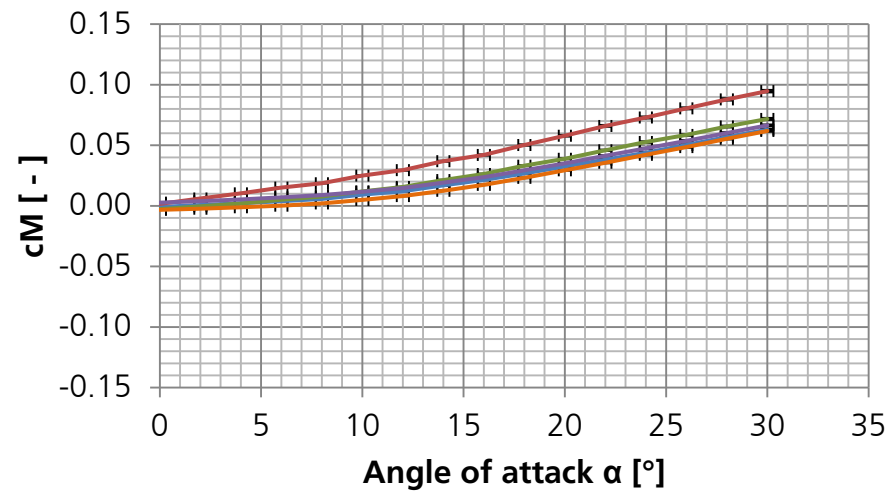
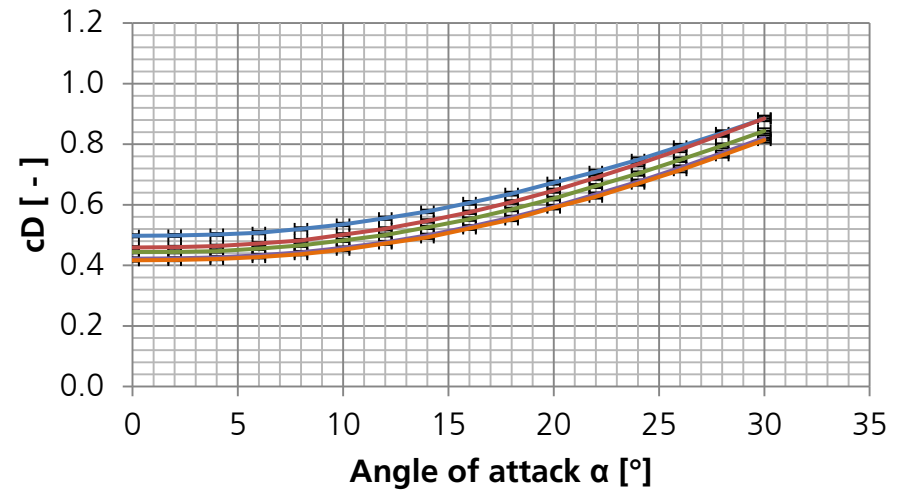
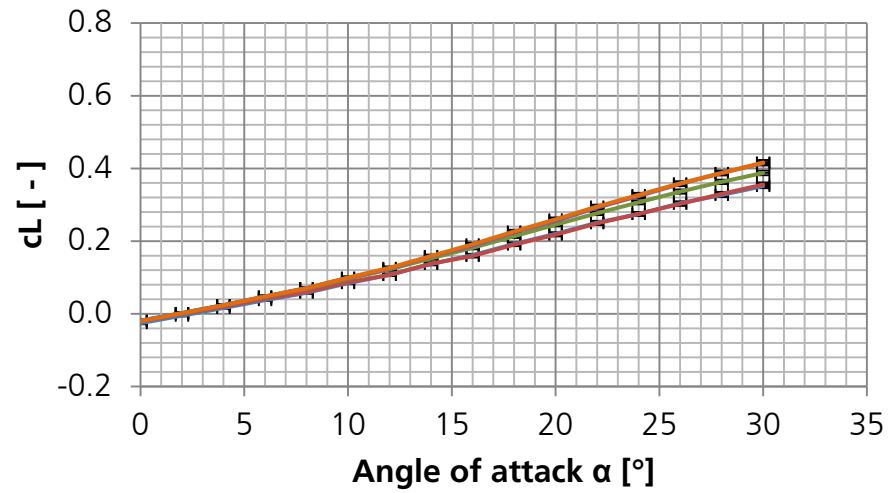
— $Kn_1 = 1.92E-3,$ — $Kn_1 = 8.75E-4,$
 $M_1 = 25.7$ — $M_1 = 12.0$

Fig. 120: Rarefaction effects on aerodynamic coefficients ($Re_1 = 2.0e+4$, COLIBRI)



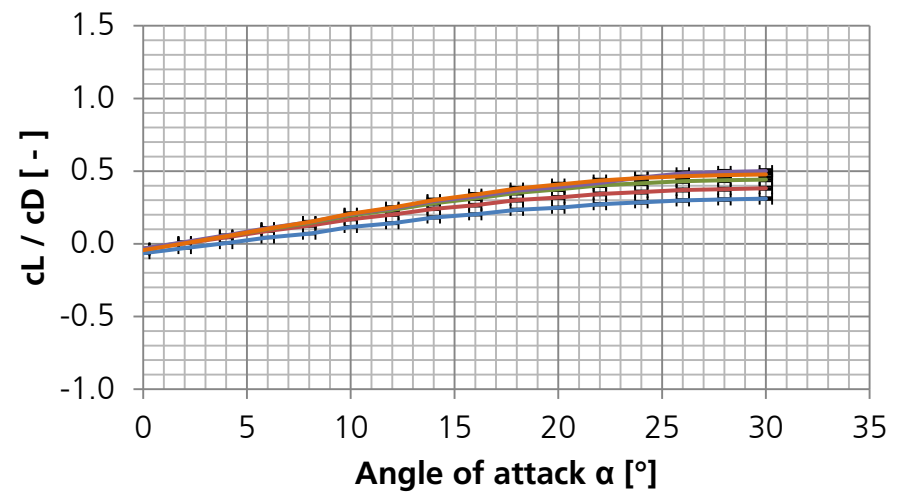
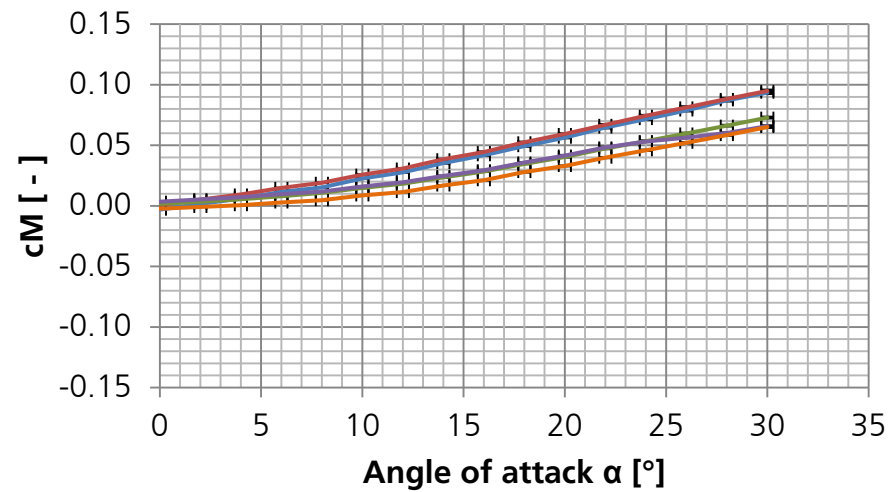
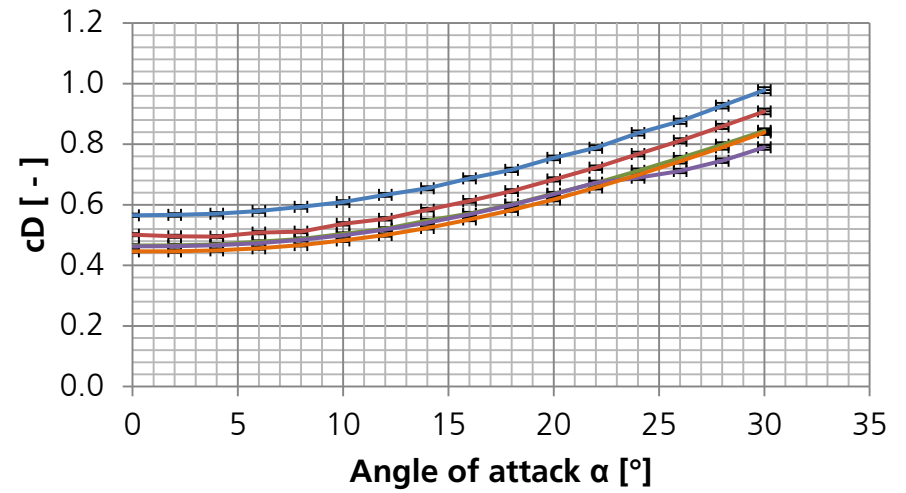
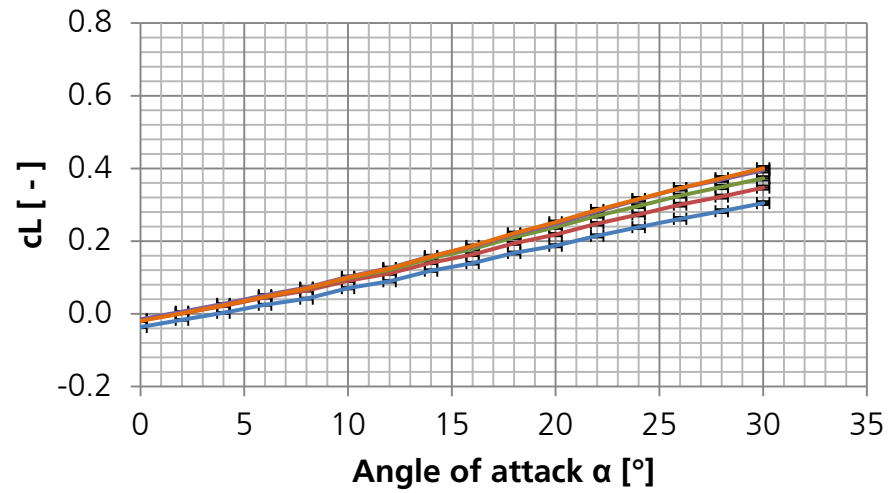
— $Kn_1 = 3.35E-3, M_1 = 25.1$
 — $Kn_1 = 2.89E-3, M_1 = 22.9$
 — $Kn_1 = 2.22E-3, M_1 = 17.9$
 — $Kn_1 = 1.78E-3, M_1 = 14.2$
 — $Kn_1 = 1.36E-3, M_1 = 11.4$

Fig. 121: Rarefaction effects on aerodynamic coefficients ($Re_1 = 1.2e+4$, COLIBRI)



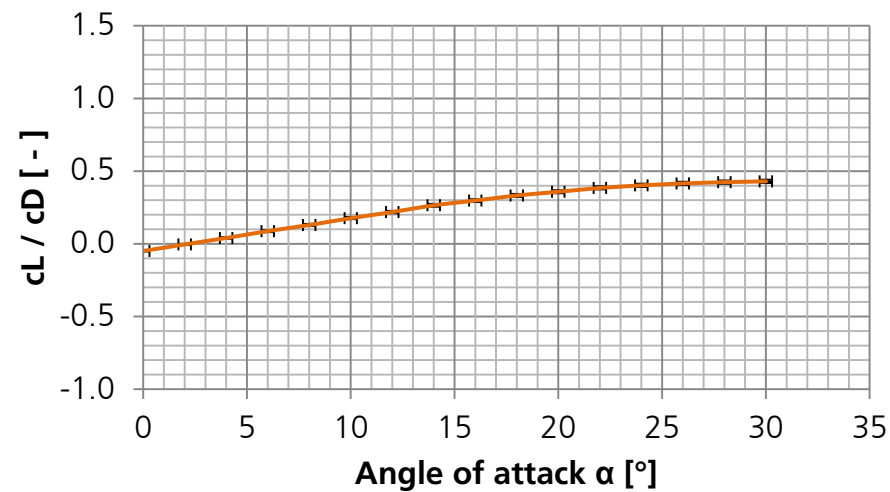
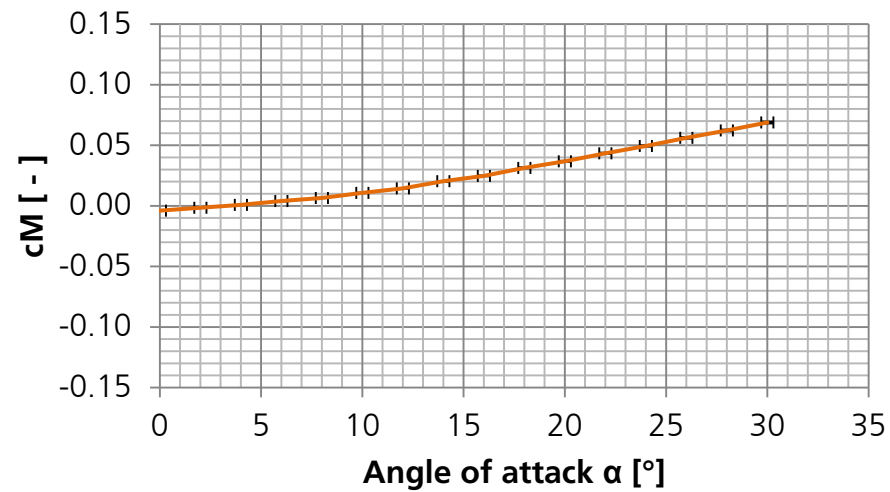
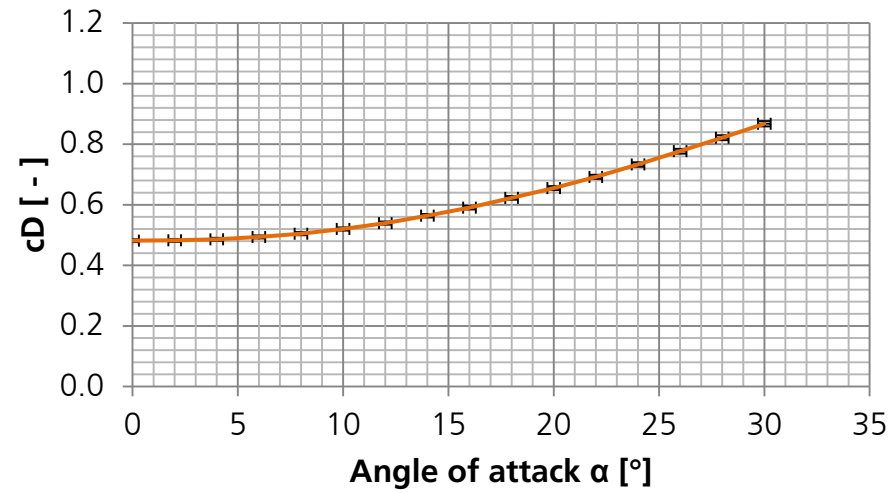
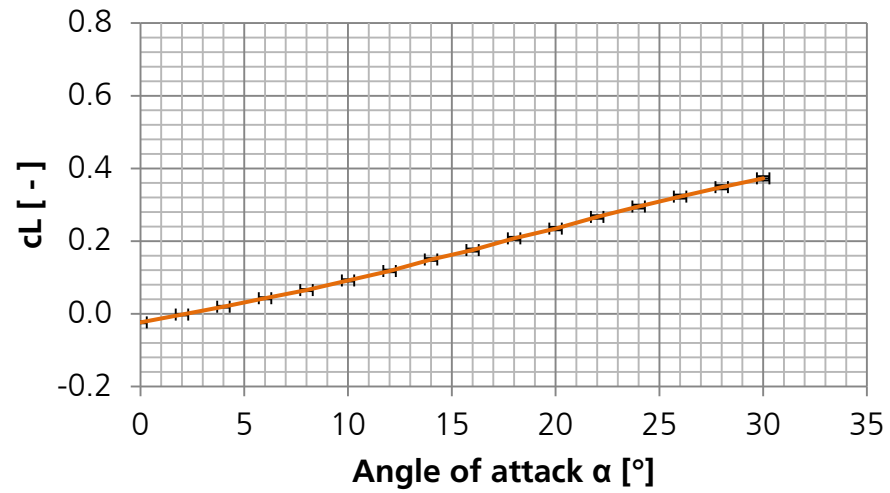
— $Kn_1 = 5.58E-3,$ $M_1 = 24.3$
 — $Kn_1 = 4.80E-3,$ $M_1 = 21.2$
 — $Kn_1 = 3.64E-3,$ $M_1 = 15.9$
 — $Kn_1 = 3.07E-3,$ $M_1 = 13.5$
 — $Kn_1 = 2.62E-3,$ $M_1 = 11.2$

Fig. 122: Rarefaction effects on aerodynamic coefficients ($Re_1 = 6.4e+3$, COLIBRI)



— $Kn_1 = 8.84E-3, M_1 = 23.3$
 — $Kn_1 = 7.41E-3, M_1 = 19.4$
 — $Kn_1 = 5.49E-3, M_1 = 13.8$
 — $Kn_1 = 5.21E-3, M_1 = 12.3$
 — $Kn_1 = 4.47E-3, M_1 = 11.2$

Fig. 123: Rarefaction effects on aerodynamic coefficients ($Re_1 = 3.8e+3$, COLIBRI)



— $Kn_1 = 7.03E-3,$
 $M_1 = 10.4$

Fig. 124: Rarefaction effects on aerodynamic coefficients ($Re_1 = 2.2e+3$, COLIBRI)

